



**UNIVERSITY OF CATANIA**

**CIVIL ENGINEERING AND ARCHITECTURE DEPARTMENT**

**Ph.D. Course in  
Evaluation and Mitigation of Urban and Land Risks  
XXXIV Cycle**

**Title of thesis:**

*Urban regeneration strategies and sustainable design solutions for mitigation of the Urban Heat Island phenomenon and the improvement of the outdoor thermal-hygrometric wellbeing of Mediterranean cities*

**Ph.D. student: Detommaso Maurizio**

**Advisor: Prof. Francesco Nocera**

**Co-advisors: Prof. Francesco Martinico**

**Co-advisors: Ph.D. Vincenzo Costanzo**

## TABLE OF CONTENTS

<b>Abstract</b> .....	5
1.1 Significance of the study.....	5
1.2 The objective of the research.....	6
1.3 Novelty.....	6
1.4 Research framework.....	6
<b>Chapter two: General background and problem statement</b> .....	<b>8</b>
2.1 Structure and outline of the chapter.....	9
2.2 Extreme heat events and their impacts on the cities.....	9
2.3 The Urban Heat Island (UHI) phenomenon.....	11
2.4 Description of UHI causes and of the underlying physical phenomena.....	13
2.5 The heat stress impacts on humans' health.....	20
2.6 Building and energy use.....	22
2.7 Air pollution.....	23
2.8 Urban heat stress mitigation strategies.....	23
2.9 Approaches and methods for the estimate of the Mean Radiant Temperature ( $T_{mrt}$ ).....	32
2.10 Outdoor thermal comfort estimation methods.....	34
<b>Chapter three: Research Methodology</b> .....	<b>39</b>
3.1 Structure and outline of the chapter.....	40
3.2 Methodology.....	40
3.2.1 Calibration and validation of the urban Macroscale model.....	42
3.2.2 Calibration and validation of the urban Microscale model.....	44
3.3 Local Climate Zone (LCZ) Classification: state of the art, input, and output data.....	46
3.3.1 State of the art.....	46
3.3.2 Methods for LCZ mapping.....	55
3.3.3 GIS method for LCZ mapping of the investigated area.....	58
3.4 Urban Multi-scale Environmental Predictor (UMEP): state of the art, input and output data...	61
3.4.1 UMEP: features and framework.....	61
3.4.2 SOLWEIG: Features, physical and mathematic model, input and output data.....	62
3.4.3 SUEWS: Features, physical and mathematic model, input, and output data.....	69
3.5 ENVI-met: state of the art, input, and output data.....	72
3.5.1 Features and physical model.....	72
3.5.2 Microclimate analysis limitations.....	77

3.6 Outdoor Microclimate parameters and thermal comfort indices .....	79
3.6.1 Mean Radiant Temperature .....	79
3.6.2 Universal Thermal Climate Index .....	81
3.7 Proposed urban heat stress mitigation strategies .....	82
3.7.1 Urban Greening Infrastructures and renovation scenarios .....	83
3.7.2 Compact and high built-up density areas: a design scenario .....	83
3.7.3 Open and low-rise area: Urban Heat Mitigation strategies .....	85
3.7.3.1 Cool materials .....	86
3.7.3.2 Cool roof .....	86
3.7.3.4 Green roof .....	87
<b>Chapter Four: Case study and analysis of results at urban Microscale and at large-scale .....</b>	<b>88</b>
4.1 Structure and outline of the chapter .....	89
4.2 The case study .....	89
4.2.1 UMEP modelling: Morphological input for Local Climate Zones classification .....	90
4.3 Local Climate Zones (LCZs) classification of the study area .....	92
4.4 Description of the morphological features of the heat stress risk area .....	101
4.4.1 Morphological features of the investigated area .....	101
4.4.2 Description of two representative sites selected as heat stress risk areas .....	103
4.5 Macroscale climate analysis .....	106
4.5.1 Geometrical modelling of the investigated area .....	106
4.5.2 Thermo-physical data of the urban Macroscale model .....	109
4.5.3 Rural weather data morphed through SUEWS for model calibration .....	110
4.5.4 Validation of SOLWEIG model with field measurements .....	113
4.5.5 Assessment of the urban energy balance .....	117
4.5.6 2D spatial distribution of Mean Radiant Temperature in the investigated area .....	118
4.5.7 Relationship between Universal Thermal Climate Index (UTCI) and Mean Radiant Temperature .....	120
4.5.8 Assessment of the potential effectiveness of heat stress mitigation scenario .....	123
4.5.8.1 Morphological properties and modelling of the investigated area in design scenario .....	123
4.5.8.2 Assessment of the effects of design scenario on the outdoor thermal comfort	125
4.5.9 Heat stress risk analysis .....	132
4.6 Microscale climate analysis .....	135

4.6.1 Article - Application of weather data morphing for calibration of urban ENVI-met microclimate models. Results and critical issues. Urban Climate, 2021, 38, 100895	136
4.6.2 Extract of the article “A risk index for assessing heat stress mitigation strategies. An application in the Mediterranean context”	160
4.6.3 Article - Sustainable Urban Greening and Cooling Strategies for Thermal Comfort at Pedestrian Level. Sustainability 2021, 13, 3138.	166
4.7 Macroscale modelling vs Microscale modelling: a comparison in terms of $T_{mrt}$	190
<b>Chapter five: Conclusions and perspectives</b>	<b>194</b>
<b>Acknowledgements</b>	<b>201</b>
<b>References</b>	<b>202</b>

## **Abstract**

### **1.1 Significance of the study**

The climate change is strongly impacting cities, which currently have to face more frequently the effects caused by extreme weather events.

Cities have a crucial role, not only as potential targets of climate vulnerability but also as the main contributor. The specific composition of people and their activities, as well as urban morphology, exacerbates heat waves because of the Urban Heat Island (UHI) effect.

Climate change projections often do not include the effects of the UHI and this implies that the actual magnitude of future impacts on the health of urban residents is underestimated.

One of the most pressing and unifying issues is the maintenance of comfortable outdoor conditions under rising air temperatures and increasing extreme heat events. To inform urban planners and city officials, the assessment of outdoor thermal comfort has gained remarkable interest.

Nowadays, the assessment of urban climate and outdoor thermal comfort in cities is dealt with field measurements and numerical modelling.

Although measurements can deliver highly accurate data, they are rather expensive and time-consuming endeavors that can only inform us about specific thermal conditions that exist at a given place and time. On the contrary, numerical modelling allows the prediction of the potential effects of urban warming in the next years in order to assess future climate scenarios as well as to grasp the spatial and temporal variability of outdoor human thermal comfort conditions. In this way, numerical modelling can be used as a predictor instrument to alert urban residents about the most heat wave-risk days. Thereby, suitable design scenarios aimed at the mitigation of the urban warming can be fine-tuned.

Nowadays, most studies deal with the outdoor climate analysis of densely built-up areas using an approach based on neighborhood scale or urban Microscale. Although Microscale models allow an accurate evaluation of the effects of potential UHI mitigation strategies, they are characterized by spatial and temporal limitations. Since the urban climate is influenced by processes taking place on different scales, the urban Macroscale-based climate analysis should be adopted to evaluate the intra-urban areas climate interactions. Macroscale analysis approach is particularly interesting for the analysis of urban heat stress events distributions. In fact, the Macroscale allows limitations to be overcome the of single-station data provided by most of the meteorological stations and can represent intra-urban temperature differences at relatively small scales, which correspond to the spatial detail of information needed for the design of interventions in the urban space. An urban Macroscale analysis thus allows identification the most sensitive heat wave risk areas and planning of suitable mitigation heat stress scenarios in relation to their climate and morphological features.

## 1.2 The objective of the research

The objective of this research was to analyse urban microclimate and identify the potential heat stress mitigation strategies in the most risky areas at urban Macroscale level.

To identify the urban areas more prone to heat stress risk, a new **Local Climate Zone (LCZ)** classification is proposed based on both geometrical and thermal features of the urban fabric.

Urban Macroscale and Microscale simulations were run in order to appraise the differences in the outcomes (if any) and to design suitable mitigation strategies.

## 1.3 Novelty

The innovations introduced in this study were:

- The analysis of outdoor microclimate parameters by means of top-down approach (from the Macroscale down to the Microscale).
- Urban morphing of the rural/suburban climate data
- The identification of heat stress risk areas through a new Local Climate Zones (LCZs) classification.
- The identification of a potential correlation (if any) between a widely used outdoor thermal comfort metrics such as the **Universal Thermal Climate Index (UTCI)** and heat stress risk for more vulnerable people.

## 1.4 Research framework

A framework that summarizes the main processes and procedures used to achieve the research objectives is shown in Figure 1.1.

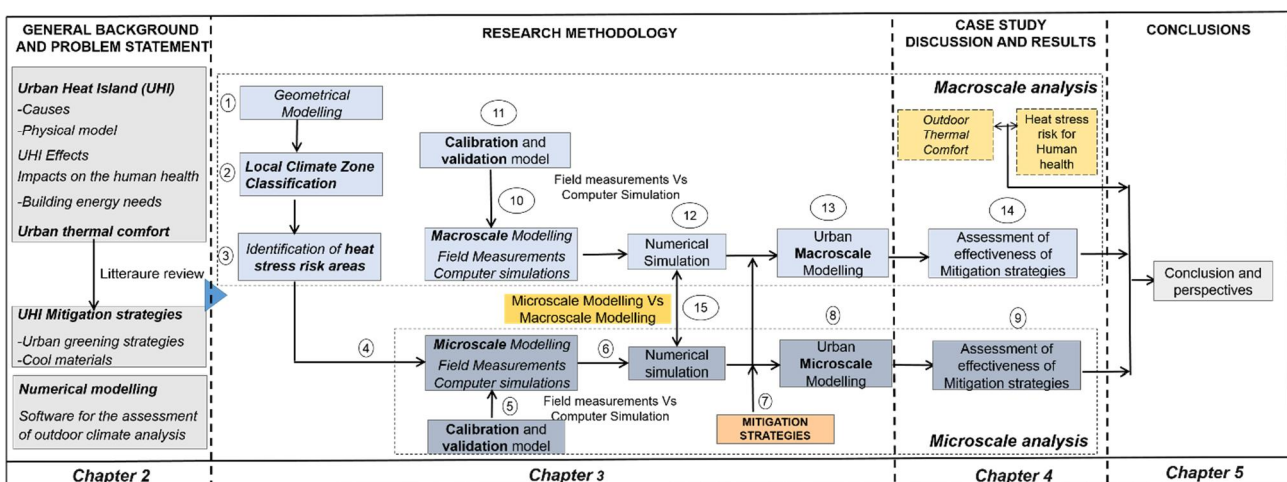


Figure 1.1. Research framework.

The research framework is divided into four sections. In the second section, the general background related to the Urban Heat Island (UHI) phenomena, their impact on the cities and vulnerable people was described. In this section, the urbanization factors that affect the formation of UHI, the causes of the physical phenomena and the effects of heat waves on the human health of urban residents, building energy needs and issues regarding outdoor thermal comfort, were discussed. Literature review of UHI mitigation strategies and their effects on the outdoor microclimate in the urban environment was carried out. In particular, the role of vegetation and cool materials in mitigating urban heat stress and how they should be applied in relation to morphological features of urban contexts was described. To this aim, the results of several studies about the effects of urban greening strategies (green roof, green façade, and street trees) and cool roofs are reported. Furthermore, the background of the approaches and methods used to analyse urban climate and outdoor thermal comfort at different scales was described.

The third section describes the methodology adopted in this research.

A new Local Climate Zones (LCZs) classification based on large scale analysis was carried out in order to identify the heat stress risky areas.

A large scale analysis of the almost entire urban area of investigated city was carried out on a calibrated and validated Macroscale numerical model developed with the UMEP (Urban Multi-scale Environmental Predictor) tool.

The most sensitive heat stress risk areas were analyzed using an approach based on Macroscale models and detailed Microscale models to define the more suitable strategies for heat stress mitigation. The numerical Microscale models of the investigated areas were calibrated and validated according to criteria explained in chapter 3. Microscale models were developed by means of ENVI-met software.

Based on validated models, numerical simulations of current and mitigation scenarios were carried out in order to estimate the potential effectiveness of the proposed UHI mitigation strategies. Mitigation strategies were defined according to the morphological and geometrical features of the investigated areas. The results derived by implementation of UHI mitigation strategies in the investigated areas both at urban Microscale and Macroscale levels were discussed in section 4.

Both urban Macroscale and Microscale simulations of the risky areas were compared in order to assess the reliability of the numerical modelling at large-scale.

The fifth section discussed the meaningful conclusions extracted from the simulation models based on Microscale and large-scale models respectively. Furthermore, recommendations and suggestions of perspectives for further research in the future are pointed out.

**CHAPTER TWO: GENERAL BACKGROUND  
AND PROBLEM STATEMENT**



## **2.1 Structure and outline of the chapter**

This chapter discusses the background and problem statement and is outlined as follow:

- Section 2.2 describes the background related to extreme heat events and the role of the cities as potential targets/contributors of heat.
- Sections 2.3 and, 2.4 give a description of the urbanization factors that affect the formation of Urban Heat Island and of the underlying physical phenomena.
- Sections 2.5, 2.6, and, 2.7 describe the effects of heat stress on human health, energy consumption of buildings, and air pollution.
- Section 2.8 describes urban heat island mitigation strategies and their effects on the outdoor microclimate.
- Section 2.9 discusses the methods currently employed in the literature to analyse the urban microclimate such as field measurement and numerical modelling.
- Section 2.10 describes the features and issues, the main models and indices used to estimate outdoor thermal comfort.

## **2.2 Extreme heat events and their impacts on cities**

Recent research has found that of all natural disasters, extreme high temperature events are the main cause of weather-related mortality (de' Donato et al., 2015; Petkova et al., 2014; Gabriel and Endlicher, 2011), and they are also expected to be the main factor responsible for additional deaths due to climate change in the coming years (WHO, 2018). Against this background one of the more challenging issues cities and metropolitan areas need to address is the increasing magnitude and frequency of heatwaves. In fact, over the last half-century, the probability of extreme heat events has already changed by orders of magnitude in almost every region of the world, with occurrences that are now up to a hundred times more in respect to a century ago (Eckstein et al., 2019; WMO, 2019). As a result, the frequency and severity of extreme heat have become more visible (Hintz et al., 2018). As a point of fact, cities are hotspot locations, because they are characterized by an addition of several degrees warmer than their surroundings due to specific urban features and their albedo as well as urban waste heat and GHG emissions from infrastructure (Rosenzweig et al., 2011). Therefore, the compact urban settings of cities - through the reduced evaporative cooling caused by lack of vegetation and the production of waste heat - lead bring to elevated surface and air temperatures, generating the conditions for the urban heat island (UHI) phenomenon (Rosenzweig et al., 2011; Oke, 1982; Breil et al., 2018).

To date, more than 54% of the world's population live in urban areas and by 2050 this portion is projected to include two-thirds of the people around the globe (United Nations D of E and SA, 2014).

In Europe, it is proved that more than two-thirds of the population live in urban areas (EU Report, Cities of tomorrow 2011). More than 20 million people are expected to live in cities by 2025 according to the current trend. In the Mediterranean area, the urban population rate is 68% (World Development indicators, 2020). Therefore, an increase in the urbanization process is predicted. This will lead to a remarkable increase of energy use that, in turn, will lead to an increase of carbon dioxide and exploitation of natural resources. Moreover, cities are the heart of the contemporary economy, which means that heatwaves can hamper the economic structures of many regions and can promote budgetary problems and loss of competitiveness (Kamal-Chaoui, 2008). Despite the urbanized area currently covers less than 1% of the earth surface (Oke, 1997), cities are the largest emitters of carbon dioxide, greenhouse gas (GHG), tropospheric ozone and chlorofluoro carbons. Since 85% of global emissions come from cities, Cities have a crucial role (Oke, 1997).

Climate projections (Representative Concentration Pathways, RCPs) as well as socio-economic scenarios (Shared Socio-Economic Pathways, SSPs), which describe respectively alternative climate pathways associated with emission levels (van Vuuren et al., 2011) and societal development trends (Jiang and O'Neill, 2017), estimate an increase of UHI effects due to changes related, among others, to urban density and urban land cover (Oke, 1982; Chapman et al., 2017).

In addition, it is widely demonstrated that the progressive increase of global warming will raise urban temperatures and heat island effect. The UHI phenomenon is predicted to increase with climate change, since mean temperatures, the frequency of heat waves and their duration are forecasted to rise (Vanos et al., 2010).

The heat-related epidemiology literature emphasizes that population expansion under an increasing frequency, intensity, and duration of heatwaves is increasing social vulnerability, exacerbating temperature-mortality relationships (de' Donato et al., 2015; Petkova et al., 2014; Martinez et al., 2018; Michelozzi et al., 2008; McMichael et al., 2008). This is a crucial factor especially for the older people if is considered that they are the more vulnerable people to the effects of heat stress and that nowadays, the aging process of the European population is a long-term trend that is unprecedented in demographic history (EuroStat, 2020). In fact, demographic, and social changes – combined with climate change – are the main reasons why cities are becoming particularly vulnerable places (Panayiotis et al., 2019).

In this context, to understand how cities and urban authorities plan to anticipate and cope with extreme high temperature events, in terms of monitoring and data organization, identification of main stressors and relationships between diverse and relevant factors and providing input for sound political responses is of paramount importance.

On a closer look it becomes evident that conditions within cities are not equal in all their parts and identifying those areas which are particularly vulnerable to heat, either to their physical form or characteristics of their inhabitants, is particularly important. As a point of fact, there is today growing evidence showing that many cities are becoming key players in shaping and implementing new initiatives aimed at dealing with the challenges brought about by climate change, at urban scale, through mitigation and adaptation measures (Carter, 2011; Carter et al., 2015). In order to identify areas more vulnerable to heat stress risk and implement aimed mitigation strategies, it is necessary to increase efforts towards the application of methods based on urban Macroscale analysis (Hu et al., 2019).

### **2.3 The Urban Heat Island (UHI) phenomenon**

Urban and industrial growth and their implied environmental changes have altered the urban climate. The urbanization process has remarkably increased the impervious surface reducing dramatically the pervious surfaces and vegetation areas thus producing a radical change in the nature of the earth's surface and the atmospheric properties in an urban area. Such changes have a direct effect on the local climate of urban spaces increasing the air temperature and the surface temperatures with regards to suburban or rural areas.

The air temperature difference between urban and suburban rural areas is known as "Urban Heat Island" (UHI). During this phenomenon, much higher air temperatures can be observed in the central urban areas compared to the suburban zones and the surrounding rural areas.

UHI may be defined as a phenomenon, caused by urbanization, where surface and atmospheric modifications, generally lead to modifying the urban climate that becomes warmer than the surrounding areas (Voogt, 2003, Coseo et al., 2014). Urban Heat Island describes a characteristic of the urban area in which the nocturnal temperatures are warmer than the surroundings landscape (Santamouris, 2013). Warmer urban air temperatures are a result of some interrelated causes associated with the urban modification of the natural surface, such as heat and the pollution released from anthropogenic activities in the urban environment (Morris and Simmonds, 2000).

The Urban Heat Island is associated with the development of cities and urban expansion (Taleb et al., 2013). It has a direct effect on energy efficiency, the environment, and ultimately, human comfort and health. The urban environment is characterized by some features like the high density of population and buildings, high energy consumption and the shortage of green areas (Busato et al., 2014). According to an investigation by Hathway et al., (2012) the absorption of heat from the surfaces of buildings and the ground, the loss of moisture in the air due to the reducing of vegetation and a wide area of traffic and pavement, can contribute to the occurrence of Urban Heat Island.

UHI phenomenon alters the temperature of different atmospheric layers over a city at different scales (Mesoscale, Local scale, and Microscale). Therefore, all overlying atmospheric layers included in the Planetary Boundary Layer (PBL) are affected by changes due to the urbanization process. These changes can also radically modify the environment on Mesoscale affecting the climate of areas located up to 1 km from urban boundaries (Oke, 1976).

Figure 2.1 represents the classification of the urban atmosphere layers at Mesoscale (a), Local scale (b) and Microscale (c) respectively.

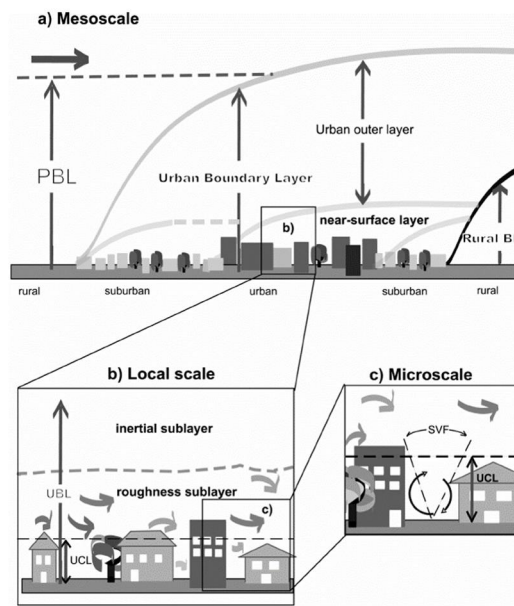


Figure 2.1. Classification of the urban atmosphere area layers. a) Mesoscale; b) Local scale; c) Microscale.

PBL can be defined as the lowest part of the atmosphere above the earth's surface which has a variable amplitude with the seasonal and daily climate variations. Over a city, planetary boundary layer takes on a characteristic form i.e., Urban Boundary Layer (UBL) (Oke et al., 2017).

Urban Boundary Layer (UBL) can be defined as a part of the planetary boundary layer that is affected by high roughness of urban surface, high frictions, and turbulent factors. Kuttler et al. (2008) refer to the urban boundary layer as the region of the atmosphere that has a higher temperature than the surroundings due to the presence of a city. UBL takes on a dome form that includes the entire city with absent or weak winds or plume form with moderate winds (Oke et al., 2017). UBL extends from 1 to 2 km during the daytime and up to 300 m above ground surface during the night respectively (Oke et al., 2017).

In urban environment, UBL is subdivided in urban outer layer and near-surface layer (see Figure 2.1a). Near – surface layer is strongly affected by surface conditions such as roughness of the terrain, heat exchanges by convection from surface layer and pollution emissions from the earth's surface.

At local scale, near-surface layer is divided in inertial sublayer (ISL), roughness sublayer (RSL) and urban canopy layer (UCL) (Oke, 1976, Hanna and Britter, 2002).

The canopy layer extends vertically from the ground up to an upper level of buildings. The top of the urban canopy layer is consequently situated above roof level, while the top of the rural canopy layer is just above the crops, the grass, or the trees.

There are various types of UHI and several methods of observing and studying them. UHI occurs at ground level, at different heights and as surface heat islands.

Atmospheric UHI may be measured within the planetary boundary layer (above the city) and in the urban canopy (up to the top of the buildings of the urban zone).

The Surface Urban Heat Island (SUHI) occurs at the level of the various urban surfaces (Yow, 2007). SUHI has a particularly strong effect on radiative environment and therefore on thermal comfort of humans in outdoor urban environments, especially in the case of strong solar radiation exposure. It can exacerbate thermal discomfort, in particular during warm summer periods: the artificial surfaces, such as asphalt and concrete absorb heat during daytime, warm up the air by convection and release heat into the atmosphere during the night (Oke, 1982; Kuttler, 2008; Armson et al., 2012). The reduction of vegetation and the increase of artificial surfaces lead to lower albedo (and the decrease of reflected shortwave radiation) and to the reduction of evapotranspiration (in other words, the decrease of cooling due to latent heat transfer).

Atmospheric and surface UHI represent an important problem during hot summer periods that occur regularly in southern Europe. The increased use of air conditioning during these periods releases more heat into the outside air which adds to the high short and long wave radiation fluxes in the urban environment resulting in extended and more frequent uncomfortable thermal periods. These in turn give rise to health problems especially among children and the elderly.

## **2.4 Description of UHI causes and of the underlying physical phenomena**

The UHI phenomenon arises from a difference in the energy balance on the earth's surface between urban and rural areas. Such difference could be caused by different factors that can be divided into three types:

- Meteorological factors (Oke, 1978).
- Morphological features and thermo-physical properties of urban materials.
- City parameters, such as the city and the population size, and the anthropogenic heat.

These factors could be classified as the temporary effect variables, such as air speed and cloud cover, and the permanent effect variables such as green areas, building materials, the sky view factor and cyclic effect variables such as solar radiation and anthropogenic heat sources.

The difference in the energy balance on the earth's surface between urban and rural areas is mainly due to the radiative properties of the surface materials. In urban areas the materials are characterized by an albedo value lower than the rural areas (Oke, 1982). In the city the albedo is averagely lower if compared to the albedo of vegetation. The albedo of vegetation is about 0.25-0.30 while the urban surfaces can reach albedo values of 0.05 (Muscio, 2018; Santamouris 2013). During the daytime, the energy absorbed by the urban surfaces is higher than that which is absorbed by rural surfaces. In urban areas, the surface occupied by parks, and green areas is much reduced and thus the evapotranspiration and cooling effects on the reduction of air temperature can be neglected.

The urban surfaces absorb a quantity of direct shortwave radiation higher compared to the rural areas and thereby an increase in surface temperature of the materials occurs. At nighttime, the energy balance on the earth's surface is only characterized by the long wave radiation which depends on the surface temperature of ground, building materials, roads, and other urban materials. Therefore, urban areas tend to emit a thermal energy flux larger with respect to the surrounding rural areas (Santamouris, 2007).

The urban heat island has the maximum intensity after sunset when the net heat stored by buildings and urban materials during daytime is slowly released in the urban environment. As a consequence, the urban area is warmer than surrounding suburban or rural areas. Therefore, the maximum temperature difference occurs when the quick decrease in the air temperature - the anthropogenic heat is negligible – it is counteracted by net heat storage flux released by impervious surfaces of the urban area.

In rural areas, the net heat stored by materials surface is very low and is rapidly released into the outdoor environment. On the contrary, the net heat stored by materials is relevant and is slowly released into the urban area at nighttime. As a result, the heat is more persistent in the urban tissue that begins to suffer the phenomenon of heat island.

As known, the net all wave radiation flux ( $Q^*$ ) is given by the shortwave (K) and long wave (L) radiation, incoming ( $\downarrow$ ) and outgoing ( $\uparrow$ ) with respect to the earth's surface (Oke, 1987). This is expressed by the following equation:

$$Q^* = K^* + L^* = K_{\uparrow} - K_{\downarrow} + L_{\uparrow} - L_{\downarrow} \quad (2.1)$$

The shortwave radiation entering a surface ( $K_{\downarrow}$ ) depends on how much the surface is irradiated by direct and diffuse solar radiation while the shortwave radiation re-emitted by a surface ( $K_{\uparrow}$ ) depends on the surface albedo.

The long wave radiation ( $L$ ) depends on the emissivity values of urban and rural surfaces.

In rural areas, the radiation exchange model is simply represented by reflection, transmission, and absorption of radiation.

In an urban environment, the net all wave radiation fluxes balance is remarkably altered by an atmospheric pollution layer which reduces about 10%-20% the intensity of direct incoming shortwave radiation ( $K_{\downarrow}$ ) compared to the surrounding rural areas (Oke, 1987).

The incoming shortwave radiation ( $K_{\downarrow}$ ) is partly backscattered and partly absorbed by gasses and particulate matter in the urban boundary layer. The radiation flux transmitted to the surface can in turn be partially reflected and undergo further absorption and backscattering.

The geometry of urban tissue has also a relevant affection on the all-wave radiation balance. The intensity of incoming and outgoing radiation fluxes respect to the urban surface depends on the sky view factor. Sky view factor is a geometric parameter that expresses the direct fraction of radiation emitted by a surface towards the sky. In the urban environment, the sky view factor depends on geometric features of buildings area represented by Aspect ratio ( $H/W$ ), where  $H$  is the height of a generic building and  $W$  is the amplitude of down road below.

The increase of aspect ratio involves a decrease of the outgoing radiation towards the sky. The outgoing radiation will tend to be blocked and trapped by urban geometry in the case of high value of aspect ratio. Since the aspect ratio tends to be higher than 1, the effect of the urban geometry is to decrease the direct component of the incoming shortwave radiation ( $K_{\downarrow}$ ). However, in the urban area, the decrease of incoming shortwave radiation ( $K_{\downarrow}$ ) is counterbalanced by the effect of albedo of materials. The outgoing shortwave radiation ( $K_{\uparrow}$ ) is lower if compared to that of the rural area. Therefore, the reduction in incoming shortwave radiation is mitigated by lower values of albedo of the urban surfaces than rural areas.

The sky emits long wave radiation ( $L_{\downarrow}$ ) which are partly transmitted to the earth surface and partly absorbed by the urban boundary layer. The air pollution of the urban boundary layer also emits long wave radiation towards the sky and earth's surface respectively (Oke et al., 2017).

In urban areas, the incoming long wave radiation ( $L_{\downarrow}$ ) is higher than surrounding rural areas because of the atmospheric particulate and the urban boundary layer that is warmer with respect to the planetary boundary layer over the rural area (Oke, 1987).

The urban surfaces release thermal energy by outgoing long wave radiation ( $L_{\uparrow}$ ) that is partly absorbed by the urban boundary layer and partly transmitted to the sky.

The urbanization process has altered the radiation balance and changes in the intensity of the incoming and outgoing shortwave and long wave radiation were caused.

In the rural areas, the urban net all-wave radiation budget during the daytime under clear sky in the light wind conditions has the following characteristics:  $K_{\downarrow}$  is reduced due to anthropogenic aerosol;  $L_{\downarrow}$  is increased due to the pollution of the urban boundary layer (UBL),  $K_{\uparrow}$  is reduced due to albedo values of urban materials that are lower compared to the rural area,  $L_{\uparrow}$  increases due to the higher values of outer surface temperature and emissivity values of urban materials in respect of those of rural areas.

The reduction in the incoming shortwave radiation ( $K_{\downarrow}$ ) is balanced by the increase of absorption of shortwave radiation by urban surface which has a lower average albedo than the pre-urbanized environment. As a result, the net shortwave radiation balance ( $K^*$ ) is positive and slightly higher with respect to the balance of rural area.

The increase in the incoming long wave radiation ( $L_{\downarrow}$ ) is balanced by the increase in long wave radiation emitted by the earth's surface ( $L_{\uparrow}$ ). The net long wave radiation balance ( $L^*$ ) is negative and lower than rural areas due to the predominance of outgoing long wave radiation ( $L_{\uparrow}$ ). The cause of the urban heat island cannot only be attributed to the changes of the net all wave radiation balance due to urbanization processes.

Figures 2.2 and 2.3 shows the net all wave radiation budget during the daytime and at nighttime in rural and urban areas respectively.

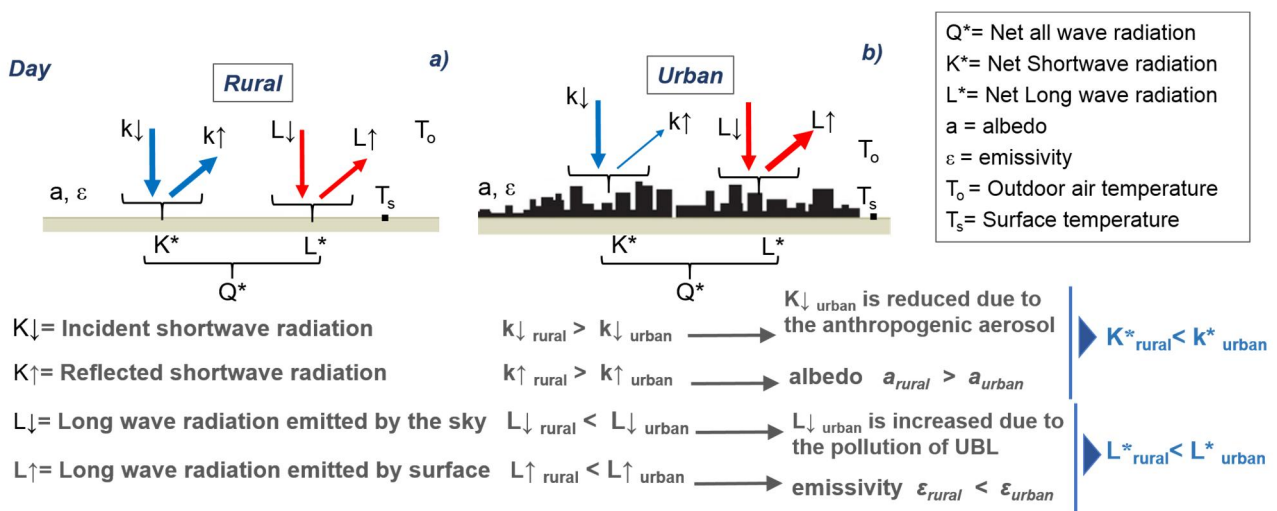


Figure 2.2. Net-all wave radiation budget during daytime: a) Rural area; b) Urban area.



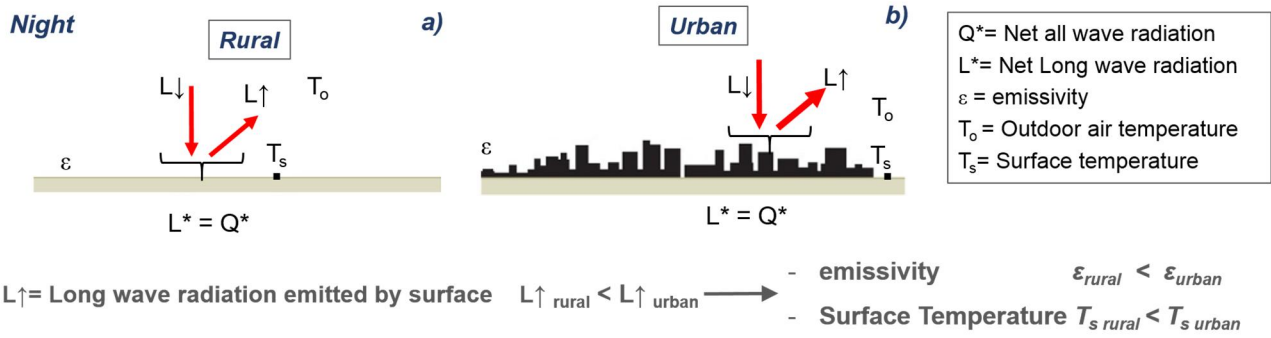


Figure 2.3. Net-all wave radiation budget at nighttime: a) Rural area; b) Urban area.

The consequences of increased urbanization involve several factors affecting the surface energy balance. The surface energy balance is fundamental to understand climate phenomena under the urban canopy layer. The surface energy budget proposed by Oke has allowed the analysis of potential factors which contribute to the formation of the urban heat island. The energy balance of the “earth’s surface – ambient air” system is characterized by energy gains and loss.

Figure 2.4 shows the incoming and outgoing heat fluxes with respect to surface energy balance in rural (a) and (b) urban areas.

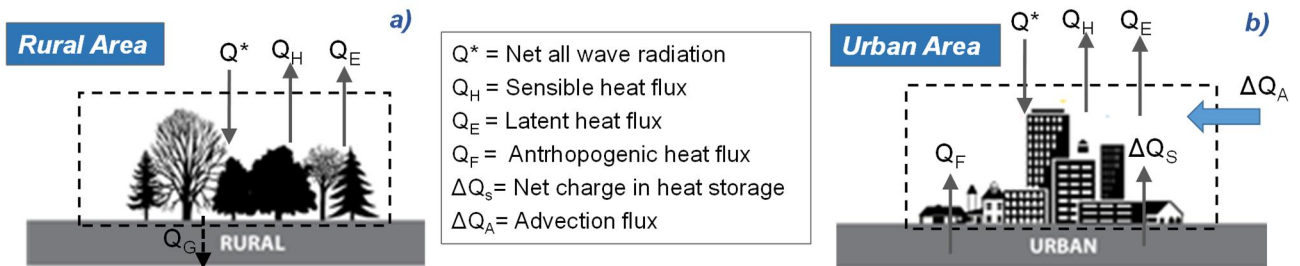


Figure 2.4. Surface energy balance: a) Rural area; b) Urban area.

The surface energy balance in pre-urbanized environment is expressed as:

$$Q^* = Q_H + Q_E + Q_G \quad (2.2)$$

Where:  $Q^*$ , net all wave radiation flux;  $Q_H$ , sensible heat flux;  $Q_E$ , latent heat flux;  $Q_G$ , sensible heat flux towards the ground.

The balance is governed by net radiative flux  $Q^*$  that allows energy exchange by shortwave and long wave radiation. During the daytime  $Q^*$  is positive and thus the earth’s surface is heated. At night, the net radiative flux becomes negative, the earth’s surface is an emitter of long wave, and the ground surface is cooled (Oke et al. 2017).

The surplus of net radiative flux  $Q^*$  is lost as sensible heat by thermal transmission towards the ground ( $Q_G$ ) and by convection ( $Q_H$ ) and as latent heat by evapotranspiration ( $Q_E$ ) towards the atmosphere respectively (Oke, 1982).

In the urbanized environment, the surface energy balance is expressed as follow:

$$Q^* + Q_F = Q_H + Q_E + \Delta Q_S + \Delta Q_A \quad (2.3)$$

In the urban area the net radiative flux  $Q^*$  is still the predominant term. There are new terms with respect to the pre-urbanized or rural area while the existing terms have a different incidence in the energy budget.

The new terms are the anthropogenic heat flux ( $Q_F$ ), net charge in heat storage ( $\Delta Q_S$ ) and the advection heat flux ( $\Delta Q_A$ ) respectively.

The anthropogenic heat flux ( $Q_F$ ) is the heat released by the combustion of fuels from either mobile systems (e.g., cars, buses, transportation etc.), or stationary sources (e.g., power generation) which contribute to warm the urban atmosphere and increasing air temperature (Roth, 2002, Arnfield, 2003, Sailor, 2011). The anthropogenic heat flux mainly depends on pro-capita energy use and population density of cities (Oke, 1998). It has been proved that anthropogenic heat flux shows a linear dependence with population density (Oke et al. 2017). Pro-capita energy consumptions are affected by heating and cooling demand, different types of human activities and city transport systems.

The term  $\Delta Q_S$  is net charge in heat storage that is a typical sensible heat flux of the urban areas because it is only exchanged in presence of opaque materials that characterize the built up areas. The replacement of natural surface with building materials and sealed surfaces has led to a radical change of thermal behaviour and to the variation of the thermal conductivity, capacity, diffusivity, thermal inertia, and admittance of surfaces. Admittance is the most important property for the analysis of the heat storage heat flux ( $\Delta Q_S$ ) because it allows investigation of thermal behaviour of building materials under dynamic regime (Oke et al. 1991).

When the admittance has high values, the heat received by a surface is rapidly exchanged as sensible heat for heating the surface below. During the night the heat stored in the surface is retransmitted as sensible heat in the atmosphere thus increasing the air temperature in surrounding areas. On the contrary, surface with low values of thermal admittance exchange the heat slowly (Oke et al. 2017). The properties of rural surfaces are largely affected by the moisture of the soils. Wet soils have thermal admittance values even seven times higher than dry surfaces.

Urban surfaces are characterized by low thermal admittance values. In cities, the definition of an average value of thermal admittance of the urban area is remarkably difficult due to the presence of different materials in terms of density, composition, and aging (Oke et al., 2017). The complex

structure of the city contributes to decreasing the thermal admittance of the urban area (Oke, 1988). This is due to the morphology of the urban tissue which has a thermal exchange surface wider compared to a rural surface.

Thermal admittance also depends on the canyon that is a typical configuration of urban settlements. In urban canyon, the incoming shortwave radiation is trapped owing to multiple reflections between the surfaces of the building walls and the outgoing long wave radiation can be partially blocked. The albedo of urban canyons can be quite reduced and be lower with respect to the albedo of the single walls of a canyon. This depends on the aspect ratio ( $H/W$ ) that is the more representative parameter to describe the behavior of a canyon. An urban canyon characterized by a high value of aspect ratio ( $H/W$ ) has a very low mean value of albedo. Therefore, aspect ratio and albedo are inversely proportional.

Considering all reasons above mentioned, an assessment of the net heat storage flux ( $\Delta Q_s$ ) is very complex. Since the estimation of ( $\Delta Q_s$ ) is difficult, the numerical model and parametrization of ( $\Delta Q_s$ ) in term of net radiative flux ( $Q^*$ ) are often adopted (Oke, 1982).

The advection heat flux ( $\Delta Q_A$ ) is the net energy transferred to or from the system through advection in the form of sensible or latent heat fluxes. However, the advection term can be neglected in central urban areas with high building density although it may be important in boundary areas where the urban and the rural environment meet (Santamouris, 2001).

Figure 2.5 depicts the daily trends of incoming and outgoing heat fluxes with respect to surface energy balance in rural and urban areas.

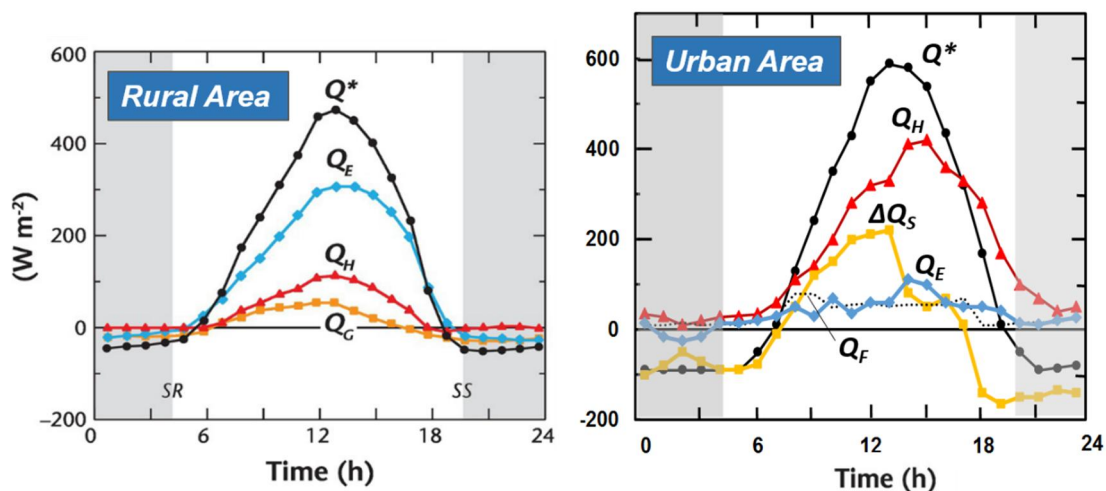


Figure 2.5 Daily trends of incoming and outgoing heat fluxes respect to surface energy balance in rural and urban areas.

The most important change that the urbanization process produces in the environment is the replacement of vegetation surfaces with impervious surfaces. Thereby, the positive action of

evapotranspiration in the mitigation of the net radiative flux ( $Q^*$ ) is dramatically reduced compared to the rural areas.

Evapotranspiration phenomena is typical of vegetation, and it is fundamental for the loss of surplus of net radiative flux ( $Q^*$ ). In high built-up density areas, the evapotranspiration phenomena can be neglected or absent (Oke, 1987). Therefore, the surplus of net radiative flux ( $Q^*$ ) can only be lost by sensible heat flux ( $Q_H$ ). In a similar context, the sensible heat flux is predominant and consequently an increase of air temperature is achieved. On the contrary, the presence of a relevant vegetation surface would have counteracted the increase in air temperature by means of evapotranspiration. This would have removed part of the sensible heat as latent heat thanks to the evaporation of water from vegetated surfaces reducing the air temperature.

In the rural environment, the net radiative heat flux ( $Q^*$ ) is mainly exchanged by latent heat flux ( $Q_E$ ) thanks to evapotranspiration.

In the urban environment, the sensible heat flux ( $Q_H$ ) and net storage heat flux ( $\Delta Q_S$ ) are the most important fluxes in surface energy balance while the latent heat flux ( $Q_E$ ) can be neglected.

It is worth highlight that the peak of sensible heat flux ( $Q_H$ ) is delayed some hours if compared to the peak of net radiative flux ( $Q^*$ ). The trend of  $Q_H$  shows high values in evening hours and positive values at night. This is owing to net heat stored flux ( $\Delta Q_S$ ) that is released as heat sensible to outdoor air of the urban area in the evening and at nighttime. The heat stored by building walls and roofs, roads, and paved areas during the daytime can represent even 30% of net radiative flux ( $Q^*$ ). In light of this, the net charge in heat storage is one of the main causes of Urban Heat Island (Oke et al., 1991).

## **2.5 The heat stress impacts on human health**

The excessive heat from UHI can potentially increase the magnitude and duration of heat waves within cities through increased temperatures. This influences the health and welfare of the urban residents (Ellena et al., 2020). In a study, it was found that the summer heat waves can dramatically increase the mortality rate (Kovats e Hajat, 2008). In addition, the nighttime experience can be harmful during a heat wave, as it deprives the urban dwellers of the cooler relief found during this time. Another study has shown that the mortality rate during a heat wave increases exponentially with the increase in air temperature and such effect is exacerbated by UHI (Kovats e Hajat, 2014).

The impact of heat waves can vary from moderate level to severe level and depends on the characteristics of the population affected by the phenomenon i.e., health conditions, and type of prevention measures adopted (Kovats e Hajat, 2008). In Europe and in the United States, some studies have shown that the highest rate of mortality was registered for people who live in poor quality

buildings with no adequate ventilation conditions and low socio-economic level (Michelozzi et al., 2005).

Among the pathologies related to excessive heat from urban warming, heat stroke, heat cramps and collapse are worth highlighting. Heat stroke can occur when the internal body temperature exceeds 40°C and it can lead to death in a few hours (Paravantis et al., 2017).

Older people and children are the population categories which are more vulnerable to the effects of heat waves phenomena.

Children can suffer dehydration while older people can suffer from cardiac problems. The health of old people may also be worsened by previous conditions such as cardiovascular and respiratory diseases, reduced mobility, mental illness, and the use of medication (Åström et al., 2011).

A study has shown that during the heat waves of the 2003 and 2007 summers in Athens, the average mortality from cardiovascular causes of the elderly over 65 years increased by about 50% when the temperature exceeded 40°C (Paravantis et al., 2017). In addition, the same study highlighted that the extension of the heat wave is associated with the progressive increase of mortality.

In Mediterranean cities, the mortality rate rapidly increases when the air temperature is higher than 29.6°C. Over the threshold level of 29.6°C, the mortality rate may increase by 3.12% for each 1°C (Paravantis et al., 2017). Higher environmental temperatures increase chemical reactivity of airborne pollution (NO<sub>x</sub>, PAN, etc) and this leads to a rise in concentration of respiratory or eye irritants. This will also affect vulnerable individuals, e.g. asthmatics, in a more serious way than healthy individuals, and may be life threatening (Watkins et al., 2007).

It is worth highlighting that the most of these studies have predominantly used simple temperature anomalies in order to assess heat-related health impacts. Since population ageing has a direct impact on health and vulnerability conditions in the urban context, a parameter that takes into account microclimate variations and age of urban residents should be considered.

In this light, a study developed for Stockholm County (1990–2002) linked the increased risk of heat related mortality to threshold values of mean radiant temperature ( $T_{mrt}$ ), a commonly used physical variable that accounts for the radiant heat exchange between people and their surroundings (Thorson et al., 2014). It was found that an increase in the risk of mortality of more than 5% for  $T_{mrt}$  values higher than 58.8 °C for the 45-79 age group, and 55.5 °C for people over 80 years old. Over 59.4 °C, the increased risk for heat related death is >10% for eldest group (Thorson et al., 2014). Such outcomes are in line with previous studies (Åström et al., 2011), and can be explained by the fact that heat tolerance decreases with ageing because of the reduced thermoregulation capacity of people. Consequently, it takes longer for elderly people to recover from excessive heat exposure and, as such, they are more likely to suffer from exhaustion. Distinctive features and different climate conditions

should be considered when the impact of heat on people's health in different cities is evaluated. It is worth highlighting that there is a lack of studies on the critical thresholds of mean radiant temperature correlated to the risk for human health of more vulnerable people in Mediterranean cities.

## **2.6 Building and energy use**

The synergic effects of the urban heat island and climate changes are responsible for increasing the urban temperatures, exacerbating the consumption of energy for cooling purposes, increase the peak electricity demand, intensifying pollution problems, increasing the urban footprint and causing human discomfort and health problems (Hassid et al., 2000; Santamouris et al., 2001; Cartalis et al., 2001; Santamouris et al., 2007 a,b; Stathopoulou et al., 2008).

According to the predictions of several climatology studies, the increase of the "heat waves" phenomenon will contribute to raising the summertime cooling demands of buildings characterized by materials with high values of absorption coefficients to shortwave radiation and low values of emissivity (Akbari, 2001). As well as having a direct impact on outdoor thermal comfort, the urban environment alters the need for energy to modify indoor conditions (Watkins et al., 2007).

In summer, the increase in the outdoor air temperature involves an overheating of the indoor spaces of buildings and consequently potential indoor thermal discomfort conditions for the urban residents (Sakka et al., 2012). As a result, the indoor environment in buildings may be characterized by severe overheating and thus the use of air conditioning systems to keep thermal comfort conditions is necessary (Santamouris, 2015a).

As reported by Wong and Yu (2009), the use of air conditioning systems is becoming pervasive as society becomes more affluent, and this has resulted in a drastic increase in the demand for electricity consumption.

A study of Akbari et al. (2001) found that peak urban electric demand rose by 2% to 4% for each 1°C rise in daily maximum temperature.

Another study revealed that the energy demand for indoor space cooling of typical buildings in urban areas was averagely higher than 13% if compared to the similar buildings located in rural areas (Santamouris, 2014).

An average increase in the electricity consumption for indoor space cooling of +1.6% per unit of 1°C in Spain, and +1.1% per unit of 1°C in Greece was found (Santamouris et al., 2015b).

The predictions of an increase in air temperature and of extreme thermal conditions during the summer period for the Mediterranean area suggest a consequent increase in cooling energy demand. This led to an increase of the anthropogenic heat flux about 13% (Chrysoulakis and Grimmond, 2016).

The widespread use of air conditioning systems in a densely built-up area has led to an increase in air temperature of 2 – 3°C in summertime (Santamouris et al. 2001).

The increase of energy consumption to supply the air conditioning systems for indoor space cooling will lead to an increase of carbon dioxide, nitrogen oxide and sulphur and other pollutants emissions (Zauli Sajani et al., 2016).

## **2.7 Air pollution**

Air and water pollution can increase in the presence of urban heat island. Elevated temperatures can directly increase the rate of ground level ozone formation. It is believed that ground-level ozone is formed when nitrogen oxides (NO<sub>x</sub>) and volatile organic compounds (VOCs) react in the presence of sunlight and hot weather. Normally, the NO<sub>x</sub> arises mainly from the combustion of fossil fuels in urban areas (Emmanuel, 2005). In fact, more ground-level ozone will form as the environment becomes sunnier and hotter (EPA, 2000). This pollution is one of the major problems, due to the ultraviolet sunlight and moisture that cause this photochemical reaction (NO<sub>x</sub> and VOC) (Wong and Yu, 2009).

Another effect is accumulation of smog because it is believed that atmosphere pollution can be aggravated by the accumulation of smog related to the combination of higher temperatures and the presence of air pollutants (Wong and Yu, 2009). Due to light wind, pollution dispersal is difficult. It has also been found that the level of suspended particulate (SPM) often exceeded the threshold levels established by World Health Organization (WHO, 2018).

## **2.8 Urban heat stress mitigation strategies**

Urban overheating can be counteracted with multiple strategies and techniques which allow the reduction of all incoming heat flux with respect to urban energy balance. The literature is as clear about the need to reduce the incoming heat flux as with the fact that the combination of different mitigation strategies provides a lower contribution than the theoretical sum of the effects of the individual approaches (Santamouris et al. 2017).

This occurs as different mitigation strategies are in part complementary and in part overlapping, as they target different terms of the surface energy balance (Oke, 1982).

To counterbalance the impact of higher ambient urban temperatures, various mitigation technologies have been developed and implemented in numerous cities. Reflective materials and greenery are the most accepted and implemented systems in order to mitigate the effects of urban warming and improve outdoor microclimate (Santamouris et al., 2018).

Several studies have highlighted that surface characterized by high albedo values and greening strategies can attenuate the effect of urban heat island (Akbari et al., 2006; Shashua e Hoffman, 2000; Yu e Wong, 2006; Wong et al., 2007).

In another study, Computational Fluid-dynamic simulations at Microscale level or neighborhood scale have revealed that the effects of urban warming on cooling energy demand of buildings can be attenuated by means of the adoption of reflective materials for paved areas and roofs and re-forestation of urban areas.

Some studies carried out by means on site measurements and numerical predictor tools have shown that the increase in albedo of urban surfaces and green cover ratio are able to reduce the temperature on the urban surfaces and air temperature at pedestrian level (Taha, 2007). Therefore, the effects due to the change of urban surfaces by means of the implementation of materials with high reflective and the integration of green areas and the role of each solution by perspective of urban heat mitigation worth being discussed.

Santamouris et al. (2017) considered 220 mitigation projects. The separate use of extensive and intensive greening solutions can reduce the peak air temperature by 1.2 °C and 1.5 °C, respectively, while an average increase of the albedo of a given area by 0.2 may lead to a drop of 1.5 °C. When greenery and reflective materials are used in the same area, the peak reduction is of 2.3 °C, thus 0.5–0.7 °C less than their sum. Also, different vegetation strategies when combined do not provide a cumulative effect.

Specifically, the increase of albedo allows a remarkable reduction in the outdoor air temperature contributing to an improvement of air quality and reduction of energy consumption (Akbari et al., 2005).

In the Greek city of Florina, microclimate analysis by means of computational fluid dynamics (CFD) simulations have revealed that the replacement of conventional materials by “cool” materials can result in the reduction of the mean surface temperature by 3.52 °C while the mean maximum air temperature can be reduced by 1.39 °C during noon of the warmest day (Zoras et al. 2014).

A study carried out on passive cooling techniques (cool materials, green spaces, etc.) in a densely built and populated area have demonstrated that the proposed measures contribute to a decrease in local temperatures of up to 2.0 °C on summer days (Santamouris et al., 2001).

Some studies focused on the thermal behavior of reflective materials in urban areas have revealed that the high values of albedo increase the mean radiant temperature at pedestrian height. Computational Fluid-dynamic simulations of microclimate models have shown that a relevant decrease in surface temperatures can be achieved on the surfaces of roads, pedestrian paths, and paved areas respectively where reflective materials are implemented. Nevertheless, no improvement was



found if the mean radiant temperature values at pedestrian level are considered. Consequently, the outdoor thermal comfort conditions of pedestrians are worse. Some studies have revealed that the implementation of reflective materials can lead to an increase in comfort thermal indexes at pedestrian level. The reasons for such an increase are due to the high value of albedo which favours multiple reflections of shortwave radiation between urban surfaces. Thereby, the flux of incoming shortwave radiation received by urban and building surfaces is increased (Yuan et al., 2016). The incoming shortwave radiation on building wall surfaces are partly absorbed by the surface and partly reflected towards other surfaces and so on (Yuan et al., 2016).

The intensive use of reflective materials on outer surfaces of buildings, paved areas and on the ground surface level can lead to further increase in reflected radiation (Vallati et al., 2018). As a result, the mean radiant temperature at pedestrian level is increased.

It was proved that the adoption of reflective materials on building roofs (cool roofs) has a positive effect on the reduction of effects of warming under Urban Canopy Layer (UCL). In addition, cool roof allows for improvement of indoor thermal comfort in buildings under heat waves phenomena (Santamouris, 2013).

Figure 2.6 shows some examples of building roofs coated with reflective paints.



Figure 2.6. Building roofs coated with reflective paint: (a) Romeo, 2012; (b-c) Bozonnet et al., 2011; (d) Synnefa et al., 2012.

Cool roofs allow a reduction in the air temperature in Urban Canopy Layer due to high values of thermal reflectance of materials. In the daytime, the fraction of shortwave radiation absorbed by roofs is reduced because a relevant part of incoming radiation is reflected towards the sky. Thereby, the heat stored in building materials is reduced and this is crucial for the reduction of the magnitude of

net storage heat flux in urban area. Cool roofs are not responsible for the multiple reflections and thus the mean radiant temperature is not increased in urban spaces.

The role of greenery in mitigating the urban heat island phenomenon at mesoscale and improving the wellbeing of urban residents at Microscale has been widely investigated and demonstrated by a variety of modelling and experimental field studies all around the world. Much of the literature dealing with mitigating urban warming recommends extensive tree planting as the natural strategy for improving outdoor human thermal comfort and providing clean air and social, health and economic benefits. In light of these reasons, urban greening has been recommended as an important adaptation strategy and relevant approach to mitigate the heat island phenomenon and reduce the health-related consequences of increased air temperatures.

The adoption of greenery in the built environment provides cooling through evapotranspiration and shading. When applied to individual buildings, the cooling potential of urban greenery is very well studied and documented. In a similar way, many studies have evaluated the cooling impact of vegetation in cities (e.g., Hamada, 2010; Bowler et al. 2010).

It is worth highlighting that the identification of greenery effects as mitigation strategies of outdoor climate of cities is difficult to assess because the planting of vegetation and its thermal effects depends on morphology of urban areas.

Cities are complex environments for greenery because of the high level of impervious surfaces, reduced level of soil moisture, lack of nutrient and rooting volume. In such contexts, vegetation plays a fundamental role in improving the microclimate by providing shade and aiding human thermal comfort via evapotranspiration. The shading effect and evapotranspiration rate of a tree depends on the total height and canopy geometry, foliage characteristics, and mature shape of the tree.

Urban greenery is able to produce a double benefit due to evapotranspiration and local shading, but, at the same time, also being an “alive” strategy, has to be carefully evaluated since its effect may be related to particular meteorological conditions and the greenery maintenance regime and configuration itself.

The first condition is mostly related to super dry or/and super wet conditions, being responsible for the evapotranspiration phenomenon.

The latter condition affects greenery morphology and therefore, its potential shading contribution. Both these variables may hugely compromise urban greenery mitigation effects at both local and mesoscale level, in terms of outdoor thermal comfort at pedestrian level. Given the typical high expectation rate associated with greenery benefits perceived by citizens, the variability of these two conditions may be crucial for determining its reliability during particularly hot times of the day or, even worse, super dry or super wet heat waves. The frequency of these events has increased over

recent decades and interaction with UHI phenomenon (Ghobadi et al.2018; Ward et al.2016) may thus exacerbate the human risks imputable to overheating in future years.

Gill et al. (2007) demonstrated how green infrastructures may reduce the thermal stress in general urban conditions but, in case of severe drought conditions, such benefit is remarkably reduced due to the lack of water supply to the vegetation that is responsible for its transpiration capability.

Cooling by evapotranspiration varies by climate, canopy physical and geometrical properties and also season but is typically by 2–3 °C, sometimes higher (Jonsson 2004; Ellis et al. 2017; Skoulika et al. 2013; Doick et al. 2014; Taha 2015a).

In response to the main scientific challenges such as urban expansion, overpopulation, climate change and poverty, recent scientific research has developed and proposed innovative solutions, and has provided new knowledge on several issues related to the capacity of greenery to mitigate urban heat. These include the optimum integration of greenery in densely built-up cities, with the selection of more performant vegetation species and the enhancement of the synergetic operation between vegetation and the other mitigation technologies.

Based on a comprehensive analysis of the recent research on the cooling capacity of urban greenery, progress on greenery selection, plant configuration and urban morphology, research is included on:

- Performance of urban greenery in mitigating urban heat island in high-density cities.
- Plant configurations and urban morphology.
- Development of environmental assessment tools to evaluate the mitigation potential of vegetation.

A strong relationship was found between urban morphological parameters, thermal performance of Urban Greening Infrastructure (UGI), and plant structural characteristics indicating the potential of these parameters, e.g., sky-view factor or aspect ratio as a tool for implementing the right green infrastructure in the right place. This also allows the right plant species to be chosen especially for the purpose of urban heat mitigation.

At the Microscale level (Oke 2002), both the arrangement of green infrastructure and the morphological properties of individual vegetation species (Deak Sjöman 2016) become relevant. The arrangement of vegetation (dispersed, clumped, linear, single or multiple rows), its height (shrubs, hedges, small / tall trees), the type and density of foliage and seasonal variation (Bartesaghi Koc et al. 2017) determine the capacity of green infrastructure to achieve the above-mentioned outcomes.

Green roof, green facades and planting of trees constitute green sustainable infrastructure for urban heat mitigation.

Experimental studies on the potential mitigation of air temperature of green roofs implemented in a neighborhood have shown a negligible cooling effect at pedestrian level for densely built up urban area (Berardi 2016; Morakinyo et al. 2017; Ng et al. 2012).

Figure 2.7 shows some examples of extensive greenery on building roofs.



Figure 2.7. Extensive green roof: (a) Castleton et al., 2010; (b-c) Sam and Hui, 2009; (d) Stratigraphy ([http://www.zinco-greenroof.com/EN/downloads/pdfs/ZinCo\\_Intensive\\_Green\\_Roofs.pdf](http://www.zinco-greenroof.com/EN/downloads/pdfs/ZinCo_Intensive_Green_Roofs.pdf)).

Vertical Greening Systems (VGSs) - green wall and green façade – can reduce façade surface temperatures and peak energy demand for space cooling in buildings (Cheng et al. 2010; De Jesus et al. 2017). Nevertheless, effectiveness of VGS in terms of surface and air temperature reductions and energy saving depend on location, arrangement, and typologies of plant typologies.

A recent study has revealed the importance of a higher green façade ratio (GFR) for improved urban cooling (Morakinyo et al. 2017c). This result is corroborated by other studies where isolated and low coverage façade greening did not lead to relevant difference in term of outdoor thermal comfort. However, noticeable temperature mitigation and outdoor thermal comfort improvement are only found with 80–85% and 30–50% green façade ratio in medium and high-density neighborhoods respectively.

As very high green facade coverage is unrealistic, implementation for outdoor heat mitigation is somewhat limited to high-density urban settings with at least 30% average coverage.

Nonetheless, it is important to underline that meaningful façade surface temperature reduction is realizable irrespective of urban density. In terms of plant selection and configuration, high foliage density and substrate moisture content were found to be the most crucial factors in obtaining the

optimum thermal effect from plants, whereas other factors such as radiative properties of leaves have negligible effect on urban heat mitigation (Dahanayake et al. 2017; Hoelscher et al. 2016).

Figure 2.8 shows examples of green façades and the specific anchored structures.



Figure 2.8. Green facades and support structures: (a-d) Typical green walls with self-clinging climbing plants (Kontoleon et al., 2010); (b-f) Green facades with modular trellis panel systems (Perez, et al. 2014).

Some authors found that the adoption of a GFR of 30–50% in the high-density urban setting of Hong Kong cause a reduction in air temperature of  $\sim 1$  °C. This could help to improve daytime pedestrian thermal comfort by at least one thermal class (Morakinyo et al. 2017).

A validated Computational Fluid-Dynamic (CFD) model with horizontal grid size of  $5 \times 5$  m and a vertical grid size of 3 m was used for assessing  $T_{mrt}$  variations for five scenarios of green façades. Based on the orientation and Greened Façade Ratio (GFR), temperature reductions of about 2.0 °C, 0.9 °C and 0.5 °C were attained in the case of façade oriented to East-West (GFR=67%), East (GFR=33%) and West (GFR=33%) (Morakinyo et al. 2018).

A study investigated the outdoor microclimate of a densely built up urban area under different green roof scenarios (50%, 75%, 100% of total roof area) and green walls scenarios (50% and 100% of total wall area (East-West oriented)) in Colombo (Sri Lanka) with an approach based on microclimate modelling. CFD simulations of a validated ENVI-met model for a hot, humid, summer sunny climate conditions in August have highlighted reductions in air temperature by 2.0°C at 3.00 p.m. on a typical day under green wall in East–West direction while a temperature reduction of 1.6 °C for 100% green roof compared to baseline case is attained (Herath et al. 2018).

Among the urban green infrastructures, ground level trees are the most effective for urban heat mitigation. Nonetheless, there are many limitations on greenery in urban areas, especially for tree

planting in high density districts, such as the limited size for planting potential due to the narrow footpaths and the large built areas.

However, due to the variable magnitude of temperature regulation and thermal comfort realizable with different trees species, recent studies are moving a general analysis of trees to a species-specific analysis of their thermal benefits and energy saving at building, neighborhood, and city scales (Kong et al. 2017; Morakinyo et al. 2017b; Tan et al. 2017). In order to understand the relationship between tree performance and urban density, these studies have compared the cooling benefits of certain tree species in street canyons of variable densities and different sky view factor values. Their results revealed that the performance of trees generally reduces as urban density increases.

Urban planners should consider street trees to provide more thermally comfortable urban areas but implementing of trees should be effectively planned. It is worth highlighting that extensive tree canopy is beneficial in providing daytime shade for pedestrians, but it may reduce sky-view factor of the pavement surfaces during the night. Thereby, the rate of nighttime radiation emitted from the soil surfaces to the sky is reduced and consequently the heat is trapped in the urban materials.

The deep canyons and high density built-up areas characterized by lower exposure of the surface to the sun and moreover the dense canopy prevents the humid air from escaping into the atmosphere. Consequently, trees increase the relative humidity and decrease the air temperature.

Thus, planning recommendations should include the proposition of trees with higher trunk, short crown width, and less dense species for high density areas (Sky View Factor,  $SVF \leq 0.2$ ) where the shadowing effect is more dominant (Morakinyo, Lam 2016).

In open areas and low urban density, trees should have a wider crown and shorter trunk compared to those recommended in deep canyons. Thereby, trees can lead to relevant shading in order to reduce exposition to the sun and decrease evaporation of the water from the humid loamy soil under the trees. As a consequence, tree leaves absorb less humidity from the air which becomes more humid and a decrease in air temperature is achieved. Short trees with high leaf density and a large crown are recommended in areas where shading benefit is reduced and where SVF values are higher than 0.60. As a result, the urban density mapping technique was recommended and evaluated for the selection of tree species for urban planting (Morakinyo et al. 2017b, 2018).

Figure 2.8 shows examples of recommended urban greenery in high density built-up areas (a-b) and suggested tree species in open areas and low urban density (c-e).



Figure 2.9. Urban greenery; (a-b) Street trees in high density built-up areas (Ng, et al. 2012; Chen et al. 2012); (c-e) Tree species in open and low urban density (Aboelata, et al, 2020; Irmak et al., 2018).

Several studies based on quantitative analysis were conducted to evaluate the effects attainable by tree planting along the roads in high and medium density urban areas. Such studies have predominantly adopted an approach based on urban Microscale or neighborhood scale using Computational Fluid-dynamic microclimate models. Most studies have adopted ENVI-met as the CFD calculation code.

As an example, Wang et al. (2016) found that adding 10% of vegetation coverage through tree planting on wide streets can improve the outdoor thermal comfort of urban spaces at pedestrian level with respect to the current scenario. Further detailed, CFD simulations of a validated ENVI-met model showed reductions in average values of  $T_{mrt}$  of 6.2°C in the high-rise area and 6.1°C in the middle-rise area in Toronto at 1.8 m above the ground in open areas at 3.00 p.m. of a typical summer day (Wang et al., 2016).

Another study investigated the outdoor microclimate conditions in a neighborhood in Hong Kong where its existing greenery coverage ratio of 7.2% was compared to a speculative case with “no vegetation” and one with 30% of green coverage ratio respectively (Morakinyo et al. 2018). CFD simulations revealed that dense foliage trees are recommended for urban areas with high sky view factors in shallow canyons. On the other hand, sparse foliage trees are suggested for urban areas with low sky view factors such as deep canyons. In addition, this research showed that a green coverage ratio of 7%, consisting of sparse crown trees planted along streets characterized by SVF values lower than 0.3, can averagely decrease the mean radiant temperature of 4.0°C at pedestrian level at 3.00 p.m. on a typical summer day with respect to a none-vegetation scenario (Morakinyo et al. 2018).

It is worth considering a study aimed at finding the best urban vegetation ratio in order to improve the microclimate in high and low density built-up areas in a hot and arid climate located in Cairo. Two areas (Imbaba - 65% urban density, Elsalam district - 23% urban density) were chosen with different sky view factor values. They were compared in terms of the cooling effect considering a tree ratio of 30% and 50% respectively. The microclimate of all investigated scenarios was performed using ENVI-met simulation tool. This study found that a 50% tree scenario is the most effective at reducing air temperature in the compact area. Trees were planted with a height of 5 m and 10 m respectively on one side of the sidewalks, with gaps between the trees of 3 m. The outcomes have revealed that street trees can reduce daily air temperature by 0.2–0.4 °C in very high density built-up areas (Aboelata, et al. 2020).

## **2.9 Approaches and methods for the estimate of the Mean Radiant Temperature ( $T_{mrt}$ )**

Radiation heat flux has detrimental effects on outdoor thermal comfort and buildings energy consumption in urban areas (Gong et al., 2019). Because of the high concentration of buildings, narrow streets, and low values of sky view factor, both long wave and shortwave radiation have strong reflection components (Chen et al., 2020). These factors constitute the complex urban radiation field. Therefore, a better quantification method of solar irradiance and the distribution law of the urban radiation field will greatly improve understanding of the interactions between radiation heat fluxes in the urban environment (Liu et al., 2020).

The parameter governing outdoor human thermal comfort (HTC) on warm, clear-sky days is radiation. The effects of the complex radiation field on HTC are accounted for by mean radiant temperature ( $T_{mrt}$ ) (Mayer et al., 1987). Mean radiant temperature ( $T_{mrt}$ ) is one of the four environmental parameters (next to air temperature, relative humidity, and wind speed) that govern the human energy balance, and thus, plays an important role in human thermal comfort. The mean radiant temperature ( $T_{mrt}$ ) is a widely used physical parameter to characterize the effects of well-being on people and their thermal comfort conditions (Fanger, 1972; Höpfe, 1982; Ali-Toudert et al., 2007, Thorsson et al., 2011). Nowadays,  $T_{mrt}$  is considered one of the most important parameters in the investigation of thermal comfort and heat stress in outdoor environments because of its capability to identify and capture significant spatial differences due to radiant fluxes coming from buildings, ground surfaces and trees, which other indices such as the air temperature ( $T_a$ ) cannot take into account (Chen et al., 2016; Thorsson et al. 2011).

Numerous studies have shown that  $T_{mrt}$  is the driving parameter of human thermal comfort in outdoor spaces during summertime (Cohen et al., 2012; Kántor and Unger, 2011; Holst and Mayer, 2011; Mayer et al., 2008; Thorsson et al., 2007). The main thermal comfort indicators are more sensitive to



the  $T_{\text{mrt}}$  variations compared to those of air temperature and relative humidity respectively. Although the mean radiant temperature is central for the calculation of outdoor thermal comfort indicators,  $T_{\text{mrt}}$  is difficult to estimate in the urban environment.

The complexity and importance of the urban radiation field has determined the adoption of different approaches to evaluate the distribution of  $T_{\text{mrt}}$  in urban areas. Several methods exist for deriving mean radiant temperature from both modeled and observed data. An overview of these approaches is given by Kántor and Unger (2011).

In recent years, simulation analysis has become the main approach in this field because of the advantages of the high capacity to handle the complexities and nonlinearity of urban climate systems. Most importantly, these simulation models are viable and efficient in saving time and resources (Sailor et al. 2006). According to the theoretical basis of calculation methods, the simulation models can be divided into three categories, namely, models based on energy balance equation (TEBE), cluster thermal time constant (TCTTC), and computational fluid dynamics (CFD) (Yanwen, 2016). TEBE has strong shortwave and long wave radiation calculation capabilities (Yanwen, 2016). RayMan, SOLWEIG and Urban Weather Generated (UWG) are based on the energy balance equation. SOLWEIG (Solar and Long wave Environmental Irradiance Geometry) is a plug-in of UMEP (Urban Multilevel Environmental Predictor).

Computational Fluid-dynamic simulation tools are focused on the movement of air and convection, and the models of heat conduction and radiation are coupled and calculated. These types of simulation tools are mainly used to predict air temperature, wind speed, and surface temperature (Nestoras et al., 2019). Specialized radiation calculation modules are implemented in CFD simulation tools, such as ENVI-met, Phoenics, and SOLENE Microclimate. Nevertheless, spatial, and temporal limitations affect the numerical simulation models.

Currently, ENVI-met and SOLWEIG are the simulation tools more used to calculate the radiation field. These tools have good radiation calculation capabilities (Song et al., 2014; Kleerekoper et al., 2017). Both estimate the shielding of radiation by green plants and buildings in urban radiation fields (Yin et al., 2019).

By conducting a spot test, some authors verified the accuracy of outdoor urban microclimate simulated by ENVI-met. The reliability of ENVI-met in different contexts was investigated based on several studies focused on calibration and validation processes of microclimate models. ENVI-met was considered a reliable tool for relative comparison of urban dynamics (Jamei et al. 2019). However, as pointed out by Tsoka et al. (2018), the largest share of validation studies focuses on the ability of models to reproduce observed air temperatures. In contrast, the number of studies validating the ENVI-met model with parameters other than air temperature is still limited, albeit increasing.

Most studies evaluating the performance of models in terms of mean radiant temperature rely on black or grey globe temperature measurements (Acero and Arrizabalaga, 2018; Acero and Herranz-Pascual, 2015; Forouzandeh, 2018; Morakinyo et al., 2017; Zhang et al., 2018; Zhao and Fong, 2017). The performance of the SOLWEIG model in estimating radiation fluxes and  $T_{mrt}$  values has been assessed by numerous studies (Lindberg et al., 2008; Lindberg and Grimmond, 2011; Konarska et al., 2014; Chen et al., 2014; Jänicke et al., 2015; Chen et al., 2016; Lau et al., 2016; Lindberg et al., 2016; Kántor et al., 2018).

Lindberg et al. (2008) reported that SOLWEIG is able to calculate variations in radiation flux and mean radiation temperature of a large-scale outdoor space at different moments. Dmitrieva et al. (2008) simulated the mean radiation temperatures of a grand square in Gothenburg, Sweden, using SOLWEIG. The predicted results were found to be consistent with the measured values.

The number of studies focused on model validation, based on the comparison between the predicted results from a single simulation tool and observed data is broad. Few studies have conducted horizontal comparisons of the results of multiple tools simulating the same urban area.

In addition, the number of simulation tools to calculate radiation fluxes in a complex urban environment is increased. Thus, the selection of a suitable calculation method and simulation tool to achieve the expected simulation results has become crucial.

Gál and Kántor (2020) have compared the predicted values of  $T_{mrt}$  derived by SOLWEIG and ENVI-met respectively with the  $T_{mrt}$  measured data in a complex urban area.

A comparison between SOLWEIG and ENVI-met in term of shortwave and long wave radiation was also carried out by Liu et al. (2020).

## **2.10 Outdoor thermal comfort estimation methods**

Due to rapid and intensified urbanisation trends, the attention to the condition of people's health, wellbeing, comfort, and liveability of our cities has become pivotal. Consequently, it is essential to adopt models to understand and predict the thermal sensation of pedestrians in the outdoor environment in order to prevent consequences related to heat stress.

In an outdoor environment the climatic parameters vary to a substantially larger extent than in an indoor environment: in particular, long wave, and shortwave radiation, air movement, surface, and air temperatures. As a consequence, the human body needs to adapt to the extended range of environmental outdoor conditions through its thermoregulation system, in order to maintain a constant deep body temperature. Thermal comfort is a state where a constant deep body temperature can be maintained by the least energy exchange occurring at the body's surface.

As concerns human thermal comfort outdoors, conductive heat fluxes can be neglected. On the contrary, radiative, and convective fluxes play an important role in the heat balance of the human body. Convective fluxes of latent and sensible heat are modified mainly by air humidity and air temperature, respectively, while both are influenced by wind speed (Kántor et al., 2012). However, Mean Radiant Temperature is the key factor affecting thermal comfort in case of strong direct solar radiation.

The outdoor comfort models and the related physical variables can be divided as:

- Indexes based on human energy balance.
- Empirical indexes.
- Indexes based on linear equations.

Among comfort indexes based on the human energy balance, PMV (Predicted Mean Vote), PET (Physiological Equivalent Temperature), PT (Perceived Temperature), OUT\_SET\* (Standard Effective Temperature for outdoor), SET (Standard Effective Temperature), UTCI (Universal Thermal Climate Index) are most known.

A literature analysis on the primary models used highlights that although many thermal indices are available for the assessment of outdoor comfort, each of them presents some drawback with different levels of error or approximation (Coccolo et al., 2016).

Fanger developed a comfort theory based on human body heat exchange that led to defining the PMV (Predicted Mean Vote). The PMV was introduced to predict the thermal sensation of a person through a heat balance equation based on six variables (i.e., dry bulb temperature, mean radiant temperature, air velocity, relative humidity, metabolic activities, and clothing insulation).

PMV should be used to predict the general thermal sensation and degree of discomfort of people exposed to moderate thermal environments when the main parameters are within a specified range (i.e., air temperature between 10 °C and 30 °C), as highlighted in the ISO 7730, (2005). Applying Fanger's theory for estimating outdoor thermal comfort when temperatures are higher than 34 °C involves a thermal sensation above the highest rate of +3 (Fang, 2017). Thereby, when a person experiences a "very hot" or "extreme hot" sensation outdoors the seven-point scale is not sufficient. In order to consider wider variations of outdoor climate conditions, a few studies used a nine-point thermal sensation scale as an extension of ASHRAE seven-point scale, from -4 (very cold) to +4 (very hot) (Zhang et al., 2013).  $PMV > 4$  can be attained in the hours of maximum solar radiation in hot summers.

Table 2.1 summarizes information about the main thermal comfort indices.

Table 2.1. Main models and thermal indices used to assess outdoor thermal comfort.

Year	Index	Reference	Model type	Notes
1970	PMV	Fanger (1972)	Steady-state energy balance (One-node model)	PMV scale: from -3 to +3 Metabolic rate: 46 – 232 W·m <sup>-2</sup> (0.8 – 4 met) Clothing thermal resistance: 0 – 0.310 m <sup>2</sup> K·W (0 – 2 clo) Ambient air temperature: 10 – 30 °C Mean radiant temperature: 10 – 40 °C Air velocity: 0 – 1 m·s <sup>-1</sup>
1981	PMV (extended version)	Jendritzky and Nubler (1981)	Klima-Michel Model (One-node model)	PMV scale: from -4 to +4 Metabolic rate: 172.5 W·m <sup>-2</sup> Weight: 75 kg
1986	SET*	Gagge et al. (1986)	Transient Energy (Two-node model)	SET* scale (°C): SET* < 17, 17 ≤ SET* ≤ 37, SET* > 37 Air Temp. = Mean Radiant Temp. Relative humidity: 50% Air velocity: 0.15 m·s <sup>-1</sup> Clothing thermal resistance: 0.6 clo Metabolic rate: 1.0 met The same mean skin temperature and skin wettedness as the person in the actual complex environment
1999	PET	Höppe (1999)	Munich Energy Balance model for individuals (Two-node model)	PET scale (°C): PET < 4, 4 ≤ PET ≤ 41, PET > 41 Air Temp. = Mean Radiant Temp. Air temperature: 20 °C Air velocity: 0.1 m·s <sup>-1</sup> Vapor pressure in the air: 12 hPa Relative humidity: 50% Metabolic rate: 80 W·m <sup>-2</sup> Clothing thermal resistance: 0.9 clo
2000	PT	Jendritzky et al. (2000)	Klima-Michel Model (Two-node model)	PT scale (°C): PT < -39, -39 < PT < 38, PT > 38 Relative humidity: 50% Metabolic rate: 135 W·m <sup>-2</sup> Clothing thermal resistance: 1.75 clo (winter), 0.5 (summer)
2001	UTCI	Jendritzky et al. (2014) Fiala (2001)	UTCI-Fiala model (Multi-node model)	UTCI scale (°C): UTCI < -40, -40 < UTCI < 46, UTCI > 46 °C Air Temp. = Mean Radiant Temp. Metabolic rate: 2.3 met Walking speed: 1.1 m·s <sup>-1</sup> Air velocity: 0.5 m·s <sup>-1</sup> (10 m above ground). Relative humidity: 50%

Jendritzky et al. (1980) managed to make Fanger’s approach applicable to outdoor conditions by adding outdoor radiation to adjust the model to complex outdoor conditions. Their model takes into account the direct and diffuse shortwave radiation and the long wave radiation fluxes originating from the ground, building surfaces and free atmosphere (Jendritzky et al. 1981). This approach, also known as the “Klima Michel Model” does not provide any description of thermal body conditions (Matzarakis et al., 2008). In this model, the sweat rate is a function of metabolic activity only and it does not include the effects due to weather conditions (Höppe, 1999).

More widely applicable are the models that enable prediction of the “real values” of thermal quantities of the body, i.e., skin temperature, core temperature, sweat rate or skin wetness. To this purpose, it is necessary to take into account all basic thermoregulatory processes like the constriction or dilation of peripheral blood vessels and the physiological sweat rate (Höppe, 1999).

The Physiologically Equivalent Temperature (PET) is based on a thermo-physiological heat-balance model called “Munich Energy Balance Model for Individuals” (MEMI) (Höppe, 1999). It was developed to explicitly compare the actual outdoor environmental conditions with equivalent indoor conditions, thus making it possible to evaluate comfort in the outdoor environment in terms of indoor standards. MEMI calculates the physiological sweat rate as a function of skin temperature and core temperature. MEMI offers an analytical solution of the human energy balance for steady-state conditions and avoids temporal integration compared to transient models. In the MEMI model, the mean clothing temperature, mean skin temperature and sweat rate depend also on climatic conditions. Separate calculations for the heat fluxes from body surface parts that are covered or uncovered by clothing are carried out as well.

The index  $OUT\_SET^*$  was developed for adapting the indoor comfort index SET to the outdoor environment (Pickup and de Dear, 2000). This index provides physiological representation of outdoor human thermal comfort and stress across almost unlimited combinations of air and mean radiant temperatures, humidity, air velocity, clothing thermal insulation and metabolic rate. For the body’s surface area participating to the radiant heat exchange, the outdoor mean radiant temperature  $OUT\_MRT$  is calculated taking into account the amount of outdoor irradiation absorbed by the body and by subtracting the outgoing fluxes (Pickup and de Dear, 2000; Blazejczyk, 1998).

The main limitation of the indices based on energy balance lies in the steady-state conditions that do not fully reflect how people experience the thermal equilibrium in outdoor environments. Thus, such models exclude the evaluation of transient thermal conditions, e.g., when a pedestrian is moving into an Area (Steiger et al. 2012).

PMV and PET are the most widely used indexes in several studies regarding the mitigation strategies of urban warming and evaluation of the effectiveness of regeneration plans based on urban greenery forestation on the urban microclimate (Coccolo et al. 2016). PMV does not take into account the dynamic adaptive response of the human body and instead references a punctual static state. In light of this, its use in outdoor environments may often give misleading results (Cheng et al., 2012).

PET is a thermal index that can be used as an alternative to PMV for evaluating the comfort in outdoor environments. The main drawback of this index, although the outcomes are well correlated with onsite monitoring and questionnaires, is the underestimation of latent heat fluxes and overestimation of radiant heat flows (Cheng et al., 2012).

However, the calculation of outdoors mean radiant temperature (OUT\_MRT) shows relevant deficits, especially in the long wave range, resulting in an unrealistic overestimation of the absorbed radiant energy (Pickup and De Dear, 1999).

Outdoor thermal indices based on a steady-state energy balance of the human body (e.g., PMV, PT and PET) are not appropriate for assessing short-term exposure in the outdoor environment (Fang, 2019). UTCI-Fiala multi-node approach overcomes this shortcoming and provides the highest level of detail concerning the body model as well as the clothing ensemble (Blazejczyk et al. 2012).

There are many effective measures and strategies to mitigate heat stress in urban areas, whose effectiveness can be properly investigated through numerical models that combine many microclimatic parameters to estimate the thermal sensation of people.

Nowadays, tools for simulating project scenarios are increasingly available and updated, allowing the reproduction of complex urban areas. Table 2.2 reports the most used software tools for predicting the indices discussed so far.

*Table 2.2. A comprehensive list of simulation tools for outdoor microclimate and thermal comfort, with their models and calculation capabilities*

<b>Simulation Tool</b>	<b>Output Indices</b>	<b>References</b>
SOLENE-MICROCLIMATE	LWR, Tse, CHTC	Azam et al. (2018), Morille et al. (2015), Musy et al. (2015).
ERA5-HEAT	MRT, UTCI	Di Napoli et al. (2020)
PALM (Parallelized Large-Eddy Simulation Model)	PT, UTCI, PET	Raasch and Schröter (2021), Maloney (2011), Maroga et al., (2015)
UMEP (Urban Multi-scale Environmental Predictor)	T <sub>s</sub> , Ta <sub>2m</sub> , SW <sub>down</sub> , SW <sub>up</sub> , LW <sub>down</sub> , LW <sub>up</sub> , MRT, PET, UTCI	Lindberg et al. (2017)
RayMan	MRT, PET, PMV SET*, PT, UTCI	Matzarakis et al. (2006 and 2007)
ENVI-met	PMV, PET, SET*, UTCI, MRT, T <sub>sk</sub>	Salvati et al. (2020). Koerniawan et al. (2015)

**CHAPTER THREE:  
RESEARCH METHODOLOGY**

### 3.1 Structure and outline of the chapter

The structure of the research methodology is outlined as follows:

- Section 3.2 describes the overall methodology framework adopted in the present research.
- Section 3.3 discusses the state of the art, input and output data of Local Climate Zones (LCZs) classification.
- Section 3.4 describes the state of the art, features, physical model, input, and output data of UMEP (Urban Multi-scale Environmental Predictor) tool.
- Section 3.5 describes the state of the art, physical model, input and output data of ENVI-met software.
- Section 3.6 provides a description of the thermo-physical parameters used to characterize the urban microclimate and outdoor thermal comfort of the study area such as Mean Radiant Temperature ( $T_{mrt}$ ) and Universal Thermal Climate Index (UTCI).
- Section 3.7 describes the mitigation strategies adopted in the studied areas.

### 3.2 Methodology

The present thesis deals with the analysis of the urban microclimate and identify the potential heat stress mitigation strategies in the highest risk areas by means of top-down approach (from the Macroscale down to the Microscale).

To identify the most sensitive risk areas, a Local Climate Zones (LCZs) classification was carried out by means of UMEP (Urban Multi-scale Environmental Predictor) tool.

Climate simulations of almost the entire urban area of the investigated city was carried out by means of a Macroscale approach based on SOLWEIG module (UMEP). The SOLWEIG model was calibrated and validated according the procedure described in section 3.4. Among risk areas, two areas named “Area 1” and “Area 2” were selected on the basis of their morphological and thermo-physical features. “Area 1” is a compact and densely high built-up area with few trees while “Area 2” is characterized by open arrangement of low-rise buildings. Such areas were analyzed with an approach based on urban Microscale modelling carried out by means of ENVI-met software. Simulations of the calibrated and validated models were run. Based on simulation results and morphometric features of the investigated areas, heat stress mitigation strategies were proposed.

Subsequently, urban Macroscale and Microscale simulations of the risky areas were compared in order to assess the reliability of the numerical modelling at large-scale of the entire area realized by means of UMEP. With this aim, the discrepancy between the SOLWEIG and ENVI-met simulations results was analysed by means of statistical indices and cumulated frequency distributions.

Figure 3.1 summarizes the workflow of the proposed methodology.



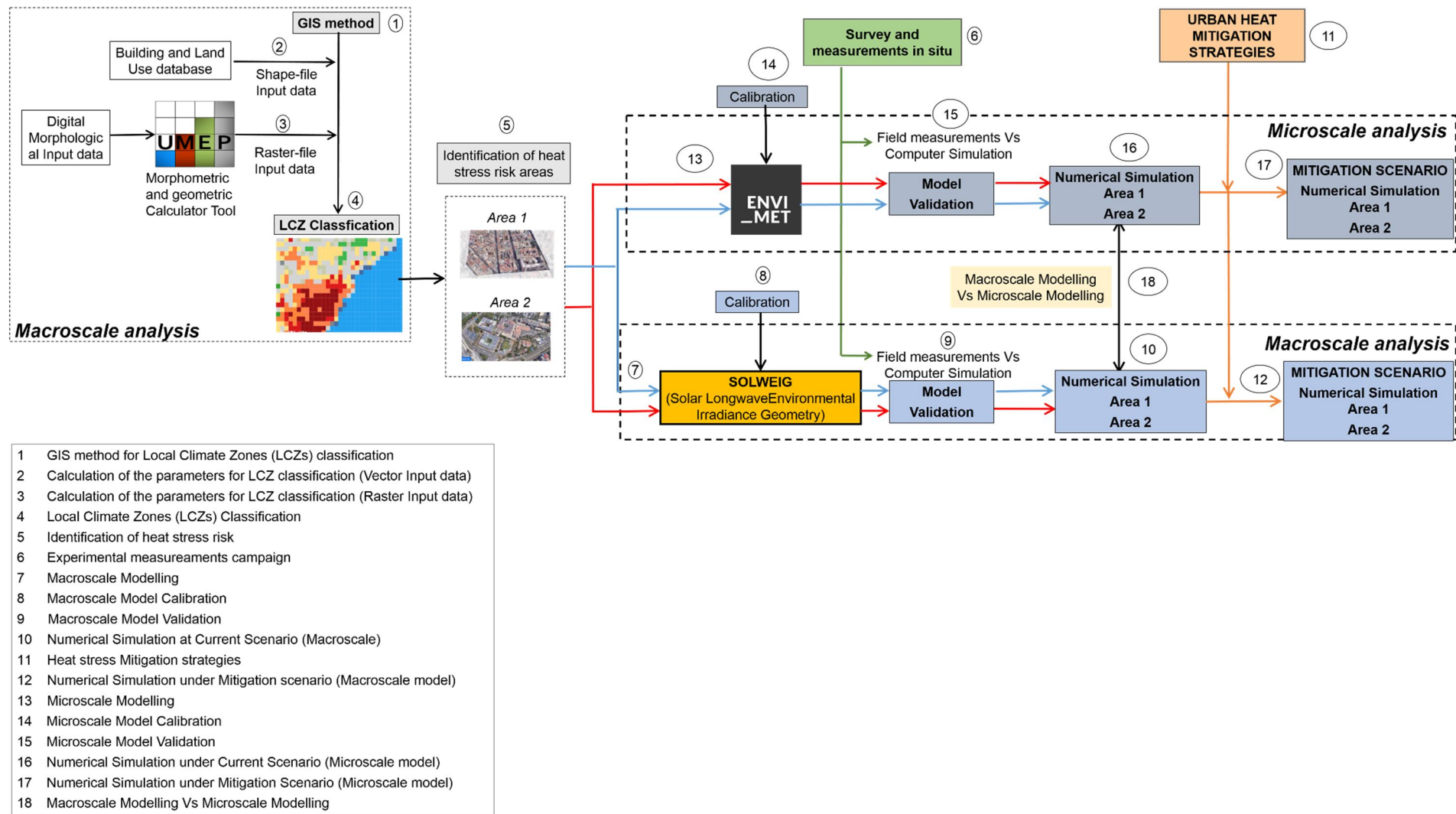


Figure 3.1. Workflow of the research methodology.

Based on a validated Macroscale model, proposed heat stress mitigation strategies were modelled at large-scale level. In order to assess the potential effectiveness of proposed mitigation strategies Macroscale simulations were carried out under a mitigation scenario.

Notwithstanding the SOLWEIG module being reliable, it is suggested to design the mitigation strategies at Microscale level because the ENVI-met software is more accurate and detailed with respect to SOLWEIG module under modelling phase of the urban space model.

Mean radiant temperature ( $T_{mrt}$ ) and Universal Thermal Climate Index (UTCI) were adopted as the key analysis parameters.

### 3.2.1 Calibration and validation of the urban Macroscale model

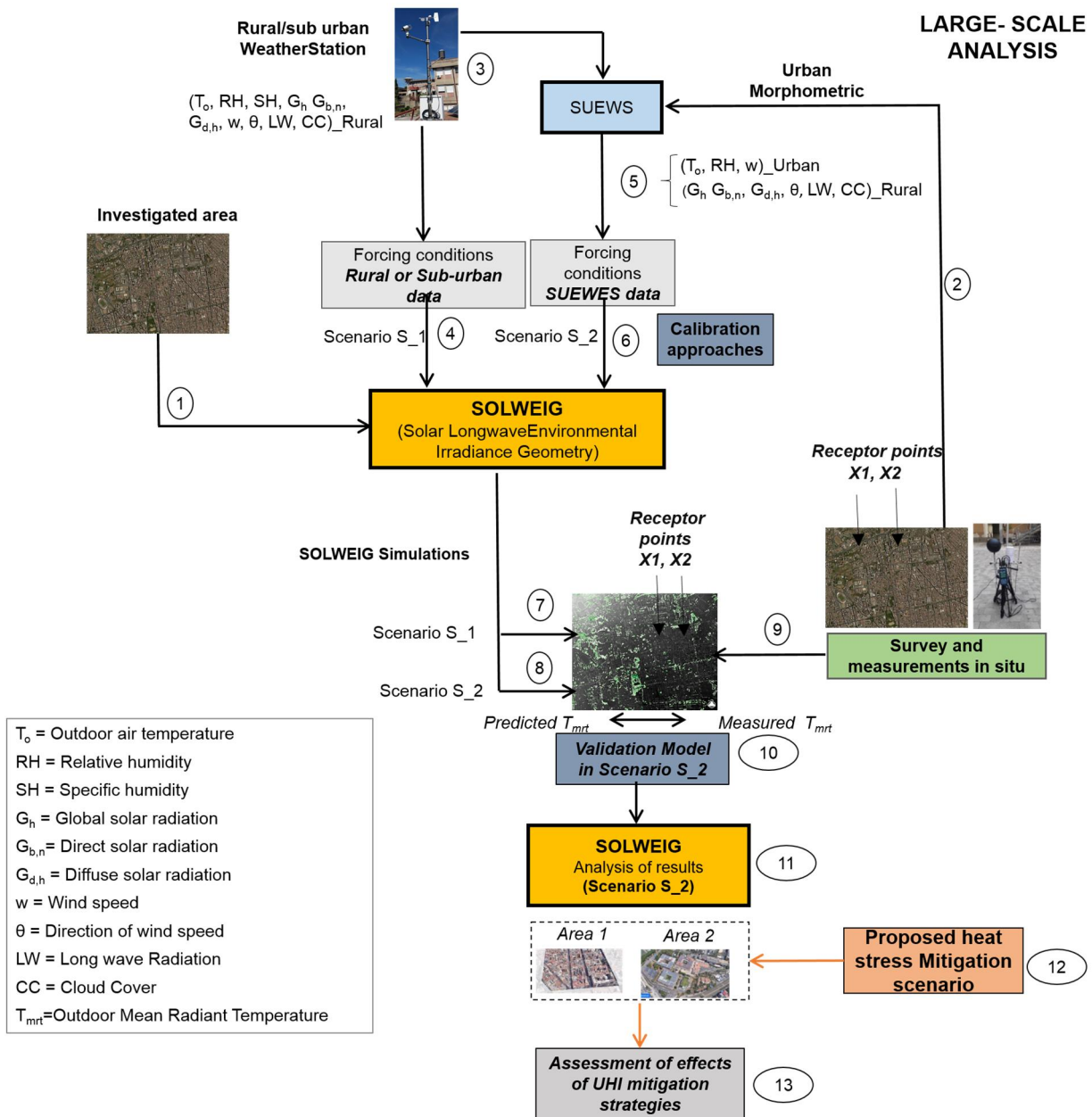
The large-scale analysis was carried out by means of a calibrated and validated model implemented in the Multi-scale Environmental Predictor (UMEP) tool. In UMEP, simulations are ran through the SOLWEIG (Solar and Long Wave Environmental Irradiance Geometry) module.

The calibration of the SOLWEIG model was carried out using an approach based on the urban morphing of rural weather data in order to overcome the lack of stationary weather stations in the investigated urban area. On the other hand, air temperature, relative humidity and wind speed in the urban canopy layer were calculated by means of SUEWS (Surface Urban Energy and Water Balance Scheme) that is a plug-in integrated in the UMEP (Urban Multi-scale Environment Predictor) tool. Global, diffuse, and direct solar radiation, wind speed and direction were recorded by a stationary weather station in the rural area.

Meteorological data recorded at a stationary weather station in rural or suburban areas, as well as geometrical and morphological data of the investigated area were used as input in SUEWS. The hourly values of air temperature, relative humidity, and wind speed at 10 m above ground level collected at rural weather station – which are the environmental variables more affected by the Urban Heat Island (UHI) effect – were first morphed through SUEWS and subsequently implemented in SOLWEIG in order to take into account urban site-specific characteristics (calibration phase).

To demonstrate the validity of such an approach, an on-site measurement campaign was carried out with a portable microclimate station to measure the mean radiant temperature. These measurements were eventually compared against the predictions of simulations run in SOLWEIG using both rural weather data (scenario S\_1) and the weather data morphed by SUEWS (scenario S\_2) as forcing conditions through suitable statistical indices (validation phase).

Figure 3.2 shows the workflow of the calibration and validation processes of the large-scale model.



- 1 Large-scale Modelling of the investigated area
- 2 Urban morphometric
- 3 Climate data recorded by rural/suburban weather station
- 4 Calibration of the Macroscale model with rural/suburban meteo data (Scenario S\_1)
- 5 Urban morphing of rural/suburban meteorological data by means of SUEWS
- 6 Calibration of the Macroscale model with morphed climate data (Scenario S\_2)
- 7 SOLWEIG simulations under Scenario (S\_1)
- 8 SOLWEIG simulations under Scenario (S\_2)
- 9 Comparison between SOLWEIG simulations and measurements on site
- 10 Model Validation
- 11 Analysis of the simulation results of the risk areas
- 12 Modelling of the heat stress Mitigation strategies in risk areas
- 13 Assessment of the effectiveness of heat stress Mitigation strategies

Figure 3.2. Workflow of the calibration and validation processes of the Macroscale model.

### 3.2.2 Calibration and validation of the urban Microscale model

The calibration approach of the ENVI-met model proposed in this research is carried out by forcing the software using hourly data of global, direct, and diffuse solar radiation, air temperature, relative humidity, wind speed and direction, as recorded by a meteorological station placed in a suburban area outside the city centre.

The hourly values of air temperature and relative humidity collected at this station were first morphed through the Urban Weather Generator (UWG) tool and then implemented in ENVI-met to account for site-specific characteristics (calibration phase).

UWG is a simulation program developed at MIT in the US that estimates air temperature and relative humidity in the urban canopy layer (UCL) using meteorological data measured at an operational weather station located in an open area outside the city.

UWG allows the designer to identify an urban area and describe it geometrically through three parameters: average building height, horizontal building density, and vertical to horizontal area ratio. District parameters transform the complex, heterogeneous urban structure into a homogenous depiction as defined by the Town Energy Balance (TEB) scheme (Masson, 2000).

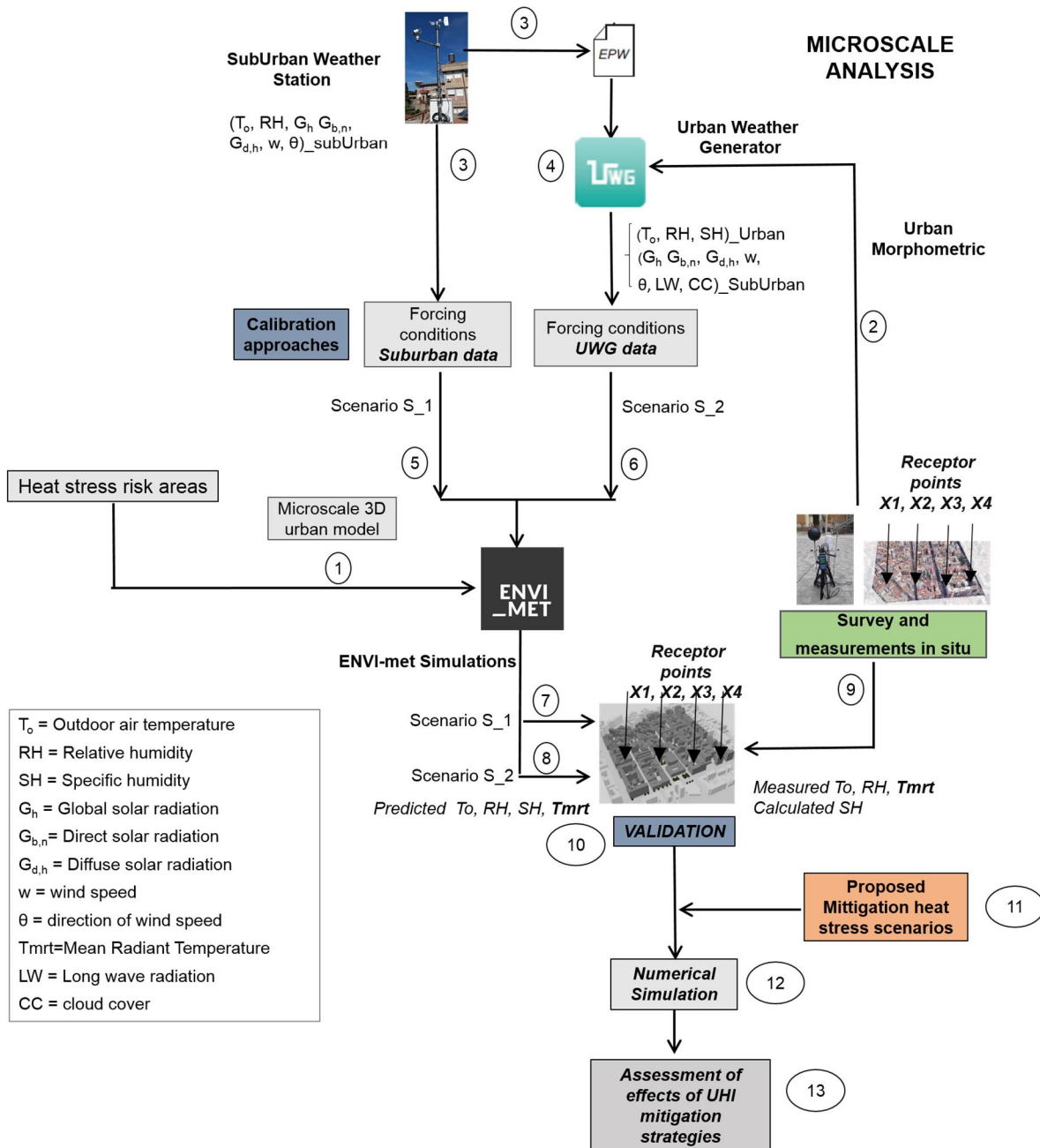
To demonstrate the validity of such an approach, two on-site measurement campaigns were carried out with a portable microclimate station to measure air temperature and relative humidity.

These measurements are eventually compared against the predictions of simulations run in ENVI-met using both suburban weather data (scenario S\_1) and the weather data morphed by UWG (scenario S\_2) as forcing conditions through suitable statistical indices (validation phase).

The approach based on the use of morphed values of air temperature and relative humidity recorded by the weather station (Scenario S\_2) was adopted for the calibration of the ENVI-met model of area 1 because such area is distant from the location of the weather station.

Since the weather station is located in Area 2, the model calibration of Area 2 was carried out using the meteorological data recorded by the same weather station (Scenario S\_1).

Figure 3.2 shows the workflow of the calibration and validation processes of the urban Microscale model.



- 1 Microscale Modelling of the risk areas
- 2 Urban morphometric
- 3 Climate data recorded by rural/suburban weather station
- 4 Urban morphing of rural/suburban meteorological data by means of UWG
- 5 Calibration of the Microscale model with rural/suburban meteo data (Scenario S\_1)
- 6 Calibration of the Microscale model with morphed climate data (Scenario S\_2)
- 7 ENVI-met simulations under Scenario (S\_1)
- 8 ENVI-met simulations under Scenario (S\_2)
- 9 Comparison between ENVI-met simulations and measurements
- 10 Model Validation
- 11 Modelling of the heat stress Mitigation strategies in study areas
- 12 Numerical simulations under Mitigation scenarios
- 13 Assessment of the effectiveness of heat stress mitigation strategies

Figure 3.3 Workflow of the calibration and validation process of the urban Microscale model.

### **3.3 Local Climate Zone (LCZ) Classification: state of the art, input, and output data**

#### 3.3.1 State of the art

The measurement of the urban heat island (UHI) effect through simple comparisons of “urban” and “rural” air temperatures has been under the light of several researchers for many decades. The conventional approach was based on gathering temperatures for two or more fixed sites and/or from mobile surveys. Sites were classified as either urban or rural, and their temperature differences ( $\Delta T_{U-R}$ ) indicated the UHI magnitude. Most investigators simply relied on the so-called urban and rural qualifiers to describe the local landscapes of their measurement sites.

Classifying measurement sites into urban and rural categories has given researchers a simple framework to separate the effects of city and country on local climate (Lowry 1977). Nevertheless, different studies have shown that the popular use of urban–rural classification and its methods have suffered critically (Stewart and Oke, 2012).

A relevant issue regarding the methodology used to detect UHI magnitude was found. This issue is the tremendous variety in landscapes considered as “rural” or “urban. The term urban has no single, objective meaning, and thus no climatological relevance. Therefore, the term urban can be defined universally for its physical structure, its surface properties, or its thermal climate.

In densely populated regions, the social, political, and economic space that separates cities and countryside is no longer distinguished by a clear urban–rural divide (Stewart and Oke, 2012).

Urban shape is becoming increasingly dispersed and decentralized as traditional and nontraditional land uses coexist. Currently, urban theorists contend that there is not a strong spatial demarcation between urban and rural areas, and that the relation between city and country can be more accurately deemed as a continuum, rather than as a dichotomy (Gugler 1996). It was recognized that a similar approach is limited in scope and function.

In light of this, several studies are focused on the development of different methods for classifying the cities on the basis of their climate in order to assess the effect of Urban Heat Island (UHI).

Chandler (1965) was perhaps the first heat island investigator to develop a climate-based classification of the city. He divided Greater London into four local regions, each distinguished by its climate, physiography, and built form.

Auer (1978) proposed an urban rural classification for the city of St. Louis, Missouri. He recognized 12 “meteorologically relevant” land uses in St. Louis, based on the city’s vegetation and building characteristics. Ellefsen (1991) derived a system of 17 neighborhood-scale “urban terrain zones” (UTZs) respectively from the geometry, street configuration, and construction materials of 10 U.S. cities.

In some European countries, the “climatope” system was traditionally used to classify urban terrain and climates, largely for planning purposes. Climatopes was derived from local knowledge of wind, temperature, land use, building structure, surface relief, and population density. These data were integrated in an urban area to reveal special climates of local places. It is worth highlighting that Wilmers (1991) identified nine such climates for the city of Hannover, Germany, based on vegetation, surface structure, and land use criteria. It was found that the model has several limitations. A full set of surface properties was not used to define climate classes. A complete set consists of the physical properties of surface structure, cover, fabric, and metabolism (Oke 2004). Although the climatope concept was well adapted to most urban settings, its class names and definitions varied widely with place, and thus could not provide classification systems with a means for comparison.

Grigg (1965) listed several criteria that a classification system should satisfy. Firstly, the system should invoke a simple and logical nomenclature by which objects/areas can be named and described. Second, a classification system should facilitate information transfer by associating objects/areas in the real world with an organized system of generic classes. Users can then make comparative statements about the members belonging to each class. A properly constructed classification system should simplify the objects/areas under study, and thereafter promote theoretical statements about their properties and relations. According to Grigg’s criteria, a new classification system at local scale of urban and rural field sites for heat island assessment, inclusive of all regions, independent of all cultures, and quantifiable according to class properties that are relevant to surface thermal climate is proposed by Oke (2008).

Combining features of both Auer’s and Ellefsen’s schemes, Oke designed a simple and generic classification of city zones to improve siting of meteorological instruments in urban areas. His scheme divides city terrain into seven homogenous areas called “urban Climate Zones” (UCZs), which range from semi-rural to intensely developed sites. The zones are distinguished by their urban structure (building/street sizes), cover (permeability), fabric (materials), metabolism (human activity), and potential to modify the natural, or “preurban,” surface climate. The classifications of Chandler, Auer, Ellefsen, and Oke are all predisposed to the form and function of modern, developed cities, so their use in more different economic settings is limited.

Most recently, Grimmond and Loridan (2011) developed “urban zones for characterizing energy partitioning,” or UZEs.

Stewart and Oke have introduced the Local Climate Zones (LCZs) to standardize the classification of urban and rural field sites for observational UHI studies. Given the disparity in how individual researchers interpret the urban landscape, LCZs are necessary instruments for a coherent and uniform

classification of landscapes for ground-based climate studies. the LCZ system prompts investigators to recognize and separate urban from nonurban influences on temperature.

The LCZ scheme aims to overcome the simple approach based on the comparison of “urban” and “rural” air temperatures with a universally understood, climate-based classification of urban and rural sites. The classification of weather stations and observatories into LCZ classes, rather than “urban” and “rural” classes, could lead to more accurate assessments of urban bias. Unlike climatopes, LCZs are developed from generalized knowledge of built forms and land cover types that are universally recognized, not from specialized knowledge of local topography and climatology.

LCZs represent a generic, easily understood, culturally neutral description of land-use and land-cover. The universe for the LCZ classification is “landscape,” defined as a local-scale tract of land with physical and/or cultural characteristics that have been shaped by physical and/or cultural agents.

The landscape universe is divided according to properties that influence screen-height temperature, namely surface structure (height and spacing of buildings and trees) and surface cover (pervious or impervious).

All classes to emerge from logical division of the landscape universe are called “local climate zones” (LCZs). The name is appropriate because the classes are local in scale, climatic in nature, and zonal in representation. LCZs represent a simple composition of buildings, roads, plants, soils, rock, and water, each in varying amounts and each arranged uniformly into 17 recognizable patterns.

The landscape universe consists of 17 standard LCZs, of which 15 are defined by surface structure and cover and 2 by construction materials and anthropogenic heat emissions.

The standard set is divided into “built types” 1–10, and “land cover types” A–G (Table 3.1). Built types are composed of constructed features on a predominant land cover, which is paved for compact zones and low plants / scattered trees for open zones. Land cover types can be classified into seasonal or ephemeral properties (i.e., bare trees, snow-covered ground, dry/wet ground).

The LCZ classification is based on 10 quantifiable properties relating to surface structure (sky view factor, aspect ratio, roughness element height), surface cover (plan fraction occupied by buildings, pervious, and impervious ground), surface fabric (thermal admittance, surface albedo), and human activity (anthropogenic heat output)”, which have been gathered from a large body of literature and extensive field work.

Surface structure affects local climate through its modification of airflow, atmospheric heat transport, and shortwave and long wave radiation balances, while surface cover modifies the albedo, moisture availability, and heating/cooling potential of the ground

The logical structure of the LCZ system is supported by observational and numerical modelling data (Stewart and Oke 2010). The parameters values for each LCZ type are reported in table 3.2 and 3.3.



Table 3.1. Definition of Local Climate Zone (Stewart and Oke, 2012).













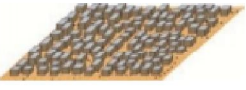
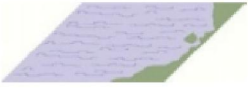



Built types	Definition	Land Cover types	Definition		
<b>1.Compact high-rise</b> 	Dense mix of tall buildings to tens of stories. Few or no trees. Land cover mostly paved. Concrete, steel, stone and glass construction materials.	A. Dense trees 	Heavily wooded landscape of deciduous trees. Land cover mostly pervious (low plants). Zone function is natural forest, tree cultivation, or urban park.		
<b>2.Compact -midrise</b> 	Dense mix of midrise buildings (3-9 stories). Few or no trees. Land cover mostly paved. Stone, brick, tile and concrete construction materials.	B. Scattered trees 	Lightly wooded landscape of deciduous and/or evergreen trees. Land cover mostly pervious (low plants). Zone function is natural forest, tree cultivation, or urban park.		
<b>3. Compact low-rise</b> 	Dense mix of low-rise buildings (1-3 stories). Land cover mostly paved. Stone, brick, tile and concrete construction materials.	C. Bush, scrub 	Open arrangement of bushes, shrubs, and short, woody trees. Land cover mostly pervious (bare soil or sand). Zone function is natural scrubland or agriculture.		
<b>4. Open low-rise</b> 	Open arrangement of tall buildings to tens of stories. Abundance of pervious land cover (low plants, scattered trees). Concrete, steel, stone and glass construction materials.	D. Low plants 	Featureless landscape of grass or herbaceous plants/crops. Few or no trees. Zone function is natural grassland, agriculture or urban park		
<b>5. Open midrise</b> 	Open arrangement of midrise buildings (3-9 stories). Abundance of pervious land cover (low plants, scattered trees). Concrete, steel, stone and glass construction materials.	E. Bare rock or paved 	Featureless landscape of rock or paved cover. Few or no trees or plants. Zone function is natural desert (rock) or urban transportation.		
<b>6. Open Low-rise</b> 	Open arrangement of low-rise buildings (1-3 stories). Abundance of pervious land cover (low plants, scattered trees). Wood, steel, stone and glass construction materials.	F. Bare soil or sand 	Featureless landscape of soil or sand cover. Few or no trees or plants. Zone function is natural desert or agriculture.		
<b>7. Lightweight Low-rise</b> 	Dense mix of single-story buildings. Few or no trees. Land cover mostly hard-packed. Lightweight construction materials (e.g., wood, thatch, corrugated metal)	G. Water 	Large, open water bodies such as seas and lakes, or small bodies such as rivers, reservoirs, and lagon.		
<b>8. Large Low-rise</b> 	Open arrangement of large low-rise buildings (1-3 stories). Few or no trees. Land cover mostly paved o hard packed. Steel, concrete, metal, and stone construction materials.	<b>Variable Land Cover Properties</b> Variable or ephemeral land cover properties that change significantly with synoptic weather patterns, agricultural practices, and/or seasonal cycles.			
<b>9. Sparsely built</b> 	Sparse arrangement of small or medium-sized buildings in a natural setting. Abundance of pervious land cover (low plants, scattered trees)			b. bare trees	Leafless deciduous trees (e.g., winter). Increased sky view factor. Reduced albedo.
				s. snow cover	Snow cover >10 cm in depth. Low admittance. High albedo.
				d. dry ground	Parched soil. Low admittance. Large Bowen ratio. Increased albedo
<b>10. Heavy Industries</b> 	Low-rise and midrise industrial structures (towers, tanks, stacks). Few or no trees. Land cover mostly paved or hard packed. Metal, steel, and concrete construction materials.	w. wet ground	Waterlogged soil. High admittance. Small Bowen ratio. Reduced albedo.		

Table 3.2. Values of geometric and surface cover properties for local climate zones (Stewart and Oke, 2012).

Local Climate Zone (LCZ)	Sky View Factor <sup>a</sup> (SVF)	Aspect Ratio <sup>b</sup> (H/W)	Building surface fraction <sup>c</sup> (BSF)	Impervious surface fraction <sup>d</sup> (ISF)	Pervious surface fraction <sup>e</sup> (PSF)	Height of roughness elements <sup>f</sup> (zd)	Terrain roughness <sup>g</sup> (z <sub>0</sub> )
LCZ 1 <i>Compact high-rise</i>	0.2-0.4	> 2	40-60	40-60	< 10	> 25	8
LCZ 2 <i>Compact midrise</i>	0.3-0.6	0.75 -2	40-60	30-50	< 20	10-25	6-7
LCZ 3 <i>Compact low-rise</i>	0.2-0.6	0.75 -1.5	40-70	20-50	< 30	3-10	6
LCZ 4 <i>Open low-rise</i>	0.5-0.7	0.75 -1.25	20-40	30-40	30-40	> 25	7-8
LCZ 5 <i>Open midrise</i>	0.5-0.8	0.3 -0.75	20-40	30-50	20-40	10-25	5-6
LCZ 6 <i>Open low-rise</i>	0.6-0.9	0.3 -0.75	20-40	20-50	30-60	3-10	5-6
LCZ 7 <i>Lightweight low-rise</i>	0.2-0.5	1-2	60-90	< 20	< 30	2-4	4-5
LCZ 8 <i>Large low-rise</i>	> 0.7	0.1 -0.3	30-50	40-50	< 20	3-10	5
LCZ 9 <i>Sparsely built</i>	> 0.8	0.1-0.25	10-20	< 20	60-80	3-10	5-6
LCZ 10 <i>Heavy Industry</i>	0.6-0.9	0.2-0.5	20-30	20-40	40-50	5-15	5-6
LCZ A <i>Dense trees</i>	> 0.4	> 1	< 10	< 10	> 90	3-30	8
LCZ B <i>Scattered trees</i>	0.5-0.8	0.25-0.75	< 10	< 10	> 90	3-15	5-6
LCZ C <i>Bush scrub</i>	0.7-0.9	0.25-1.0	< 10	< 10	> 90	< 2	4-5
LCZ D <i>Low plants</i>	> 0.9	< 0.1	< 10	< 10	> 90	< 1	3-4
LCZ E <i>Bare rock or paved</i>	> 0.9	< 0.1	< 10	> 90	< 10	< 0.25	1-2
LCZ F <i>Bare soil or sand</i>	> 0.9	< 0.1	< 10	< 10	> 90	< 0.25	1-2
LCZ G <i>Water</i>	> 0.9	< 0.1	< 10	< 10	> 90	-	1

<sup>a</sup>Ratio of the amount of sky hemisphere visible from ground level to that of an unobstructed hemisphere.

<sup>b</sup>Mean height to width ratio of street canyons (LCZs 1-7), building spaces (LCZs 8-10) and tree spacing (LCZs A-G).

<sup>c</sup>Ratio of building plan area to total plan area (%).

<sup>d</sup>Ratio of impervious plan area (paved, rock) to total plan area (%).

<sup>e</sup>Ratio of pervious plan area (bare soil, vegetation, water) to total plan area (%).

<sup>f</sup>Geometric average of building heights (LCZs 1-10) and tree/plant heights (LCZs A-F).

Table 3.3. Values of thermal, radiative, and metabolic properties for local climate zones (Stewart and Oke, 2012).

Local Climate Zone (LCZ)	Surface admittance <sup>a</sup>	Surface albedo <sup>b</sup>	Anthropogenic heat output <sup>c</sup>
LCZ 1 <i>Compact high-rise</i>	1,500-1,800	0.10-0.20	50-300
LCZ 2 <i>Compact midrise</i>	1,500-2,200	0.10-0.20	< 75
LCZ 3 <i>Compact low-rise</i>	1,200-1,800	0.10-0.20	< 75
LCZ 4 <i>Open low-rise</i>	1,400-1,800	0.12-0.25	< 50
LCZ 5 <i>Open midrise</i>	1,400-2,000	0.12 -0.25	< 25
LCZ 6 <i>Open low-rise</i>	1,200-1,800	0.12 -0.25	< 25
LCZ 7 <i>Lightweight low-rise</i>	800-1,500	0.15-0.35	< 35
LCZ 8 <i>Large low-rise</i>	1,200-1,800	0.15 -0.25	< 50
LCZ 9 <i>Sparsely built</i>	1,000-1,800	0.12-0.25	< 10
LCZ 10 <i>Heavy Industry</i>	1,000-2,500	0.12-0.30	> 300
LCZ A <i>Dense trees</i>	unknown	0.10–0.20	0
LCZ B <i>Scattered trees</i>	1,000-1,800	0.15-0.25	0
LCZ C <i>Bush scrub</i>	700-1,500	0.15-0.30	0
LCZ D <i>Low plants</i>	1,200-1,600	0.15-0.25	0
LCZ E <i>Bare rock or paved</i>	1,200-2,500	0.15-0.30	0
LCZ F <i>Bare soil or sand</i>	600-1,400	0.20-0.35	0
LCZ G <i>Water</i>	1,500	< 0.1	0

<sup>a</sup>Ability of surface to accept or release heat ( $\text{J m}^{-2} \text{s}^{-1/2} \text{K}^{-1}$ ). Varies with soil wetness and material density. Few estimates of local-scale admittance exist in the literature; values given here are therefore subjective and should be used cautiously. Note that the “surface” in LCZ A is undefined and its admittance unknown.

<sup>b</sup>Ratio of the amount of solar radiation reflected by a surface to the amount received by it. Varies with surface color, wetness, and roughness.

<sup>c</sup>Mean annual heat flux density ( $\text{W m}^{-2}$ ) from fuel combustion and human activity (transportation, space cooling/heating, industrial processing, human metabolism). Varies significantly with latitude, season, and population density.

Table 3.4 reports the classification of effective terrain roughness and the correspondence with LCZs.

Table 3.4. Classification of effective terrain roughness (Davenport, 2000)

Davenport class	Roughness length $z_0$ (m)	Landscape description	LCZ correspondence
1. Sea	0.0002	Open water, snow-covered flat plain, featureless desert, tarmac, and concrete, with a free fetch of several kilometers.	E, F, G
2. Smooth	0.0005	Featureless landscape with no obstacles and little if any vegetation (e.g., marsh, snow-covered or fallow open country).	E, F
3. Open	0.03	Level country with low vegetation and isolated obstacles separated by 50 obstacle heights (e.g., grass, tundra, airport runway).	D
4. Roughly open	0.10	Low crops or plant covers; moderately open country with occasional obstacles (e.g., isolated trees, low buildings) separated by 20 obstacle heights.	7, C, D
5. Rough	0.25	High crops, or crops of varying height; scattered obstacles separated by 8 to 15 obstacle heights, depending on porosity (e.g., buildings, tree belts).	5-10, B, C
6. Very rough	0.5	Intensely cultivated landscape with large farms and forest clumps separated by 8 obstacle heights; bushland, orchards. Urban areas with low buildings interspaced by 3 to 7 building heights; no high trees.	2, 3, 5, 6, 9, 10, B
7. Skimming	1.0	Landscape covered with large, similar-height obstacles, separated by 1 obstacle height (e.g., mature forests). Dense urban areas without significant building-height variation.	2, 4
8. Chaotic	$\geq 2$	Landscape with irregularly distributed large obstacles (e.g., dense urban areas with mix of low and high-rise buildings, large forest with many clearings).	1, 4, A

These properties were selected from urban climate observational and numerical modelling literature. Measured and estimated values of geometric, thermal, radiative, metabolic, and surface cover properties were gathered from urban and rural field sites worldwide Anderson et al. (1976), Auer (1978), Ellefsen (1990/91), and Oke (2004), and from reviews of empirical urban climate literature (Grimmond and Oke, 1999).

Local climate zones are defined as regions of uniform surface cover, structure, material, and human activity that span hundreds of meters to several kilometers in horizontal scale. LCZ is referred to as a local (or neighborhood) scale and lies between climatological micro and mesoscales.

This concept allows a certain range of appropriate scales, which implies different “valid” LCZ maps depending on the resolution. The LCZ system is inherently generic and cannot capture the peculiarities of every urban and rural site.

The scheme of classification was designed to be “sufficiently generic”, i.e., it is inclusive of all regions and cultures and abandons excessive regional/architectural detail. Its view of the landscape universe, it is highly reductionist, and, like all classifications, its descriptive and explanatory powers are limited. The scheme has a reasonable level of complexity, while retaining universal meaning.

The LCZ classes are each physically discrete in surface structure and land cover, such that the boundaries separating most classes can be delineated on a city map or aerial photograph.

When an entire city is discretized, each class will unavoidably have a certain amount of internal heterogeneity, since it is composed of a variety of urban landscapes that are part of a continuum rather than discrete types. The class boundaries become crucial, demanding a precise formulation of the boundaries between the classes. Generally, no “overlaps” or “holes” exist for the parameter combinations of the 17 standard classes the concept of LCZs.

The internal homogeneity portrayed by each LCZ is unlikely to be found in the real world, except in planned or intensely managed settings. The 17 patterns should nevertheless be familiar to users in most cities and should be adaptable to the local character of most sites.

However, the thermal climate across those boundaries is spatially continuous—the screen-level air temperature of one zone blends gradually into that of its neighboring zones. This effect arises from advection of heat and moisture across areas of different surface structure, land cover, and human activity. As air crosses the border between neighboring zones, it gradually adjusts to a new set of internal boundary conditions, forming thermal transitions—not sudden breaks at zone borders.

The upwind fetch required for air at screen height to become fully adjusted to its underlying surface is typically 200–500 m, depending on surface roughness, building geometry, and atmospheric stability conditions (Oke 1987). Therefore, each LCZ should have a minimum diameter of 400–1,000 m (i.e., a radius of 200–500 m) so that the adjusted portion of its internal boundary layer lies entirely within the zone and does not overlap with surrounding LCZs of different structure.

Users must collect appropriate site metadata to quantify the surface properties of the area to be classified. This is best done by a visit to the field sites in person to survey and assess the local horizon, building geometry, land cover, surface wetness, surface relief, traffic flow, and population density. If a field visit is not possible, secondary sources of site metadata include aerial photographs, land cover/land use maps, satellite images (e.g., Google Earth), and published tables of property values.

In the case of area of influence for a field site being too heterogeneous to derive locally representative values from its surface properties, users are advised to designate the site “unclassified” and to find a more homogeneous setting for observation. In order to select the local climate zone, metadata should lead users to the best, not necessarily exact, match of their field sites with LCZ classes.

Metadata are unlikely to match exactly with the surface properties values of one LCZ class. If the measured or estimated values align poorly with those of the LCZs, the process of selecting a best-fit class becomes one of interpolation rather than straight matching. Users should first look to the surface cover fractions of the site to guide this process.

The lack of a suitable match should be highlighted to the users so that they can highlight the main difference(s) between their site and its nearest equivalent LCZ. LCZ class should be identified by these differences and described with the appropriate LCZ name. Alternatively, users can create new subclasses for sites that deviate from the standard set of classes.

New subclasses represent combinations of built types, land cover types, and land cover properties. The notation for new subclasses is LCZ  $X_{ai}$ , where X is the higher parent class in the standard set of LCZs, a is the lower parent class from the standard set, and i is a variable or ephemeral land cover property

Land cover properties are selected from the subset of bare trees (b), snow cover (s), dry ground (d), and wet ground (w). Identifiers a and i may each be assigned one or more classes or properties.

For example, a site whose building geometry is open midrise (LCZ 5) but whose surface cover is predominantly bush, scrub (LCZ C) should be notated as LCZ 5C to represent the main features of its two parent classes, the first in a higher position of the LCZ order (baseline character 5) and the second in a lower position (subscript C).

By this convention, other subclasses include open midrise with paved ground (LCZ 5<sub>E</sub>), open midrise with open low-rise (LCZ 5<sub>6</sub>), open low-rise with dense, bare trees (LCZ 6<sub>AB</sub>), low plants with wet ground (LCZ D<sub>w</sub>), and bare soil with dry ground (LCZ F<sub>d</sub>).

Although subclasses add flexibility to the LCZ system, they do not have surface property values and thus their thermal climates may not be known a priori. At best, it can be estimating the surface property values—and surface air temperatures—by weighting the known values of two (or more) standard classes.

The thermal climate of an LCZ subclass is not expected to differ significantly from either of its two (or more) parent classes, because maximum thermal contrasts between successive zones in the standard set are typically no more than 1–2 K (Stewart and Oke, 2010).

In addition, the purpose of LCZs is to ease the process of site classification and metadata reporting for heat island investigators. Creating too many, or too complex, subclasses undermine this principal function.

While subclasses may enhance the physical description of a site, they may not improve communication or comparison of that site with others.

Subclasses are justified when they describe sites whose secondary features are thought to affect the local climate, or whose features may otherwise relate to the aims of a climate investigation. The definition of subclasses should be allowed in specific instances where the climatic effect is not negligible and the subclass is applicable to larger areas. Generally, subclasses should be used cautiously since the higher accuracy comes at the cost of reduced universality.

Existing LCZ classes provide a disjoint and largely complementary discretization of the (urban) landscape universe that covers most existing urban forms. The framework based on LCZs allows to assess the UHI magnitude by means LCZ temperature difference (e.g.,  $\Delta T_{LCZ 1 - LCZ D}$ ), not an “urban–rural” difference ( $\Delta T_{u-r}$ ).

To date, the integration of urban climate knowledge with city planning has not been especially useful or successful, in part because urban climatology has advanced slowly around issues of scale and communication. The LCZ system could advance these issues because it offers a basic package of urban climate principles for architects, planners, ecologists, and engineers.

### 3.3.2 Methods for LCZ mapping

The recently developed Local Climate Zones (LCZs) classification system was initially not designed for mapping but to classify temperature observation sites. Nevertheless, as a need arose to characterize areas based on their distinct thermal field, utilizing LCZ classes for mapping was a logical step. Methods used in LCZ classification include in-situ measurements, geographic information system (GIS)-based and remote-sensing-image-based calculations. These methods have their own advantages and limitations.

In-situ measurement is the most basic method used in LCZ classification. An advantage of in-situ measurement is its ease of operation, but the high time costs limit its popularity.

GIS-based methods are common techniques for mapping out LCZs. They rely on GIS data of urban morphology, urban planning and building information to calculate each contributing factor for classifying LCZs. The input data for GIS-based method includes building and land use data (including greenery information) under shape-file format. Building data include three layers (building height, building surface fraction, and Sky View Factor). They are generated from the original input of building data with QGIS software. The whole studied area is sampled in grid cells in order to identify LCZs of the investigated area on the basis of the LCZ classification criteria developed by Stewart and Oke (2012), all inputs metadata into grid cells are questioned by means combined query operation in QGIS environment. Since the metadata of GIS-based methods are derived from real urban morphologies, GIS-based methods usually achieve high accuracies. Several researchers used this method to develop LCZs classification maps of their target regions (Perera et al., 2012; Lelovics et al., 2014; Gál et al., 2015). The GIS-based approach was tested for Szeged (Hungary) and was conducted on lot area polygons derived from a 3D building database. The approach is quite objective but requires specific data that are generally unavailable for most cities. In addition, it is worth highlighting that one limitation is that city GIS data are not always complete or accessible to the public. The remote-sensing-image-based method is another widely used way to classify LCZ classes.

Several kinds of remote sensing images (such as Landsat images, panchromatic VHR) are used as input data for LCZ classification. Among these satellite images based LCZ classification methods, World Urban Database and Access Portal Tools (WUDAPT) deserves to be mentioned.

WUDAPT is a global initiative based on a scientific community volunteer program. WUDAPT was designed to be a universal, simple, and objective method to be used as part of a global protocol to derive information about the form and function of cities. It aims to develop an easier LCZ classification scheme applying free satellite images and free software and it can be handled without expert remote sensing knowledge. WUDAPT uses free software such as SAGA GIS and Google Earth (GE). WUDAPT include three levels: 0, 1 and 2 levels. Level 0 contains mainly 2-dimensional urban morphological information and rough urban function based on their effect on the local air temperature.

Levels 1 and 2 provide more detailed 3-dimensional urban morphological information, material composition data and anthropogenic functions at building level, so they are suitable for various weather and climate models (Ching et al., 2017). Levels 1 and 2 are not still completely developed. WUDAPT level 0 method includes three main steps:

- Pre-processing of Landsat data.
- Digitization of training areas in GE according to the LCZ scheme.
- Classification in SAGA-GIS.

In pre-processing of Landsat data, Landsat 5 satellite images are selected as input image data because they contain urban structure information, like thermal information, which can be used to classify and map LCZs. Digitization of training areas in Google Earth allows the representation of each area belonging to LCZ classes through the selection of polygons as training sample. The LCZ classification is carry out using the System for Automated Geoscientific Analyses (SAGA) software. The pre-processed Landsat images and the selected training areas are fed into SAGA-GIS.

The LCZ classification of the study areas is calculated and conducted by the random forest classifier by comparing the similarity between the training samples and the rest of the study areas. A random forest is a prediction model which represents a mapping between attributes of each LCZ class and the identified LCZ type. The forest can be used to classify the whole input image into different LCZ classes. Several world-wide researchers have adopted and applied the WUDAPT method in their UHI studies (Brousse et al., 2016; Kaloustian and Bechtel, 2016; Wang et al., 2018).

Figures 3.4 and 3.5 show the workflow of GIS-based and WUDAPT methods respectively.



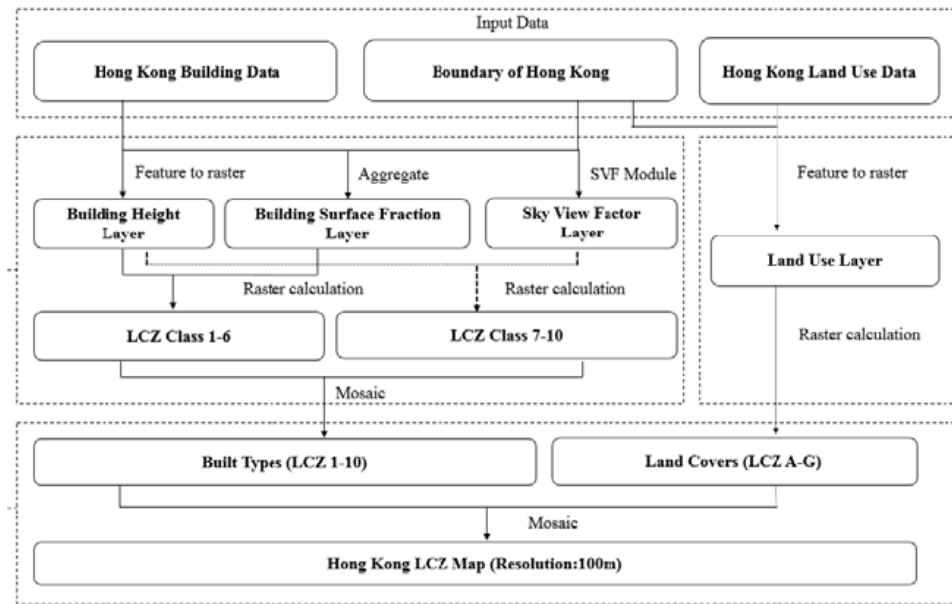


Figure 3.4. Workflow of GIS-based Method (Wang et al. 2018).

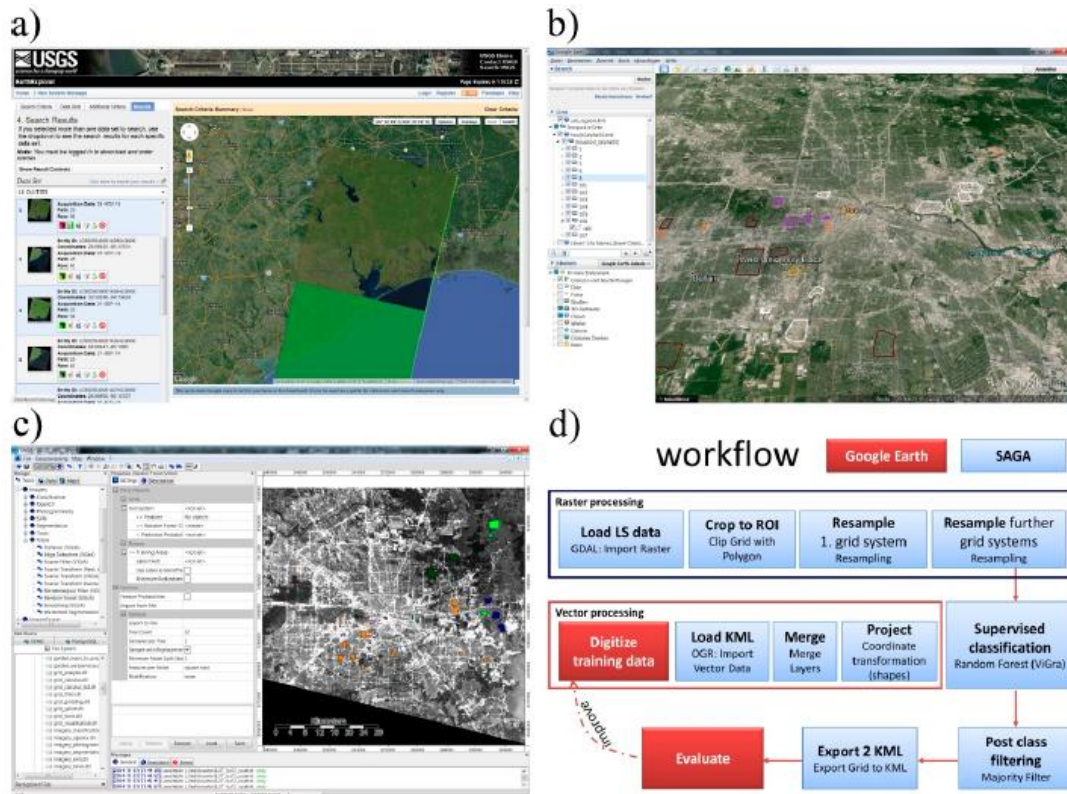


Figure 3.5. Overview of the mapping procedure of WUDAPT method: a) Acquisition of Landsat data in USGS Earth-Explorer; (b) Digitation of training areas in Google Earth; c) Classification in SAGA-GIS; d) Workflow (Betchel et al., 2015).

GIS-based and WUDAPT methods are the two most popular ways to classify and to map LCZs. A comparison of accuracies of the WUDAPT and GIS-based methods has found that in general the overall accuracy of the GIS-based method is higher than that of the WUDAPT method. Substantially, the WUDAPT method is relatively less accurate than the GIS-based method because it is based on

the digitation of training samples of potential seventeen LCZs obtained by visual interpretation from Google Earth.

In particular, the relatively low accuracy of the WUDAPT method regard LCZ 1-6 built types.

GIS-based method is relatively more accurate because it classifies built types based on actual building data to define the parameters of LCZ 1-6 precisely.

The WUDAPT method is a kind of machine learning algorithm, depending significantly on the quantity and quality of training samples as well as remote sensing images and local urban morphological characteristics. The ground truth data also has its own limitations and may not truly represent the real conditions of study areas. In addition, a lack of building height information in the Landsat images can also lead to the lower accuracy of LCZ 1-6 generated by the WUDAPT method. Hence, a general LCZ concept mapping without building data will lead to low classification accuracy. The accuracy of the WUDAPT method is less satisfactory when specific LCZ classes need to be examined thoroughly. This method may not be so helpful for researchers hoping to look into details at a district level. Most dominant built types in the urban districts are classified correctly when the GIS-based methods are applied. Therefore, the GIS-based method is better when detailed analyses have to be conducted (Perera et al., 2012; Lelovics et al., 2014; Gál et al., 2015).

### 3.3.3 GIS method for LCZ mapping of the investigated area

In order to identify the more critical sites from a climate perspective in the studied area, a Local Climate Zones (LCZs) classification was carried out.

Based on advantages and limitations about LCZ mapping methods discussed in 3.3.2, the GIS method was adopted to determine the parameters necessary for LCZ classification.

In this study, the LCZ classification process is subdivided into four main steps: (1) Discretization of the investigated area; (2) Calculation of the parameters of surface structure and surface cover necessary for LCZ classification; (3) Setting of queries for grid cells of the investigated domain; (4) LCZ mapping.

Step 1: A polygon grid was applied to the whole studied area in order to discretize the entire investigated area in square cells. Based on a minimum diameter of 400–1,000 m (i.e., a radius of 200–500 m) for each LCZ as discussed above, grid cells with dimensions 200 x 200 m<sup>2</sup> were adopted. These dimensions represent a good compromise to discretize the area for LCZ classification according to the recommendations discussed in 3.3.2.

Step 2: Standard set parameters introduced by Oke and Stewart are represented by ten quantifiable properties relating to surface structure (sky view factor, aspect ratio, roughness element height, Terrain roughness class), surface cover (plan fraction occupied by buildings, pervious, and impervious ground), surface fabric (thermal admittance, surface albedo) and human activity

(anthropogenic heat output). Based on available databases of the investigated area, 6 of the 10 properties identified by Stewart & Oke (2012) were determined.

From the initial set of parameters used for LCZ classification, the aspect ratio (height: width,  $H : W$ ), surface albedo ( $\alpha$ ), Thermal admittance ( $Y$ ), and the anthropogenic heat output are omitted. The aspect ratio has been disregarded as it tends to be too theoretical, and it can only be clearly calculated for regular street networks with straight streets, rectangular intersections and blocks of buildings filling in the available area between roads. Surface albedo, thermal admittance and anthropogenic heat output were disregarded, as no data were available for the study area.

Therefore, the parameters such as Building Surface Fraction (BSF), Pervious Surface fraction (PSF), Impervious Surface Fraction (ISF), Roughness element height ( $z$ ), Terrain roughness class ( $z_0$ ) and Sky View Factor (SVF) were adopted for LCZ classification of the investigated area.

Unlike the Gis-methods for LCZ classification currently available in literature studies, the Gis-method adopted in this study uses the morphometric calculator tool of UMEP for the calculation of parameters such as Sky View Factor (SVF) and Terrain roughness class ( $z_0$ ).

Other parameters (Building surface Fraction (BSF), Pervious Surface fraction (PSF), Impervious Surface Fraction (ISF) and Roughness element height ( $z$ )) were determined on the basis of original input Databases under shape-file format. A mean value of each parameter for each grid of the investigated domain was calculated by Mathematical operations implemented in QGis Environment. The values of such parameters, as associated to each grid cell are included in a attribute table of “Grid” shapefile. Figure 3.6 summarizes the steps adopted for LCZ classification of investigated area.

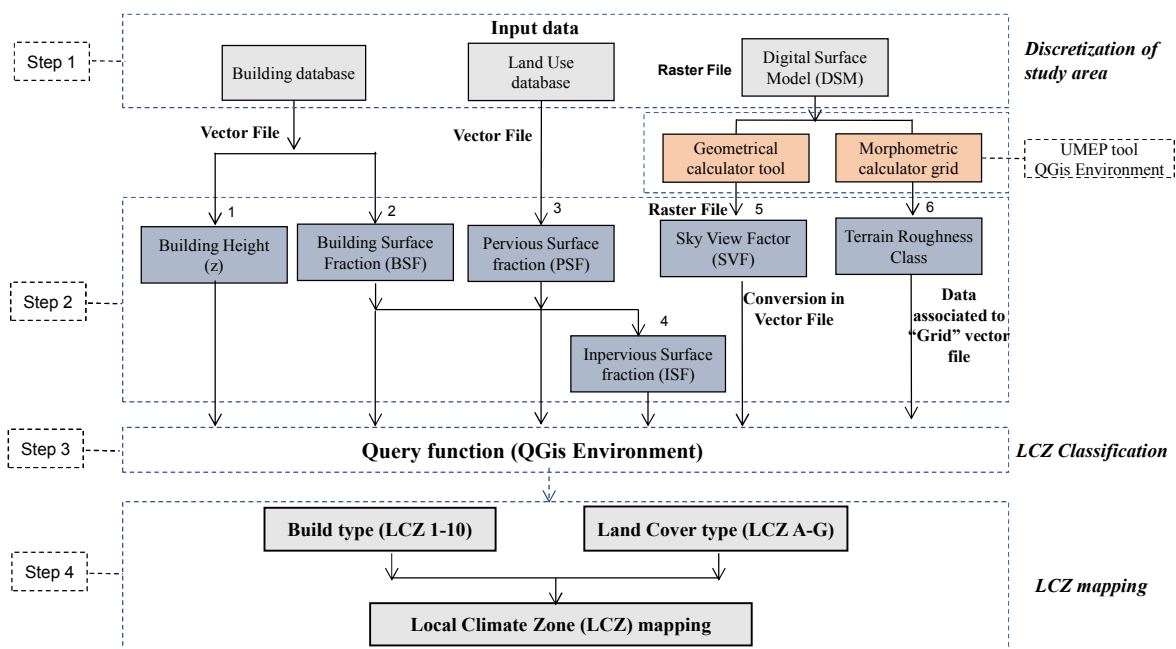


Figure 3.6. Flow Chart of the steps related to the LCZ classification process.

The input data and the calculation processes of the parameters are presented in the flowchart reported in figure 3.4. LCZ classification parameters were calculated as follow:

- Building surface fraction (BSF) is the fraction of ground surface covered by buildings. Building footprints and the lot area polygons, were obtained from the 3D building database. 3D building database in shapefile format contains building footprint areas as polygon-type data and information on building heights those were derived by means of photogrammetric methods.
- Pervious Surface Fraction (PSF) is the ratio of pervious cover and ground surface. The pervious surface data was derived by original specific databases realized on the basis of aerial photogrammetric view of the investigated area.
- Impervious Surface Fraction (ISF) was derived from the building surface fraction (BSF) and the Pervious Surface Fraction (PSF) using the formula  $ISF = 1 - (BSF + PSF)$ . This formula was set in the attribute table associated to “Grid” vector file.
- Height of roughness elements was calculated as a mean height of buildings and vegetation weighted by the building and vegetation areas. The input data of buildings were also attained from the 3D building database.
- Sky view factor (SVF) was calculated at the street level for all points of the investigated domain by morphometric calculator of UMEP tool implemented in QGIS Environment. The SVF calculation takes into account the effect of trees and buildings, but the effects of pitched roofs are disregarded as buildings were considered to be flat roofed. For LCZ classification the average value of SVF referred to each grid cell was adopted.
- Terrain roughness height was calculated by means of the morphometric calculator grid tool associated with the Digital Surface Model of the investigated area. Terrain roughness was determined using the Davenport roughness classification method (Davenport et al. 2000).

Step 3. Based on the ranges of all parameters required for LCZ classification defined by Stewart & Oke (2012) (see Table 3.2), a system of combined query in QGIS environment for build types (LCZ 1-10) and Land Cover types (LCZA-G) was set to identify the Local Climate Zones (LCZs) in the investigated area. Each query includes the specific ranges of BSF, PSF, ISF, z, zo and SVF parameters for each type of LCZ.

The grid cells that have all parameters (such as BSF, PSF, ISF, z, zo, SVF) within the ranges required by Stewart and Oke’s criteria were classified as standard LCZ.

The grid cells that have two parameters did not comply with the matched standard ranges set by Stewart and Oke were notated as LCZ\*\*x, while LCZ\*x was used to indicate that a standard range did not complied with.

x indicates the nearest parent class in the standard set of LCZs according to the scheme of Stewart and Oke. The grid cells that have four parameters outside the standard ranges were not classified.

Step 4: LCZ mapping was carried out using bands of false color so that a single color is associated to each LCZ.

### 3.4 Urban Multi-scale Environmental Predictor (UMEP): state of the art, input and output data

#### 3.4.1 UMEP: features and framework

UMEP (Urban Multi-scale Environmental Predictor) is a freeware city-based climate analysis tool integrated in QGIS Environment (Lindberg et al, 2019). The modelling system contained within UMEP is designed to run from the street canyon to city scale ( $10^0$ - $10^5$  m) depending on the application. The potentiality of UMEP is the capacity to identify the heat waves and the effects of urban climate on human thermal stress. UMEP has broad utility for applications related to outdoor thermal comfort, urban energy balance and climate change mitigation.

UMEP allows integration of atmospheric and surface data from multiple sources, taking meteorological data measured at ‘standard’ sites and using them to be representative of the urban environment; using climate prediction data, and comparing and visualizing results or scenarios for different climate indicators.

This can all be done with a range of spatial scales consistent with end-user needs and interests.

Figure 3.7 shows the framework of the UMEP tool.

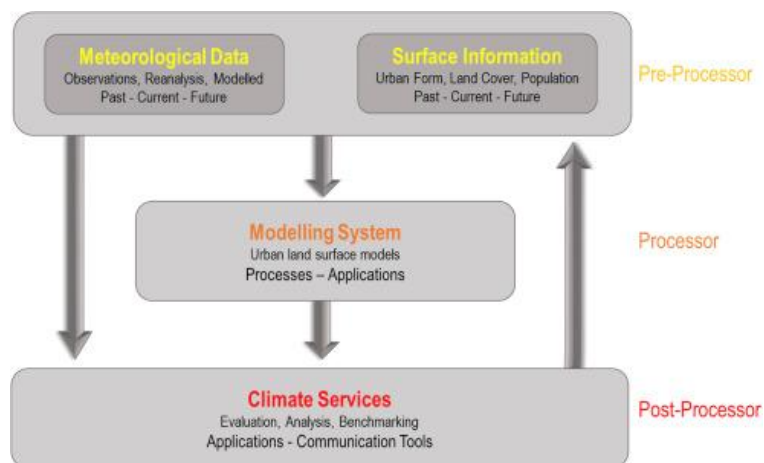


Figure 3.7. The framework of UMEP tool (Lindberg et al., 2019).

UMEP has three main elements (see Figure 3.5): pre-processor (for inputs of meteorological and surface data); processor (Modelling system e.g., Urban Land Surface Models, ULSM, Simulation engine e.g., SOLWEIG and SUEWS); and post-processor (tools to analyze the outputs, indicators of uncertainty etc.).

SOLWEIG-model (**S**olar and **L**ong **W**ave **E**nvironmental **I**rradiance **G**eometry-model) is a tool integrated in UMEP which simulates spatial variations of 3D radiation fluxes and mean radiant temperature ( $T_{mrt}$ ) in complex urban settings. The model requires a limited number of inputs, such as shortwave radiation, ambient air temperature, relative humidity, urban geometry and vegetation cover (e.g. Lindberg et al. 2008; Lindberg and Grimmond 2011).

SUEWS (**S**urface **U**rban **E**nergy and **W**ater Balance Scheme) is able to simulate the energy and water balances using just common meteorological variables and information about the surface cover (e.g. Grimmond and Oke 2002; Järvi et al. 2011).

### 3.4.2 SOLWEIG: Features, physical and mathematic model, input and output data

The module called SOLWEIG (**S**olar and **L**ong **W**ave **E**nvironmental **I**rradiance **G**eometry) is basically a three-dimensional radiation model. SOLWEIG simulates the spatial and temporal variation of shortwave and long wave radiation fluxes in complex urban environments (Lindberg et al., 2008). SOLWEIG was developed by the urban climate team of the University of Gothenburg, Sweden, in 2008. The model is based on an energy balance equation of the urban area and is integrated into QGIS Environment. This tool constructs complex urban structures through the digital elevation model (DEM) of buildings, plants, etc. with a resolution up to 1.0 m x 1.0 m.

SOLWEIG is classified as a 2.5-dimensional model by its use of a 2.5-D DEM (i.e. x and y coordinates with height attributes) to calculate  $T_{mrt}$ .

Software structure is composed of “Pre-processor”, “Processor” and “Post-processor” sections (Lindberg et al., 2018). Figure 3.8 shows the workflow of the SOLWEIG.

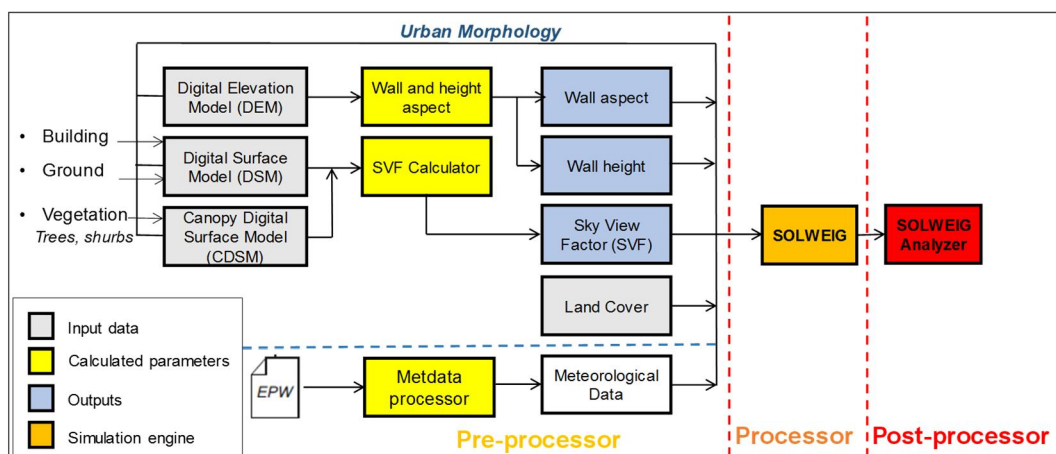


Figure 3.8. Flowchart of the SOLWEIG (Lindberg et al., 2018).

“Pre-processor” includes four type of input data: “Spatial data”, “Urban Geometry”, “Urban Land Cover” e “Meteorological Data”.

“Spatial Data” includes the spatial inputs as DEM (Digital Elevation Model), Digital Surface Model (DSM) for buildings and ground (Ground & Building DSM) and the Canopy Digital Surface Model (CDSM). These input data are fundamental because they allow the definition of other geometric input necessary to carry out the simulations. Modelling system input are described as follow:

- Digital Elevation Model (DEM) is a raster grid that includes only the height of ground above sea level expressed in meters.
- Digital Surface Model (DSM) is a raster grid which includes the heights of all objects (ground, buildings, and vegetation) above sea level.
- Ground & Building DSM is a DSM consisting of ground and building heights.
- Canopy Digital Surface Model (CDSM) only includes the pixels with vegetation heights above ground.

The “Urban geometry” section is composed of two plug-ins: “Sky View Factor Calculator” and “Wall and height aspect”.

- “Sky View Factor Calculator” is able to generate the raster grid of Sky View Factor (SVF) by means of Digital Surface Models of Ground & Building DSM and the vegetation (CDSM) as described by Lindberg and Grimmond (2011).
- “Wall and Height aspect” allows identification of the Aspect Ratio and the heights of roughness elements above the ground of the Digital Surface Model (DSM) as defined by Lindberg et al. (2015a).

“Land Cover” is the ground cover fraction of the urban domain to be simulated. Currently, Land Cover includes five different ground covers (building, paved, grass, bare soil, and water).

The “Metadata Processor” section allows implementation, in the SOLWEIG model, of any format of meteorological input file and conversion into the File format required to carry out the calibration of SOLWEIG simulations. The tool allows annual simulations to be carried out, implementing a specific Meteorological file as EPW or using detailed weather data from Era 5 module.

“Processor” section is the simulation engine of SOLWEIG while “Post-Processor” is the Analyzer of outputs of the simulations.

The radiation calculation of SOLWEIG follows the six-directional approach of Höppe (1992). It estimates short wave and long wave radiation fluxes arriving from above, below and from the four cardinal points for the height of 1.1 m a.g.l. This method assumes a standing person—conceptualized as a rectangular box—and transforms the incoming radiation fluxes accordingly.

SOLWEIG can divide the global radiation into direct and diffuse radiation and can calculate various parameters including incoming shortwave radiation ( $K_{\downarrow}$ ), outgoing shortwave radiation ( $K_{\uparrow}$ ), incoming long wave radiation ( $L_{\downarrow}$ ), outgoing long wave radiation ( $L_{\uparrow}$ ) and mean radiant temperature ( $T_{\text{mrt}}$ ).

SOLWEIG has no built-in calculation model of global incoming radiation ( $G$ ). Therefore, the incoming global radiation ( $G$ ) should be manually input in the calculation. The effects of buildings and plants on the global radiation intensity are accounted for.

A notable approximation is with regards to surface temperatures. Such approximation is represented by the following assumptions:

- The adopted surface temperature parametrization assumes that surface temperatures will return to the temperature of the air within two hours of shade or in the absence of direct solar radiation (i.e. at night);
- The surface temperature parametrization for different ground covers is derived from observations conducted over horizontal surfaces with relatively large SVFs. However, surfaces with different tilts and exposures have different peak temperatures and diurnal patterns.
- There are approximations introduced to the calculation of solid surface emitted long wave flux components as well. In upward fluxes estimation, a domain-wide mean surface temperature of walls and grounds is used. On one hand, this can lead to overestimated fluxes in shade and underestimated ones when the sites are sunlit.

The strength and weakness of SOLWEIG is its surface temperature parametrization: it allows for a quick estimation of long wave fluxes, but it cannot account for all surface-exposure-based differences. Some of the approximations introduced in the model include the way shortwave reflected fluxes are accounted. For estimating the share of fluxes originating from sunlit and shaded surfaces, the model utilizes a theoretical approach for deriving the sunlit wall fraction. The approach adjusts the available reflected shortwave radiation as a function of the solar altitude angle and the Sky View Factor (SVF). However, it distributes the amount of reflected fluxes equally among the cardinal points (Lindberg et al., 2016; Lindberg et al., 2008). As a consequence, the approach tends to underestimate or overestimate reflected fluxes when the distribution of sky obstructions is less uniform such as next to a building.

The output parameters such as  $K_{\downarrow}$ ,  $K_{\uparrow}$ ,  $L_{\downarrow}$ ,  $L_{\uparrow}$  and  $T_{\text{mrt}}$  can be shown on 2D maps in Qgis Environment. Physiological Equivalent Temperature (PET) and Universal Thermal Climate Index (UTCI) can be calculated in specific points into the domain model. The outputs, in two dimensions ( $x$ ,  $y$ ) at a



specified height ( $z=1.1$  m) above the surface, has an hourly temporal resolution. The  $z$  value is based on the centre of mass of an ‘average’ person (Fanger 1972).

The flow chart of the calculation process and its inputs and outputs are reported in Figure 3.9.

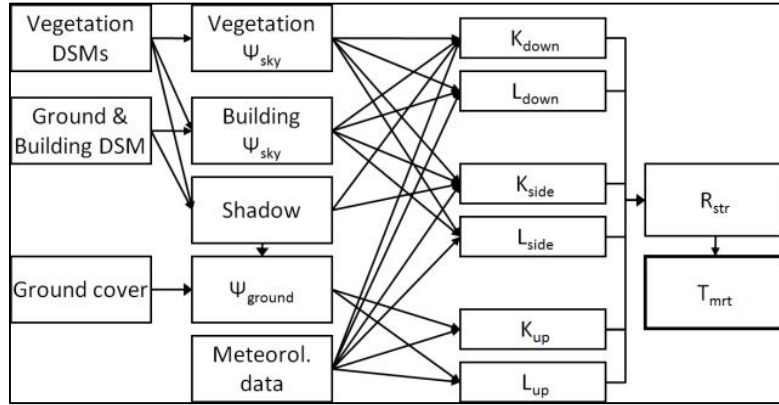


Figure 3.9. Flow chart of the calculation process of SOLWEIG model (Lindberg et al., 2018).

The calculation of  $T_{mrt}$  requires six long wave and shortwave radiation fluxes (upward, downward and from the four cardinal points) to be determined from inputs of global shortwave radiation ( $K_1$ ), air temperature ( $T_a$ ) and relative humidity (RH) (Höppe 1992).

In order to determine  $T_{mrt}$  (units, °C), the mean radiant flux density ( $R_{str}$ ) is calculated. The term  $R_{str}$  is defined as the sum of all fields of long wave ( $L_i$ ) and shortwave ( $K_i$ ) radiation in three dimensions ( $i=1-6$ ), together with the angular ( $F$ ) and absorption ( $\alpha_p$ ) factors of a person.

$$R_{str} = \alpha_p \sum_{i=1}^6 K_i F_i + \varepsilon_p \sum_{i=1}^6 L_i F_i \quad (3.1)$$

where  $F_i$  are the angular factors between a person and the surrounding surfaces.

For a rotationally symmetric standing or walking person,  $F_i$  is set to 0.22 for radiation fluxes from the four cardinal points (east, west, north, and south) and 0.06 for radiation fluxes from upward and downward directions (Fanger 1972). The term  $\alpha_p$  is the absorption coefficient for shortwave radiation and  $\varepsilon_p$  is the emissivity of the human body (VDI 1994, 1998). From  $R_{str}$ , the  $T_{mrt}$  is calculated from Stefan Boltzmann’s law.

An important influence of vegetation on  $T_{mrt}$  comes from shadowing.

The 3-D characteristics of a tree include the presence of a trunk zone (i.e. volume underneath the canopy). The approach taken is to introduce two new DEMs to account for the vegetation: (1) for the canopy and (2) for trunk zone. For the vegetation pixels, the canopy DEM has the height of bushes and/or trees, whereas the trunk zone DEM has the height of the base of the canopy. Thus, each tree has its own shape which is dependent on the spatial resolution of the DEMs. To model the 3-D radiant fluxes and  $T_{mrt}$ , the following assumptions are made with respect to the vegetation:

- Surface temperature of vegetation is considered equal to air temperature.
- Transmission of shortwave radiation through foliated vegetation ( $\tau$ ) is given a constant value (e.g. Oke 1987; Robitu et al. 2006).
- Transmission of long wave radiation through foliated vegetation is set to a default value of 0%
- Albedo and emissivity of vegetation are treated as constant with values of 15% and 90%, respectively.

SOLWEIG uses the unobstructed three components of shortwave radiation: direct (I), diffuse (D) and global (G). As these are not commonly available the model also allows calculation of D from G in conjunction with ambient air temperature ( $T_a$ ) and relative humidity (RH) using the Reindl et al. (1990) approach.

Direct shortwave radiation (I) on a surface perpendicular to the Sun is estimated as follow:

$$I = (G - D) / \sin \eta \quad (3.2)$$

where  $\eta$  is the Sun's altitude angle above the horizon.

Typically within the urban environment, the sky may be obscured by objects (e.g. buildings or trees). Thus, the incoming shortwave radiation ( $K_{\downarrow}$ ) for a grid cell (x, y) is a function of diffuse (D), direct (I) and global (G) as well as view factors ( $\Psi$ ). The incoming shortwave radiation ( $K_{\downarrow}$ ) is calculated as:

$$K_{\downarrow} = I \left[ S_b - (1 - S_v)(1 - \tau) \right] \sin \eta + D \left[ \Psi_{sky,b} - (1 - \Psi_{sky,v})(1 - \tau) \right] + G \alpha \left[ 1 - \left( \Psi_{sky,b} - (1 - \Psi_{sky,v})(1 - \tau) \right) \right] \times (1 - f_s) \quad (3.3)$$

The first and second terms on the right-hand side of Eq. 3.3 represent direct and diffuse radiation fluxes, respectively. The third term in Eq. 3.3 is a simplified representation of reflected radiation.

S accounts for shadow for buildings (subscript b) and vegetation (v) and is indicated as Boolean value (presence=0 or absence=1); the subscripts associated with  $\Psi$  indicate what aspects are being accounted for (e.g. sky seen by building), and  $\alpha$  is the surface albedo. Currently,  $\alpha$  is treated as a constant with a default value of 0.15;  $\tau$ , is the transmissivity of shortwave radiation through vegetation;  $f_s$  is the fraction of wall that is shadowed.

The outgoing shortwave radiation ( $K_{\uparrow}$ ) is estimated as:

$$K_{\uparrow} = \alpha \left\{ \begin{aligned} & I \left[ \Psi_{g(\text{sunlit})} (1 - \tau) \right] \sin \eta + D \left[ \Psi_{sky,b} - (1 - \Psi_{sky,v})(1 - \tau) \right] + \\ & + G \alpha \left[ 1 - \left( \Psi_{sky,b} - (1 - \Psi_{sky,v})(1 - \tau) \right) \right] \times (1 - f_s) \end{aligned} \right\} \quad (3.4)$$

where  $\Psi_{g(\text{sunlit})}$  is the view factor of the ground (subscript g) with respect to the amount of sunlit area on the ground seen at  $z=1.1$  m above the ground. When  $\Psi_{g(\text{sunlit})}=1$  only sunlit surfaces are seen from that specific pixel.

The shortwave radiation from the four cardinal points ( $K \rightarrow$ ) in the case of Sun's azimuth angle ( $\theta$ ) is  $\theta > 0^\circ$  and  $\theta \leq 180^\circ$ , can be estimated as follow:

$$K \rightarrow = I \left[ S_b - (1 - S_v)(1 - \tau) \right] \cos \eta \sin \theta + D \left[ 1 - (w_{E\text{wall}} + w_{E\text{veg}}(1 - \tau)) \right] + G\alpha \left[ w_{E\text{wall}} + w_{E\text{veg}}(1 - \tau) \right] (1 - f_s) \quad (3.5)$$

Where  $w$  are angular weighting factors.

In the case of  $\theta > 90^\circ$  and  $\theta \leq 270^\circ$ , the terms  $w_{E,\text{wall}}$  and  $w_{E,\text{veg}}$  are replaced with  $w_{S,\text{wall}}$  and  $w_{S,\text{veg}}$ .

Incoming long wave radiation ( $L_\downarrow$ ) is estimated using an equation modified from Jonsson et al. (2006) that is expressed as follow:

$$L_\downarrow = (\Psi_{\text{sky},b} + \Psi_{\text{sky},v} - 1) \varepsilon_{\text{sky}} \sigma T_a^4 + (2 - \Psi_{\text{sky},v} + \Psi_{\text{sky},vb}) \varepsilon_{\text{wall}} \sigma T_a^4 + (\Psi_{\text{sky},vb} - \Psi_{\text{sky},b}) \varepsilon_{\text{wall}} \sigma T_s^4 + (2 - \Psi_{\text{sky},b} - \Psi_{\text{sky},v}) (1 - \varepsilon_{\text{wall}}) \varepsilon_{\text{sky}} \sigma T_a^4 \quad (3.6)$$

The first term on the right-hand side is the direct sky long wave radiation, the second is the radiation originating from vegetation, the third is the wall radiation and the fourth is the reflected radiation. The terms  $\varepsilon_{\text{sky}}$  and  $\varepsilon_{\text{wall}}$  are the sky and wall emissivity,  $T_s$  is average surface temperature of building walls and ground, and  $T_a$  is ambient air temperature. All temperatures are in Kelvin.

Outgoing long wave radiation ( $L_\uparrow$ ) is estimated by means of the following equation:

$$L_\uparrow = \varepsilon_g \sigma (T_s + \Psi_{g(\text{sunlit})} (T_s - T_a))^4 \quad (3.7)$$

Where  $\varepsilon_g$  is the ground emissivity.

The long wave radiation from each of the cardinal points is calculated using the exemplified equations for the easterly component. The long wave radiation fluxes from each cardinal point toward the sky ( $L_{E \rightarrow \text{Sky}}$ ), vegetation ( $L_{E \rightarrow \text{Vegetation}}$ ), ground ( $L_{E \rightarrow \text{Vegetation}}$ ) and the component reflected in the case of sun and shadow are calculated respectively by the following equations.

$$L_{E \rightarrow \text{Sky}} = (\Psi_{\text{sky},Eb} + \Psi_{\text{sky},Ev} - 1) \varepsilon_{\text{sky}} \sigma T_a^4 w_{E\text{sky}} \times 0.5 \quad (3.8)$$

$$L_{E \rightarrow \text{Vegetation}} = \varepsilon_{\text{wall}} \sigma T_{\text{veg}}^4 w_{E\text{veg}} \times 0.5 \quad (3.9)$$

$$L_{E \rightarrow \text{Ground}} = L_\uparrow \times 0.5 \quad (3.10)$$

$$L_{E \rightarrow \text{Reflected}} = (L_{\downarrow} + L_{\uparrow}) w_{E, \text{refl}} (1 - \epsilon_{\text{wall}}) \times 0.5 \quad (3.11)$$

$$L_{E \rightarrow \text{Sun}} = \epsilon_{\text{wall}} \sigma (T_a^4 + T_{\text{wall}}^4 \sin \theta) w_{E, \text{refl}} (1 - f_{\text{sw}}) \times \cos \eta \times 0.5 \quad (3.12)$$

$$L_{E \rightarrow \text{Shadow}} = \epsilon_{\text{wall}} \sigma T_a^4 w_{E, \text{wall}} f_s \times 0.5 \quad (3.13)$$

As only half of the hemisphere is taken into account for each cardinal point all terms are multiplied by 0.5.

The model of shortwave and long wave radiation fluxes is extensively documented in Lindberg et al. (2008, 2016), Lindberg and Grimmond (2011) and Konarska et al. (2014).

Few studies were addressed to the evaluation of performance of SOLWEIG in terms of its ability to estimate  $T_{\text{mrt}}$  values in complex urban environments.

It is worth mentioning research developed by Gàl and Kàntor (2020) who have compared the  $T_{\text{mrt}}$  calculated by SOLWEIG, ENVI-met and RayMan models of a “mid-rise compact” area in the center of Szged in Hungary. ENVI-met, SOLWEIG and RayMan models were calibrated with meteorological data recorded by a stationary weather station in a suburban area. In the investigated area, four points were selected for experimental measurements campaign conducted with a meteorological station during 26-hour-long field experiment. Statistical analysis related to  $T_{\text{mrt}}$  estimation during analyzed period has shown RMSE and index of agreement values of 5.02°C and 0.97 respectively for SOLWEIG. In ENVI-met model, a RMSE value of 6.92°C and a coefficient of determination comparable to those from SOLWEIG were achieved (Kàntor et al., 2020). The comparison in terms of  $T_{\text{mrt}}$  has shown that both models systematically underestimate nighttime mean radiant temperatures. In SOLWEIG, such outcome is due to the surface temperature parametrization scheme. Since  $T_{\text{mrt}}$  estimation errors are low during daytime in relation with high dimensions and resolution of the domain, SOLWEIG has appreciable accuracy level (Kantòr, 2020).

Another study conducted by Szűcs et al. (2014) dealt with the comparison of data obtained by measurement and computational simulation in Campo de Ourique, a densely populated city district of Lisbon. The measurements were carried out in a park and in the surrounding canyon streets for four summer days. Computational simulation tools such as SOLWEIG, RayMan and ENVI-met were adopted. In case of direct solar exposure RayMan and SOLWEIG provided particularly good approximation (with an average difference of 6 and 9%, respectively), whereas an average overestimation of  $T_{\text{mrt}}$  attained by ENVI-met was around 20%. High correlation coefficients, between computer simulated and observed data for shade and sun, were obtained with the RayMan ( $R^2 = 0.87$ ), the ENVI-met ( $R^2 = 0.96$ ) and the SOLWEIG models ( $R^2 = 0.87$ ). SOLWEIG provided more precise

results than ENVI-met for the solar exposure case, with about 4-5°C difference to the measured  $T_{mrt}$  values.

Chen et al., 2016 have investigated the spatial variation of  $T_{mrt}$  in two different urban settings in Shanghai. A comparison between measured and modeled  $T_{mrt}$  values for a standing person based on the flux density data measured in a square and in a street canyon was carried out respectively. Predicted  $T_{mrt}$  values showed a good agreement with measured values, with  $R^2$  higher than 0.9. In the early afternoon with strong shortwave radiation reflected from building facades, SOLWEIG tended to underestimate  $T_{mrt}$  by around 3°C for the street canyon. Other than that, SOLWEIG normally overestimated  $T_{mrt}$  by around 4°C, which could be attributed to the overestimated lateral long wave radiant fluxes. Nevertheless, the comparisons proved that with accurate input data of building morphology and vegetation cover, SOLWEIG can accurately simulate the spatial variation of  $T_{mrt}$ . In light of these results, SOLWEIG can be considered as reliable tool to estimate the thermal comfort of large-scale outdoor spaces.

#### 3.4.3 SUEWS: Features, physical and mathematical models, input, and output data

SUEWS (Surface Urban Energy and Water Balance Scheme) is a simulation tool integrated in UMEP (Urban Multi-scale Environmental Predictor).

SUEWS allows the energy and water balance exchanges for urban areas to be modelled. The thermal fluxes are calculated at the local scale (e.g., from  $10^2$  to  $10^4$  m) and at height of about 2-3 times the mean height of the roughness elements in the roughness sublayer (RSL).

SUEWS is able to simulate the thermal, energy and water balances using just commonly measured meteorological variables from the weather stations and information about the urban land use fractions (Järvi et al. 2011, Ward et al. 2016). SUEWS allows calculation of the air temperature ( $T_a$ ), Relative Humidity (RH) and wind speed ( $w$ ) at different heights within Roughness Surface Layer (RSL) based on the net energy balance in an urban area.

Since the thermal features and land cover of an urban area are accounted for in the model, an urban morphing of the meteorological data recorded by a rural weather station can be carried out by means of SUEWS.

SUEWS utilizes an evaporation-interception approach (Grimmond et al. 1991) to model evaporation from urban surfaces.

The theoretical basis of SUEWS, the urban evaporation-interception scheme of Grimmond and Oke (1991) and the urban water balance model of Grimmond et al. (1986), are combined with additional modules to reduce the number of required input variables and to include more fully the energy and water exchange processes. This has provided a widely usable model for the researchers and urban

planners who deal with the evaluation of the effectiveness of UHI mitigation strategies on urban energy balance in larger scale models.

SUEWS plugin structure includes Pre-processor, Processor and Post-processor sections. The workflow of SUEWS is shown in Figure 3.10.

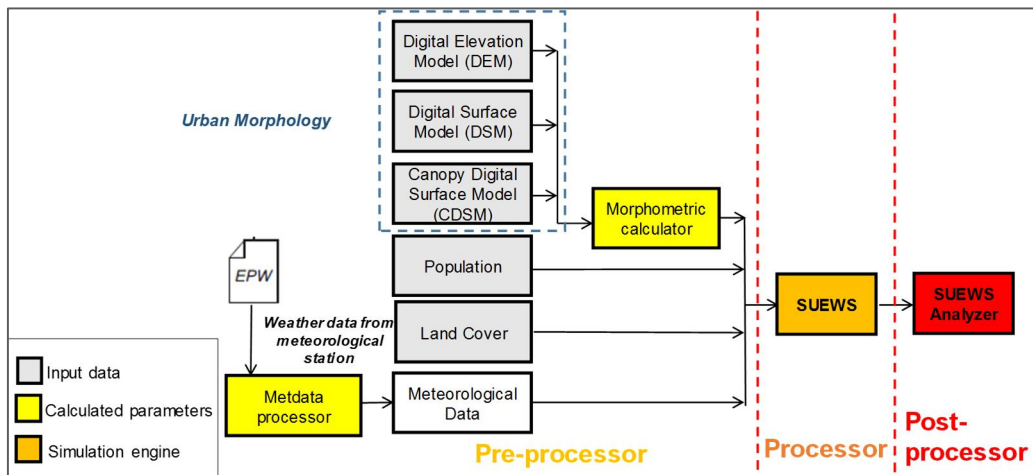


Figure 3.10. Workflow of the plug-in SUEWS (Lindberg et al., 2018).

Pre-Processor includes geometric and morphological inputs, population density data and meteorological inputs.

Geometric and morphological inputs are building and tree morphology and Land Cover fractions. They are derived from Digital Surface Models (DSMs) in QGIS Environment or generated by means of Morphometric Calculator Plugins.

**Building morphology parameters** are Mean Building Height (zH), in m, Frontal Area Index (Area of the front face of a roughness element exposed to the wind relative to the plan area) and Plan Area Index (Area of the roughness elements relative to the total plan area). They are usually derived from Digital Surface Models (DSMs) or generated by means Image Morphometric Calculator (Point) plugin. These data input can be also entered manually when building databases are available in QGIS Environment.

**Tree morphology parameters** are Mean Vegetation Height (zH), in m, Frontal Area Index and Plan Area Index usually derived from Canopy Digital Surface Models CDSMs or generated by means of an Image Morphometric Calculator (Point) plugin. These data input can be also entered manually when tree database is available in QGIS Environment.

Land cover fraction includes seven surface types: paved, buildings, evergreen trees/shrubs, deciduous trees/shrubs, grass, bare soil, and water. Land Cover Fractions can be derived from a UMEP land cover dataset. Land Cover Fraction can be entered manually when a soil use database for investigated area is available in QGIS Environment.

Meteorological inputs are air temperature, relative humidity, specific humidity, global solar irradiance, direct solar radiation, diffuse solar radiation, wind speed and direction, recorded by a stationary weather station placed in rural or in suburban area and Long wave radiation and Cloud Cover.

“Processor” section is the simulation engine of SUEWS.

The basic time step for SUEWS is 5 min per hour and results are aggregated into daily, monthly, and annual time periods. SUEWS can be run for periods of a day (or less) to multiple years with changing surface characteristics and meteorological forcing. Thus, the changes of an urban area through time are accounted for.

“Processor” allows the determination of all terms of urban energy balance expressed by the following equation:

$$Q^* + Q_F = Q_H + Q_E + \Delta Q_S \quad (3.14)$$

Where:  $Q^*$ , net-all wave radiation, in ( $W \cdot m^{-2}$ );  $Q_F$ , anthropogenic heat flux, in ( $W \cdot m^{-2}$ );  $Q_E$ , latent heat flux, in ( $W \cdot m^{-2}$ );  $Q_H$ , Sensible heat flux, in ( $W \cdot m^{-2}$ );  $\Delta Q_S$ , storage heat flux, in ( $W \cdot m^{-2}$ ).

The magnitude of sensible and latent heat fluxes is dependent on the available energy, which is determined from the net all-wave radiation ( $Q^*$ ), net storage heat flux ( $\Delta Q_S$ ) and anthropogenic heat flux ( $Q_F$ ). The sensible and latent heat fluxes are typically calculated with a one-hour of time step.

The net all-wave radiation ( $Q^*$ ) is calculated using the net all-wave radiation parameterization scheme (NARP) (Loridan et al., 2011; Offerle et al., 2003). The NARP scheme calculates outgoing shortwave ( $K_{\uparrow}$ ), incoming ( $L_{\downarrow}$ ) and outgoing long wave ( $L_{\uparrow}$ ) radiation components based on incoming shortwave radiation ( $K_{\downarrow}$ ), air temperature ( $T_a$ ), relative humidity (RH) and surface characteristics (albedo and emissivity). The incoming long wave radiation ( $L_{\downarrow}$ ) or cloud cover ( $f_{lctd}$ ) can be used if available because both improve the net all-wave radiation parameterization (Loridan et al., 2011).

The anthropogenic heat flux ( $Q_F$ ) is calculated by means of a sub-model proposed by Järvi et al. (2011) that has modified the Sailor and Vasireddy (2006) approach developed for the calculation of residential electricity usage. The Järvi approach is based on heating and cooling degree days and population density and allows distinction between weekdays and weekends. This approach employs cooling and heating degree days (CDD and HDD, respectively) in order to take into account energy used for heating in cold periods and increased air conditioning in warm periods.

The daily anthropogenic heat flux ( $W \cdot m^{-2}$ ) per population density ( $p$ , units: capita  $ha^{-1}$ ) is calculated for weekdays (wd) and weekends (we) as follow:

$$Q_F = a_{0,\{wd,we\}} + a_{1,\{wd,we\}}CDD + a_{2,\{wd,we\}}HDD \quad (3.15)$$

The Storage Heat Flux ( $\Delta Q_s$ ) is calculated using the Objective Hysteresis Model (OHM; Grimmond and Oke, 1999, 2002). OHM approach calculates the storage heat flux using empirically fitted relations with net all-wave radiation ( $Q^*$ ).

The latent heat flux for evaporation ( $Q_E$ ) from each surface is calculated with the Penman–Monteith equation (Monteith, 1965) modified for urban areas (Grimmond and Oke, 1991):

$$Q_E = \frac{s(Q^* + Q_F - \Delta Q_s) + c_p \rho V / r_a}{s + \gamma(1 + r_s / r_a)} \quad (3.16)$$

Where:  $r_a$ , aerodynamic resistance ( $s \cdot m^{-1}$ );  $r_s$ , surface resistance ( $s \cdot m^{-1}$ );  $c_p$ , air specific heat ( $J \cdot kg^{-1} \cdot K^{-1}$ );  $\rho$ , air density ( $kg \cdot m^{-3}$ );  $V$ , deficit of air vapor pressure (hPa);  $s$ , slope of the vapor pressure curve ( $hPa \cdot h^{-1}$ );  $\gamma$ , psychometric constant ( $hPa \cdot K^{-1}$ ).

The eq. 3.16 is applicable to dry surfaces. When the surface is completely wet the surface resistance  $r_s$  is set to zero. To link the two surface stages (dry and wet),  $r_s$  is replaced with a redefined surface resistance  $r_{ss}$  (Shuttleworth, 1978).

The sensible heat flux ( $Q_H$ ) is calculated as the residual of the energy balance.

The air temperature ( $T_{a2m}$ ), relative humidity ( $RH_{2m}$ ) and wind speed ( $w_{10m}$ ) are calculated on the basis of an urban energy balance that includes all thermal fluxes above described.

The main outputs of the “Processor” are outgoing shortwave radiation ( $K_{\uparrow}$ ), incoming long wave radiation ( $L_{\downarrow}$ ), outgoing long wave radiation ( $L_{\uparrow}$ ), net-all wave radiation ( $Q^*$ ), anthropogenic heat flux ( $Q_F$ ), latent heat flux ( $Q_E$ ), sensible heat flux ( $Q_H$ ), storage heat flux ( $\Delta Q_s$ ), air temperature ( $T_a$ ), relative humidity (RH), and wind speed ( $w$ ). These outputs are given as hourly profile for investigated grid. Air temperature ( $T_a$ ), relative humidity (RH) and wind speed ( $w$ ) are provided at different heights in Roughness Surface Layer (RSL).

### 3.5 ENVI-met: state of the art, input, and output data

#### 3.5.1 Features and physical model

ENVI-met tool is selected because it is capable of suitably simulating major processes in the atmosphere that affect urban microclimate based on a well-grounded physical basis (Bruse, 2018).

ENVI-met is a numerical prognostic calculation code based on a holistic model that allows a complex modelling and detailed investigation of the urban microclimate, as well as small-scale interactions between buildings, surfaces, and plants (Ali-Toudert and Mayer, 2006).

ENVI-met estimations are based on a three-dimensional CFD atmospheric model forced by a one-dimensional model given by a vertical profile of weather data at the inflow boundary of the 3D model.



ENVI-met is deemed as one of a few computational fluid dynamic tools capable of analyzing human thermal comfort at Microscale level in an urban environment with a robust capability to evaluate the heat exchanges from and towards the vegetation at resolution as detailed as 0.5 m x 0.5 m (Bruce, 2018).

The software implements theoretical physical models as systems of nonlinear equations and solves them through mathematical formulations including three main prognostic variables that allow analysis of the interactions between the local environment and the atmosphere on a local basis (Chatzinikolaou, et al., 2018; Bruce, 1998). The analytical model is based on Navier-Stokes equations for wind flow, atmospheric flow turbulence equations, energy and momentum equations and boundary condition parameters (Bruse, 1998).

More relevant to urban studies is the fact that ENVI-met also allows the taking into account of contributions due to:

- Shortwave and long wave radiation fluxes with respect to shading, reflection, and re-radiation from building systems and the vegetation.
- Transpiration, evaporation, sensible and latent heat fluxes from the vegetation into the air including full simulation of all plant physical parameters.
- Water and heat exchange at the ground layer.

Figure 3.11 shows the workflow of ENVI-met software.

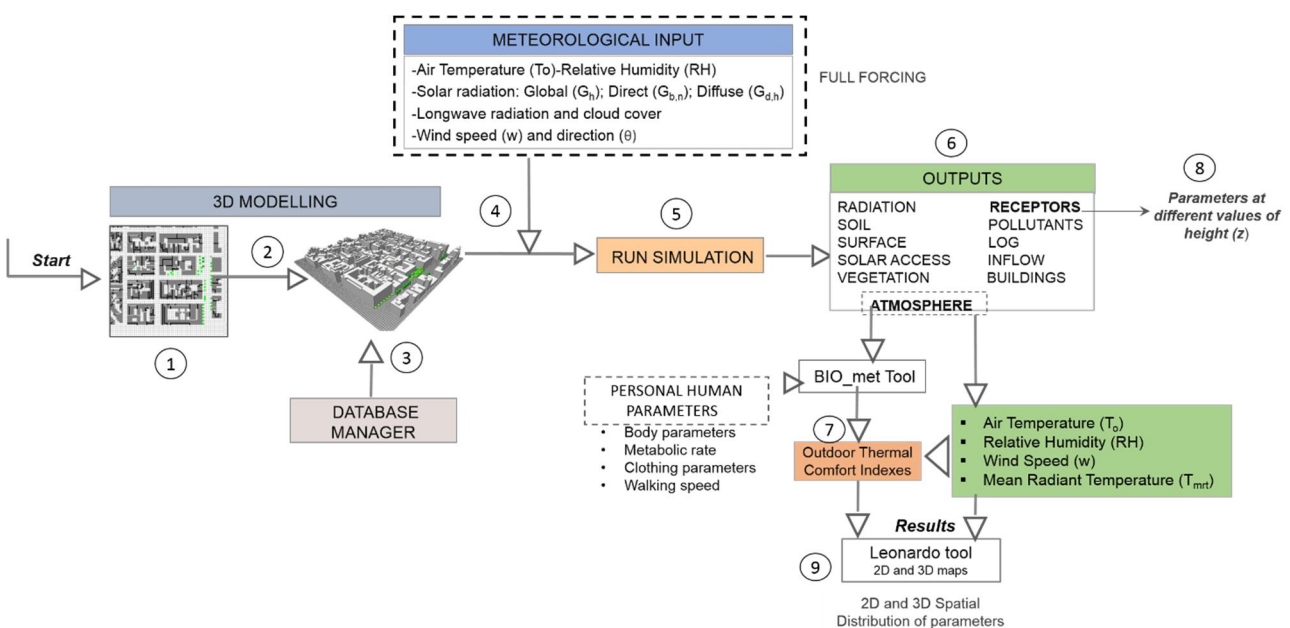


Figure 3.11. Workflow of ENVI-met software.

The calculation procedure of the simulation tool implies the following steps: (1) Generation of the mesh of the calculation grid; (2) Implementation of buildings, obstacles geometry, trees, shrubs, and low plants; (3) Definition of the radiative and thermo-physical properties of building walls and roofs and materials of roads, squares and pervious surfaces; (4) Definition of boundary conditions and entering climate data; (5) Numerical simulations; (6) Calculation of outdoor microclimate parameters; (7) Calculation of Outdoor Thermal Comfort Indicators by means of BIO-met tool; (8) Extraction of the simulation outcomes in specific points at different height; (9) Extraction of the simulation outcomes in 2D and 3D maps.

Step 1: The generation of the mesh of the calculation grid is based on the discretization of the simulation domain in finite modules. Thereby, the model is composed of many three-dimensional cells. Finite volumes can be free setting with a typical horizontal resolution from 0.5 to 5 meters and a height from 0 to 5 meters. In this way, a three-dimensional grid is defined by means points and surface of finite volumes on which computational models are applied.

In order to improve the stability of lateral boundary conditions for the core model without increasing computational time, ENVI-met allows surrounding the domain with nesting grids so that the flow field re-establishes its simple structure after it has crossed the core model.

Step 2: Geometrical modelling consists of the implementation of buildings, obstacles geometry, trees, shrubs, and plants.

Step 3: The input data for each material are thickness, absorption coefficient, transmission, reflection (albedo), emissivity, heat capacity, thermal conductivity, and density. Materials and their properties associated with the buildings, vegetation and roads are stored in Database Manager. The latter allows the editing of an existing material or the creation of a new for buildings, floors, soil, and other surfaces.

Step 4: The three-dimensional atmospheric model can be calibrated by means of the entering of meteorological data. An important progress of new version of ENVI-met software is the possibility to enter climate data input by means of a meteorological file that includes hourly values of air temperature, relative humidity, specific humidity, global, direct, and diffuse shortwave radiation, long wave radiation, wind speed and directions and cloud cover registered by a weather station.

Step 5: Numerical simulation process.

Step 6: The outcomes simulations can be extracted by different sections (Atmosphere, Radiation, Soil, Surface, Solar access, Vegetation, Buildings, Inflow etc.). From Atmosphere section can be extracted the Air Temperature, Relative Humidity, Wind speed and Mean Radiant Temperature.

Step 7: In ENVI-met, the outdoor thermal comfort indexes are calculated by means of the BIO-met tool. The latter is a calculation tool integrated in ENVI-met that includes the Klima Michel Model,

the Munich Energy Balance Model for Individuals (MEMI), two node Gagge model, and Fiala's Model respectively. In light of this, PMV (Predicted Mean Vote), PET (Physiological Equivalent Temperature), SET (Standard Effective Temperature) and UTCI (Universal Thermal Climate Index) for each hour of investigated period can be calculated when are implemented the atmospheric outputs (Air temperature, Relative Humidity, Wind speed and Mean Radiant Temperature).

Steps 8 and 9: The numerical results regarding outdoor thermal Comfort Indices and outcomes microclimate parameters such as Air Temperature, Relative Humidity, Wind speed and Mean Radiant Temperature can be showed on 2D maps of spatial distribution and at specific points at different heights above ground level.

Analytic model of ENVI-met considers the effects of direct, diffuse, and reflected radiation. The shortwave radiation flux of an arbitrary point at z height in the region can be expressed as follows:

$$Q_{sw}(z) = \sigma_{sw,dir}(z)Q_{sw,dir}^0 + \sigma_{sw,dif}(z)Q_{sw,dif}^0 + (1 - \sigma_{svf}(z))Q_{sw,dir}^0 \cdot \bar{a} \quad (3.17)$$

where  $Q_{sw}(z)$  is the shortwave radiation flux of an arbitrary point in the region at z height,  $W \cdot m^{-2}$ ;  $\sigma_{sw,dir}(z)$  is the attenuation coefficient of obstacles to direct solar radiation;  $Q_{sw,dir}^0$  is the direct solar radiation intensity at z height,  $W \cdot m^{-2}$ ;  $\sigma_{sw,dif}(z)$  is the attenuation coefficient of obstacles to diffuse solar radiation;  $Q_{sw,dif}^0$  is the diffuse radiation intensity at z height,  $W \cdot m^{-2}$ ;  $\sigma_{svf}(z)$  is the sky view factor seen from the centre of a grid cell; it ranges from 0 (no sky visible) to 1 (completely free sky); and  $\bar{a}$  is the mean reflectivity of all the walls in the model region.

Multiple reduction factors between 0 and 1 are used to describe the shielding effects of buildings and plants on long wave and shortwave radiation.

Equations (3.18-3.21) show the reduction factors of plants under direct solar radiation, diffuse radiation, upward long wave radiation, and downward long wave radiation:

$$\sigma_{sw,dir} = \exp(F \cdot LAI(z)) \quad (3.18)$$

$$\sigma_{sw,dif} = \exp(F \cdot LAI(z, z_p)) \quad (3.19)$$

$$\sigma_{lw}^{\uparrow} = \exp(F \cdot LAI(0, z)) \quad (3.20)$$

$$\sigma_{lw}^{\downarrow} = \exp(F \cdot LAI(z, z_p)) \quad (3.21)$$

where  $\sigma_{sw,dir}$ ,  $\sigma_{sw,dif}$ ,  $\sigma_{lw}^{\uparrow}$ , and  $\sigma_{lw}^{\downarrow}$  are the reduction factors of plants under direct solar radiation, diffuse radiation, upward long wave radiation, and downward long wave radiation, respectively; LAI is the leaf area index; and F is the coefficient of leaf orientation. When calculating direct solar radiation, the effect of incident sunlight angle is considered in the calculation of LAI.

Notably, it is possible to enable the Indexed View Sphere (IVS) function which analyzes and calculates in detail, multiple interactions among long wave and shortwave radiation fluxes between building surfaces in detail.

The calculation of  $T_{mrt}$  is based on VDI (1994) that has adopted the Fanger (1972) and Jendritzky e Nübler (1981) approaches. Short wave and long wave fluxes are calculated with the help of individual view factors established for the ground, buildings, sky, and the vegetation—indicating the occupied percentage of these elements, as seen from the specific grid point. These factors are calculated for both the upper and the lower hemisphere.

In calculating  $T_{mrt}$ , ENVI-met takes into account all radiation fluxes, direct, diffuse and reflected solar radiation as well as the long wave radiation fluxes from the atmosphere, ground and walls and is capable of producing  $T_{mrt}$  values for each cell of the model environment at varying heights above the ground surface (Ali Toudert 2005, Emmanuel & Fernando, 2007).

The calculation of direct shortwave radiation absorbed by a person is based on the formula of Underwood and Ward (1966), which is derived from an elliptical cylinder model with its major axis facing the sun.

When direct solar radiation is absent,  $T_{mrt}$  is calculated by the diffuse radiation components.

The model distinguishes the upper and the lower hemisphere and assumes that 50% of the radiation will arrive from the sky and 50% from the ground (Ali-Toudert, 2005; Huttner, 2012; Simon, 2016). As regards shortwave radiation fluxes from the lower hemisphere, the ground-reflected fraction of the overall incoming shortwave radiation is calculated with the albedo of the actual grid point (Huttner, 2012).

As concerns shortwave fluxes from the upper hemisphere, the diffuse shortwave radiation component incorporates the isotropic sky radiation and the reflected fraction of direct solar radiation from buildings - the latter calculated with a domain-wide mean building albedo (Huttner, 2012).

In radiation calculation, ENVI-met has some drawbacks. One of these regards the calculation of long wave radiation intensity emitted by building surface because the calculation is based on mean temperature, not on the temperature of a single surface; therefore, a relatively large error exists when calculating the long wave radiation intensity on different surfaces in an urban region (Huttner, 2012). As regards long wave radiation fluxes from the lower hemisphere, the model only accounts for the ground emitted fluxes (Huttner, 2012).

From the upper hemisphere, emitted long wave radiation from the atmosphere, the vegetation, and the building walls are considered, together with the reflected fraction from the wall of the atmospheric radiation. All these components are weighted by their corresponding view factors (Huttner, 2012).

The components of the long wave radiation emitted by surfaces are calculated with separate domain-wide mean surface temperature values of facade, ground, and vegetation (Huttner, 2012). This approximation can lead to underestimated long wave fluxes in shaded areas as well as to overestimated ones at sunlit locations.

Numerous studies have validated the ENVI-met model with respect to the air temperature and relative humidity measured values. It is worth pointing out that the number of validation studies in respect to other parameters such as mean radiant temperature and surface temperature is still limited. Within this reduced set of studies, most research works reported validation results for global radiation (Liu et al., 2018; Piselli et al., 2018), two for emitted long wave radiation by façades (Jänicke et al., 2015; Morakinyo et al., 2019) and only one for downwelling and upwelling shortwave and long wave radiation fluxes (Jänicke et al., 2015). In terms of various surface temperatures, Piselli et al. (2018) and Yang et al. (2013) reported results for ground surface temperature, Morakinyo et al. (2019) and Simon (2016) for façade temperatures, Yang et al. (2013) for soil and various substrate layer temperatures and Liu et al. (2018) for leaf surface temperature.

The most comprehensive review of available ENVI-met validation studies is given by Tsoka et al. (2018). There are many examples in related literature validating the ENVI-met model outputs (Lahme, Bruce 2003, Emmanuel and Fernando 2007) concluding that ENVI-met reproduces measured data with adequate accuracy and is a dependable tool in simulating various urban scenarios. Nevertheless, ENVI-met has some meaningful limitations that are discussed in section 3.5.2.

### 3.5.2 Microclimate analysis limitations

Notwithstanding ENVI-met suitability to approach the study of urban heat mitigation strategies, like other modelling and simulation tools, it also has its intrinsic limitations rooted in an attempt to simplify and ostensibly represent a far more complex reality. The main weaknesses of ENVI-met are reported and explained as follow:

- The possibility of modelling the areas with maximum size (500 m x 500 m).
- The complexity of the CFD model and the long time for running simulations (Chow et al., 2011).
- The albedo of the material surfaces and thermal properties of wall and roof layers are constant and cannot be varied (Emmanuel & Fernando 2007).
- The simplification of building façades to a single, averaged heat transfer coefficient (Emmanuel and Fernando, 2007).
- Building blocks have no thermal mass and consequently the thermal inertia of building envelopes is not accounted for.
- The inability to dynamically simulate heat storage for building walls and roofs (Bruse, 2006).

- Water bodies are input as a type of soil, and the processes are limited to the transmission and absorption of shortwave radiation (Bruse 2006).
- The effects due to anthropogenic heat fluxes cannot be estimated because power generation and air conditioning systems, transportation systems, vehicles and heat gains due to equipment cannot be implemented into the model (Sailor, 2011).

The possibility of modelling the Microscale urban areas with maximum size (500 m x 500 m) involves the selection and modelling of two or more areas at different building density (Compact and high built-up density area, suburban or rural areas) in order to evaluate the effects of different morphological characteristics on the outdoor microclimate and their variations. The simulations can take a long time due to the complexity of the model environment. A run time for simulation higher than 48 hours involves the use of a more powerful computer especially when a high spatial resolution is adopted. Therefore, a few days can be set as simulation time.

In addition, the software tends to under-predict temperatures, especially in the first 24 hours of simulated time. Generally, a simulation time higher than 24 hours is recommended because the first simulation day acts as a “buffer” to dampen internal model oscillations and achieve values of the output variables which are more refined concerning the initialization time (Goldberg et al. 2013).

Despite these shortcomings, Chow et al. (2014) have concluded that the model accuracy was adequate. ENVI-met remains the most comprehensive tool that combines many of the factors involved in outdoor thermal comfort. With proper input of the initial data and understanding the limitations, the software does represent an appreciable tool for outdoor microclimate estimate in a complex urban environment.

Past initiatives have tended to focus on specific processes (Herbert et al., 1998) or restricted spatial or temporal scales (Bruse and Fler, 1998), with applications most often intended for Microscale or neighborhood scales. Nevertheless, the urban climate is influenced by intra-urban climate interaction processes taking place on a range of different scales. Based on applications (e.g., thermal comfort modelling), a large scale should be considered to take into account the intra-urban interactions to make accurate estimation of the phenomena examined (Grimmond, et al., 2011).

City-based climate analysis should be adopted in order to overcome the spatial and temporal limitations of climate analysis at Microscale level (Grimmond, et al., 2011).

### 3.6 Outdoor microclimate parameters and thermal comfort indices

#### 3.6.1 Mean Radiant Temperature

The mean radiant temperature is defined as “the uniform temperature of an imaginary enclosure in which the radiant heat transfer from the human body equals the radiant heat transfer in the actual non-uniform enclosure” (ASHRAE, 2001). As such, the mean radiant temperature can be regarded as a weighted sum of all long wave and shortwave radiant fluxes (including direct, reflected and diffuse components), to which a human body is exposed (ASHRAE, 2013).

Mean radiant temperature ( $T_{mrt}$ ) is a widely used physical parameter to characterize the effects of well-being on people and their thermal comfort conditions (Fanger, 1972; Mayer, 1987; Ali Toudert, 2007).  $T_{mrt}$  is considered one of the most important parameters used to investigate thermal comfort and heat stress in outdoor environments because of its capability of identifying and capturing significant spatial differences due to radiant fluxes coming from buildings, ground surfaces and trees, which other indices such as the air temperature ( $T_a$ ) cannot take into account (Emmanuel, 2007; Thorsson, 2011; Chen, 2016). As an example, the temperature difference between a sunlit street canyon and a nearby shaded one can be as high as 30 °C for  $T_{mrt}$  while being 3 °C lower for  $T_a$ .

Different methods for the modelling/measuring of the  $T_{mrt}$  in outdoor urban settings can be used.

Various models exist which are able to predict the  $T_{mrt}$  outdoors, among which the Solar and Long Wave Environmental Irradiance Geometry (SOLWEIG) and ENVI-met are two of the most accurate and reliable (Gál and Kántor, 2020; Liu et al., 2020; Chen et al., 2016).

SOLWEIG estimates the mean radiant temperature using the six-directional approach of Höppe (1992).  $T_{mrt}$  is calculated at a height of 1.1 m above ground level (representing the height of the centre of gravity for a standing person) through the classic Stefan-Boltzmann’s equation:

$$T_{mrt} = \left( \frac{R_{str}}{\varepsilon_p \cdot \sigma} \right)^4 - 273.15 \text{ (°C)} \quad (3.22)$$

Here,  $\sigma$  is the Stefan- Boltzmann constant ( $5.67 \cdot 10^{-8} \text{ W} \cdot \text{m}^{-2} \cdot \text{K}^{-4}$ ),  $\varepsilon_p$  is the thermal emissivity of the human body that is equal to absorption coefficients for long wave radiation according to Kirchoff laws (standard value 0.97) and  $R_{str}$  is the mean radiant flux density ( $\text{W} \cdot \text{m}^{-2}$ ). The latter is defined as the sum of all shortwave ( $K_i$ ) and long wave ( $L_i$ ) radiant fluxes reaching the human body – and absorbed by it – from all four cardinal directions, as well as from upward and downward directions. Six individual values of the shortwave and long wave radiant fluxes are multiplied with the corresponding weights namely the view factors  $F_i$  ( $i = 1-6$ ) between a person and the surrounding surfaces according to Equation 3.1 (VDI, 1994, 1998) already described in section 3.4.2 and reported as follow:

$$R_{str} = \alpha_p \sum_{i=1}^6 K_i F_i + \varepsilon_p \sum_{i=1}^6 L_i F_i \quad (3.1)$$

- $K_i$ , the short wave radiant fluxes from the  $i$ -th direction.
- $L_i$ , the long wave radiant fluxes from the  $i$ -th direction.
- $F_i$ , the angular factors between a person and the surrounding surfaces ( $i = 1-6$ ).
- $\alpha_p$ , is the absorption coefficient for shortwave radiation of the human body ( $\alpha_p=0.7$ ).

$F_i$  depends on the position and orientation of the person (Fanger, 1972). The calculation of  $F_i$  is complicated for complex urban forms and simplifications are thus necessary. For a (rotationally symmetric) standing or walking person  $F_i$  is set to 0.22 for radiation fluxes from the four cardinal points (north, south, east and west) and 0.06 for radiation fluxes from above and below.

The calculation of the shortwave ( $K_i$ ) and long wave ( $L_i$ ) radiation components from the six directions is performed according to different analytical expressions that are reported in section 3.4.2 (VDI 1994, 1998). Further details regarding the calculation of field radiation can be found in Lindberg and Grimmond (2011).

ENVI-met predicts mean radiant temperature using all radiation fluxes, direct, diffuse and reflected solar radiation as well as the long wave radiation fluxes from the atmosphere, ground, and walls according to the method adopted in VDI (1998).

Estimation of mean radiant temperature by globe thermometer temperature measurements can be carried out. The temperature assumed by the globe thermometer results from a balance between the heat gained and lost by radiation and convection fluxes (ASHRAE, 2001). The globe temperature represents the weighted average of radiant and ambient temperatures. If the globe temperature, air temperature and air velocity are known the  $T_{mrt}$  can be calculated according to Eq. 3.23 (ISO 7627, 1998):

$$T_{mrt} = \left[ \left( T_g + 273.15 \right)^4 + \frac{1.1 \times 10^8 v_a^{0.6}}{\varepsilon D^{0.4}} \times \left( T_g - T_a \right) \right]^{0.25} - 273.15 \quad (3.23)$$

Here,  $T_g$  is globe temperature ( $^{\circ}\text{C}$ ),  $v_a$ , is air velocity ( $\text{m}\cdot\text{s}^{-1}$ ),  $T_a$  is air temperature ( $^{\circ}\text{C}$ ),  $D$  is Globe diameter (mm),  $\varepsilon$  is globe emissivity. The mean convection coefficient ( $1.1 \times 10^8 v_a^{0.6}$ ) is defined as the empirically derived parameter ( $v_a^{0.8}$ ).

Thorsson et al, 2014 have assumed the hourly maximum values of mean radiant temperature as hazard factor in the heat stress risk assessment in an urban context. Threshold values of  $T_{mrt}$  were used to identify outdoor microclimate conditions that can cause increase of the heat-related mortality risk for



more vulnerable people. Figure 3.12 shows the threshold values of  $T_{mrt}$  adopted in this study for the assessment of the heat stress risk.

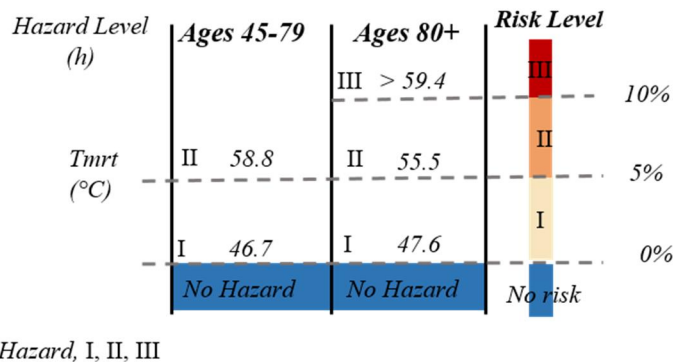


Figure 3.12. Threshold values related to the hazard of heat-related mortality.

As shown in figure 3.12, no heat stress hazard is considered for people aged below 45, while the hazard increases in a scale of zero to two (expected increase in the risk of heat-related mortality of 10%) according to different  $T_{mrt}$  values and age bands. It is worth noting that the thresholds for each class are different for age bands (45-79) and 80+. This expresses different strength capabilities of the human body with the ageing process.

### 3.6.2 Universal Thermal Climate Index

The Universal Thermal Climate Index (UTCI) is defined as an equivalent temperature of the reference environment which produces the same thermal response of a reference person in the real environment (Wheis et al., 2012).

UTCI is regarded as one of the most comprehensive indices for calculating outdoor thermal comfort conditions (Blazejczyk, 1994). The input data for calculating UTCI include meteorological and non-meteorological (metabolic rate and clothing thermal resistance) data (Farajzadeh et al., 2016).

The meteorological parameters that are taken into account for calculating UTCI involve dry bulb air temperature, mean radiant temperature, the pressure of water vapour or relative humidity, and wind speed (at an elevation of 10 m).

The UTCI reference environment shows a wind velocity of  $0.5 \text{ m}\cdot\text{s}^{-1}$  observed at 10 m above the ground, the mean radiant temperature equal to the air temperature and relative humidity of 50%. The wind speed should range from 0.5 to 17 m/s in order to calculate UTCI (Froehlich and Matzarakis, 2015).

The reference person has a body surface area of  $1.85 \text{ m}^2$ , a body weight of 73.4 kg and body fat content of 14% (Fiala et al., 2001). The metabolic rate, that is of 2.3 met (135 W), is higher than that used by the PET and SET\* model.

UTCI is a multi-node model for human thermoregulation that consists of 12 body elements comprising overall 187 tissue nodes. UTCI is based on Fiala’s advanced multi-node model (Fiala et al., 2012). UTCI allows the overcoming of limitations of outdoor thermal comfort indices based on a steady-state energy balance of the human body (PMV, PT and PET) which are not very appropriate for assessing short-term exposure in the outdoor environment (Fang et al., 2019).

Compared with the two-node models, multi-node models simulate the human body with higher detail, predicting both overall and local physiological responses. The variables under analysis include mean skin temperature, body core temperature and different forms of heat loss.

The UTCI is classified into ten thermal stress categories that correspond to a specific set of human physiological responses to the thermal environment.

Table 3.5 reports the range values of UTCI which is divided into 10 groups ranging from extreme cold stress to extreme heat stress (Young, 2017).

*Table 3.5 - Thermal sensations and different group in UTCI.*

<b>Thermal sensation</b>	<b>UTCI (°C)</b>	<b>Physiological stress</b>
very hot	> 46	Extreme heat stress
	38 ÷ 46	Very strong heat stress
hot	32 ÷ 38	Strong heat stress
warm	26 ÷ 32	Moderate heat stress
slightly warm		Slight heat stress
comfortable	9 ÷ 26	No thermal stress
slightly cool	0 ÷ 9	Slight cold stress
cool	-13 ÷ 0	Moderate cold stress
cold	-27 ÷ -13	Strong cold stress
very cold	-40 ÷ -27	Very strong cold stress
frosty	< -40	Extreme cold stress

### **3.7 Proposed urban heat stress mitigation strategies**

Two strategies for urban heat stress mitigation and the improvement of outdoor environmental microclimate conditions were proposed and evaluated:

- Urban greening infrastructures (UGIs).
- Cool materials.

Such strategies were evaluated under different separated scenarios at Microscale and large-scale respectively. Thermo-physical properties, and potential benefits of proposed solutions were described in the following sections. The reasons that have led to the choice of such strategies are explained and discussed in the following.

### 3.7.1 Urban Greening Infrastructures and renovation scenarios

Green infrastructures were integrated in a renovation scenario for heat stress mitigation at urban Microscale level and afterwards their application was extended on a large scale.

Preliminary, a selection was carried out of the more suitable urban greening strategies to the morphological and geometrical features of investigated urban areas.

Based on morphological features of the urban tissue of the two analyzed areas at urban Microscale level, two different intervention scenarios were investigated.

In compact and high built-up density area, a scenario was proposed which was based on the integration of greenery along existing street spaces rearranged according to the principles of traffic calming.

In open and low-rise built areas, an intensive greening of existing urban spaces was proposed, through the planting of high trees with large crown and the installation of extensive green roofs on the flat roofs of buildings included in the investigated area was proposed.

The interventions are addressed to increase the liveability of the public realm and improve the thermal comfort of outdoor areas.

Both scenarios aim to increase the Green Cover Ratio, and the selection of the plants was carried out based on morphological properties of individual vegetation species and urban morphology of the investigated urban contexts.

In light of this, urban greening strategies such as street trees and green roofs were selected.

### 3.7.2 Compact and high built-up density areas: a design scenario

The proposed renovation scenario for heat stress mitigation of high built-up density areas aims to increase the Green Cover Ratio using a strategy that does not imply strong urban transformations of the existing urban settlements. The spatial transformations aim at de-sealing paved spaces, mainly the ones currently used for parking, and converting them into green spaces. To this aim, the design criteria based on woonerf was adopted. Woonerf is a system introduced in the late sixties in The Netherlands, useful for containing vehicular traffic in residential areas.

The main characteristics of the woonerf strategy are:

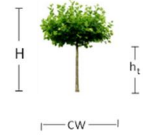
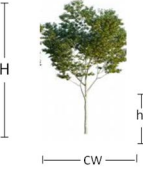
- Reduction of the road section, with a maximum width of 3.50 m.
- Reducing existing on-street parking spaces reserving them only for residents.
- Insertion of tall trees and greening surfaces.

The greening is substantially based on the addition of trees along the roads. Coherently to literature studies, the typology of trees was adopted on the basis of Sky View Factor values of the streets. The Sky View Factor (SVF) was deemed as reference parameter to choose the geometrical configuration

of plants due to the fact that a strong relationship between urban morphological parameters, thermal performance of trees, and plant structural characteristics was found. Sky View Factor (SVF) and geometrical configuration of plants are responsible for the radiant and thermal fluxes exchanged between the same trees and the surrounding atmosphere under Urban Canopy Layer (UCL).

Since the typical canyons of high built-up density areas are characterized by low values of SVF and wide shaded areas due to the mutual shadings of the buildings, the medium foliage trees, with average and/or short total height but high trunk were inserted into urban areas with SVF values predominantly between 0.20 and 0.50. The tree typologies adopted in high built-up density areas are reported in Table 3.6. It reports the name, species, morphology, and geometric features of the trees (Trunk height, Total tree height, Canopy Diameter), and Sky View Factor (SVF) values of the area of interest.

Table 3.6. Name, species, geometry features of trees and SVF values of the high built-up density areas.

Name	Species	Trunk zone height (m)	Total tree height H (m)	Diameter – canopy diameter CW (m)	Layout	Sky View Factor of the area of interest (SVF)	Local SVF value	Area of application
Platanus	Deciduous	2.0	3.0	2.0		0.2÷0.45	0.20÷0.40	Road (width: 7-10 m)
Platanus Hispanica	Deciduous	4.0	9.0	5.0		0.20÷0.45	0.30÷0.50	Road (width: 10-15 m) Car park

In the design scenario, the streets and public spaces were reorganized according to principles of woonerf. Based on the width of the streets, two configurations were accounted:

- 1) The first configuration is related to the section of the street with a width in the range 7-10 m. A row of car parking is eliminated in order to integrate a green space along the sidewalk. A row of deciduous trees such as Platanus (see Table 3.2) was inserted with a distance of 3.0 m from each other. Therefore, the seal paved area is reduced as shown in Figure 3.13b.
- 2) A second configuration is related to the street sections characterized by a width in the range 10-15 m. The row of car parking was replaced with a green space on both sides along the road. Therefore, two rows of trees such as Platanus Hispanica were inserted as shown in Figure 3.13c.

As an example, two graphical sections of a typical street before and after application of Woonerf criteria were depicted in Figure 3.13.



Figure 3.13. Cross sections of the roads: a) Existing configuration; b) and c) Design scenario.

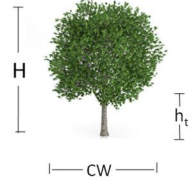
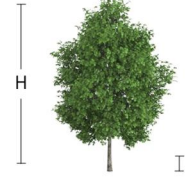
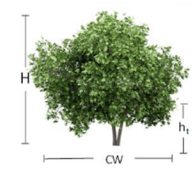
### 3.7.3 Open and low-rise area: Urban Heat Mitigation strategies

In the open and low-rise built areas, heat stress mitigation strategies based on advanced transformation were adopted. Such areas are characterized by high values of Sky View Factor ( $SVF > 0.60$ ), low buildings and are particularly exposed to the sunlit. A high priority of tree-planting was found, mainly due to largely reduced effect of shading benefit due to low height or absence of buildings. In light of this, intensive greening strategies consisting of trees with high leaf density and large crown were applied.

The planting of trees in large areas such as bare soils, paved areas and car parks was planned.

Platanus Acerifolia, Platanus occidentalis, and Ficus species were adopted. The morphology and geometric features of these trees species are reported in table 3.7.

Table 3.7. Name, species, geometry features of trees and SVF values of the open and low-rise built open areas.

Name	Species	Trunk zone height (m)	Total tree height H (m)	Diameter - canopy diameter CW (m)	Layout	Sky View Factor of the area of interest (SVF)	Local SVF value	Area of application
Platanus Acerifolia	Deciduous	2.0	10.0	6.0		0.45÷0.60	0.50÷0.60	Road (width >20 m) Car Park
Platanus occidentalis	Deciduous	1.5	18-20	10.0		> 0.60	0.60÷0.70 0.70÷0.80 0.80÷0.90	Open area (park/Green area/bare soil)
Ficus	Deciduous	1.0	10	15		>0.80	0.80÷0.90 0.90÷1.00	Open area (park/Green area/bare soil)

In open and low-rise area, green roofs and cool materials were also adopted.

Although experimental studies on the potential mitigation of air temperature of green roofs implemented in a neighborhood have shown a negligible cooling effect at pedestrian level for densely built-up urban areas, green roofs can lead to appreciable results on the surrounding environment when they are installed on the lowest buildings.

Since the open areas with high value of SVF are characterized by low-rise buildings, the installation of green roofs on the flat roofs of such buildings was also planned.

The application of reflective paints on the building roofs and pedestrian pavements was adopted because the effect of multiple reflections is low.

#### 3.7.3.1 Cool materials

The main effects of Urban Heat Island consist of human discomfort, environmental pollution, energy consumption for building cooling, peak of electricity demand, and consequently the rise of energy prices (Hassid et al. 2000). In order to counter the overheating of urban areas and reduce its impact on the communities several intervention policies in relation to space scale are available. It is possible to select three levels: urban, neighborhood, and Microscale. In recent years, in a Microscale context, a wide set of countermeasures such as cool roofs (Synnefa et al., 2012), cool pavements (Akbari et al., 2007), green roofs (Santamouris et al. 2014b), and greenery of urban surfaces (Morakinjo, 2020) have been promoted because they are capable of reducing energy consumption and improving outdoor thermal comfort (Akbari et al., 2005).

#### 3.7.3.2 Cool roof

A cool roof is substantially a roof with a highly reflective material (cool material) on its outermost surface. Cool materials are characterized by high values of solar reflectance ( $r > 0.6$ ), which strongly reduces the amount of solar radiation absorbed by the roof outer layer. Furthermore, cool roofs are also characterized by high infrared emissivity ( $0.8 < \epsilon < 0.9$ ) (Synnefa, 2012), which contributes to dissipate the heat accumulated during the day through an intensive radiant heat exchange at night (Prado et al., 2005). Nowadays, a wide range of cool materials is commercialized: paints, coatings, membranes, tiles, and pre-painted steel panels (Santamouris et al., 2015).

Cool roofs usually show lower values of the surface temperature if compared with a traditional roof, and they reduce the roof daily heat gain (Suehercke et al., 2008; Bozonnet et al., 2011). As an example, an average reduction by 30°C in the daily peak of the outer roof surface temperature has been found by Akbari et al. (2005). Several studies have investigated the effectiveness of cool roofs as an urban heat island mitigation strategy (Synnefa et al., 2007).

#### 3.7.3.4 Green roof

A green roof consists of a vegetation cover on top of a roof surface. Two types of green roofs are generally identified: extensive green roofs, whose soil thickness is below 15 cm, and intensive green roofs, with a soil thickness above 20 cm (Jaffal, 2012).

Because of their low additional loads, extensive green roofs do not require any additional strengthening, so they are suitable for building retrofitting (Ekaterini, et al., 1998). The typical layers of an extensive green roof, from the inner to the outer side, are load-bearing slabs (roof deck), vapor barrier, insulation layer, roofing membrane, root barrier, drainage layer with/without aeration and storage water, filter layer, growing substrate/porous soil and vegetation layer (Parizzotto et al., 2011; Lazzarin et al., 2005).

Several studies have highlighted the favorable environmental and energy performance of green roofs, showing how they introduce a reduction of both the heating and the cooling loads, an improvement in thermal comfort and of the urban air quality.

Moreover, it is possible to observe a reduction of noise transmission, a mitigation of the Urban Heat Island effect and the extension of roof life (Lazzarin et al., 2005; Theodosiu et al., 2003). Indeed, a green roof absorbs a high percentage of solar radiation for performing the biological functions of the vegetation, thereby only a low heat flux is transferred to the indoor space (Castelton et al., 2010). The effects of shading and evapotranspiration, as well as the thermal mass of a green roof, help to stabilize internal temperatures, delay the outdoor surface temperature peak and keep the internal conditions within the comfort range (Copozzoli et al., 2013; Parizzoto et al., 2011; Lazzarin et al., 2005; Niachou, et al., 2001; Feng et al., 2010).

**CHAPTER FOUR:  
CASE STUDY AND ANALYSIS OF RESULTS AT URBAN  
MICROSCALE AND AT LARGE-SCALE**



## 4.1 Structure and outline of the chapter

This chapter describes the case study, results of the climate analysis at urban Microscale level and at large scale as follow:

- Section 4.2 provides a description of the morphological and geometrical features of a part of Municipality of Catania.
- Section 4.3 analyzes the results of the Local Climate Zones (LCZs) classification.
- Section 4.4 describes the morphological and geometrical features of two selected urban settlements as affected by potential heat stress risk.
- Section 4.5 describes the results of the urban Macroscale-based climate analysis of a calibrated and validated model of a part of Municipality of Catania. The potential effectiveness of the proposed mitigation heat stress strategies attained at large-scale were assessed.
- Section 4.6 describes and discusses the results of the urban Microscale-based climate analysis at current state and after the application of mitigation strategies respectively of two selected areas as the most sensitive risk areas.
- Section 4.7 discusses the comparison between the outcomes of Macroscale analysis and those attained at Microscale level in order to assess the accuracy and reliability of the large-scale model.

## 4.2 The case study

This study takes in a part of the Catania Municipal Area, located in Southern-Italy (Lat. 37.30 North, Long. 15.07 East), as the study area. The weather conditions are characterized by hot and humid summers and moderately cold and wet winter seasons. In summer, the average outdoor temperature generally ranges from 20 °C to 35 °C, with peaks of 40 °C. In winter, the outdoor temperature generally varies from 5 °C to 15 °C, while in spring and autumn the climate is mild and the temperatures vary from 10 °C to 28 °C as is typical on coastal Mediterranean areas.

Table 4.1 summarizes the general and physical data of the municipality of Catania.

*Table 4.1. General and physical data of Municipality land.*

<b>Parameters</b>	<b>Value</b>	<b>Unit</b>
Surface	41.2	Km <sup>2</sup>
Average temperature in winter period (1 <sup>st</sup> December -31 <sup>th</sup> March)	11.7	°C
Average temperature in summer period (1 <sup>st</sup> June -30 <sup>th</sup> September)	25.7	°C
Wind speed	4.40	m·s <sup>-1</sup>
Prevailing wind direction	East	-
Population density	204	Inhabitants·ha <sup>-1</sup>

The region is classified as Csa - Hot-Summer Mediterranean climate class - according to the Köppen-Geiger classification (Kottek et al., 2006). Figure 4.1 shows the aerial photogrammetric view of a part of Catania municipal area.



Figure 4.1. Aerial photogrammetric view of the city of Catania and surrounding areas.

The large-scale climate analysis was not extended to the entire Municipality of Catania but an area that includes the most critical Local Climate Zones (LCZs) was analysed.

#### 4.2.1 UMEP modelling: Morphological input for Local Climate Zones classification

The Digital Elevation Model (DEM) and Digital Surface Model (DSM) of a part of Catania Municipal area were used as primary morphological and geometrical input for LCZ classification. DEM and DSM are reported in Figures 4.2 and 4.3.

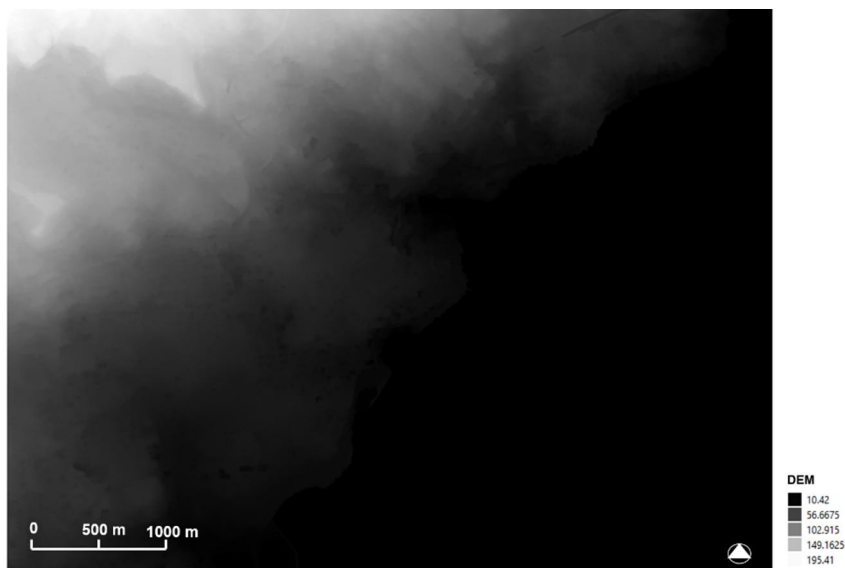


Figure 4.2. 2D map of Digital Elevation Model (DEM);



Figure 4.3. 2D map of Ground and Building DSM.

DEM and Ground and building DSM acquired from the Laboratorio per la Pianificazione Territoriale e Ambientale (LAPTA) of the Department of Civil Engineering and Architecture of the University of Catania (2021). DEM and DSM have 4 m resolution. The elevation of the terrain varies from 10 m a.s.l. along the coast to 195.41 m a.s.l. in areas located to the north and west of the Municipality land. 2D map of the Sky View Factor (SVF) was achieved by Morphometric Calculator tool that is a plugin integrated in UMEP (Urban Multi-scale Environmental Predictor). Figure 4.4 shows the 2D Map of the Sky View Factor.

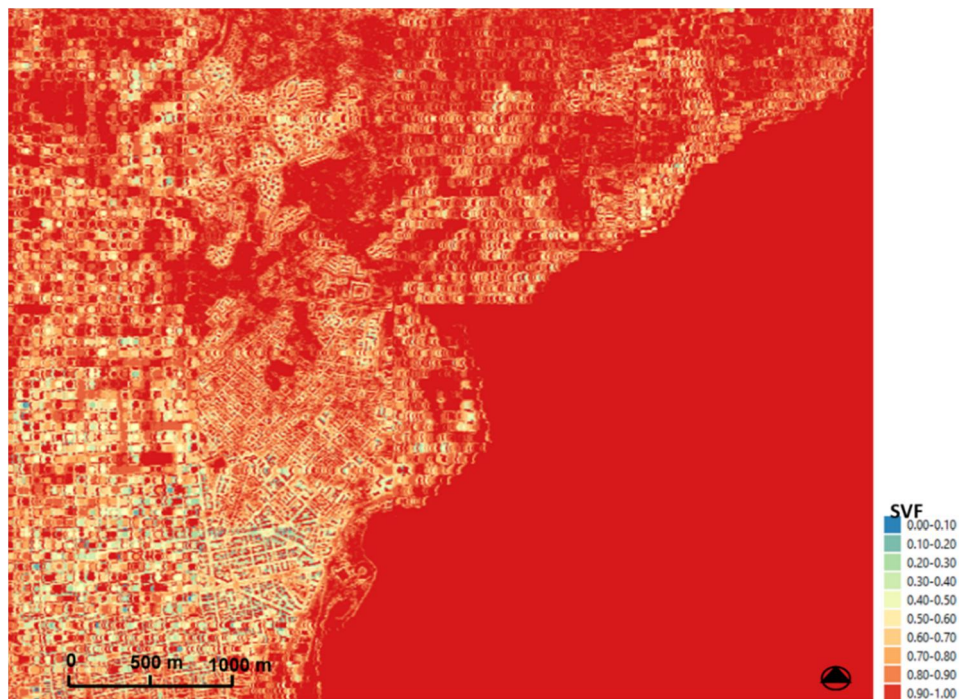


Figure 4.4. 2D digital map of the Sky View Factor.

2D map of Sky View Factor shows that the open areas have SVF values higher than 0.70. The urban areas in the city center, compacts and densely high built-up areas have SVF values predominantly between 0.30 and 0.60.

Figure 4.5 shows the 2D map of spatial distribution of buildings, pervious and impervious surfaces in the studied area. The 2D map is associated with a database file that includes the building surface fraction (BSF), impervious surface fraction (ISF) and pervious surface fraction (PSF) of the city of Catania.

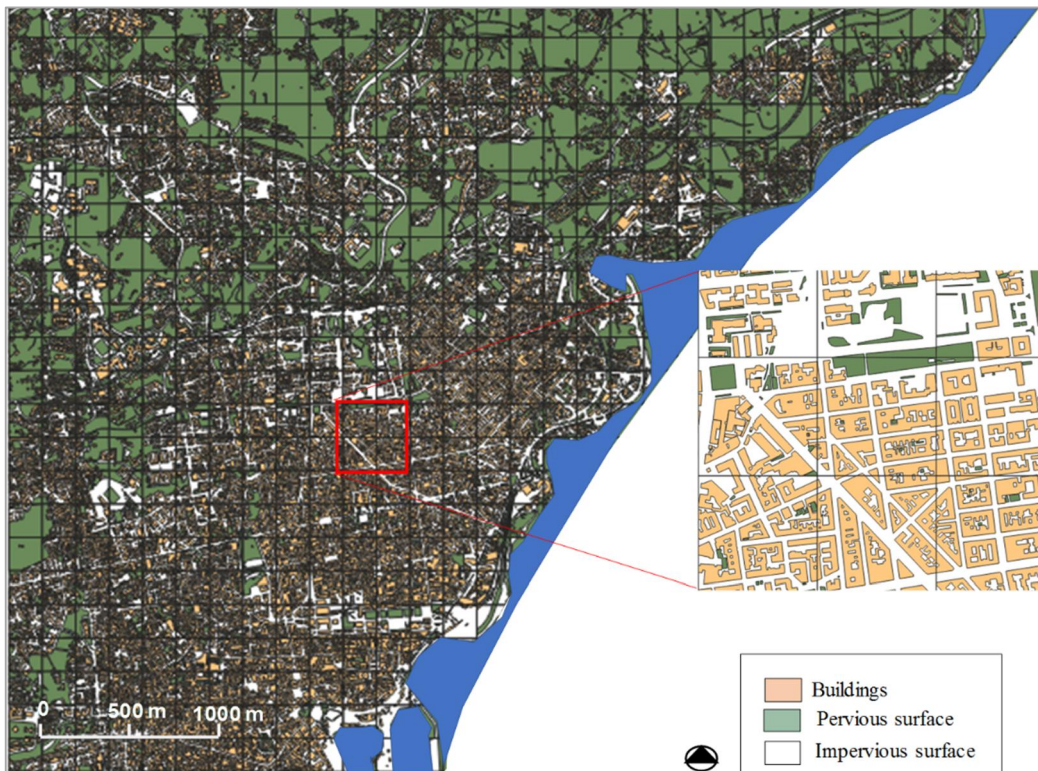
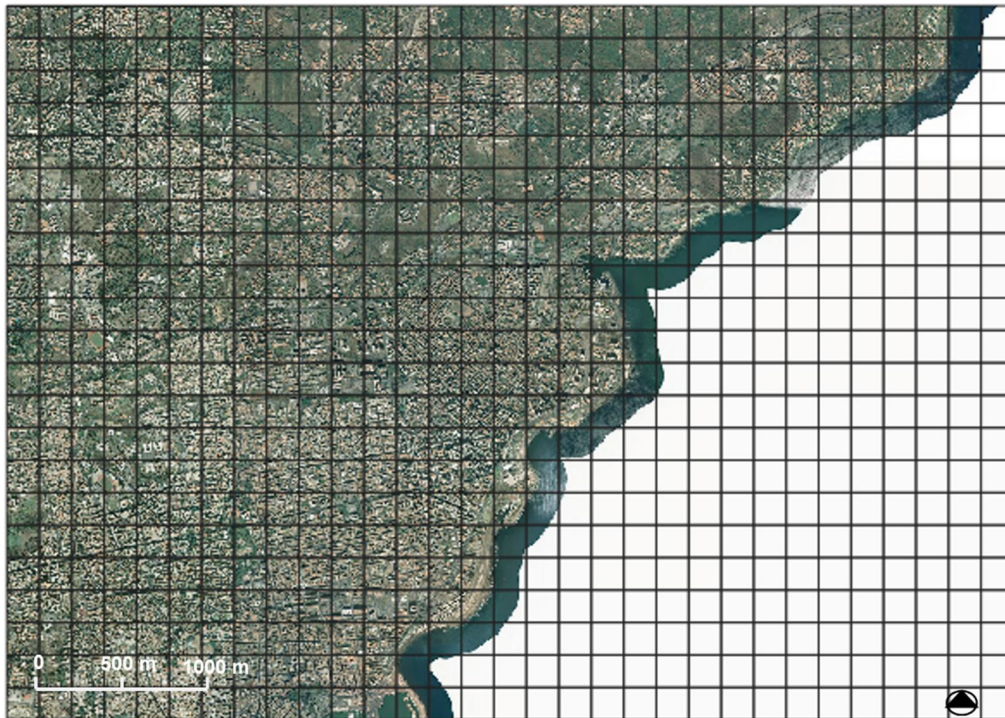


Figure 4.5. 2D map of investigated area in shapefile format in QGIS Environment.

The geometrical and morphology data of the 2D map of Digital Elevation Model (DEM), Digital Surface Model (DSM), Sky View Factor (SVF) and the building surface fraction (BSF), impervious surface fraction (ISF) and pervious surface fraction (PSF) were used to carry out the Local Climate Zones (LCZs) classification of the studied area.

### 4.3 Local Climate Zones (LCZs) classification of the study area

The Local Climate Zones (LCZs) classification was carried out on an area of the Municipality of Catania shown in the aerial photogrammetric view reported in Figure 4.1. The investigated area was discretized according to square cells of 200 x 200 m<sup>2</sup> size. (see figure 4.6).



*Figure 4.6. Grid “layer” applied to the investigated domain.*

The parameters used to classify the Local Climate Zones (BSF, PSF, ISF,  $z$ ,  $z_0$ , SVF) are aggregated in an attribute table associated to the “Grid” layer.

Therefore, the attribute table includes the georeferenced values of Building Surface Fraction, BSF (1\_pai), Impervious Surface Fraction, ISF (1\_limp), Roughness element height,  $z$  (1\_zH), Terrain roughness class,  $z_0$  (1\_z0), Pervious Surface Fraction, PSF (1\_Ip) and Sky View Factor (SVF) of each grid cell of the investigated domain.

A query was set in the attribute table of the “Grid” layer (Vector attribute) for all standard LCZs types of the Oke and Stewart classification.

Figures (4.7-4.15) show 2D location map for each LCZ type and the matched query. Figures depict the LCZs types found in the study area.

In each figure, empty cells with a dark border represent cells that did not comply with all parameter ranges required for the standard classification scheme set by Oke. These cells were noted as LCZ<sup>\*</sup><sub>x</sub>, where  $x$  indicates the nearest parent class in the standard set of LCZs according to the criteria of Stewart and Oke, and (\*) indicates that one morphological parameter did not comply with the specific requested range for standard LCZ classification, while (\*\*) indicates that two morphological parameters did not comply with the specific requested ranges for standard LCZ classification.

As shown in Figures 4.7, 4.9 and 4.10, in Built LCZs types (LCZ2, LCZ5 and LCZ6), empty cells with a dark border are characterized by values of Impervious Surface Fraction (ISF) higher than

threshold values of the ranges of standard LCZs. In particular, these grid cells have values of  $ISF > 0.50$ .

Here, such cells were classified as LCZ\*2, LCZ\*5 and LCZ\*6 respectively because these cells complied with five standards of LCZ2, LCZ5 and LCZ6 except ISF which is higher than 0.50.

In Figure 4.11, (Built type LCZ9) empty cells with a dark border complied with five standards of LCZ9 except ISF that is higher than 0.20. The LCZ\*9 class was attributed to these cells.

The same criteria were adopted to classify the cells that complied with the standard of LCZC except for the impervious surface fraction (ISF) which was higher than 0.10 (see Figure 4.12). These square cells were classified as LCZ\*C where (\*) indicates that  $ISF > 0.10$ .

Some grid cells along the coast (see Figure 4.15) did not comply with the ranges of ISF and PSF parameters of LCZG. Since all the others parameters complied with the set of standard LCZG, these cells were classified as LCZ\*\*G where (\*\*) indicates that  $ISF > 0.10$  and  $PSF < 0.90$ .

Figure 4.7 shows the 2D location map of LCZ2 and LCZ2\* in to the study area.

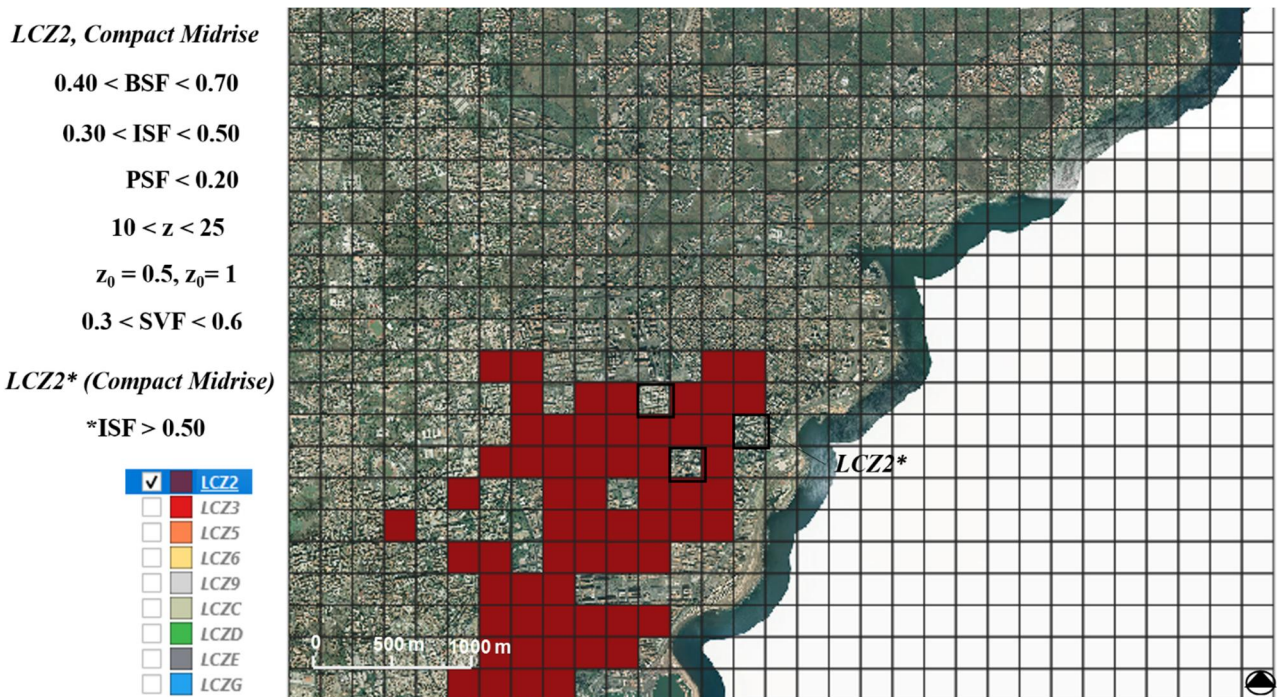


Figure 4.7. 2D location map and query of standard LCZ2 (Compact Midrise) and LCZ\*2 (Compact Midrise with  $ISF > 0.50$ ).

**LCZ3, Compact Low-rise**

$0.40 < BSF < 0.70$

$0.20 < ISF < 0.50$

$PSF < 0.30$

$3 < z < 10$

$z_0 = 0.5$

$0.2 < SVF < 0.6$

- LCZ2
- LCZ3
- LCZ5
- LCZ6
- LCZ9
- LCZC
- LCZD
- LCZE
- LCZG

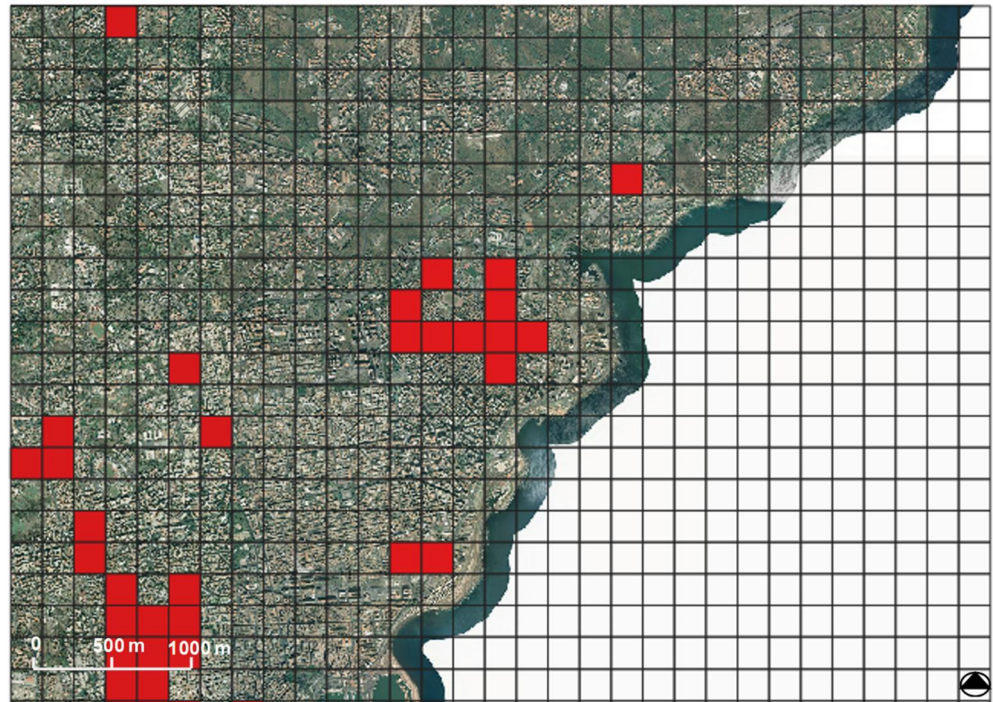


Figure 4.8. 2D location map and query of standard LCZ3 (Compact Low-rise).

**LCZ5, Open Midrise**

$0.20 < BSF < 0.40$

$0.30 < ISF < 0.50$

$0.20 < PSF < 0.40$

$10 < z < 25$

$z_0 = 0.25; z_0 = 0.50$

$0.6 < SVF < 0.8$

**LCZ5\* (Open Midrise)**

**\*ISF > 0.50**

- LCZ2
- LCZ3
- LCZ5
- LCZ6
- LCZ9
- LCZC
- LCZD
- LCZE
- LCZG

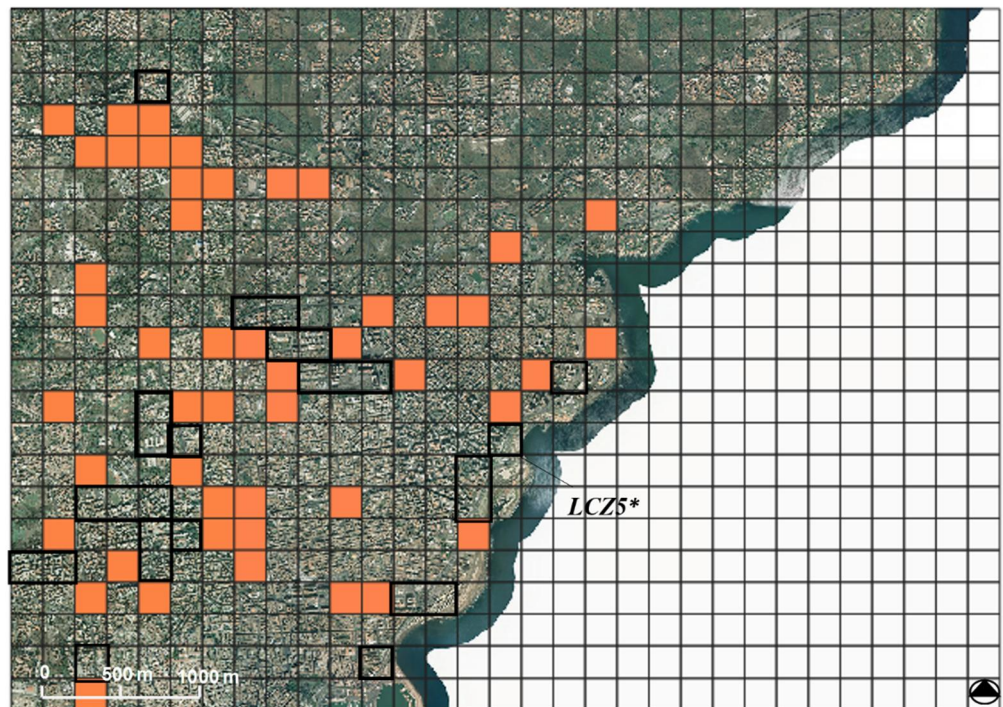


Figure 4.9. 2D location map and query of standard LCZ5 (Open Midrise) and LCZ5\* (Open Midrise with ISF > 0.50).

**LCZ6, Open Low-rise**

$0.20 < \text{BSF} < 0.40$

$0.30 < \text{ISF} < 0.50$

$0.30 < \text{PSF} < 0.60$

$3 < z < 10$

$z_0=0.50$

$0.6 < \text{SVF} < 0.9$

**LCZ6\* (Open Low-rise)**

\* $\text{ISF} > 0.50$

- 
- LCZ2
- LCZ3
- LCZ5
- LCZ6
- LCZ9
- LCZC
- LCZD
- LCZE
- LCZG

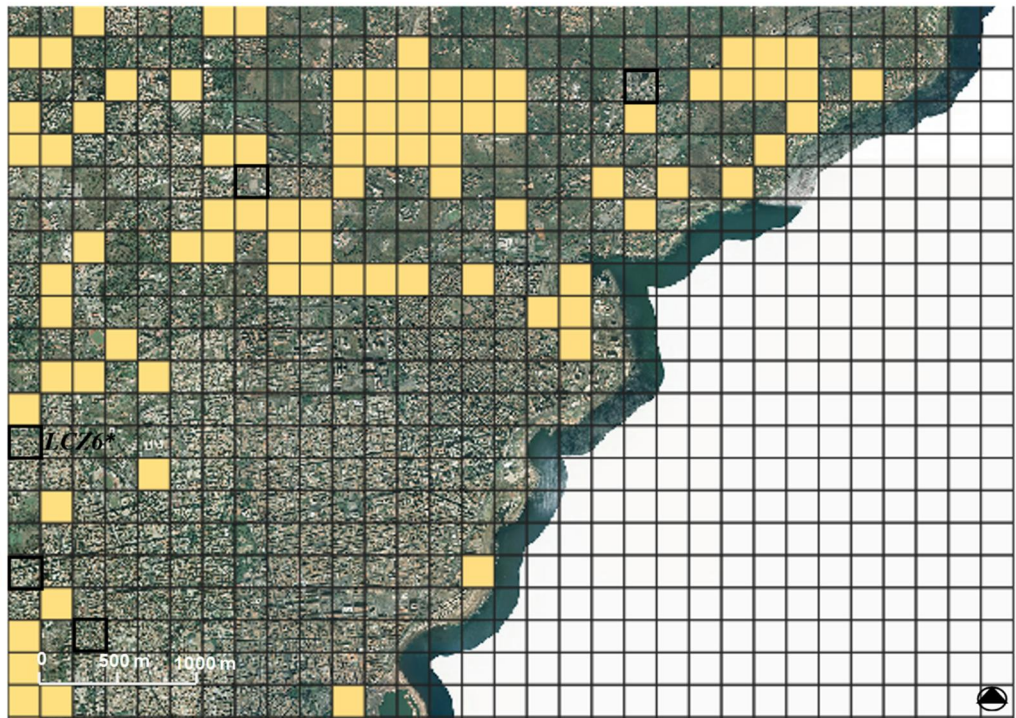


Figure 4.10. 2D location map and query of standard LCZ6 (Open Low-rise) and LCZ\*6 (Open Low-rise with ISF > 0.50).

**LCZ9, Sparsely Built**

$0.10 < \text{BSF} < 0.20$

$\text{ISF} < 0.20$

$0.60 < \text{PSF} < 0.80$

$3 < z < 10$

$z_0=0.50$

$\text{SVF} > 0.8$

**LCZ9\* (Sparsely Built)**

\*  $\text{ISF} > 0.20$

- 
- LCZ2
- LCZ3
- LCZ5
- LCZ6
- LCZ9
- LCZC
- LCZD
- LCZE
- LCZG

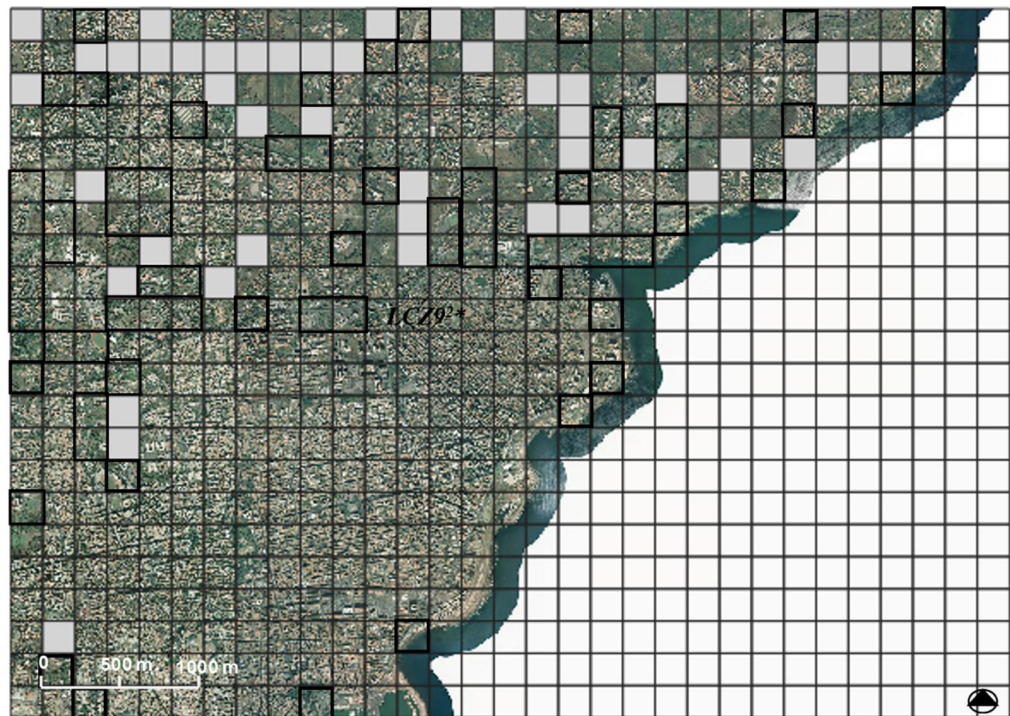


Figure 4.11. 2D location map and query of standard LCZ9 (Sparsely Built) and LCZ\*9 (Sparsely Built with ISF > 0.20).



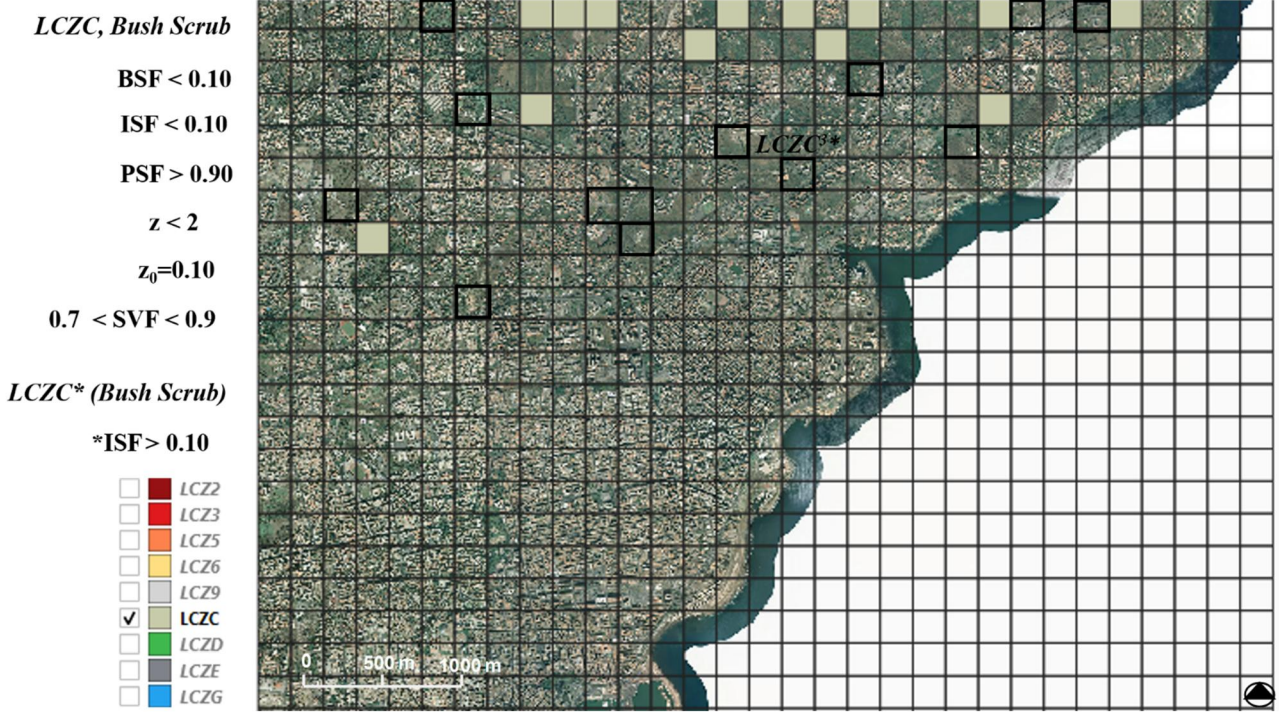


Figure 4.12. 2D location map and query of standard LCZC (Bush scrub) and LCZ\*C (Bush Scrub with ISF > 0.10).

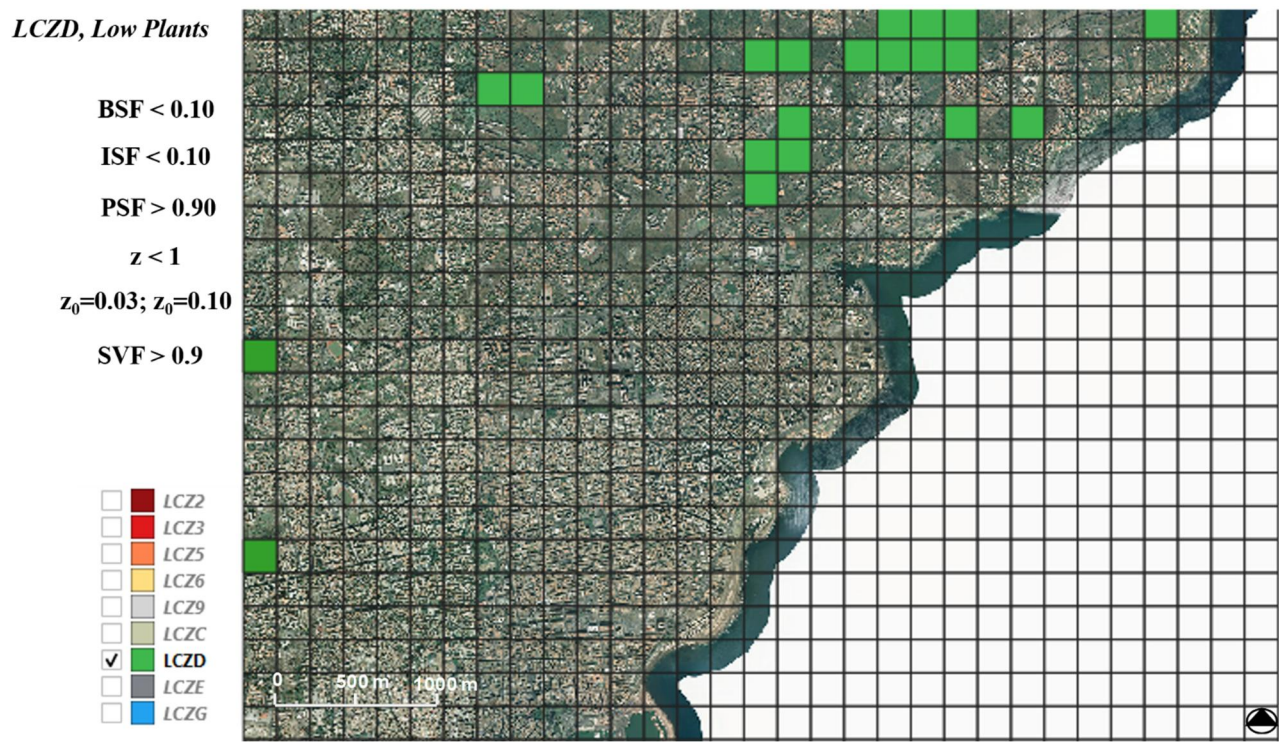


Figure 4.13. 2D location map and query of standard LCZD (Low Plants).

*LCZE, Bare rock or paved*

BSF < 0.10  
 ISF > 0.90  
 PSF < 0.10  
 z < 0.25  
 z<sub>0</sub>=0.0005  
 SVF > 0.9

- LCZ2
- LCZ3
- LCZ5
- LCZ6
- LCZ9
- LCZC
- LCZD
- LCZE
- LCZG

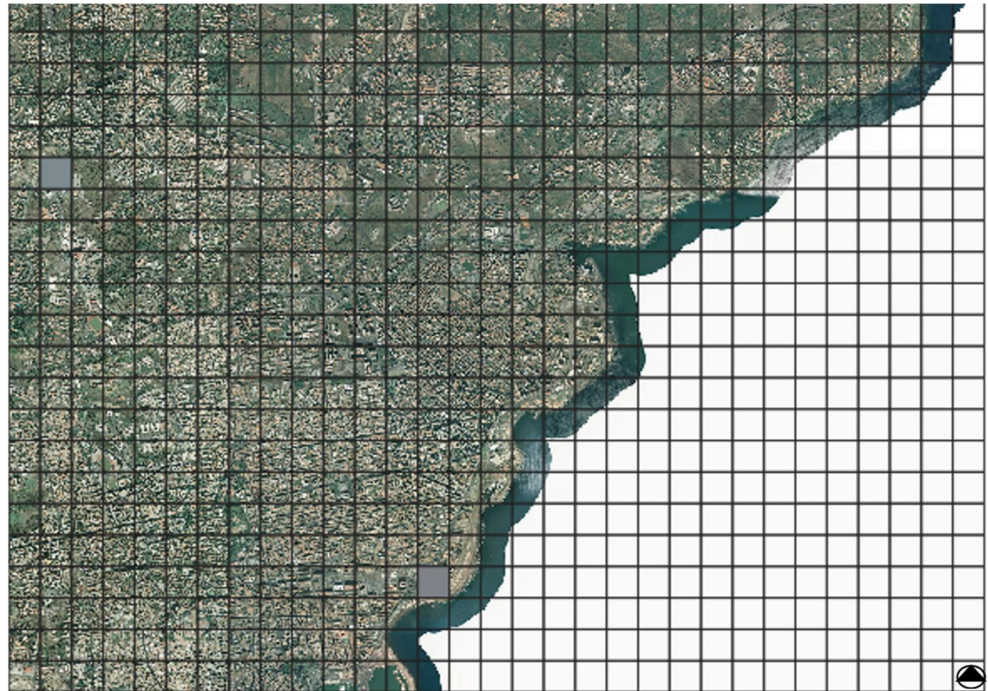


Figure 4.14. 2D location map and query of standard LCZE (Bare rock or paved).

*LCZG, Water*

BSF < 0.10  
 ISF < 0.10  
 PSF > 0.90  
 z = -  
 z<sub>0</sub>=0.0002  
 SVF > 0.9

*LCZG\*\* (Water)*

\*\* (ISF > 0.10, PSF < 0.90)

- LCZ2
- LCZ3
- LCZ5
- LCZ6
- LCZ9
- LCZC
- LCZD
- LCZE
- LCZG

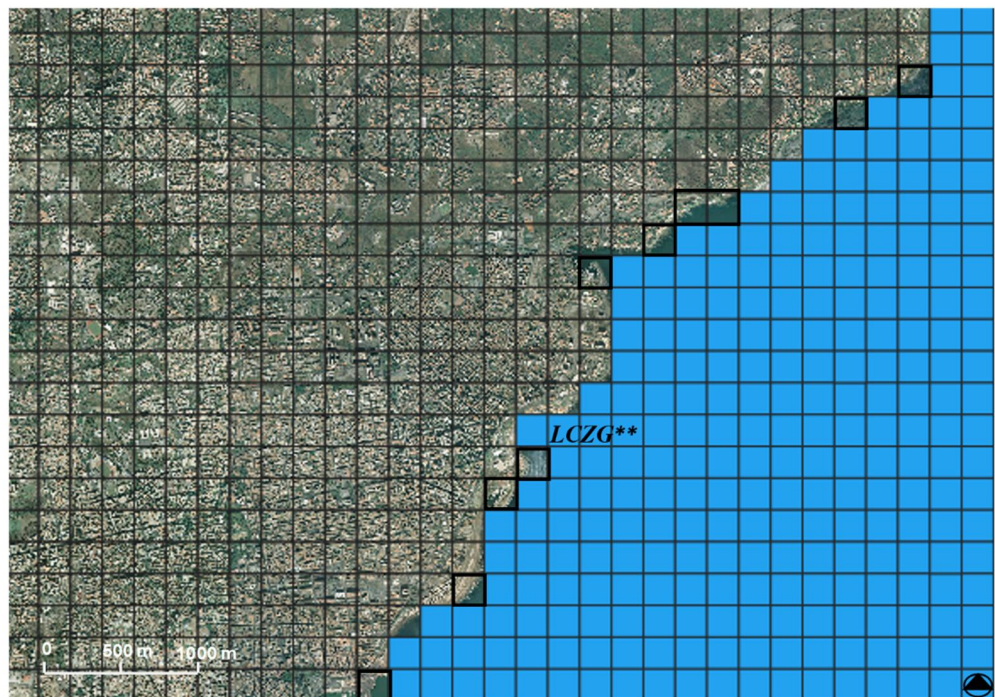


Figure 4.15. 2D location map and query of standard LCZG (Water) and LCZ\*\*G (Water with ISF > 0.10 and PSF < 0.90).

Figure 4.16 shows the 2D digital map of spatial distribution of LCZs in the study area. LCZs were represented by means of a band false colours.

For sake of clarity all the grid cells matched to LCZ\*2, LCZ\*5, LCZ\*6, LCZ<sup>2</sup>\*9, LCZ<sup>3</sup>\*C were represented with the same colors of the corresponding to standard LCZs. It can be observed that LCZ\*\*G was represented with a different colour in respect of the LCZG.

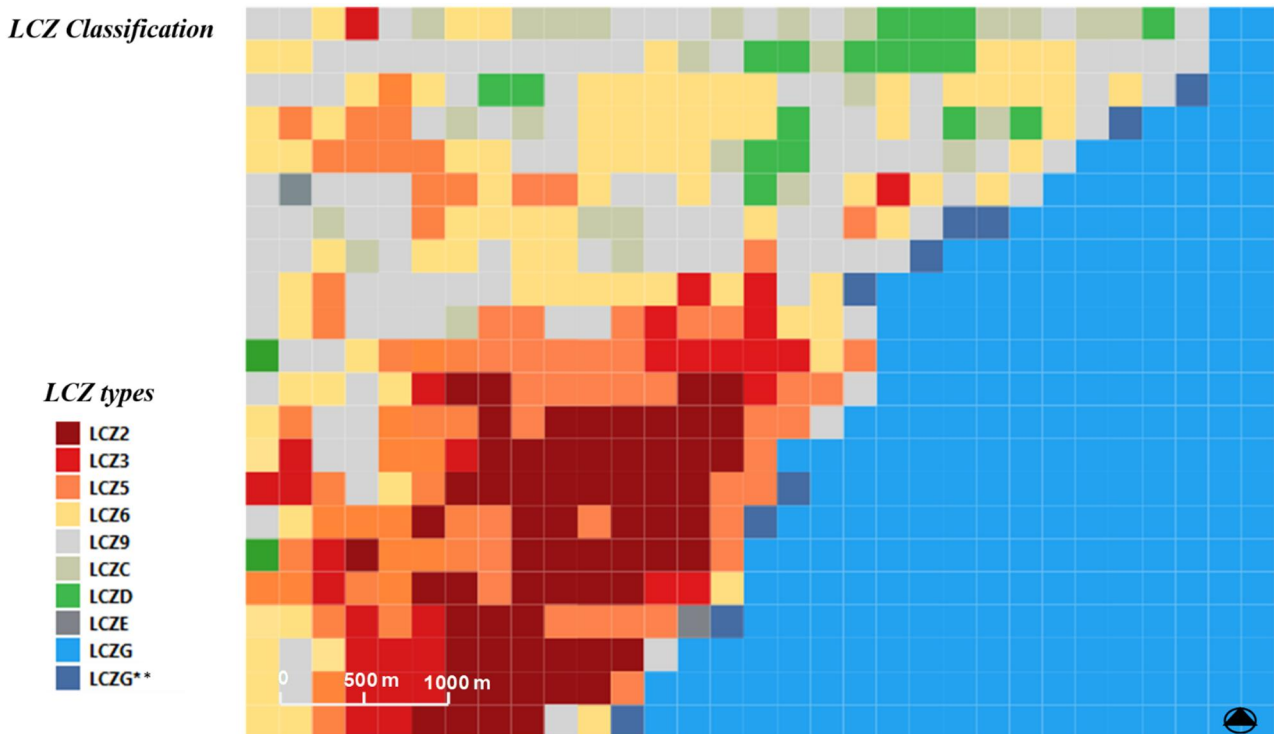


Figure 4.16. 2D map of spatial distribution of Local Climate Zones (LCZs).

The spatial distribution of LCZs shows that the ‘built’ LCZ types are predominant with respect to the “Land Cover” LCZ types. Some “built” LCZ classes such as high-rise (LCZs 1 and 4), the lightweight low-rise (LCZ 7), Large Low-Rise (LCZ 8) and the heavy industrialized (LCZ 10) classes were not found in the study area. The fraction of the investigated area occupied by different types of LCZs is reported in table 4.2.

The “Built” LCZ types are 86.5% of the study area whereas the “Land Cover” LCZ types are 13.5%. LCZ2 (Compact Midrise), LCZ5 (Open Midrise) and LCZ6 (Open Low-rise) are “built” LCZ types most present in the study area.

The large-scale analysis was focused on the area that includes the most critical Local Climate Zones such as Compact Midrise (LCZ2) and Low-rise (LCZ3) zones. The investigated area is shown in Figure 4.17.

Table 4.2. Local Climate Zones (LCZs): type, name, area ( $A_i$ ) and surface fraction (%) respect to the surface of the studied area ( $A_i/A_{tot}$ )

Type LCZ	Name	$A_i$ (km <sup>2</sup> )	$A_i/A_{tot}$ (%)	Parameters not in accordance with the standard scheme set by Oke
<b>Built</b>	LCZ2	3.9375	14.2%	-
	LCZ3	2.1875	7.9%	-
	LCZ5	3.0625	11.0%	-
	LCZ6	5.2500	18.9%	-
	LCZ9	2.8125	10.1%	-
	LCZ2*	0.1875	0.7%	ISF > 0.50
	LCZ5*	1.9375	7.0%	ISF > 0.50
	LCZ6*	0.4375	1.6%	ISF > 0.50
	LCZ9*	4.1875	15.1%	ISF > 0.20
	<b>Total</b>	<b>24.00</b>	<b>86.5%</b>	
<b>Land Cover</b>	LCZC	0.8125	2.9%	-
	LCZD	1.2500	4.5%	-
	LCZE	0.1250	0.4%	-
	LCZC*	0.8125	2.9%	ISF > 0.10
	LCZG**	0.7500	2.7%	ISF > 0.10 and PSF < 0.90
	<b>Total</b>	<b>3.7500</b>	<b>13.5%</b>	

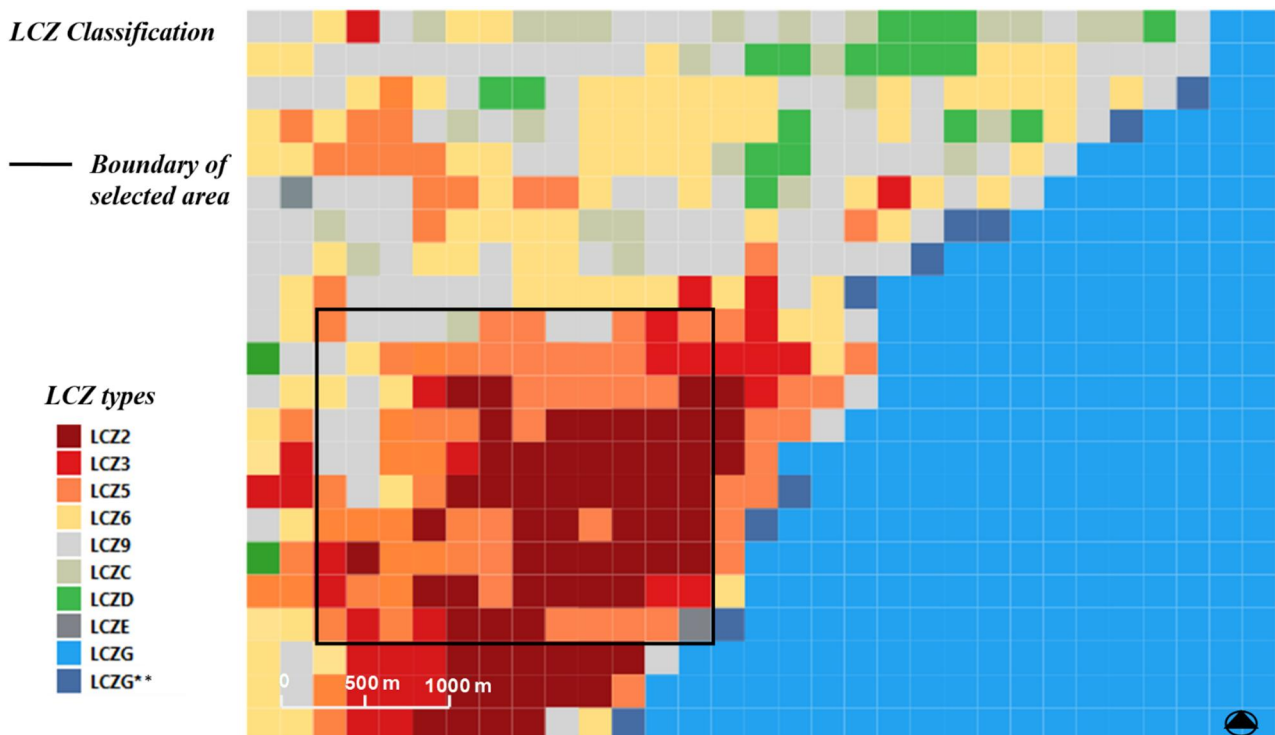


Figure 4.17. 2D map of spatial distribution of LCZs and boundary of investigated area.

## 4.4 Description of the morphological features of the heat stress risk area

### 4.4.1 Morphological features of the investigated area

The investigated area has a surface of 7.5 km<sup>2</sup> and it is included in the General Master Plan approved in 1969. Figure 4.18 shows the digital aerial view of the selected area.



Figure 4.18. 2D digital map of the investigated area.

The land cover is predominantly characterized by an impervious surface (ISF) of 47.2%, while the building surface fraction (BSF) accounts for 34.9% of the investigated area and the pervious surface covers the remaining 17.9% of the selected area. Figure 4.19 shows the soil use surface fractions of the area.

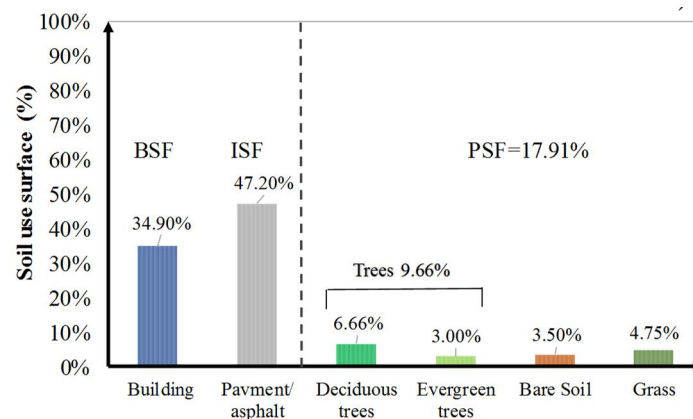


Figure 4.19 Soil use surface fractions of the investigated area.

The land cover fraction and building morphology data are instead reported in Table 4.3.

*Table 4.3. Land Cover fraction and average building height.*

Parameters		Unit	Value	Fraction (%)
Area	$A_{site}$	$m^2$	7505993	-
Pervious surface	$A_{per}/A_{Site}$	$m^2$	1338022	<b>17.90</b>
Impervious surface	$A_{imp}/A_{Site}$	$m^2$	3543582	<b>47.20</b>
Building surface	$A_{Build}/A_{Site}$	$m^2$	2618395	<b>34.90</b>
Average Building height	$h_{w,Build}$	m	12.3	-

The pervious surface is occupied by trees, and grass for 9.66% and 4.75% of the investigated area respectively (see Figure 4.19). The percentage of vegetation surface is low if compared to that of the impervious surface fraction. Tables 4.4 and 4.5 report the percentage of pervious surfaces and those of the trees respectively.

*Table 4.4. Pervious surface fractions.*

Parameters		Unit	Value	Fraction (%)
Bare Soil	$A_{soil}/A_{Per}$	$m^2$	262399	<b>3.50</b>
Grass	$A_{imp}$	$m^2$	356803	<b>4.75</b>
Trees	$A_{Tree}$	$m^2$	718819	<b>9.66</b>

*Table 4.5. Tree type surface fractions and average height trees.*

Parameters	-	Unit	Value	Fraction (%)
Deciduous trees	$A_{Tdec}$	$m^2$	262399	<b>6.66</b>
Evergreen trees	$A_{T,ever}$	$m^2$	356803	<b>3.00</b>
Average height trees	$h_{w,t}$	m	7.07	-

Deciduous trees such as *Platanus acerifolia* and *Citrus* are the types predominant along the roads and in open areas. Urban morphological features such as average building height, site coverage ratio, vegetation area and tree coverage, and sky view factor come from the Digital Surface Model (DSM) in GIS environment and specific GIS database of Catania.

#### 4.4.2 Description of two representative sites selected as heat stress risk areas

Two areas were identified as prone to potential heat wave risk sites and selected for detail analyses based on critical properties of their surface structure, cover land, and particular urban texture (morphology).

The two areas - named “Area 1” and “Area 2”- are included in “built” LCZ types: “Area 1” is classified as “LCZ2” (Compact midrise) while “Area 2” belongs to “LCZ5” (Open Low-rise). Figure 4.20 shown the localization of the two selected areas into the investigated urban context.

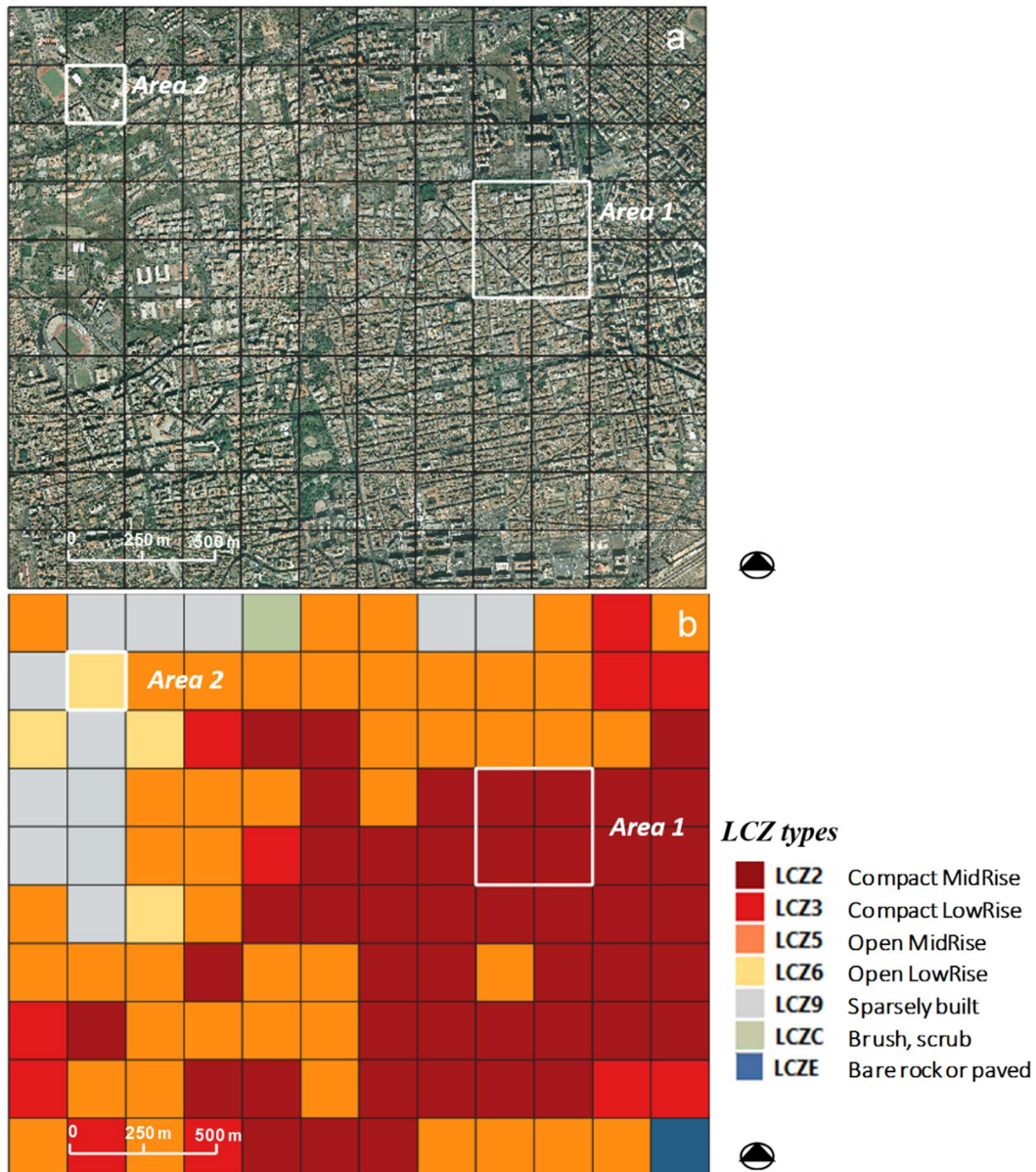


Figure 4.20. Location of areas 1 and 2 in the investigated area. a) Extract of aerial photogrammetric view; b) Extract of Local Climate Zones (LCZs) mapping.

Figure 4.21 shows the aerial photogrammetric views of the area 1 and 2 and the localization of the two selected points of interest into the two areas.

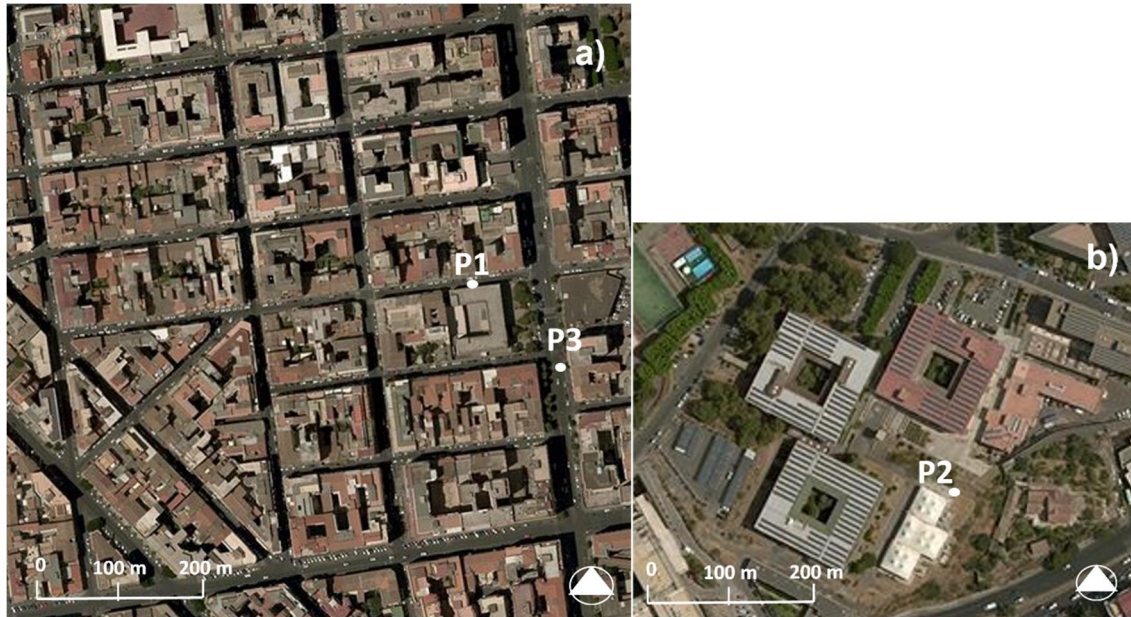


Figure 4.21. Aerial view of the studied areas and localization of the points of interest: a) Area 1; b) Area 2.

Area 1 has an urban settlement pattern characterized by remarkable repetitiveness and low quality, and poor quality public space characterized by lack of vegetation.

Area 2 is an open area characterized by large buildings with an average height between 5.0 m and 15.0 m. Urban spaces are predominantly covered by paved areas and bare soil.

Both zones have buildings realized with stone and concrete construction materials and urban surfaces such as roads, pedestrian pavements predominantly dark and grey with a low value of surface albedo. The areas have urban tissue of different geometric configuration, as summarized by their average canyon ratio.

The morphometric characteristics and land cover fractions of the two areas are reported in Table 4.6.

Table 4.6. Morphometric and land cover characteristics of the areas 1 and 2.

Area	Avg. building height (m)	Avg. street width (m)	Avg. canyon ratio (-)	Building surface (%)	Impervious surface (%)	Bare soil (%)	Trees (%)	Grass (%)
1	20.45	14	1.79	42.0	57.0	0	1	0
2	9.50	18	0.50	25.0	36.0	19	18	2

Various points of interest (POIs) were selected to derive detailed values of the most important radiant heat components that make up the radiant heat balance on the human body. Such points were also selected for their placement with respect to sensible locations to heat wave phenomena such as schools, hospitals, wide streets in the central areas, and compact midrise areas characterized by lack of trees. The characteristics of such POIs are shown in Table 4.7, which reports on their geometric (i.e., sky view factor (SVF), Aspect ratio) and optical properties (i.e., albedo and thermal emissivity).



Table 4.7. Characteristics of the selected points of interest (POIs).

Point of interest	Local climate zone (LCZ)	Street orientation	SVF (-)	H/W	Land cover	Thermal emissivity $\epsilon$ (-)	Avg. ground albedo (-)
P1	LCZ2	West-East	0.25	3	Paved	0.90	0.20
P2	LCZ2	North-south	0.60	0.4	Paved	0.90	0.20
P3	LCZ6	-	0.80	0.3	Paved	0.90	0.25

In particular, P1 is near a school while P2 is located in a wide street in the densely high compact built-up area (Area 1) as reported in Figure 4.21a. P3 is located on pedestrian pavements in the university Campus of Catania (Area 2) as shown in Figure 4.21b

## 4.5 Macroscale climate analysis

### 4.5.1 Geometrical modelling of the investigated area

Large-scale modelling of the investigated area was developed using digital terrain and surface models (DEM and DSM) with 4 m resolution extracted by DEM and DSM reported in Figure 4.2 and 4.3 respectively.

Figures 4.22a and 4.22b show DEM and DSM of the investigated area.

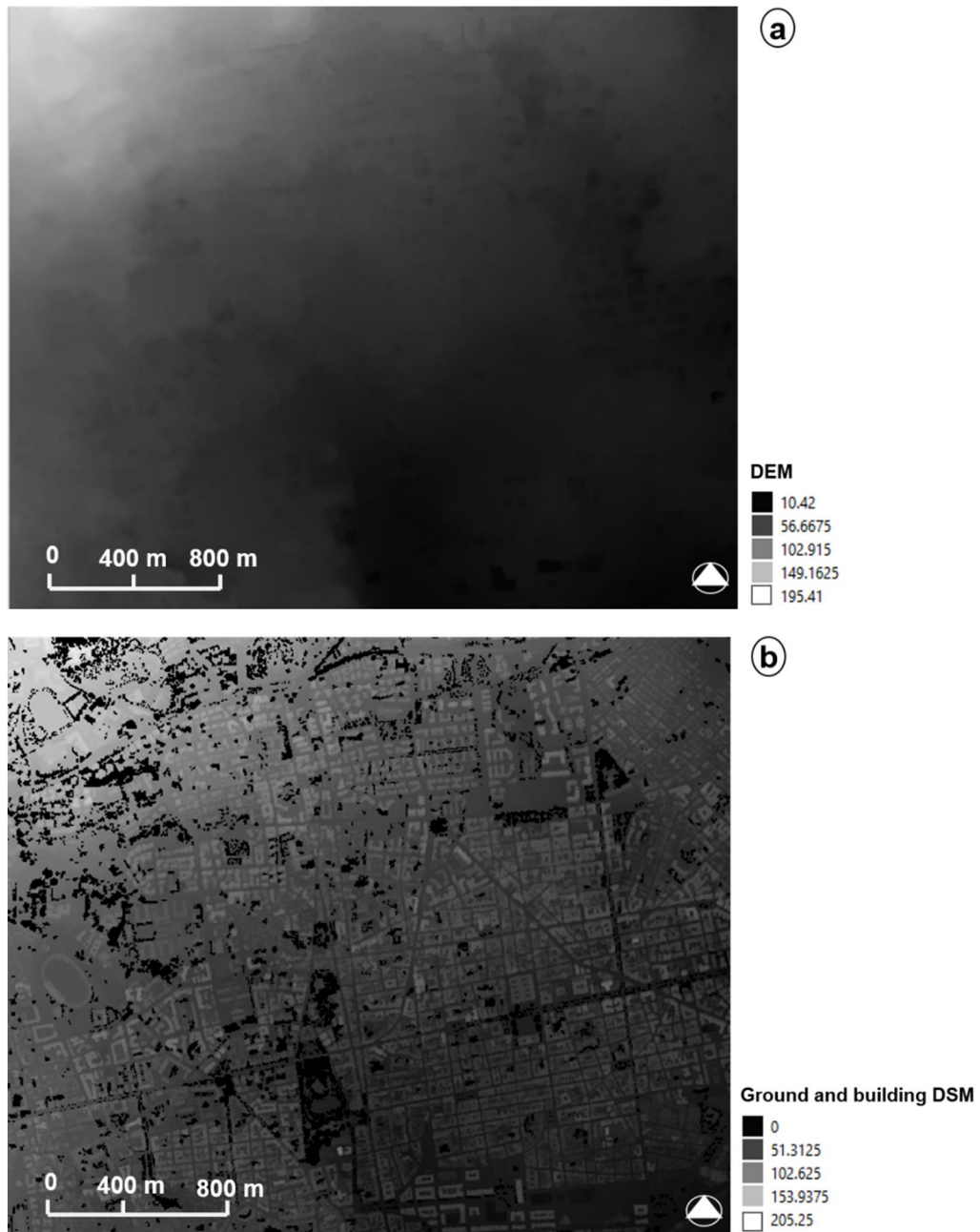


Figure 4.22. 2D Digital map: a) Digital Elevation Model (DEM); b) Ground and Building DSM.

The Ground and Building DSM comprise only the height of ground plus buildings. The vegetation is only included in the Canopy Digital Surface Model (CDSM) which is a raster grid containing only trees taller than 2.50 m.

Figure 4.23 shows the CDSM raster overlying the raster of Ground and Building DSM of the investigated area.

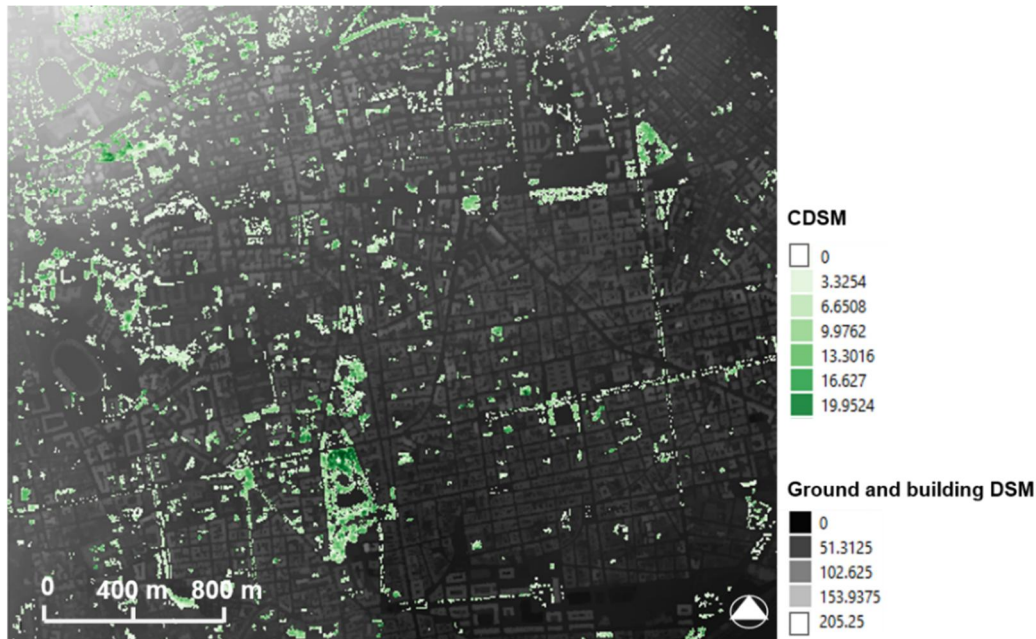


Figure 4.23. 2D map of Digital Ground and Building DSM + Canopy Digital Surface Model (CDSM).

The residential neighborhoods are located in the centre of the investigated area which is densely packed with residential buildings normally 1-5 storeys high.

Surrounding areas are characterized by taller buildings compared to the centre but none of them is taller than 35.0 m. The area is dominated by the East-West and North-South street orientations.

The trees are predominantly in a park located in the centre of the city as can be seen in Figure 4.23.

Due to the limited space, vegetation such as trees and shrubs is scarce, and in some narrow streets there is literally no urban greenery.

Wall height, wall aspect and sky view factor parameters have a fundamental role in the urban radiation and energy balance because the radiation field changes due to the shading of the buildings and trees.

2D Map of wall aspect, wall height and sky view factor are reported in figures 4.24, 4.25, and 4.26.

2D spatial distribution of Sky view factor shows that a relevant part of the investigated area is characterized by open and sunlit areas (such as squares, paved areas and bare soil surfaces without trees) with SVF values between 0.80 and 1.

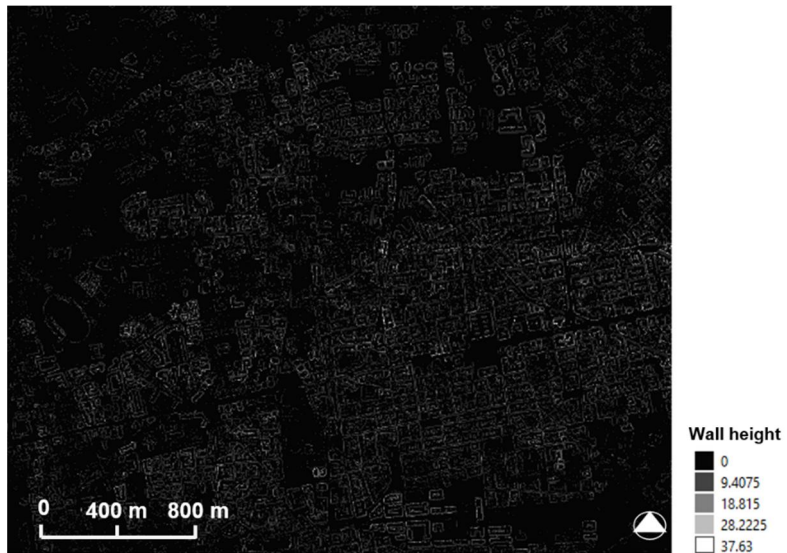


Figure 4.24. 2D Digital map of wall height.

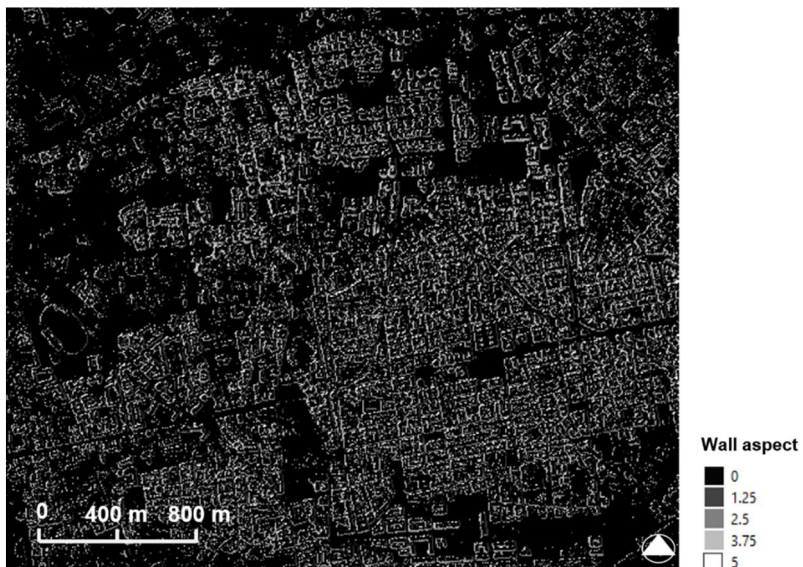


Figure 4.25. 2D Digital map of wall aspect.



Figure 4.26. 2D Digital map of the Sky View Factor (SVF).

#### 4.5.2 Thermo-physical data of the urban macro scale model

Materials of the urban fabric play a very important role in the urban thermal balance as they absorb incident solar radiation and dissipate a percentage of the absorbed heat through convective and radiative processes in the atmosphere, thus increasing the outdoor air temperature (Akbari et al, 2016; Morini et al., 2016; Zinzi, 2015). Radiative properties such as albedo and emissivity affect the surface temperature of the materials and outdoor air temperature in the surrounding environment (Santamouris, 2013). Surface albedo is responsible for the multiple reflections and absorption of shortwave radiation whereas the emissivity determines the intensity of long wave radiation emitted by surfaces (Taha, 1988).

In the SOLWEIG model, a value of surface albedo of 0.20 and an emissivity of 0.90 were adopted for building walls while an albedo of 0.15 and an emissivity of 0.95 were selected for ground surface. All the input data and thermo-physical parameters of SOLWEIG model are summarized in table 4.8.

*Table 4.8. Thermo-physical data and parameter settings for SOLWEIG simulations.*

	<b>Required input</b>	<b>Value</b>
Thermo-physical parameters of urban materials	Façade albedo	0.2
	Ground albedo	0.15
	Emissivity of facades	0.9
	Emissivity of ground	0.95
	Transmissivity of short wave radiation through trees	0.15
	Transmissivity of long wave radiation through trees (Lindberg et al., 2011; Oke, 1987)	0
	Parameters for the calculation of $T_{mrt}$ (people)	Absorption coefficients for short wave radiation
	Absorption coefficients for long wave radiation	0.97
	Posture	Standing

The albedo and emissivity of the urban surfaces in the simulation model were adopted based on several literature studies about albedo and emissivity values of urban surfaces. As examples, Taha et al. (1988) have revealed that urban albedo typically varies in the range from 0.10 to 0.20. Much of the urbanized basin of U.S. and European cities are characterized by an albedo between 0.12 and 0.16 (Taha, 1997).

According to Oke's study, a mean albedo of 0.2 for all urban surface well represents the typical average albedo of an urban area (Oke et al. 1987). The albedo varies from 0.1 to 0.35 for concrete walls, from 0.2 to 0.4 for brick walls, from 0.1 to 0.35 for tiled roofs, and from 0.05 to 0.2 for ground that includes asphalt roads, and paved areas (Oke et al., 1987).

In a recent study, a mean weighted albedo of 0.13 for the city of Modena was used well (Muscio et al., 2011).

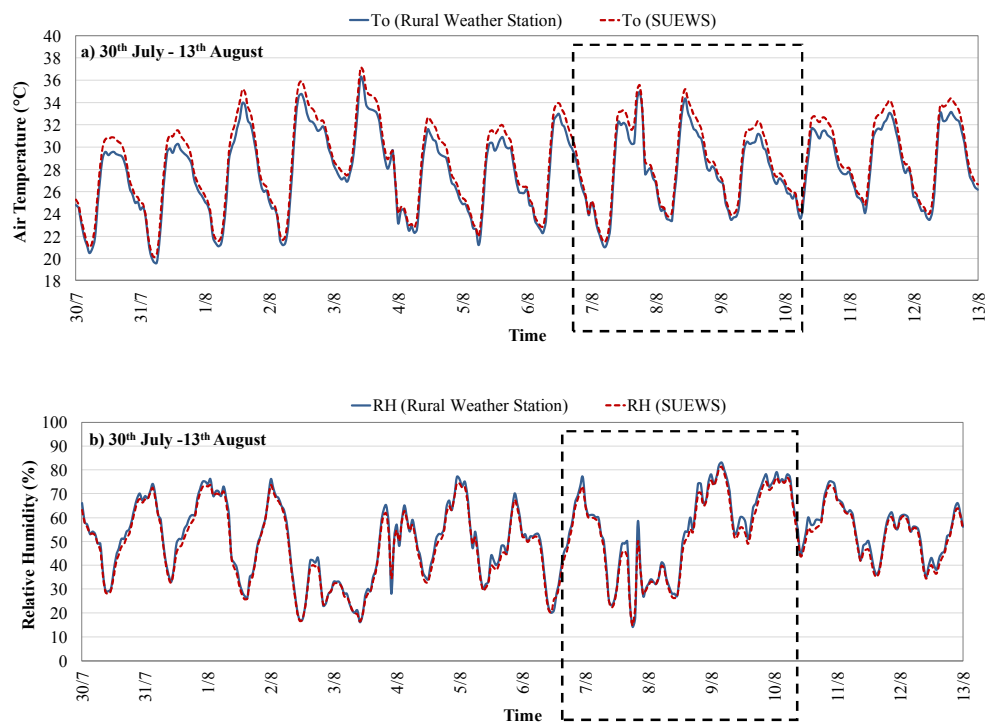
Urban materials are also characterized by high infrared emissivity, thus making them able to emit and dissipate the stored heat towards the sky during the night. Emissivity values of building and ground surfaces adopted in this model were selected according to the emissivity of common building materials (e.g. concrete, bricks, glass) and range between 0.85 and 0.98 depending on the composition of materials and the age. For ground surface such as asphalt and paved area, emissivity values range from 0.93 to 0.95 (Carnielo & Zinzi, 2013).

As regards the street and park trees, such as *Platanus acerifolia* and citrus, the transmissivity values of short wave radiation through trees at around 0.15 were adopted based on the study of Cânton et al. (1994). For tree foliage, a mean and constant value of albedo of 0.15 was set by default in the SOLWEIG model (Lindberg et al., 2011; Konarska et al., 2014).

The mean radiant temperature was calculated considering a standing person with an absorption coefficient for shortwave radiation and an emissivity of the human body of 0.7 and 0.97, respectively (VDI 1994, 1998). An isotropic model for diffuse radiation was used to calculate the mean radiant temperature according to the Perez method (Perez et al., 1986).

#### 4.5.3 Rural weather data morphed through SUEWS for model calibration

Figure 4.27 depicts the hourly profiles of air temperature, relative humidity and wind speed at 10.0 m a.s.l. calculated by SUEWS in comparison with those registered by the reference weather station during a warm week (30<sup>th</sup> July-13<sup>st</sup> August).



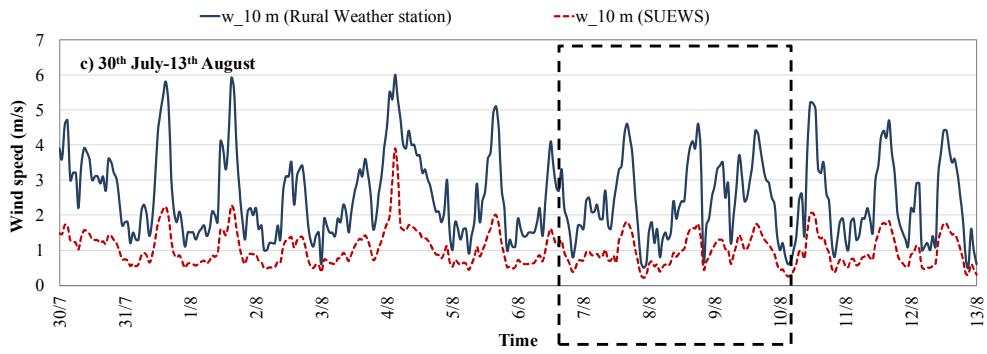


Figure 4.27. Comparison between rural weather data and SUEWS data during (30<sup>th</sup> July-13<sup>st</sup> August): a) Air Temperature; b) Relative Humidity; c) wind speed at 10 m.

Air Temperature ( $T_o$ ) and relative humidity (RH) were calculated at height of 2 m while the wind speed ( $w$ ) was calculated at height of 10 m a.s.l. A zoom of the hourly trend of  $T_o$ , RH and  $w$  during period (7<sup>th</sup> -9<sup>th</sup> August) is shown in Figure 4.28.

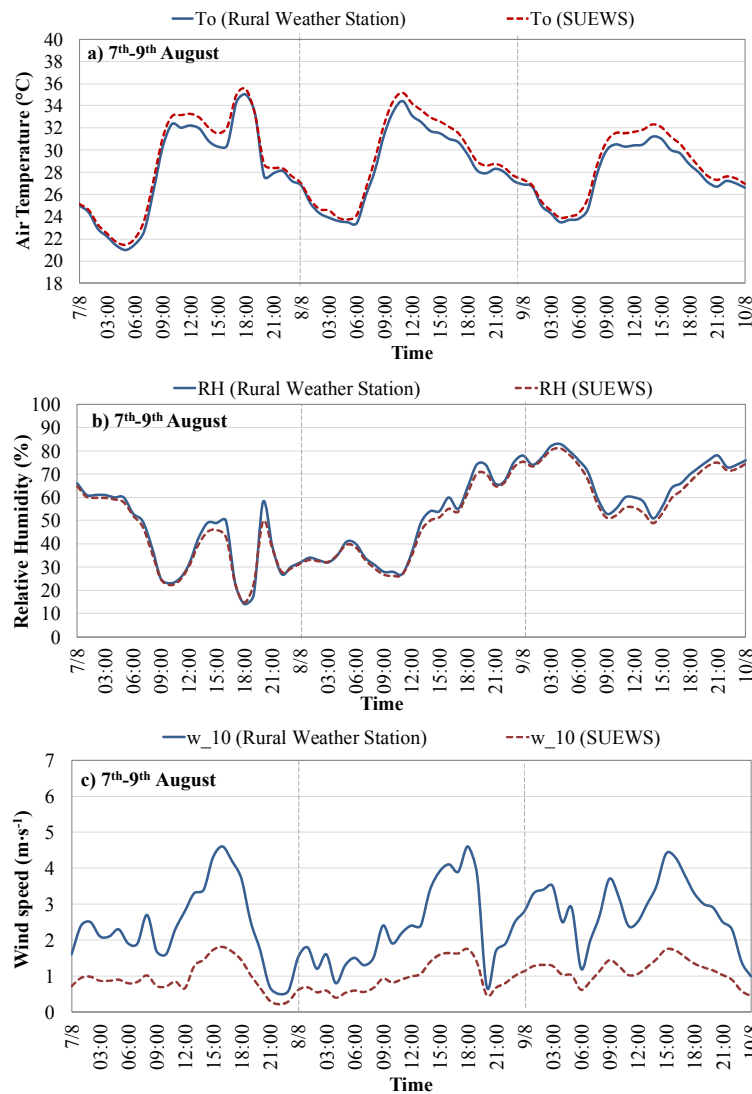


Figure 4.28. Comparison between rural weather data and SUEWS data during (7<sup>th</sup>-9<sup>th</sup> August): a) Air Temperature; b) Relative Humidity; c) wind speed at 10 m a.s.l.

This period (7<sup>th</sup> -9<sup>th</sup> August) was selected because it represents the three hottest consecutive days of the year in Catania.

It is worth noting that the hourly values of outdoor air temperature calculated by SUEWS are around 1 – 2 °C higher in the morning and early afternoon (13.00-15.00) if compared with those recorded by the reference weather station during the period 7<sup>th</sup>-9<sup>th</sup> August (Figure 4.28a). An average increase of about 0 – 1 °C with respect to the air temperature registered by the stationary meteorological station can be observed at nighttime.

As a consequence, a decrease in the relative humidity of about 3-5% in the urban area was achieved with respect to the rural area during the analyzed period (Figure 4.28b).

The increase of air temperature in the urban area is likely to be due to the different surface net-wave radiation budget between the rural and urban environment, the anthropogenic heat and net stored heat flux by building structures and urban surfaces.

The net storage heat flux is typical of densely built-up districts of urban area and is very low or absent in rural areas. In urban areas, surfaces and building materials absorb and store more solar radiation than vegetation or bare soil surfaces. As a result, the outdoor surface temperature in the urban areas is higher than that of the surrounding rural areas (so-called **Surface Urban Heat Island effect**, SUHI). In the evening and at nighttime, the energy budget is determined by the long wave radiation among surfaces and the sky, so the urban area releases – by means of infrared radiation and also convection with the air – a remarkable heat flux towards the surroundings.

In addition, the low surface fraction of vegetation contributes to increase the outdoor surface temperature. Indeed, during the day, the potential fraction of radiant heat flux that can be reduced through shading and evapotranspiration by vegetation is lower than the rural area. As a consequence, the air temperature was found to have increased.

The urban microclimate is also affected by a remarkable reduction of wind speed at height of 10 m a.g.l. as shown in Figure 4.28c. The roughness elements of the urban settlements have attenuated the wind speed down to a maximum value of 2.0 m·s<sup>-1</sup>. As a result, a decrease of heat exchanged by convection between urban material surfaces and the air was found.

The cumulative frequency distribution was also calculated for the hourly values of air temperature, relative humidity and wind speed during the summer season (1<sup>th</sup> June – 30<sup>th</sup> September).

Figure 4.29 reports the cumulative frequency distribution of T<sub>o</sub> and RH at height of 2 m a.g.l. and wind speed at height of 10 m a.g.l respectively.



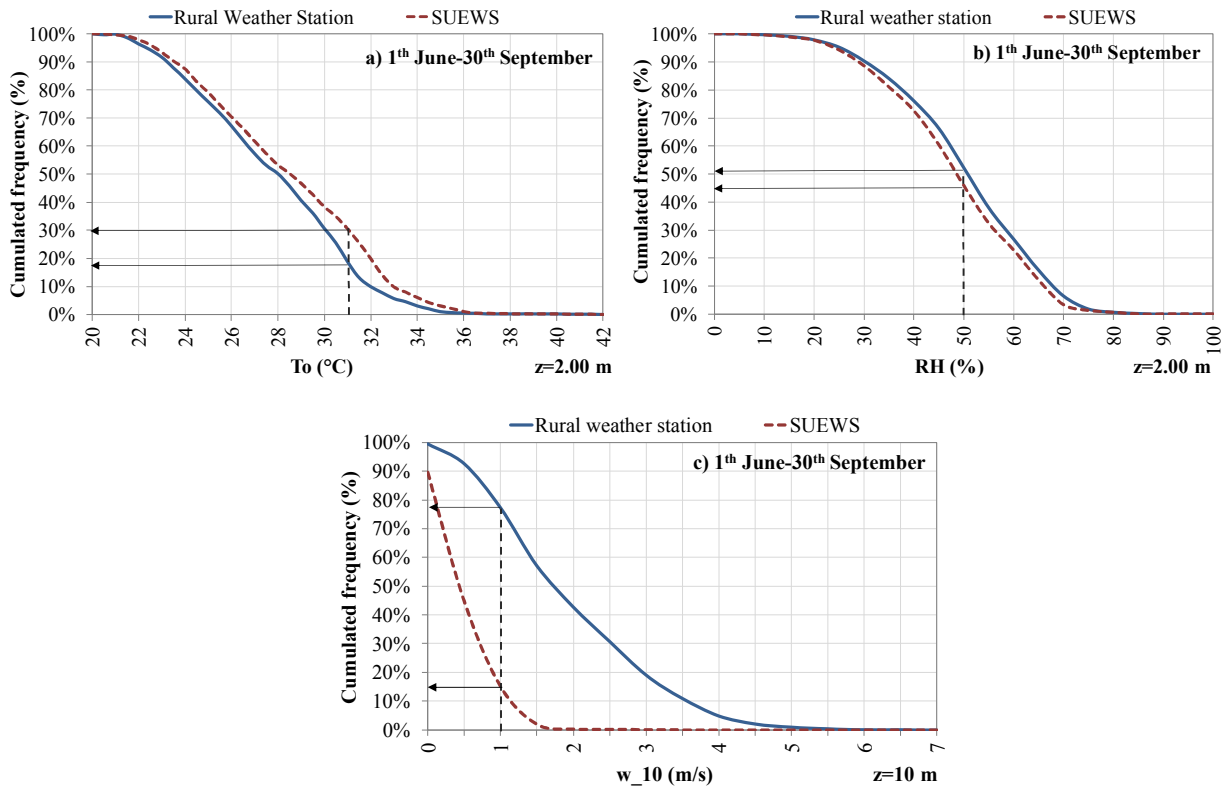


Figure 4.29. Cumulative frequency distribution of outdoor air temperature (a), relative humidity (b), and wind speed at 10 m a.g.l. during period (1<sup>st</sup> June – 30<sup>th</sup> September).

The outdoor air temperature calculated by SUEWS was found to always be higher compared to the air temperature recorded by the rural weather station during the period (1<sup>st</sup> June – 30<sup>th</sup> September). It is worth emphasizing that the air temperature  $T_o$  calculated by SUEWS exceeded the values of 31 °C for 30% of the time. Therefore, the latter scenario was worse with respect to the rural weather data which exceeded 31 °C for about 20% of the time (Figure 4.29a).

As shown in Figure 4.29b, relative humidity calculated by SUEWS was always lower than that recorded by the rural weather station.

The wind speed calculated by SUEWS never exceeded 1.5 m·s<sup>-1</sup> and, thus, it was significantly lower than the wind speed registered by the rural weather station during the entire analyzed period (see Figure 4.29c).

#### 4.5.4 Validation of the SOLWEIG model with field measurements

The profiles of mean radiant temperature calculated by SOLWEIG under scenario S\_1 (forcing with rural weather data) and scenario S\_2 (forcing with SUEWS weather data) were compared against those of the on-site experimental measurement campaign.

The comparison was carried out in two receptors, named R1 and R2, located in area 1 and area 2 which were identified as risk areas as described in section 4.4.2.

Two receptors (R1, R2) at pedestrian level ( $z=1.10$  m) were selected for their placement with respect also to the locations sensitive to heat wave phenomena, geometric features (i.e., sky view factor (SVF), Aspect ratio) and orientation.

R1 is located in the paved internal courtyard of a school in a highly compact densely built up area characterized by lack of trees with a sky view factor (SVF) of 0.20 and an aspect ratio of 2.

R2 is located on the pedestrian pavement in the university campus in an open low-rise buildings area with few trees, characterized by a sky view factor (SVF) of 0.8 and a low aspect ratio value. The receptor R2 corresponds to the measurement point P2.

Figure 4.30 shows the location of the receptors R1 and R2 in the investigated area (a) and in the areas 1 and 2 (b-c). In figure 4.30a are also shown the two receptors R1 and R2 corresponding to points where the portable weather stations were placed to measure the mean radiant temperature values.

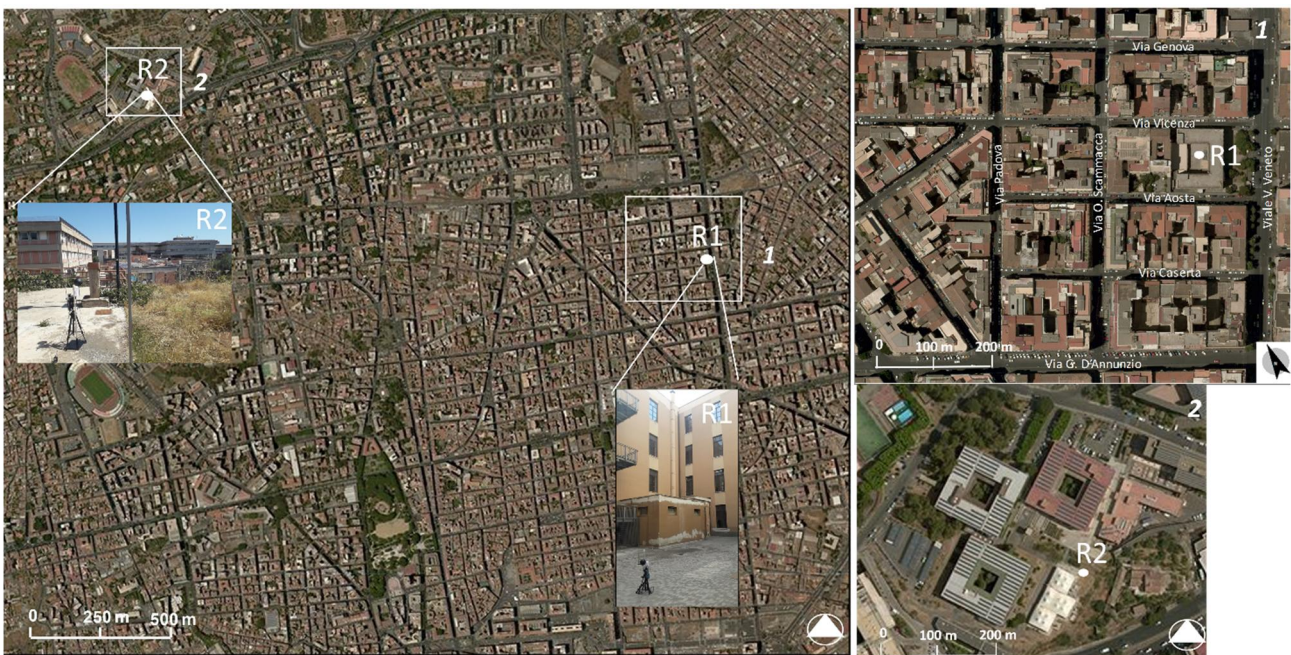


Figure 4.30. Localization of the receptors R1 and R2 in the investigated area (a) and into the area 1 (b) and area 2 (c). R1 and R2 views of the locations of receptors R1 and R2 where the microclimate portable stations were placed to measure mean radiant temperature values.

The characteristics of the two receptors R1 and R2 are summarized in Table 4.9.

Table 4.9. Location and investigated periods selected for measurements survey.

No	Points	Measurements time	Location	Height a.g.l. (m)	SVF (-)
1	R1	12:00 a.m. on August 7- 10:00 a.m. August 8	School Courtyard of a School	1.10	0.25
2	R2	08:00 a.m. on July 30 - 09:00 a.m. July 31	Pedestrian pavements University Campus	1.10	0.80

Figure 4.31 shows the comparison between the actual mean radiant temperature measurement at R1 and R2 receptors and the corresponding simulated profiles during period (from 12.00 a.m. on 7<sup>th</sup> August to 10.00 a.m. on 8<sup>th</sup> August) and (from 8.00 a.m. on 30<sup>th</sup> July to 9.00 a.m. on 31<sup>st</sup> July).

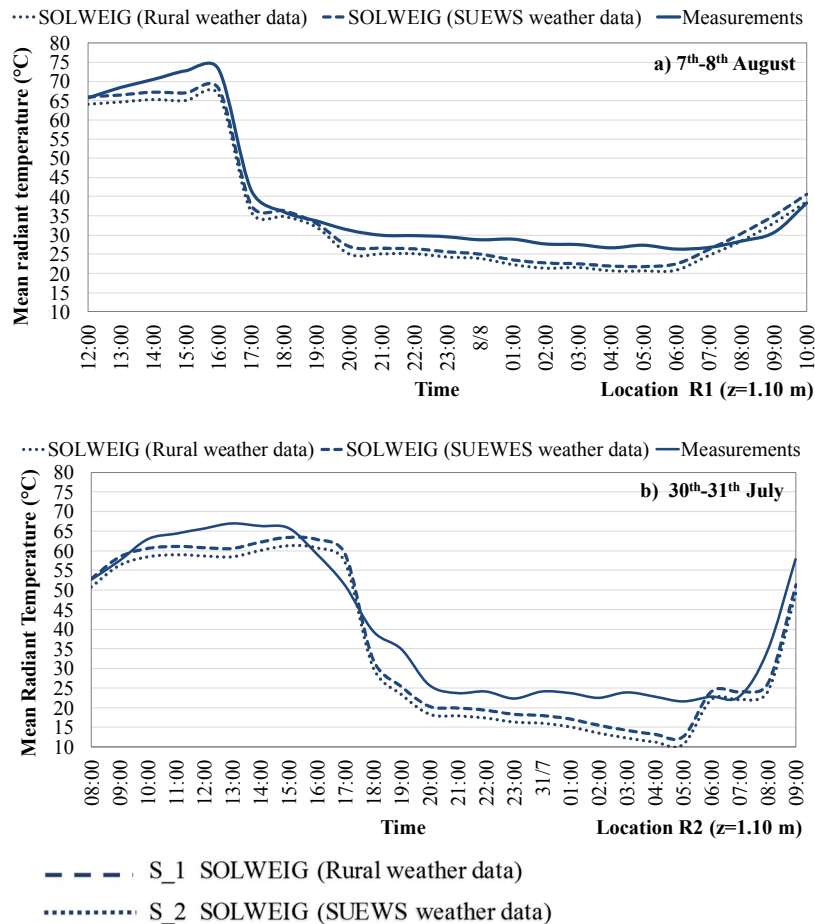


Figure 4.31. Comparison between simulated and measured mean radiant temperature at receptors R1 (a) and R2 (b).

The comparison reveals a good agreement between measured data (solid blue lines) and simulated data from scenarios S\_1 (dashed blue lines) and S\_2 (dotted blue line) throughout the days considered. Both predicted scenarios have very similar trends from early morning until late evening. Nevertheless, simulated scenarios are below the actual measured profile predominantly during the night period. A difference in the mean radiant temperature around 4 – 5°C between the simulated and measured data was found from 8.00 p.m. to 6.00 a.m. in the receptor R1 (Figure 4.31a). In the receptor R2, a discrepancy higher than that of the receptor R1 was found at nighttime (Figure 4.31b). Despite both scenarios predicting rather similar results, it can be observed that  $T_{mrt}$  simulated profile of Scenario S\_2 is always higher with respect to that of Scenario S\_1. This difference is at around 2.0°C during the selected period. As a consequence,  $T_{mrt}$  simulated profile achieved by SOLWEIG forcing with SUEWS weather data has better approximation with the measured values if compared with the profile of Scenario S\_1 (SOLWEIG forcing with rural weather data).

To numerically evaluate the deviation between the modelling outputs and the actual measured data, statistical indices were calculated and reported in Table 4.10 for Receptors R1 and R2.

Table 4.10. Validation indices of the SOLWEIG model for both scenarios S\_1 and S\_2 in the receptors R1 and R2.

Variable	Indices	R1 (7 <sup>th</sup> – 8 <sup>th</sup> August)		R2 (30 <sup>th</sup> – 31 <sup>th</sup> July)		
		S_1	S_2	S_1	S_2	
$T_{mrt}$	%error	-	13%	10%	19%	14%
	MAE	°C	4.38	3.37	6.95	5.19
	RMSE	°C	4.90	3.77	7.02	6.44
	d	-	0.97	0.98	0.97	0.98
	r	-	0.97	0.99	0.98	0.98
	$R^2$	-	0.97	0.97	0.97	0.97

Table 4.10 shows that Scenario S\_2 has a percentage of errors, values of MAE and RMSE lower than those attained in the Scenario S\_1 in all two receptors. As an example, Scenario S\_2 shows values of MAE = 3.37°C and RMSE = 3.77°C while Scenario S\_1 has MAE = 4.38°C and RMSE = 4.90°C respectively in the receptor R1. This confirms that the Scenario S\_2 better reflects experimental measurements than Scenario S\_1 does. A graphical representation of the results obtained by both simulation scenarios is given also in Figure 4.32, where regression lines are plotted for mean radiant temperature data along with the attained coefficient of determination  $R^2$ .

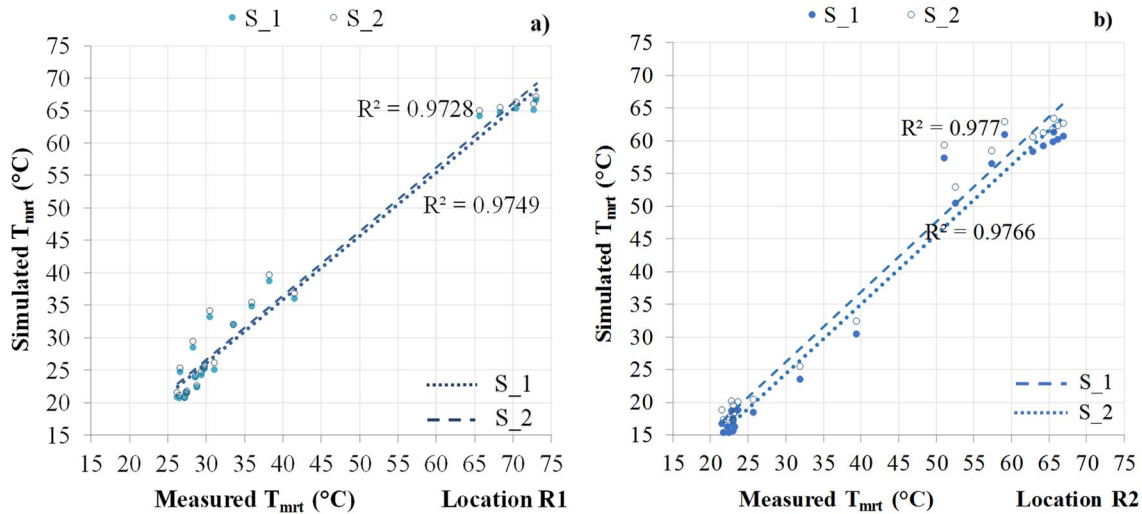


Figure 4.32. Linear regression of mean radiant temperature (measured vs predicted) at R1 (a) and R2 (b) receptors.

As shown in Figures 4.32a and b, both simulated scenarios S\_1 and S\_2 have almost the same Pearson coefficient and a high correlation with the observed data ( $R^2 = 0.97$ ) in the receptors R1 and R2. Since under the scenario S\_2, the lowest MAE and RMSE values were attained, the simulations of the SOLWEIG model calibrated with rural weather data morphed by SUEWS were accounted.

Therefore, all the results relating to the 2D spatial distribution and hourly trend of mean radiant temperature and outdoor thermal comfort indices presented in this research are referred to the Scenario S\_2.

#### 4.5.5 Assessment of the urban energy balance

The energy balance of the investigated urban area was calculated yearly using the SUEWS Simple plug-in.

The incoming and outgoing radiation fluxes energy balance and the surface energy balance of the outgoing and incoming thermal fluxes with respect to the investigated model were analyzed in a warm summer week. The results relating to the period (7<sup>th</sup>-9<sup>th</sup> August) are shown in Figures 4.33 and 4.34 respectively.

Figure 4.33 shows the incoming and outgoing shortwave and long wave radiation exchanged with respect to the Urban Canopy Layer.

The radiative heat balance shows high values of the incoming shortwave radiation ( $K_{\downarrow}$ ) during maximum sunshine hours (900  $W \cdot m^{-2}$  at 12.00) and low values of outgoing shortwave radiation ( $K_{\uparrow}$ ).

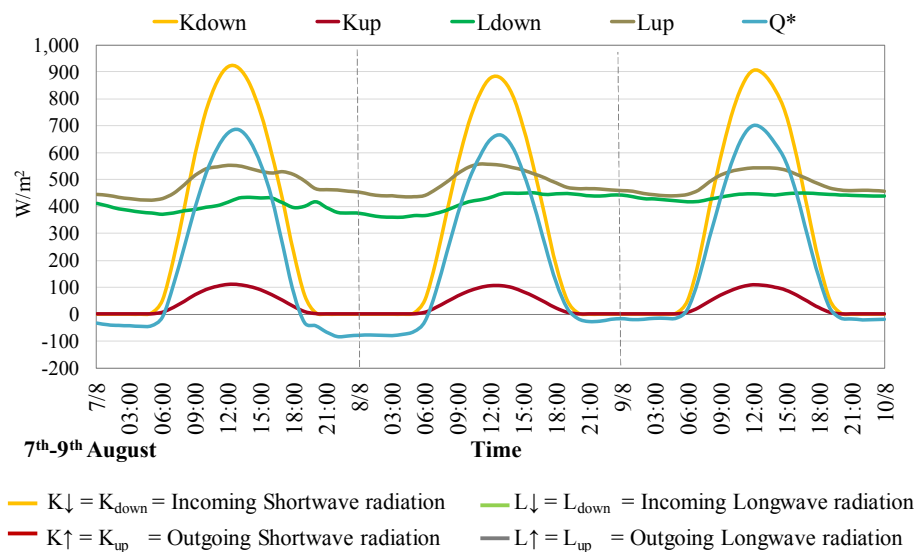


Figure 4.33. Incoming and outgoing radiation fluxes balance during period (7<sup>th</sup>-9<sup>th</sup> August).

The net shortwave flux is significantly influenced by high values of incoming radiation and low values of albedo of buildings and impervious surfaces.

The outgoing long wave radiation ( $L_{\uparrow}$ ) is the predominant term of the long wave radiation. This depends on the radiative properties of the building materials and urban surfaces. The materials that are characterized by low values of albedo and emissivity experience the increase of their outer surface temperature. As a consequence, high-magnitude heat fluxes are re-emitted by the outer surface of

building structures and paved areas. Therefore, the net long wave flux is negative due to high values of long wave radiation ( $L_{\uparrow}$ ) both daily and during night hours.

Figure 4.34 shows the trend of incoming and outgoing of heat fluxes on the urban heat surface balance.

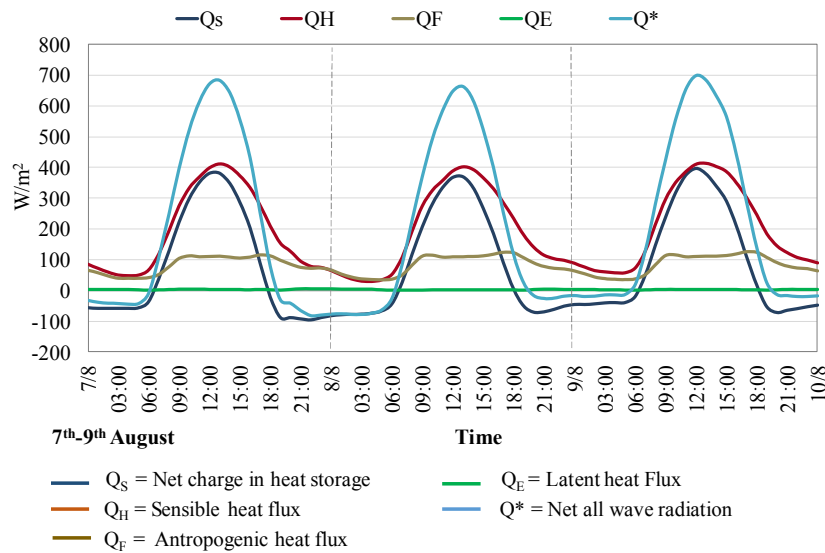


Figure 4.34. Heat flux surface balance during the investigated period (7<sup>th</sup>-9<sup>th</sup> August).

The energy balance shown in Figure 4.34 is typical of urban areas with high impervious surface fractions and very low surface fraction occupied by vegetation. The lack of trees and grass surface is relevant, and the contribution of latent heat flux ( $Q_E$ ) is very low and therefore it can be neglected. Since the evapotranspiration effect is fundamental to reduce the net all wave radiation ( $Q^*$ ), the sensible heat flux ( $Q_H$ ) is predominant because it is the only term that can dissipate by convection the radiant heat flux ( $Q^*$ ) and the anthropogenic heat ( $Q_F$ ).

It is worth highlighting that the peak of sensible heat flux ( $Q_H$ ) keeps relatively high in the evenings and is relevant even at nighttime. This phenomenon is due to the net heat flux stored in building structures that is released as sensible heat flux during the night from walls, roofs, roads and surfaces exposed to the solar radiation during daily hours.

As a result, the sensible heat flux is relevant and an increase in the air temperature may be achieved in the district urban area.

#### 4.5.6 2D spatial distribution of Mean Radiant Temperature in the investigated area.

2D spatial distribution of  $T_{mrt}$  in the investigated area is shown in three representative hours of a sunny summer day. The 2D distribution of  $T_{mrt}$  values is related to the simulation scenario S\_2.

Figure 4.35 depicts the 2D maps of  $T_{mrt}$  at 11.00 (a), 14.00 (b) and 17.00 (c) on 7<sup>th</sup> August respectively.

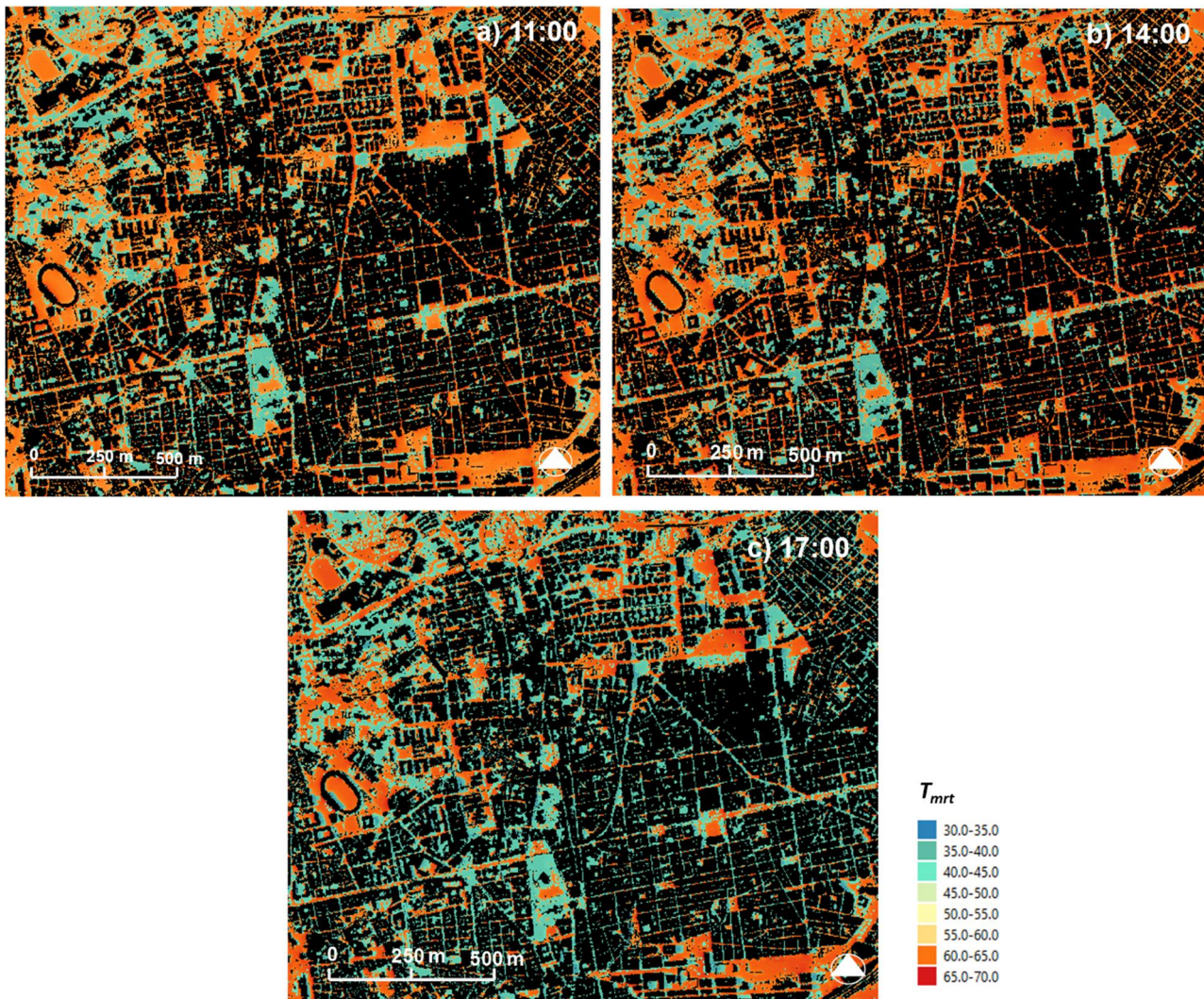


Figure 4.35. 2D Map of  $T_{mrt}$  of the investigated area at 11:00 (a), at 14:00 (b) and 17:00 (c) on 7<sup>th</sup> August.

The open areas have predominantly  $T_{mrt}$  values at around 50 – 60°C at all investigated hours. In a more extreme condition (at 14.00), the same areas show  $T_{mrt}$  values between 60°C and 65°C.

High  $T_{mrt}$  values occur in sunlit areas, in particular where the Sky View Factor (SVF) values are above 0.60. In narrow streets, where SVF values lie between 0.20 and 0.30, the areas shaded by buildings show  $T_{mrt}$  values at around 35.0 °C - 40.0°C. It is worth noting that areas covered by trees have  $T_{mrt}$  values between 30.0°C and 40.0°C.

A cumulated frequency distribution of the  $T_{mrt}$  values occurring over the entire area at a selected point in time (11.00, 14.00 and 17.00) respectively is accounted for. Here, the threshold values of  $T_{mrt}$  over which heat-related mortality risks increase by 5% and 10% respectively in people aged over 80 were adopted according to classes introduced by Thorson et al. 2014.

Figure 4.36 shows the cumulated frequency distribution of the  $T_{mrt}$  in the investigated area at 11.00, 14.00 and 17.00 on 7<sup>th</sup> August respectively.

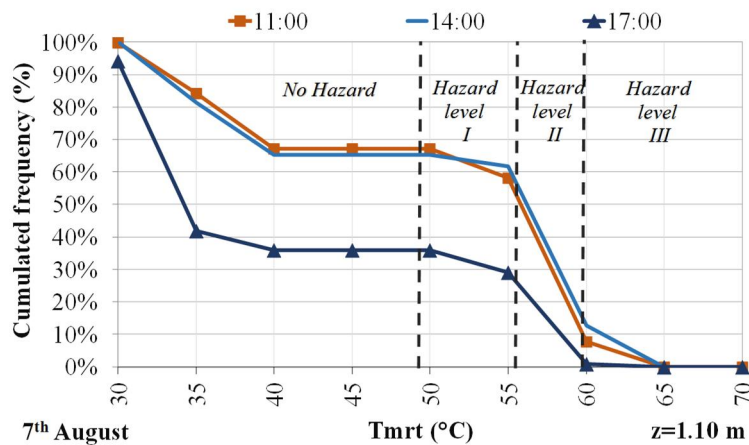


Figure 4.36. Cumulated frequency distribution of the  $T_{mrt}$  values over the investigated area at 11.00, 14.00, and 17.00 on 7<sup>th</sup> August.

As shown in Figure 4.36,  $T_{mrt}$  values higher than  $55.5^{\circ}\text{C}$  – i.e. the threshold over which heat-related mortality risk increase by 5% in people aged over 80 – occurred in about 53% of the entire area at 11.00.

At 14.00 on the same day (Figure 4.36),  $T_{mrt}$  was within the hazard level II in about 58% of investigated area. At the same time,  $T_{mrt}$  values of  $59.4^{\circ}\text{C}$  - i.e. threshold value over which heat-related mortality risk increases by 10% (Hazard Level III) - were reached for 17% of the entire area. However, in a less extreme situation (Figure 4.36) – e.g. at 17:00 on the same day – spatial distribution of  $T_{mrt}$  exceeded  $55.5^{\circ}\text{C}$  for 30% of the whole investigated area.  $T_{mrt}$  values were below  $60^{\circ}\text{C}$  in every point of the area, and thus suggested the major role played by direct sunlight.

It is worth highlighting that such results depend on the meteorological conditions of the investigated day. Therefore, the fractions of the investigated domain within the Hazard levels I, II and III respectively could change in relation to solar radiation, air temperature and relative humidity of the analyzed period.

#### 4.5.7 Relationship between Universal Thermal Climate Index (UTCI) and Mean Radiant Temperature

In order to recognize the behaviour of the Universal Thermal Climate Index (UTCI) in relation to the variation of mean radiant temperature, a sensitive analysis of UTCI with mean radiant temperature and air temperature variations is described.

With this aim, the Universal Thermal Climate Index (UTCI) values were computed for specific air temperature values. The computation was done at intervals from  $20^{\circ}\text{C}$  to  $35^{\circ}\text{C}$  according to the common range of air temperatures recorded during summer periods in a warm and temperate climate. Two meteorological parameters were considered constant and one third was variable. The constant values of the relative humidity ( $\text{RH} = 50\%$ ) and the wind speed ( $w = 0.5 \text{ m}\cdot\text{s}^{-1}$ ) were used in this



study. The difference between mean radiant temperature and air temperature ( $T_{mrt}-T_a$ ) was variable from  $-5^{\circ}\text{C}$  to  $40^{\circ}\text{C}$ . Such interval corresponds to a variation of mean radiant temperature from  $15^{\circ}\text{C}$  to  $60^{\circ}\text{C}$ .

Figure 4.37 shows the dependency of the UTCI on the difference between mean radiant temperature and air temperature ( $T_{mrt}-T_a$ ) for  $\text{RH}=50\%$  and  $w = 0.5 \text{ m}\cdot\text{s}^{-1}$ .

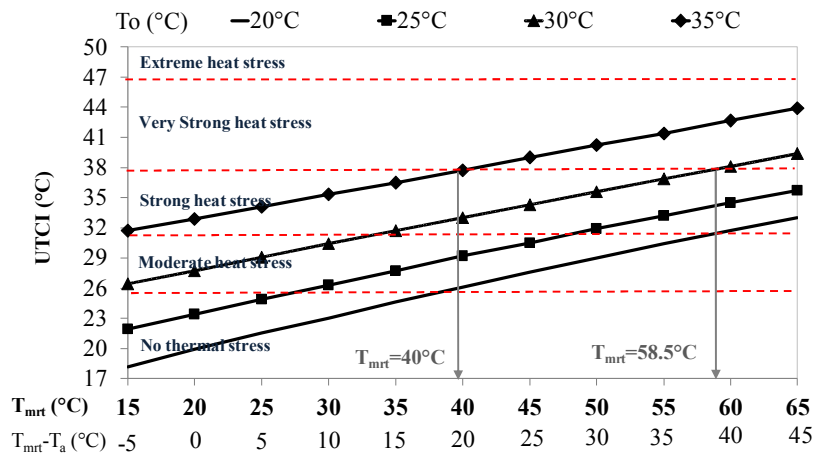


Figure 4.37. The dependency of UTCI on the difference between mean radiant temperature and air temperature  $T_{mrt}-T_a$  (for  $\text{RH}=50\%$ , and  $w=0.5 \text{ m}\cdot\text{s}^{-1}$ ).

Figure 4.37 shows that UTCI depends on the mean radiant temperature ( $T_{mrt}$ ) linearity.

UTCI values significantly increase with the increase in positive difference ( $T_{mrt}-T_a$ ). The difference between air temperature and UTCI is very low for a ‘light radiant situation’ ( $T_{mrt}\sim T_a$ ) whereas the UTCI values are about  $10^{\circ}\text{C}$  higher than air temperature for a full radiant situation (typically clear sky in the early afternoon).

It can be noted that “Very strong heat stress” class can be attained for air temperature of  $30^{\circ}\text{C}$  and mean radiant temperature of  $58.5^{\circ}\text{C}$ . “Very Strong heat stress” conditions can also be attained for  $T_{mrt}$  values of around  $40.0^{\circ}\text{C}$  when the air temperature is  $35.0^{\circ}\text{C}$ .

In order to understand what heat-related risk level for human health could be attained on the basis of UTCI values calculated by SOLWEIG simulations, the hourly profiles of  $T_{mrt}$  and UTCI at specific points at pedestrian level were plotted for the warmest days.

Figure 4.38 depicts the hourly profiles of  $T_{mrt}$  and UTCI overlaid on a double axis graph. The reference values of UTCI reported on the graduate y-axis were calculated with constant values of  $\text{RH}$  and  $w$  ( $\text{RH}=50\%$  and  $w = 0.5 \text{ m}\cdot\text{s}^{-1}$ ) on the basis of  $T_{mrt}$  values variable in the range ( $15^{\circ}\text{C}$ - $65^{\circ}\text{C}$ ) as above described. The heat stress categories were overlaid on the graph according to Standard classification of UTCI represented as band of false colours.  $T_{mrt}$  threshold values of the heat-related mortality risk according to the scheme shown in methodology were also reported in Figures.

The profiles of  $T_{mrt}$  and UTCI achieved by means of SOLWEIG simulations are related to points P1, P2, and P3 located in areas 1 and 2 (see Figure 4.21-section 4.4.2) at pedestrian level ( $z = 1.10$  m a.g.l.) during period (7<sup>th</sup> - 9<sup>th</sup> August).

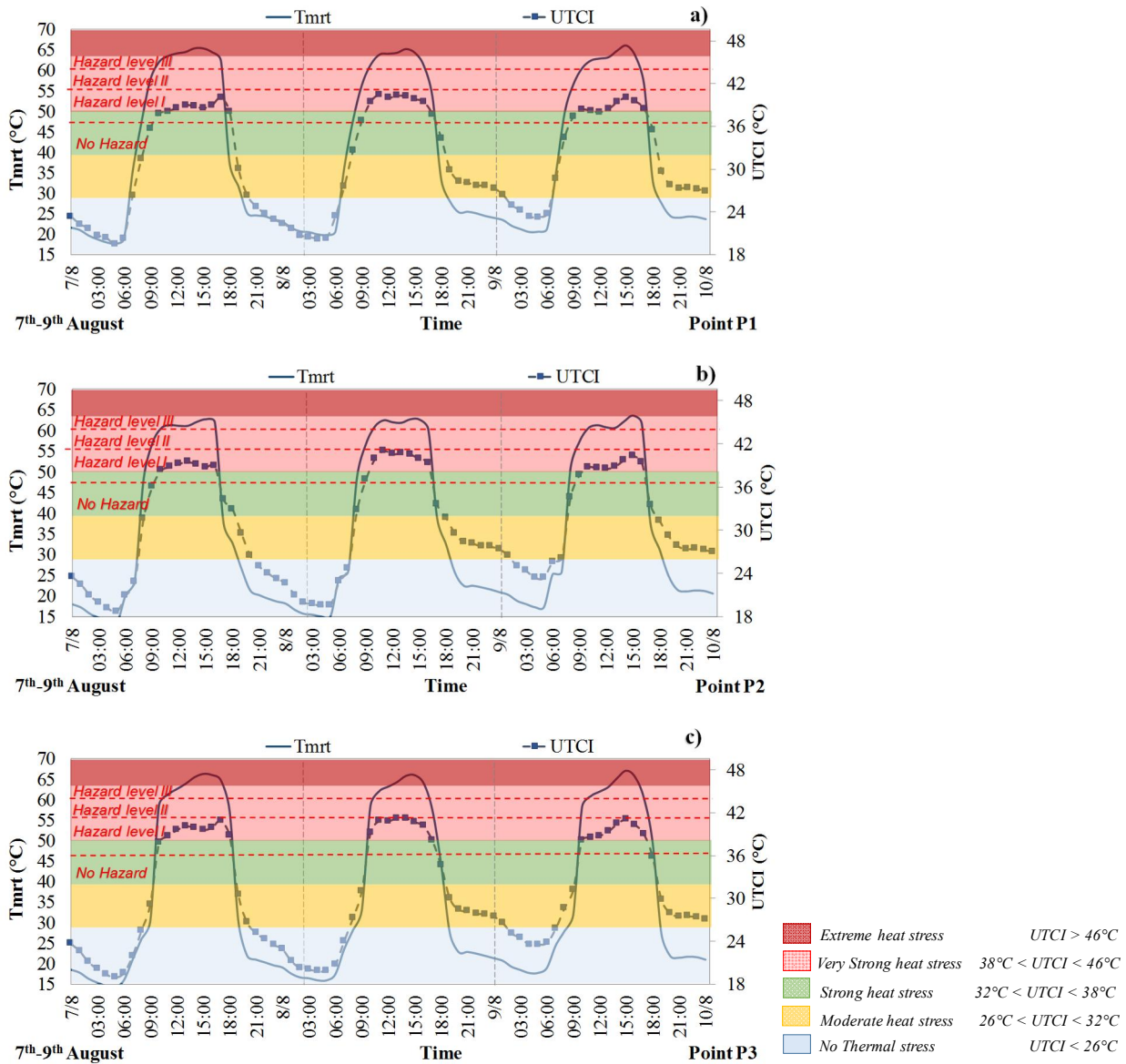


Figure 4.38. Hourly profiles of  $T_{mrt}$  and UTCI at pedestrian level during period (7<sup>th</sup>-9<sup>th</sup> August), Hazard threshold levels of  $T_{mrt}$  and Heat stress categories related to UTCI classification: a) Point P1, b) Point P2, and c) Point P3.

For UTCI values between 36.0°C and 38.0°C, “Strong heat stress”, the corresponding  $T_{mrt}$  values are within Hazard level II ( $T_{mrt}$  values between 55.5°C and 59.4°C).

It is worth highlighting that under conditions of “Very strong heat stress”, UTCI values between 38°C and 42°C, it was found that the hourly profile of  $T_{mrt}$  is predominantly within Hazard Level III characterized by  $T_{mrt}$  values higher 59.4°C over which the heat-related mortality risk for people age band 80+ is increased by 10%.

#### 4.5.8 Assessment of the potential effectiveness of heat stress mitigation scenario

##### 4.5.8.1 Morphological properties and modelling of the investigated area in design scenario

Based on the criteria explained in section 3.7, an urban heat stress mitigation scenario was proposed. As described in sections 3.7.1 and 3.7.2, a design scenario was planned based on the planting of trees in compact and densely high built-up areas and in open low-rise areas respectively.

A new scenario was modelled in UMEP by means of the implementation of trees into the raster grid of the Building and Ground DSM of the current state. Therefore, a new Canopy Digital Surface Model (CDSM) was created through the “tree generator tool” of UMEP.

The proposed tree types in sections 3.7.1 and 3.7.2 were implemented as Vector “Point” files in the UMEP model. Each tree is represented by a point and the geometrical and morphological features of trees were inserted in an associated attribute table. Tree species (Deciduous or Conifer), Trunk zone height in m, Total tree height in m and Canopy diameter in m are included in the attribute table.

Trunk Digital Surface Model (TDSM), Canopy Digital Surface Model (CDSM) of existing trees and all geometry parameters (ttype, trunk height, total height, Diameter of crown) were used in the “tree generator tool” of UMEP to generate a new Canopy Digital surface model (CDSM).

In order to show the morphological changes due to the urban greenery, the new Canopy Digital Surface Model (CDSM) was put beside the existing CDSM.

Figure 4.39 shows the 2D map of Canopy Digital Surface Model (CDSM) in the Current scenario (a) and in Design scenario (b) respectively.

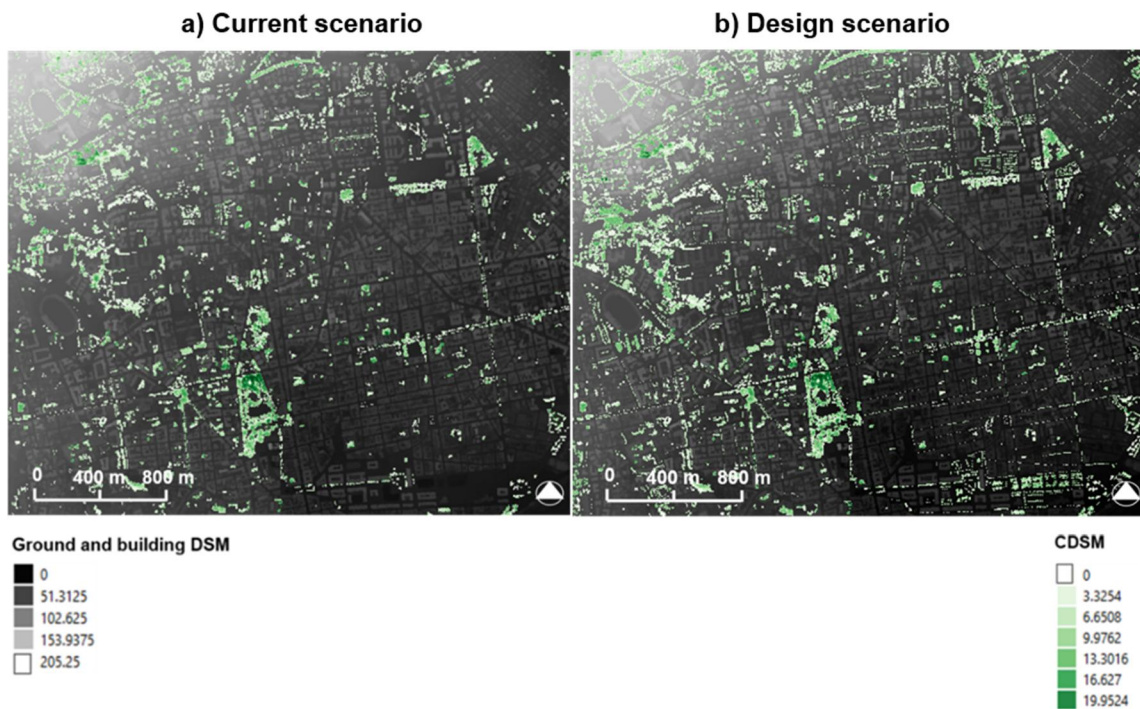


Figure 4.39. Canopy Digital Surface Model (CDSM) on the Building and ground DSM: (a) Current scenario; (b) Design Scenario.

At Current scenario, the surface occupied by trees is 9.66% of the investigated area.

In Design scenario, the planting of trees has increased by +6.34% the surface covered by trees with respect to the current state. Therefore, after the integration of vegetation in urban spaces the surface covered by the trees is 16% of the investigated area.

The introduction of trees reduced the surfaces of bare soil and impervious area which now are 1% and 43.4% respectively of the investigated area. As a result, an increase of 3.79% in the Pervious surface (PSF) was achieved.

Figure 4.40 reports the percentage of the soil using fractions of the investigated area in the Current scenario (a) and Design scenario (b) respectively.

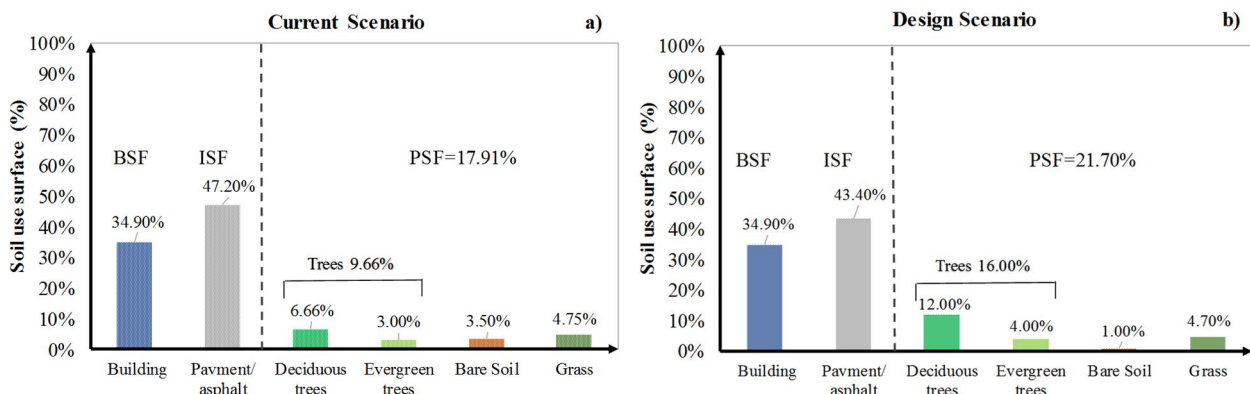


Figure 4.40. Land use fraction of the investigated area: a) Current scenario; b) Design scenario.

Figure 4.41 shows the 2D map of Sky view factor (SVF) in the Current scenario (a) and in Design scenario (b) respectively.

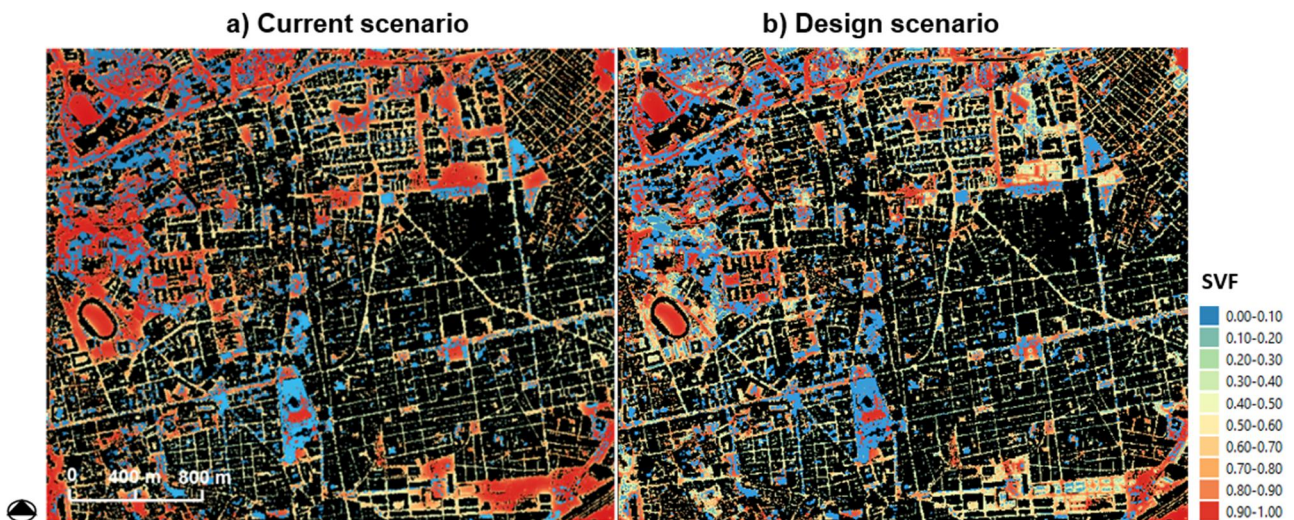


Figure 4.41. 2D digital map of Sky view factor: a) Current scenario; b) Design scenario.

As shown in Figure 4.41b, the addition of the trees according to the design approach described in section 3.7 leads to an increase of the shaded areas which have Sky View Factor (SVF) values between 0 and 0.10.

#### 4.5.8.2 Assessment of the effects of design scenario on outdoor thermal comfort

In order to describe the spatial variations and potential reductions of  $T_{mrt}$  in a mitigation heat stress scenario, Figure 4.42 shows 2D map of  $T_{mrt}$  spatial distribution on the entire area on 7<sup>th</sup> of August at 14:00 in a false color scale in Current and Design scenarios respectively.

2D distribution of  $T_{mrt}$  values in Current and Design Scenarios were calculated using the weather data morphed by SUEWS as meteorological input. Namely  $T_{mrt}$  were computed using the SOLWEIG model calibrated with weather data morphed by SUEWS (Scenario S\_2).

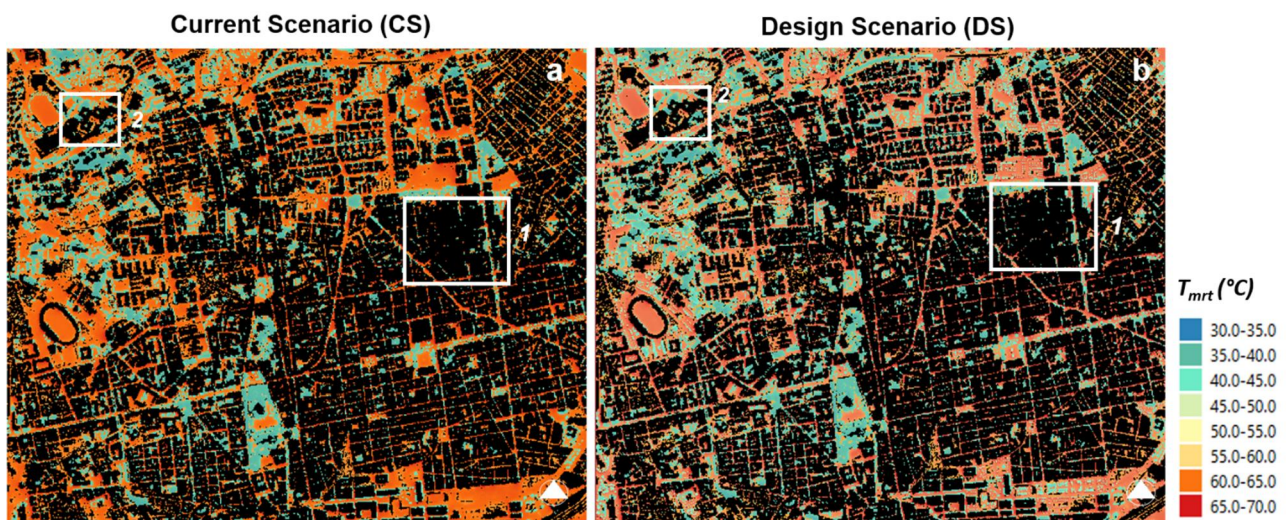


Figure 4.42. 2D map of spatial distribution of mean radiant temperature at 14.00 on 7<sup>th</sup> August. a) Current Scenario (CS); b) Design Scenario (DS).

As can be seen in Figure 4.42, the proposed Design scenario (DS) shows relevant mean radiant temperature reductions in open areas and along the roads where the trees were integrated compared to the Current Scenario (CS). In these areas,  $T_{mrt}$  value is reduced down to 20°C where the soil or pavement surface is covered by trees. These reductions occur in the areas characterized by SVF values between 0 and 0.10. The surrounding areas near the trees are characterized by a meaningful decrease of  $T_{mrt}$  values because they are affected by evapotranspiration of the vegetation.

Although the highest  $T_{mrt}$  reductions occur near the trees, the entire investigated area has slightly lower  $T_{mrt}$  values with respect to the Current Scenario (CS). This result reveals that even areas far from away vegetation are affected by evapotranspiration effects.

A frequency cumulative distribution of the  $T_{mrt}$  values occurring over the entire area at a selected point in time (14.00) in Current and Design scenarios respectively was reported in Figure 4.43.

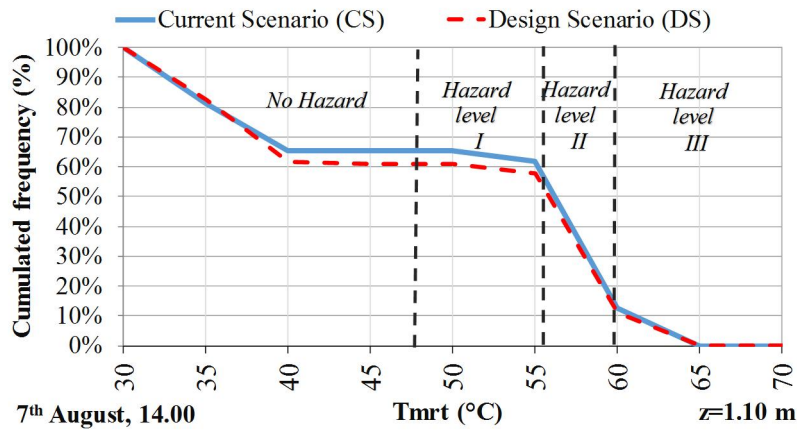


Figure 4.43. Spatial frequency cumulative distribution of the  $T_{mrt}$  values over the entire area at 14.00 on 7<sup>th</sup> August.

Figure 4.43 shows that the Current Scenario (CS) has  $T_{mrt}$  values higher than 55.5°C - i.e. the threshold over which heat-related mortality risks increase by 5% in people aged over 80 - in about 55% of the entire area whereas the corresponding curve for Design Scenario (DS) exceeds the same threshold value for 51% of the investigated area.

As a consequence, the proposed strategy has reduced by 4% the fraction of investigated domain that exceeds the  $T_{mrt}$  threshold of 55.5°C. This result reveals that a forestation intervention based on a milder approach does not allow the achievement of more impacting results on the whole area.

In light of this, a more advanced heat stress mitigation scenario based on radical transformations of the existing urban tissue should be planned to achieve meaningful results.

In order to investigate the potential effects of the vegetation on the local scale, the results attained in Area 1 and Area 2 are shown.

Figure 4.44 shows the 2D spatial distribution of mean radiant temperature at 14.00 on 7<sup>th</sup> August for the selected areas 1 and 2, along with the identification of every POIs (Point of interest) within them. Figures (a-b) depict the Current and Design scenarios respectively for Area 1 while Figures (c-d) show Current and Design scenarios for Area 2.

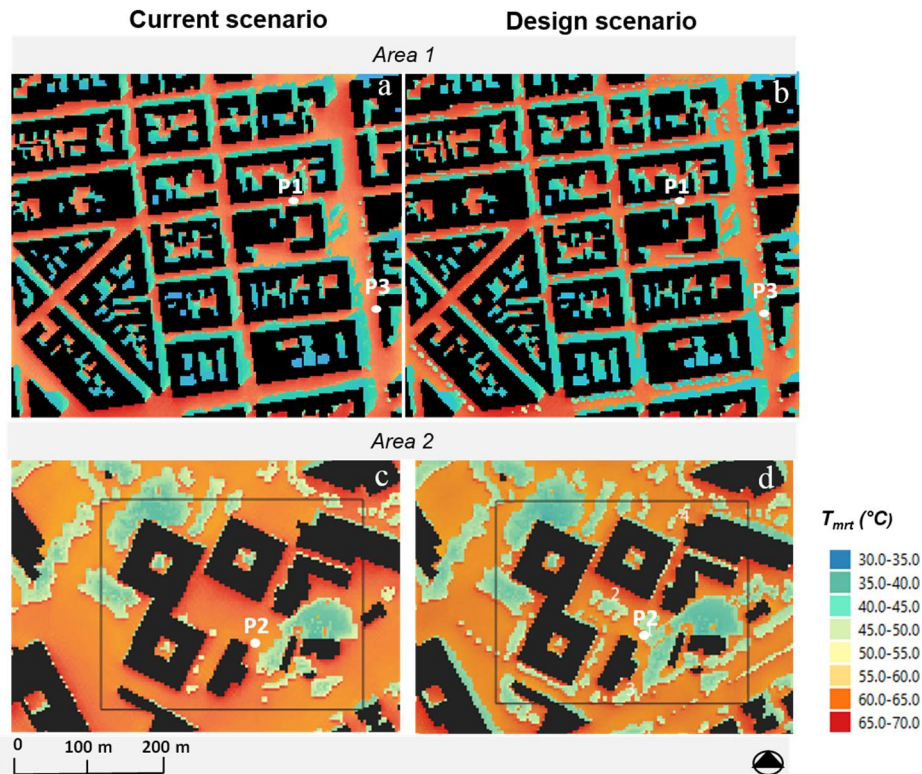


Figure 4.44. 2D maps of spatial distribution of  $T_{mrt}$  in Current and Design scenarios for Area 1 (a-b) and Area 2 (c-d) at 14.00 on 7<sup>th</sup> August.

As it is possible to see, Figures show the highest  $T_{mrt}$  values in Area 2 with peaks at around 68 °C, followed by Area 1. Despite a meaningful surface of Area 1 being shaded, a significant surface characterized by  $T_{mrt}$  values between 65°C and 67°C was found. In Area 2, high peak values of  $T_{mrt}$  are located at some points in the investigated domain. This can be explained by the fact that the areas 1 and 2 have a different urban morphology.

Area 2 has large open areas and wide streets and thus, aspect ratio has low values. Although the canyon ratio is lower than that in 1 and as such pedestrians are directly exposed to solar radiation, Area 2 is characterized by a vegetation surface higher than Area 1. As a result, the areas near buildings and between the buildings have  $T_{mrt}$  values higher than surroundings areas (see Figure 4.44c).

The geometric configuration of Area 1 with its courtyards and taller buildings contributes to lowering  $T_{mrt}$  values, especially in proximity of the east facing façades that show values in the range from 40°C to 50°C (see Figure 4.44a). Nevertheless, the absence of vegetation such as trees, shrubs, and grass in the urban spaces determines rather high  $T_{mrt}$  values close to the buildings. The lowest  $T_{mrt}$  values, in the range of 35°C to 40°C, were found in the internal courtyard and shaded areas (Figure 4.44a).

In Design Scenario, Area 2 shows  $T_{mrt}$  reductions higher respect to that of Area 1. The different effects of the vegetation on the  $T_{mrt}$  reductions in areas 1 and 2 can be explained by two factors that are closely related to each other. Firstly, the typology and quantity of trees and shrubs that can be planted

in relation to the geometry of the urban tissue. Secondly, the morphology of the study area such as shaded areas and available public spaces.

In Design Scenario, both areas show remarkable  $T_{mrt}$  reductions – around  $20^{\circ}\text{C}$  - under trees thanks to their shading effect. The surrounding areas around the trees are characterized by  $T_{mrt}$  reductions below  $5^{\circ}\text{C}$ . Although the decrease of  $T_{mrt}$  is very low in areas far from away the vegetation, the adding of trees seems to affect the  $T_{mrt}$  spatial distribution over the entire studied area.

The assessment of the potential effects of the proposed scenario in the  $T_{mrt}$  reduction was carried out by means of spatial cumulative frequency distribution of  $T_{mrt}$  values occurring over the entire area at a selected point in time.

Figure 4.45 shows the curves that describe the cumulated frequency of  $T_{mrt}$  values occurring over the entire area at 14.00 on 7<sup>th</sup> August in Current Scenario (CS) and Design Scenario (DS) respectively for areas 1 (a) and 2 (b).

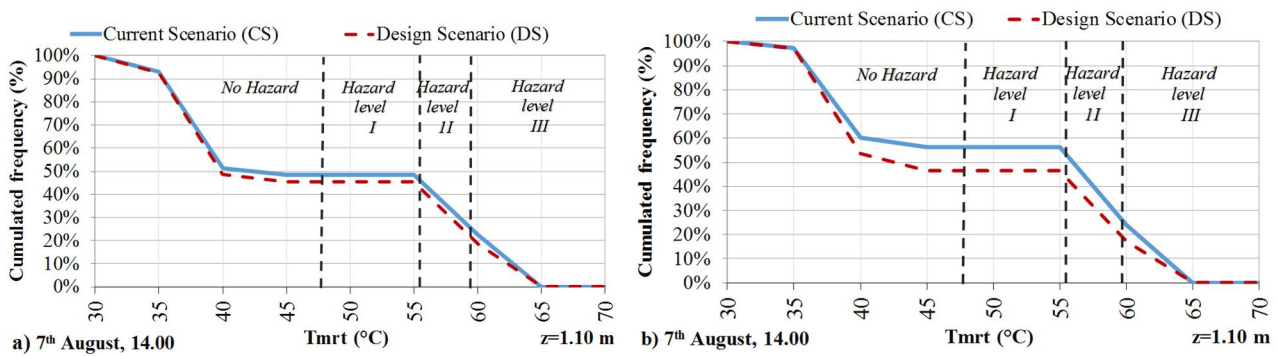


Figure 4.45. Spatial cumulative frequency distribution of mean radiant temperature for Current Scenario (CS) and Design Scenario (DS) in the study areas on 7<sup>th</sup> August at 14.00: a) Area 1; b) Area 2.

In Current Scenario (CS), both study areas have about 25% of the investigated domain where the  $T_{mrt}$  values are higher than  $59.4^{\circ}\text{C}$  ( $T_{mrt}$  value over which heat-related mortality risk increases by 10% in people aged over 80).

In Design Scenario (DS),  $T_{mrt}$  is higher than  $59.4^{\circ}\text{C}$  in about 23% of Area 1, while the corresponding figures for Area 2 is 17%. It is worth highlighting that Design Scenario (DS) has the highest influence in the  $T_{mrt}$  reduction in Area 2. Here, the cumulative frequency of  $T_{mrt}$  spatial distribution on the entire area is mostly lower of 10% than existing scenario.

In order to better explain the outcomes in both analysed scenarios, the magnitude of the radiant heat forces acting on the different POIs was plotted against the corresponding  $T_{mrt}$  values in Figure 4.46.



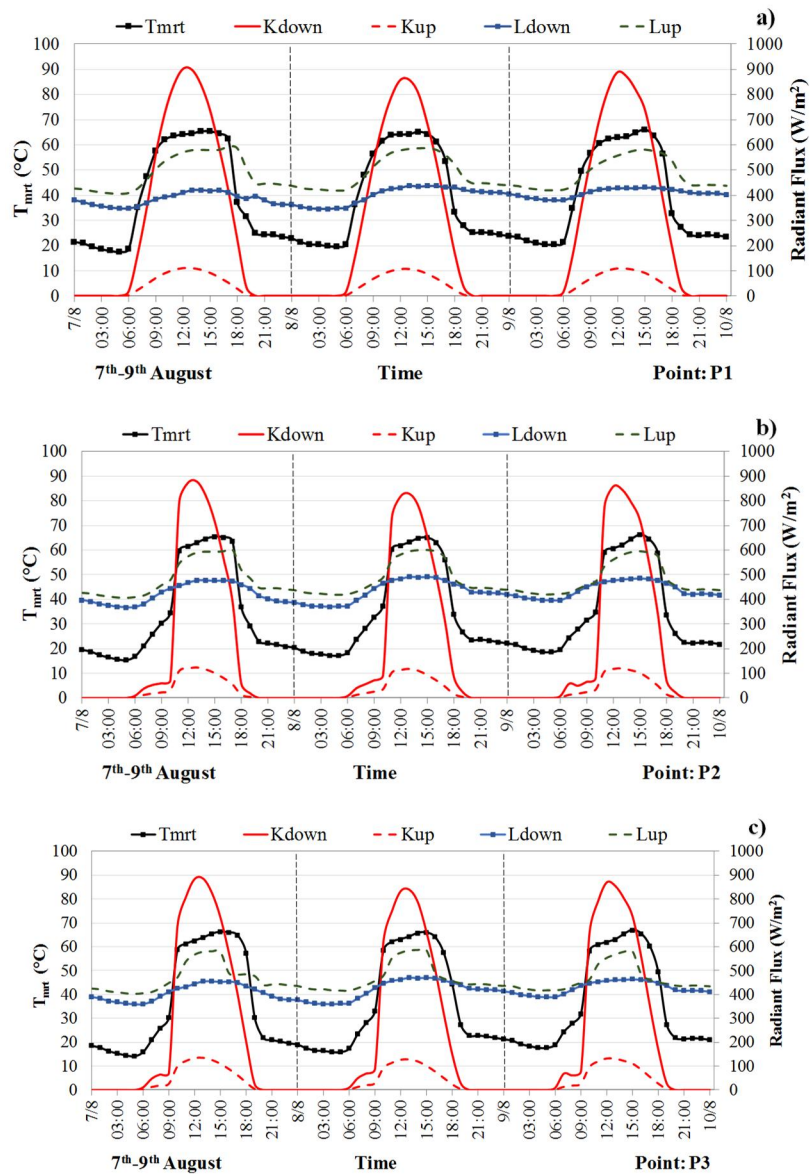


Figure 4.46. Radiant energy balance and mean radiant temperature profile for POIs during three consecutive warm days in Current Scenario (CS): a) P1; b) P2 and c) P3.

In Current Scenario (CS), what immediately emerges is the predominance of the downward shortwave radiation from the sky ( $K_{DOWN}$ , red solid line) during daytime, with peaks of around  $900 \text{ W}\cdot\text{m}^{-2}$  between 13:00 and 14:00 for POIs P1, P2 and P3: in these points, which are always sunlit during daytime,  $T_{mrt}$  closely follows the pattern of  $K_{DOWN}$ . By contrast, when the POI is shaded for most of the time,  $L_{UP}$  ( $L_{\uparrow}$ ) and  $L_{DOWN}$  ( $L_{\downarrow}$ ) turn out to be the predominant radiant forces. As a general rule, both long wave terms range between  $400$  and  $600 \text{ W}\cdot\text{m}^{-2}$ :  $L_{UP}$  is mainly determined by the high rate of heat absorbed by the ground – and then re-emitted in the long wave range – whereas  $L_{DOWN}$  is due to the infrared radiation directly coming from the sky and eventually reflected from the façades. Finally, the lowest contribution to  $T_{mrt}$  comes from the shortwave radiation reflected by the ground ( $K_{UP}$ , orange dashed line), which in each POI peaks below  $200 \text{ W}\cdot\text{m}^{-2}$  at the same time of  $K_{DOWN}$ .

It is worth noting that the simplification imposed by SOLWEIG of considering a fixed albedo value for all the façades can undermine not only the prediction of the shortwave radiation coming from the four cardinal directions when the POI is close to one or more façades, but also that of  $K_{UP}$  that accounts for the same façades' reflection. On the other hand, the magnitude of the long wave radiation coming from the four cardinal directions is comparable to  $L_{UP}$  and strongly depends on the POIs' sky view factor (i.e., proximity to building façades).

Figure 4.47 shows the radiant energy balance and mean radiant temperature profiles for the same POIs (P1, P2, and P3) in Design Scenario (DS).

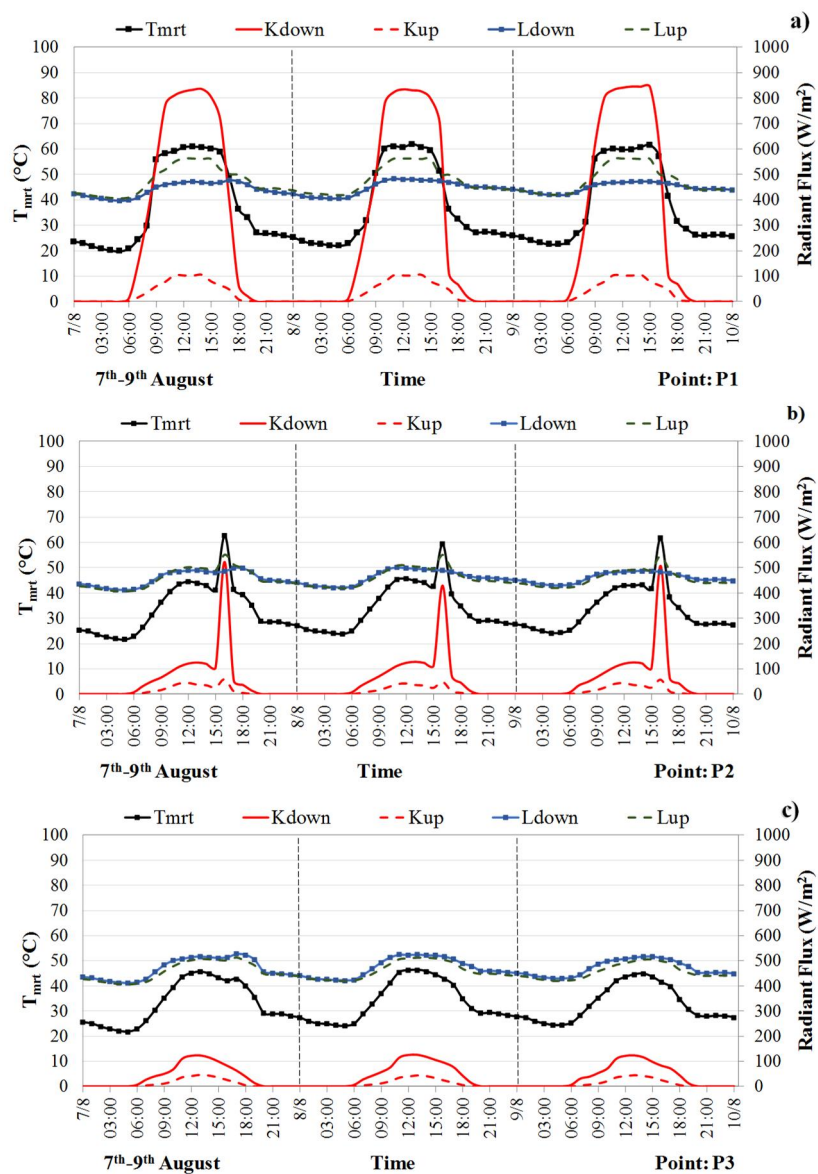


Figure 4.47. Radiant energy balance and mean radiant temperature profile for POIs during three consecutive warm days in Design Scenario (DS): a) P1, b) P2, and c) P3.

By contrast, when the POI are shaded by the trees for most of the daytime (P2 and P3 points), a relevant decrease in peak value of the mean radiant temperature was attained.  $K_{DOWN}$  is remarkably

reduced and  $L_{UP}$  and  $L_{DOWN}$  turn out to be the predominant radiant forces. This is the case of P2 and P3 points.

In P2 (see Figure 4.47b), a relevant decrease in  $T_{mrt}$  was achieved except during the short time interval (around 16:00) where sun rays coming from west hit the POI and determine a sudden (but short) increase in  $K_{DOWN}$  and  $T_{mrt}$ . Since P3 is below a tree with a dense and wide crown,  $T_{mrt}$  values are further reduced with respect to P2 point (Figure 4.47c). In Design Scenario, P1 is placed near to the trees and as a consequence the mean radiant temperature is slightly reduced during daytime.

Figure 4.48 (a-b-c) shows the hourly profiles of  $T_{mrt}$  at the selected POIs (P1, P2 and P3) in the Current Scenario (CS) and Design Scenario (DS) respectively during period (7<sup>th</sup> – 9<sup>th</sup> August). The threshold values of  $T_{mrt}$  of heat-related mortality risk for age band 80<sup>+</sup> (dashed red lines) were represented.

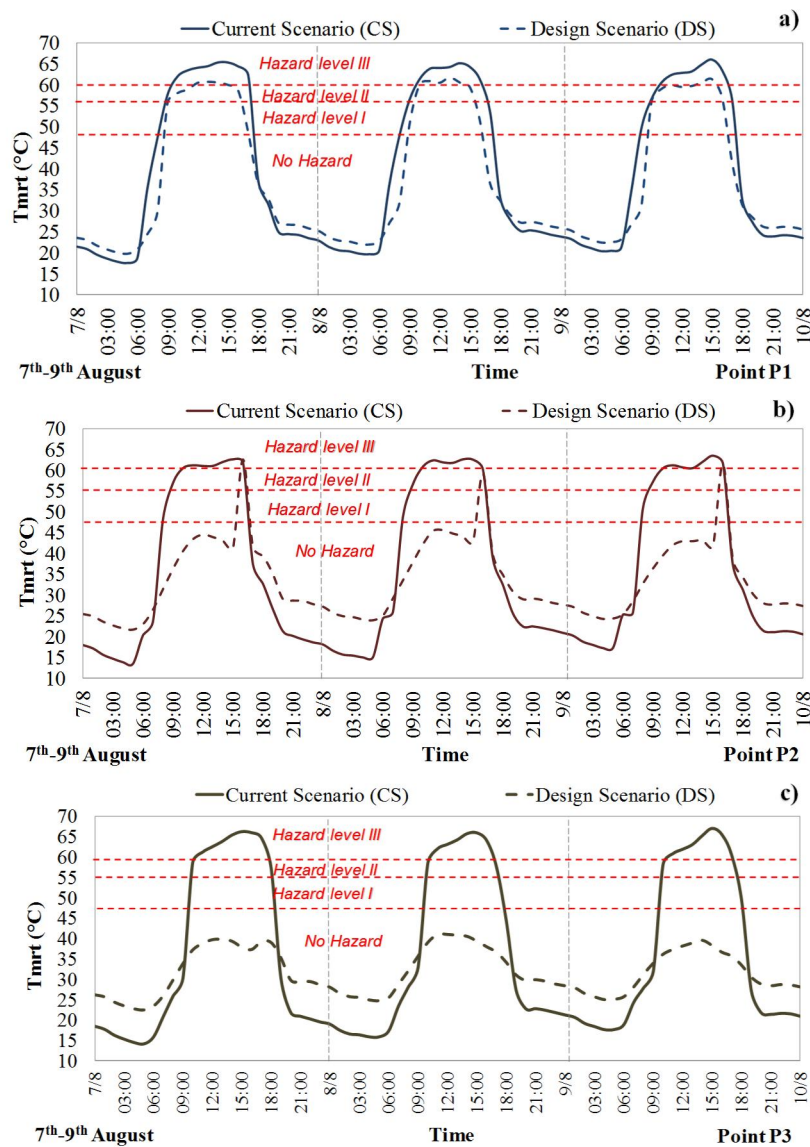


Figure 4.48. Mean radiant temperature ( $T_{mrt}$ ) profiles during three consecutive warm days in Current Scenario (CS) and Design Scenario (DS) in Point a) P1, b) P2, and c) P3.

The selected points of interests (POIs) at pedestrian height ( $z = 1.10$  m) were described in Table 4.6 and reported in Figure 4.21 (Section 4.4.2).

All three points are sunlit during daytime at current scenario. P1 is located in an urban canyon with Sky View Factor (SVF) value below 0.40 and an aspect ratio ( $H/W=3$ ) whereas points P2 and P3 are in areas with  $SVF > 0.60$  (see Table 4.6).

In P1, surrounding areas at around the trees (see figure 4.45a), the profile of  $T_{mrt}$  is reduced at about  $5^{\circ}\text{C}$  during the sunny hours of the day respect to the Current Scenario (CS). This showed that  $T_{mrt}$  reductions could be up to  $5.0^{\circ}\text{C}$  in points located nearby sparse canopy trees due to the evapotranspiration phenomenon. This result is meaningful because, during the warmest hours, the peak of  $T_{mrt}$  can be lowered below the threshold value over which heat-related mortality risk increases by 10% in people aged over 80 (see Figure 4.48a).

At nighttime, a slight increase in the minimum values of  $T_{mrt}$  was found. This is due to the fact that the crown of trees reduces the Sky View Factor (SVF) values and hinders the heat transfer via long wave radiation towards the sky ( $L_{UP}$ ). Thereby, the rate of nighttime radiation emitted from the soil surfaces to the sky is reduced and consequently the heat is trapped in the urban canopy layer. However, the increase of  $T_{mrt}$  in P1 is very low if compared to that occurred in open areas (P2 and P3 points) where the SVF value is markedly reduced due to the wide crown of trees planted in P2 and P3. Indeed, in Compact Midrise area, the adoption of the morphology of trees with sparse crown and high trunk counteract the reduction of SVF of the pavement and soil surfaces.

Trees with higher dense foliage screen the incoming shortwave radiation and provide extensive shading at pedestrian level. The extensive shading lowers the temperature of the ground surface reducing radiant heat load and mitigating the heat stress. A decrease in peak values of mean radiant temperature even higher than  $20^{\circ}\text{C}$  can be attained in points shaded by trees (points P2 and P3) (see Figure 4.48b and c). In open areas, the tall trees with wide crowns can reduce the  $T_{mrt}$  values until to  $40^{\circ}\text{C}$ . Thereby, the peak values of  $T_{mrt}$  are below the threshold of risk level.

#### 4.5.9 Heat stress risk analysis

Figures 4.49 and 4.50 identify hazard areas using the daily maximum value of  $T_{mrt}$  thresholds for ages 80 and older in Current (a-c) and Design Scenarios (b-d) for areas 1 and 2. To this aim, a 2D spatial distribution of  $T_{mrt}$  values at 14.00 on a warm and sunny summer day (7<sup>th</sup> August, 2019) was considered.

The comparison between hazard maps of the Current and Design scenarios respectively revealed that trees can be an effective measure for mitigating heat stress in urban areas. In fact, the areas nearby the trees showed a reduction in mean radiant temperature of up to  $20^{\circ}\text{C}$ . As a consequence, such areas

fall within “no hazard” levels in Design Scenario. However, the majority of the surface of the study areas is in hazard levels II and III. This could be explained by the fact that the area shaded by the trees becomes rather limited due to high elevation of the sun at noon or in the early afternoon. However, such result depends on the approach used to plan the planting of the trees and the hour that is taken into account for the investigation.

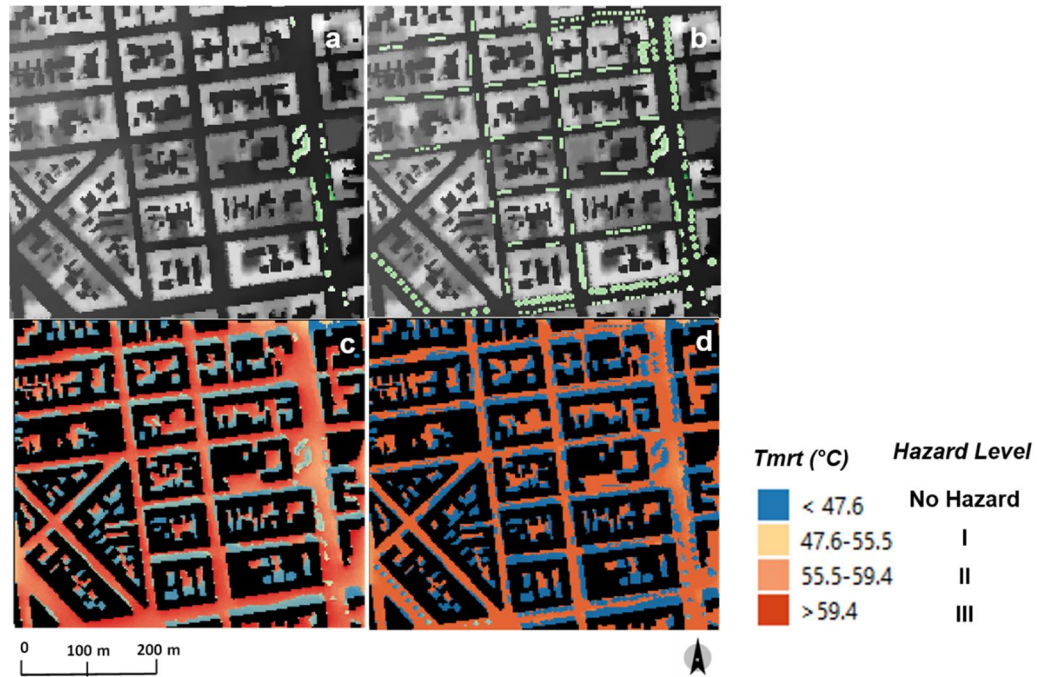


Figure 4.49. 2D Spatial variations of  $T_{mrt}$ , and identification of hazard areas in the high built-up densely district (Area 1) at 14.00 on 7<sup>th</sup> August: (a-c) Current Scenario (CS); (b-d) Design Scenario (DS).

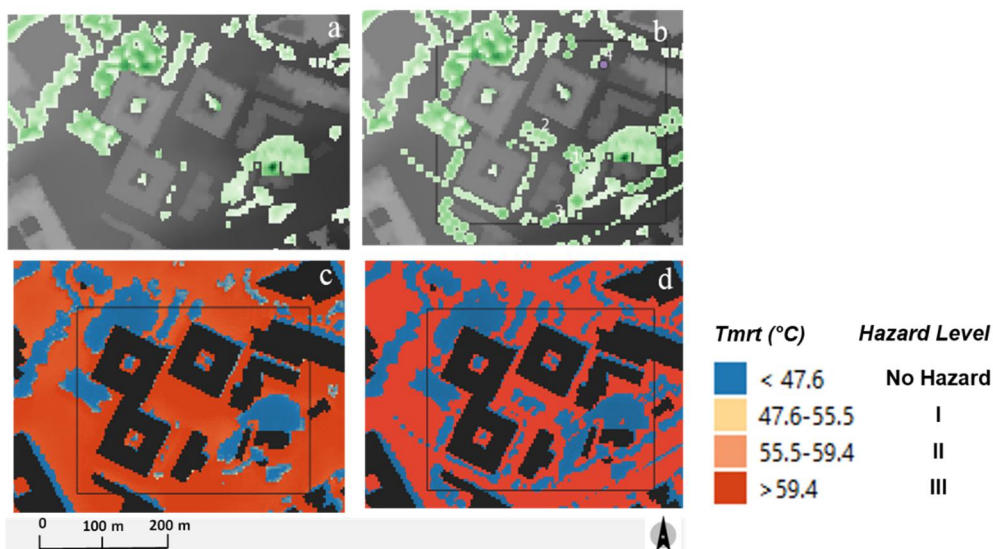


Figure 4.50. 2D Spatial variations of  $T_{mrt}$ , and identification of hazard areas in the open Low-rise district (Area 2) at 14.00 on 7<sup>th</sup> August: (a-c) Current Scenario (CS); (b-d) Design Scenario (DS).

Figure 4.51 shows the cumulative frequency  $f$  (%) of the domain area falling within different hazard levels during daytime (from 8.00 to 18.00) on 7<sup>th</sup> of August in Current Scenario (CS) and Design Scenario (DS) for areas 1 and 2 respectively.

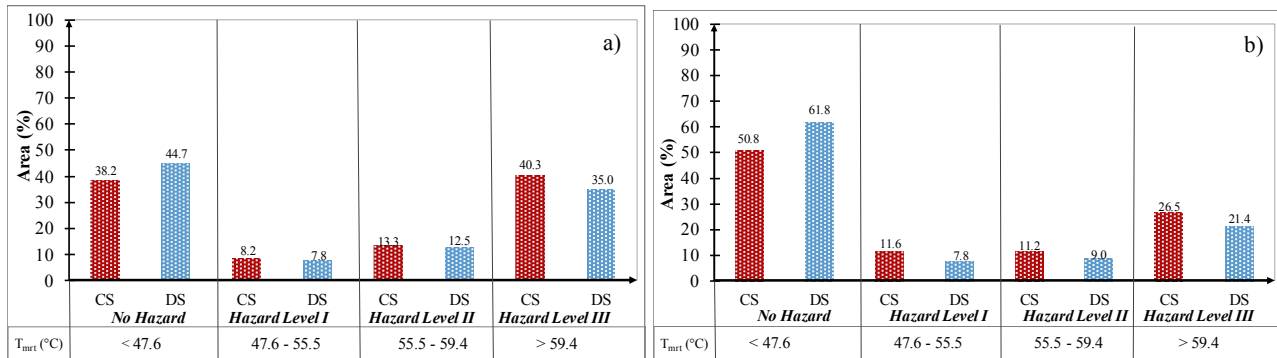


Figure 4.51. Cumulative frequency of domain area within specific hazard levels of heat stress related mortality in Current Scenario (CS) and Design Scenario (DS) for Area 1 (a) and Area 2 (b).

This analysis has shown that Current Scenario falls within the “No-Hazard” class for 38.3% and 50.8% of the domain of area 1 and 2 respectively. Area 2 shows a cumulated frequency of  $T_{mrt}$  falling within No-Hazard level higher than Area 1. In both areas,  $T_{mrt}$  distribution is predominantly within No-Hazard and Hazard level III respectively. This depends on the fact that during daily hours of maximum solar radiation the  $T_{mrt}$  values are predominantly between 60°C and 65°C in sunlit areas and between 35°C and 45°C in shaded areas.

Design scenario (DS) increases the fraction of investigated domain that is included within “No-Hazard” class. In areas 1 and 2, Design scenario falls into No-Hazard for 44.7% and 61.8% of the investigated domain. As a result, an increase of 6% and 11% of the entire domain characterized by values lower than 47.6°C was found in area 1 and 2 when a Design Scenario is considered.

Overall, the cumulative frequency of  $T_{mrt}$  included in Hazard levels I, II and III are reduced under Design scenario (DS).

It is worth highlighting that the areas characterized by high values of  $T_{mrt}$  are more sensitive to the effectiveness of the increase of vegetation included in Design scenario. The reduction of cumulative frequency of  $T_{mrt}$  that fall within hazard level III is reduced by 5% with respect to the Current scenario.

#### **4.6. Microscale climate analysis**

The outdoor microclimate of the two identified sites as risky areas was investigated using an urban Microscale approach based on accurate CFD models by means of ENVI-met calculation code.

Based on the Microscale analysis of calibrated and validated models of the two selected areas (Area 1 and Area 2), different heat stress mitigation strategies were planned in relation to the morphological features of the two studied areas. The results achieved were presented and discussed in two papers published in Urban Climate and Sustainability journals respectively. Both articles are attached to the present thesis in order to show the effectiveness of proposed UHI mitigation strategies on the outdoor microclimate.

Based on the proposed methodology, first, the results of the heat stress mitigation of compact and high density built-up area (Area 1) were described and thereafter, those of the open low-rise area characterized by less urban density (Area 2).

It has to be highlighted that the article published on Urban Climate - “Application of weather data morphing for calibration of urban ENVI-met microclimate models. Results and critical issues” – addresses calibration approach of an urban micro scale three-dimensional CFD model with weather data calculated by the morphing procedure of UWG, and the validation of the same model comparing the hourly-simulated outputs in specific points of the calculation domain with on-site measurements. In light of this, the extract of an article entitled “A risk index for assessing heat stress mitigation strategies. An application in the Mediterranean context”, currently under review, is also attached. This latter deals with the assessment of the effects of heat stress mitigation strategies on the reduction of the risk for human health of the same urban district analyzed in the paper published in Urban Climate journal.

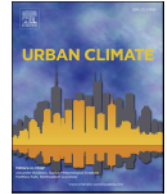
Subsequently, the paper “Sustainable Urban Greening and Cooling Strategies for Thermal Comfort at Pedestrian Level” was written.



ELSEVIER

Contents lists available at ScienceDirect

## Urban Climate

journal homepage: [www.elsevier.com/locate/uclim](http://www.elsevier.com/locate/uclim)

# Application of weather data morphing for calibration of urban ENVI-met microclimate models. Results and critical issues

Maurizio Detommaso, Vincenzo Costanzo<sup>\*</sup>, Francesco Nocera

Department of Civil Engineering and Architecture, University of Catania, Via Santa Sofia, 64, 95123 Catania, Italy

## ARTICLE INFO

### Keywords:

Urban microclimate  
UWG  
ENVI-met  
Model calibration  
Experimental campaign

## ABSTRACT

The detailed analysis of the urban microclimate calls for the use of Computational Fluid Dynamics (CFD) tools able to model complex heat and mass transfer mechanisms. ENVI-met is one of the most used and reliable tools for microclimate analysis if an accurate calibration is performed. The calibration process is fundamental to have a reliable model in order to perform microclimate analysis, but requires accurate on-site measurements of urban weather data and it is usually difficult to have urban meteorological data of the required granularity because of the lack of on-site stationary weather stations. To overcome such an issue, this paper explores the use of weather data retrieved from suburban meteorological stations and morphed for the urban context under study through the Urban Weather Generator (UWG) tool. UWG generates an urban weather file in the hourly .epw format that is eventually used for forcing the ENVI-met model of the investigated area. This approach is validated against on-site measurements at different times for various points located in a district of the city center of Catania (Italy). The validation process presented a very good correlation for most of the study points in the district during nighttime, while during daytime some discrepancies may occur.

## 1. Introduction

The increasing awareness of the issues coming from frequent heat waves in cities has inspired a growing number of studies dealing with urban physics and the Urban Heat Island (UHI) effect in particular. Different approaches such as Computational Fluid Dynamics (CFD) (Li et al., 2013), analytical and empirical algorithms (Ignatius et al., 2015) and physical models based on an urban canopy energy balance (Lee and Park, 2008) are typically employed, with a preference given to CFD models because of their capability to drive the design, analysis and optimization of various urban environment scenarios. In this context, the ENVI-met software is largely used for predicting outdoor climate conditions at urban micro or neighborhood scales (Giridharan and Emmanuel, 2018; Ma et al., 2019).

Despite the advancements in the field of CFD analysis, simulation practice has a recognized obstacle that is the discrepancy, sometimes significant, between actual and predicted values (Mao, 2018). This issue is due to the complex interactions amongst several built environment parameters that makes it difficult to obtain an accurate representation of these real-world systems (Forouzandeh, 2018). The model errors are mainly caused by software limitations and inaccurate parameter descriptions that cannot be completely known – and thus modelled – a priori (Maggiotto et al., 2014; Huttner and Bruse, 2009). Because of this, model calibration and uncertainty analysis hold a particular interest and are fundamental to evaluate the degree of accuracy of a model before using its outcomes in decision-making process (Vuckovic et al., 2015). In the case of simulation-based evaluation of large-scale and costly urban

<sup>\*</sup> Corresponding author.

E-mail address: [vincenzo.costanzo@unict.it](mailto:vincenzo.costanzo@unict.it) (V. Costanzo).



interventions, the execution of a systematic calibration process is therefore essential (Maleki et al., 2014).

In the assessment of the outdoor thermal comfort conditions of urban areas, current calibration approaches usually rely on measurements of air temperature in a limited number of points of the study domain (Fabbri and Costanzo, 2020). The air temperature is deemed a suitable variable to calibrate CFD models because it is a bulk index of the local climate and is less prone to vary within a micro scale domain compared to other variables such as near ground measurements, surface temperatures and wind speed (Salvati and Kolokotroni, 2019).

As an example, Koutra et al. reviewed various ENVI-met simulations coupled with on-site measurement campaigns that most often recorded air temperature and relative humidity while less frequently considered mean radiant temperature and wind speed (Koutra et al., 2018). Nonetheless, simulation results were not always validated (or the model calibrated) against on-site measured data, thus the reliability of the simulation results appears questionable. In fact, the accuracy of a CFD model may vary substantially depending on the forcing conditions used for the simulation and, in particular, according to the meteorological boundary conditions. Accordingly, the local climate conditions determined by neighborhood characteristics should be used to force CFD microclimate simulations instead of using measurements collected at weather stations located in the peripheral zone of the cities as input boundary conditions (Salvati and Kolokotroni, 2019).

However, when urban or on-site microclimate measurements are not available, a promising way to estimate the local urban climate could be that of resorting to urban energy balance models such as in the case of the Urban Weather Generator (UWG) (Mao, 2018; Bueno et al., 2015; Salvati et al., 2016).

The goal of this paper is to propose and discuss a calibration approach of an urban micro scale three-dimensional CFD model built in ENVI-met with weather data calculated by the morphing procedure of UWG, and to validate the same model comparing the hourly-simulated outputs in specific points of the calculation domain with on-site measurements.

## 2. Methods for calibration and validation of ENVI-met models in the literature

When dealing with ENVI-met simulations, the approaches followed by most scholars make use of models validated with on-site measurements, although there are also few examples of models that are not validated as in the case of a recent research of Battista et al. about the evaluation of the UHI effect in a neighborhood in Rome (Battista et al., 2019). Also Sözen and Koçlar used non-validated ENVI-met models of different urban canyons in Madrid (Sözen and Koçlar Oral, 2018), while O'Malley et al. investigated different mitigation strategies to the UHI phenomenon to gauge resilience and promote urban sustainability in a selected area in the borough of West Kensington in London (O'Malley et al., 2015). Rui et al. reported on the relationship between greenery amount, thermal comfort and air quality according to different scenarios of green cover ratio but without any use of experimental data for calibration purposes (Rui et al., 2019). Another example is that of Li et al. who analyzed the cooling and energy-saving performances of different green wall designs in an urban district located in Chenzhou (China) using an ENVI-met model not validated (Li et al., 2019). Finally, also Gaspari et al. made use of a model not validated with on-site measurements for supporting decision makers in choosing amongst alternative design solutions with different green elements in the framework of the follow up of a design competition for a public square launched by the Municipality of Cesena (Gaspari et al., 2018).

On the other hand, researches employing measurements for calibration and validation purposes - for just one or several points in the spatial domain - are found to adopt mainly two strategies:

- Statistical analysis of one or more environmental variables;
- Trends comparison of one or more measured variables with simulated ones through graphical representations.

In the context of statistical analysis, the outdoor air temperature and relative humidity are the main indicators used to calibrate CFD models (Zhang et al., 2018). This is not only because of the easiness of their measurement process, but also because the possibility to use diurnal cycles of air temperature and relative humidity to force the models has proved to increase significantly the accuracy of the simulation results (Vuckovic et al., 2015).

Other studies, instead, considered the mean radiant temperature ( $T_{mrt}$ ) for calibrating outdoor comfort models (Elnabawi et al., 2015; Chen et al., 2014). However, despite this variable is more related to humans' thermal comfort than air temperature, the measurement of  $T_{mrt}$  outdoors via the globe thermometer or the six direction radiation method proved to be challenging and prone to errors because this variable depends on wind speed and radiant fluxes that are extremely variable outdoors (Chen et al., 2014; Andreou, 2013).

The air temperature is thus widely considered the preferred variable to calibrate ENVI-met models being a bulk index of the local climate of an urban area, less likely to vary within a microscale domain compared to other variables such as surface temperatures or wind speeds (Salvati and Kolokotroni, 2019). As an example, Mohamed et al. have assessed the microclimate of an urban area located within the Islamic Quarter of Cairo (Egypt) through ENVI-met simulations calibrated against air temperature, relative humidity and mean radiant temperature values as measured on site by mobile weather stations. The regression analysis between the measured and computed air temperature has reported a coefficient of determination  $R^2$  of 0.942 (Elnabawi et al., 2015). The comparison between the simulated values of mean radiant temperature and those measured via globe thermometer shows a good qualitative agreement until sunset. However, after sunset, it was found that the predicted values of  $T_{mrt}$  do not adequately follow the field data (Elnabawi et al., 2015). This is rebated also in the validation exercise carried out by Gal and Kantor (Gál and Kántor, 2020), where it is discussed in detail how the main cause of prediction discrepancies is the reliance on domain-wide mean values for both emitted and reflected upwelling shortwave and longwave radiation.

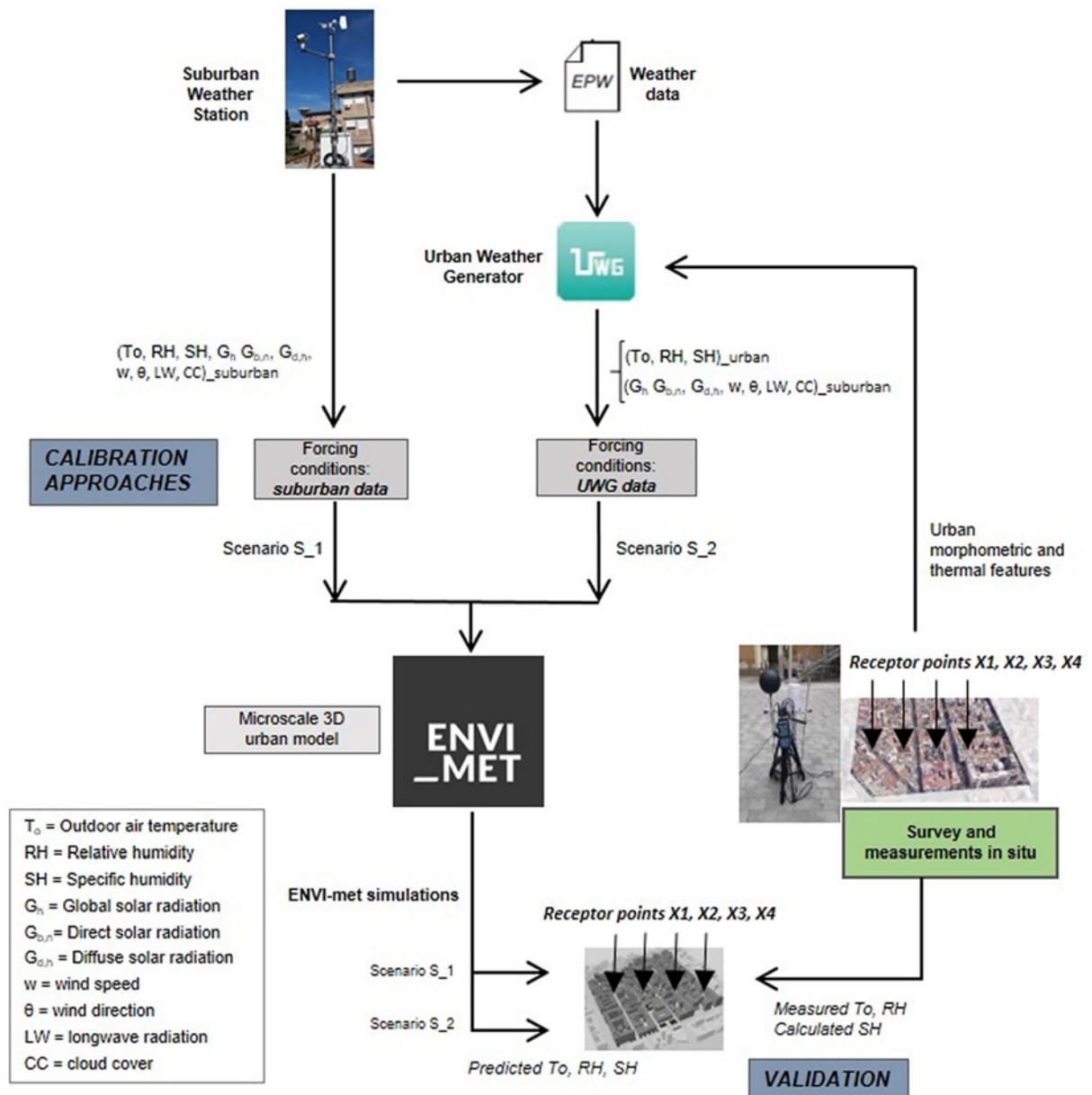


Fig. 1. Flowchart of the methodology.

Battista and De Lieto Vollaro investigated the potential effects of mitigation strategies including vegetation improvement on the outdoor comfort of a neighborhood in Rome based on a validated model realized with ENVI-met (Battista et al., 2016). The model was forced with climate data detected by a LSI Lastem micro-climate station placed at 6.5 m above the ground in the selected area. The validation process was performed by comparing the measured data with numerical results of air temperature and relative humidity of a receptor placed in the same point where the actual measurements were taken. Mean Absolute Error (MAE), Root Mean Square Error (RMSE) and the Index of Agreement (d) were adopted as statistical performance indices, and a good agreement between the measured and computed ENVI-met for air temperature was achieved (MAE = 1.28 °C, RMSE = 1.63 °C, d = 0.99).

Gusson and Duarte performed on-site microclimate measurements for the calibration of ENVI-met models of two densely populated districts in São Paulo in Brasil (Brasilândia and Bela Vista namely) with contrasting building densities and typologies. Air temperature, relative humidity, wind speed and direction, as well as globe temperature, were registered at a height of 1.50 m above ground level. For Bela Vista district, the RMSE value was 1.6 °C, the MAE value 1.4 °C and the d value of 0.85 for the dry bulb temperature, while for Brasilândia the corresponding figures were MAE = 1.8 °C, RMSE = 1.9 °C and d = 0.92 respectively (Gusson and Duarte, 2016).

Also Tsoka et al. have estimated the impact of cool pavements and greening strategies on local microclimate relying on CFD simulations. To this aim, a three-dimensional urban micro scale model with a mesh resolution of  $2.5 \times 2.5 \text{ m}^2$  was realized with ENVI-

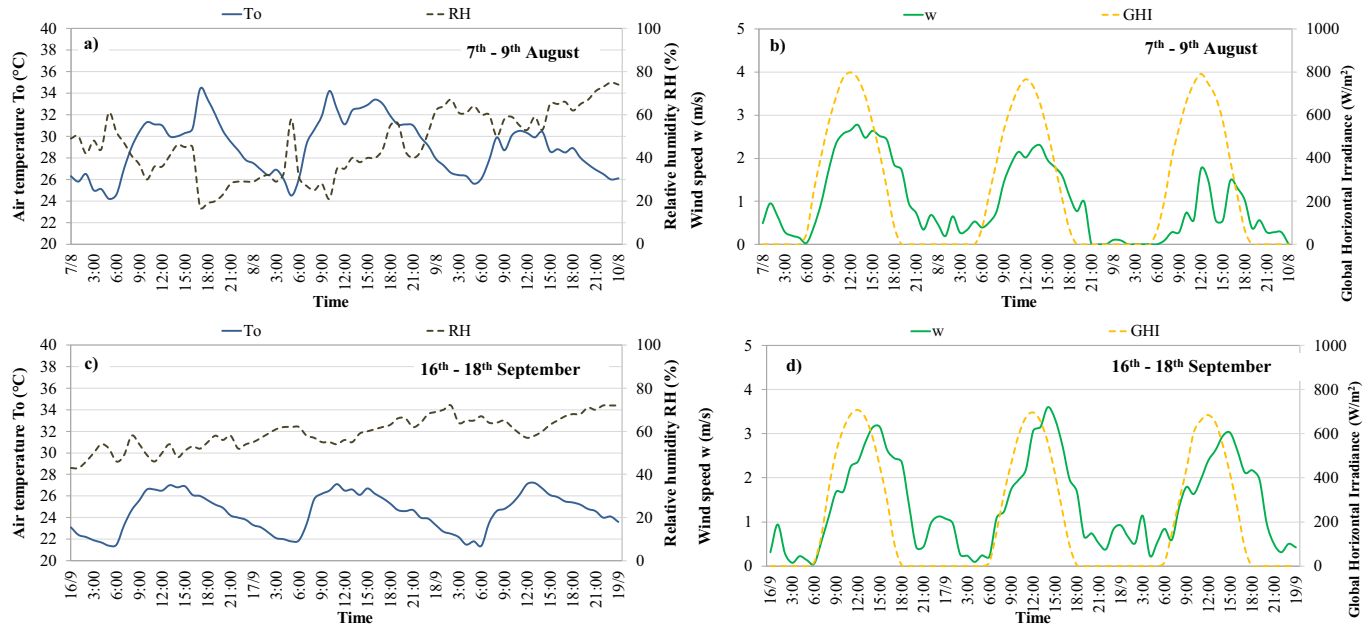


Fig. 2. Hourly values of outdoor air temperature and relative humidity (a,c), solar radiation and wind speed (b,d), recorded at the suburban weather station.

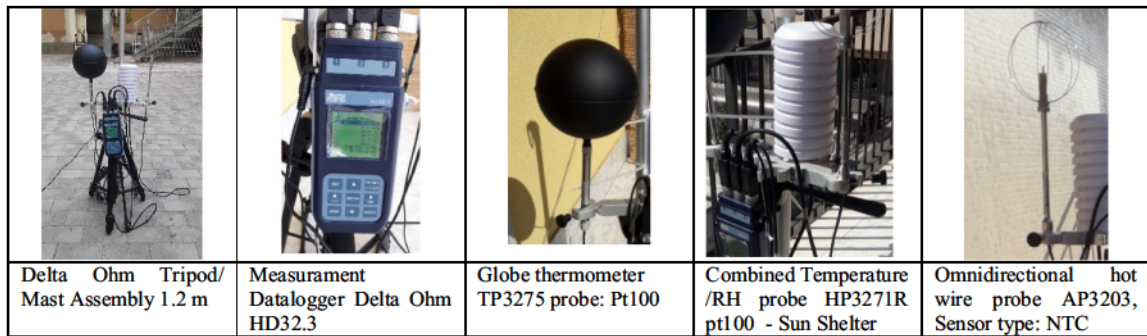


Fig. 3. Microclimate portable station and its components.

met. A good agreement between simulated values and on-site measurements was found as reported by the values of various statistical indices (MAE = 1.10 °C, RMSE = 1.85 °C,  $d = 0.90$ ) (Tsoka et al., 2017).

A good correspondence between field measurements and ENVI-met simulations was found also in a study regarding the effects of urban bioclimatic interventions in the central area of a coastal medium-sized city in Greece. The accuracy of the model was assessed by comparing the simulated values of air temperature with the corresponding measurement series, eventually reporting a RMSE equal to 0.9 °C. Additionally, the regression coefficient approaches one ( $R^2 = 0.92$ ) and then indicates a good correlation of the temperature fluctuation values (Makropoulou, 2017). In a similar fashion, also Fabbri et al. validated their model of a public square in Parma (Italy) through the calculation of the regression coefficient of air temperature values obtained from the Meteoblue weather service (Fabbri et al., 2020).

Finally, examples of CFD model calibration through a graphical process based on the comparison of measured and simulated air temperature trends can be found in Huttner's Ph.D. thesis (Huttner, 2012) that treats the application of ENVI-met simulations to a case study, in the paper of Maggiotto et al. (Maggiotto et al., 2014) with 4-points on-site measurements, and in that of Tsitoura et al. (Tsitoura et al., 2016).

### 3. Methodology

The calibration approach of ENVI-met models proposed in this research is carried out by forcing the software using hourly data of global, direct and diffuse solar radiation, wind speed and direction, as recorded by a meteorological station placed in a suburban area outside the city center. Incoming longwave radiation and cloud cover are used as well but are obtained from the local aeronautic service. The hourly values of air temperature and relative humidity collected at this station – which are the environmental variables more affected by the Urban Heat Island (UHI) effect – are first morphed through the Urban Weather Generator (UWG) tool and then implemented in ENVI-met to account for site-specific characteristics (*calibration phase*).

To demonstrate the validity of such an approach, a site survey was conducted to compile the construction characteristics of the buildings and paved areas, the location of green areas, the number and type of trees and parking lots in the study area. Furthermore, two on-site measurement campaigns were carried out with a microclimate portable station to measure air temperature and relative humidity. These measurements are eventually compared against the predictions of simulations run in ENVI-met using both suburban weather data (scenario S\_1) and the weather data morphed by UWG (scenario S\_2) as forcing conditions through suitable statistical indices (*validation phase*). The workflow of the entire process is summarized in Fig. 1.

#### 3.1. Weather data collection

The weather data implemented in the UWG and ENVI-met models, apart from incoming longwave radiation and cloud cover that were retrieved from the local aeronautic service, were taken from the stationary weather station LSI Lastem placed on top of the roof of a building of the University Campus of Catania, which is located in the suburbs of the city of Catania (Italy). The weather station is equipped with air temperature and thermo-hygrometric sensors, a black globe thermometer and an anemometer, and it is able to record dry bulb air temperature, relative humidity, global, direct and diffuse solar irradiance, wind speed and direction, with a sampling time of 1 min. The uncertainty, measurements range and characteristics of the sensors are reported as follows:

- Air temperature and relative humidity sensors: (uncertainty: 0.10 °C and 0.1%; measurements range: –50 to 100 °C and 0 to 100%);
- Radiometer: (spectral response: 300–3000 nm; operative temperature –40 °C/+80 °C; uncertainty:  $\pm 4 \text{ W/m}^2$ );
- Anemometer: (measurement range: 0–50 m/s; threshold: 0.36 m/s; uncertainty 1% below 3 m/s and 1.5% above 3 m/s; resolution: 0.06 m/s).

The hourly values of air temperature ( $T_a$ , °C), relative humidity (RH, %), Global Horizontal Irradiance ( $G_{HI}$ ,  $\text{W}\cdot\text{m}^{-2}$ ) and wind speed ( $w$ ,  $\text{m}\cdot\text{s}^{-1}$ ) recorded during the analyzed periods (7th – 9th August 2019; 16th – 18th September 2019) are depicted in Fig. 2.

**Table 1**  
Technical characteristics of the probes of the portable microclimate station.

Climatic variables	Type of probes	Accuracy	Resolution	Range
Air temperature and Relative humidity	Combined probe HP3271R pt100	Class: 1/3 DIN $\pm 2\%$ (15÷90) $\pm 2.5\%$ remaining range	0.1 °C 0.1%	10 °C÷ 80 °C 5% ÷ 98%
Wind speed	AP3203 Omnidirectional hot wire probe, Sensor type: NTC 10kohm	$\pm 0.05$ m/s (0 ÷ 1 m/s) $\pm 0.15$ m/s (1 ÷ 5 m/s)	0.01 m/s	0 ÷ 5 m/s
Globe temperature	TP3275 globe thermometer probe ( $\varnothing = 150$ mm), Sensor type: Pt100	Class: 1/3 DIN	0.1 °C	-10 ÷ 100 °C

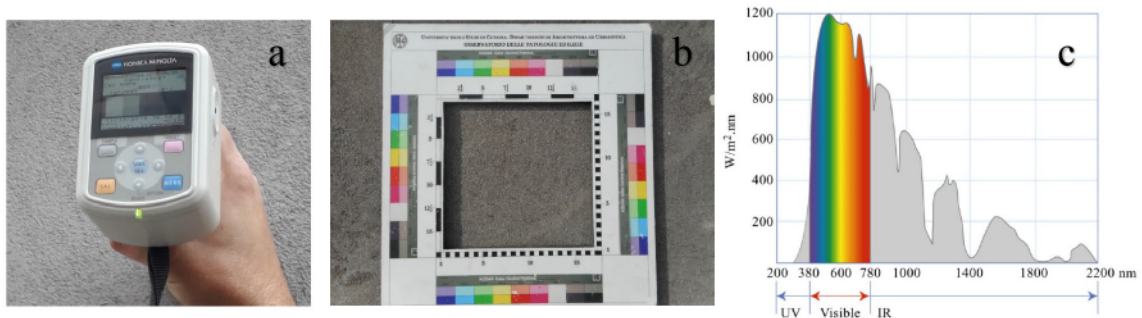


**Fig. 4.** Spectrophotometer CM-700d (a); Sample of the selected material (b); wavelength field reported as output (c).

In the period 7th–9th August, the maximum value of solar radiation (about  $800 \text{ W/m}^2$ ) occurs at around 12:00 pm (see Fig. 2b), while the outdoor air temperature varies from a minimum of  $24 \text{ }^\circ\text{C}$  (at 6.00 a.m.) to a maximum of  $34.5 \text{ }^\circ\text{C}$  (at 14.00 p.m.) as shown in Fig. 2a. The prevalent wind directions are east and south.

During 16th–18th September, the maximum GHI value is of about  $700 \text{ W/m}^2$ , while the peak of the outdoor air temperature is around  $27 \text{ }^\circ\text{C}$  and the wind predominantly blows from southeast (see Fig. 2c).

On the other hand, the validation of CFD simulations in ENVI-met has been accomplished by comparing simulation outcomes against two on-site measurement campaigns carried out with a portable microclimate station Delta ohm HD type 32. Fig. 3 shows all the components and sensors of such instrumentation: a thermo-hygrometric probe, a globe-thermometer and an omnidirectional hot wire probe. The thermo-hygrometric sensor is shielded by a white cylindrical box (20 cm height) with slits on the vertical surface for favoring ventilation and avoiding overheating. The values of air temperature ( $T_a$ ), globe temperature ( $T_g$ ), wind speed ( $w$ ) and relative humidity (RH) were recorded every minute, while the measuring instruments (whose characteristics are reported in Table 1) were tested and calibrated before the field survey. The entire measurement process complied with the suggestions of the ISO 7726 Standard (ISO 7726, 1998).

### 3.2. Spectral reflectance measurements of materials albedo

The measurements of the spectral reflectivity of various opaque materials found in the urban context were carried out by means of a spectrophotometer CM-700d UV – VIS (see Fig. 4) in accordance with ISO 7724/1 Standard (ISO 7724-1, 1984).

The spectrophotometer is based on sphere geometry with simultaneous color measurement and specular component included (SCI), and is equipped with both standard source lamp D65 and diffuse lighting with 8-degree viewing angle ( $D/8^\circ$ ). The instrument is able to measure a material's reflectivity only in the visible range (380 nm – 780 nm) by pointing a square sample of about  $16 \times 16 \text{ cm}^2$ . For each sample, ten measurements were performed with the integration time set to 2 s and finally an average value is obtained.

### 3.3. Weather data morphing: the Urban weather Generator (UWG)

The Urban Weather Generator (UWG) is a simulation tool developed at MIT that estimates air temperature and relative humidity in the Urban Canopy Layer (UCL) using meteorological data obtained at an operational rural weather station (MIT 2030 East Campus Urban Design Study, 2014; Bueno et al., 2013a; Rotach, 2005; Bueno et al., 2014).

UWG transforms the complex and heterogeneous urban structure into a homogenous urban canyon depiction according to the Town Energy Balance (TEB) scheme. TEB aims to simulate turbulent fluxes into the atmosphere at the surface of a mesoscale atmospheric model taking downward infrared radiation, direct and diffuse solar radiation on a horizontal surface as input energy fluxes along with various anthropogenic heat sources. In this way, the atmospheric model faces only a constant flux at its lower boundary, which represents the parameterization of both urban surfaces and the roughness sublayer (Masson, 2000).

In doing so, TEB treats the urban energy budget as the combined effect of surface energy budgets on roofs, walls and roads respectively, and accordingly uses the corresponding surface temperatures.

On the other hand, heat conduction through roofs, walls (e.g. with buildings) and roads (e.g. with soil) is modelled by discretizing each surface into various layers. Anthropogenic heat fluxes – specified by the user in its sensible and latent components originating from buildings, combustion and traffic processes – do not directly modify the various surface energy budgets because they are directly released into the air, and this appears to be as the main limitation of the model (Masson, 2000). The output energy fluxes allow, eventually, the direct estimation of air temperature and relative humidity values as modified by the urban structure.

A sensitivity analysis performed by Bueno et al. showed that factors governing the specific urban site's morphology, vegetative features and reference weather station, are of the greatest importance (Mao, 2018; Bueno et al., 2013a; Rotach, 2005). Hence, the rural weather file, city location, urban, district and building parameters are the main input to the UWG. The tool takes a rural or suburban \*.epw weather file and the \*.xml (or \*.xslm) input file which describes the urban canyon, and produces a morphed weather file with the same \*.epw format that captures the UHI effect by morphing air temperature and relative humidity values only that is compatible with many microclimate and building energy simulation programs.

UWG is composed of four coupled modules: Rural Station Model (RSM), Vertical Diffusion Model (VDM), Urban Boundary-Layer (UBL) model and the Urban Canopy and Building Energy Model (UC-BEM) (Bueno et al., 2013a; Bueno et al., 2014). In particular, UC-BEM estimates building energy consumption at the city scale, specifically accounting for the interactions amongst the buildings and the urban environment.

The UWG has been evaluated against field data from two cities: Basel (Switzerland) and Toulouse (France) (Bueno et al., 2013a; Rotach, 2005; Bueno Unzeta, 2010). Hourly values of urban air temperature calculated by the UWG were compared with the air temperature measured at the urban and rural sites from two boundary-layer experiments: the BUBBLE experimental campaign, carried out from 10 June to 10 July 2002 in Basel (Rotach, 2005); the CAPITOU experimental campaign carried out from February 2004 to March 2005 in Toulouse (Hidalgo et al., 2008). In Basel, a RMSE between the predictions and observations on urban site of 0.9 °C was achieved; the CAPITOU campaign showed instead a RMSE of 1.1 °C.

Another research that focused on the validation of an UWG model of downtown Abu Dhabi, reported a good agreement with the experimental measurements, with the air temperature calculated by the UWG closely following the profile of air temperature recorded by a rural weather station (Bande et al., 2019).

### 3.4. ENVI-met simulations

The ENVI-met version 4.4 is selected because it is capable of suitably simulating major processes in the atmosphere that affect urban microclimate based on a well-grounded physical basis (ENVI-met V4.4, 2020; Simon, 2016). ENVI-met is a numerical prognostic calculation code based on a holistic model that allows a complex modelling and detailed investigation of urban microclimate, as well as small-scale interactions between buildings, surfaces and plants (Ali-Toudert and Mayer, 2006).

ENVI-met estimations are based on a three-dimensional CFD atmospheric model forced by a one-dimensional model given by a vertical profile of weather data at the inflow boundary of the 3D model. An important advance of the ENVI-met version 4.4 if compared to previous versions concerns the possibility of forcing climate data input parameters by creating a user specified weather file including hourly values of dry bulb temperature, relative humidity, global, direct and diffuse solar radiation, wind speed and wind direction, longwave radiation and cloud cover (full forcing weather data input, (Emmanuel et al., 2007)).

Time step is set on the basis of the variation of the sun height in the current settings of ENVI-met. Smaller time steps are required when the solar input is high, whereas bigger ones are used in the morning or evening. A spin-up period advised to be as long as 24–48 h is needed for the model to stabilize (Chen et al., 2014; Goldber et al., 2013; Salata et al., 2016).

As concerns soil conditions, they are modelled through four layers of different depth below the ground surface: the upper layer extends 20 cm below the ground, the second layer extends down to 50 cm, the third layer goes down further until a depth of 200 cm, and finally the deepest layer goes below 200 cm of depth (Bruse, 2006). The soil temperatures assigned to the first three layers are deduced from the thermal profile of the soil based on the various months of the year, while the last one is kept constant (Busby et al., 2009).

Further, to improve the stability of lateral boundary conditions for the core model without increasing computational time, ENVI-met allows surrounding the domain with nesting grids so that the flow field re-establishes its simple structure after it has crossed the core model (Bruse, 1999; Chatzinikolaou et al., 2018).

The software thus implements theoretical physical models as systems of nonlinear equations and solves them through mathematical formulations including three main prognostic variables that allow analyzing the interactions between local environment and the atmosphere on a local basis (Bruse and Fleer, 1998; Bruse, 2018). The analytical model is based on Navier-Stokes equations for wind flow, atmospheric flow turbulence equations, energy and momentum equations and boundary condition parameters (Bruse and Fleer, 1998).

More relevant to urban studies is the fact that ENVI-met allows taking into account also the contributions due to:

- Shortwave and longwave radiation fluxes with respect to shading, reflection, and re-radiation from building systems and the vegetation;
- Transpiration, evaporation, sensible and latent heat fluxes from the vegetation into the air including full simulation of all plant physical parameters;
- Water and heat exchange at the ground layer.

**Table 2**  
Statistical indices used for model validation.

Index	Name	Formula	U.M.
% error	Percent error/difference	$\%error = \frac{m-s}{m} = 1 - \left(\frac{s}{m}\right)$	%
MAE	Mean absolute error	$MAE = \frac{\sum_{i=1}^n  m_i - s_i }{n}$	data-dependent
RMSE	Root mean square error	$RMSE = \sqrt{\frac{\sum_{i=1}^n (m_i - s_i)^2}{n}}$	data-dependent
d	Index of agreement	$d = 1 - \frac{\sum_{i=1}^n (s_i - m_i)^2}{\sum_{i=1}^n ( s_i - \bar{m}  +  m_i - \bar{m} )^2}$	-
r	Pearson correlation coefficient	$r = \frac{\sum_{i=1}^n (m_i - \bar{m})(s_i - \bar{s})}{\sqrt{\sum_{i=1}^n (m_i - \bar{m})^2} \sqrt{\sum_{i=1}^n (s_i - \bar{s})^2}}$	-
R <sup>2</sup>	Coefficient of determination	$R^2 = 1 - \frac{\sum_{i=1}^n (m_i - s_i)^2}{\sum_{i=1}^n (m_i - \bar{m})^2}$	-

Given that radiant energy fluxes are the major factors causing differences in local climate in urban environments (Bruse, 2006), the modelling equations of incoming shortwave and longwave fluxes adopted in ENVI-met are reported in the following as reference.

The shortwave radiation budget at height  $z$  can be summed up as:

$$Q_{sw}^0(z) = \sigma_{sw,dir}(z)Q_{sw,dir}^0 + \sigma_{sw,diff}(z)\sigma_{svf}Q_{sw,diff}^0 + (1 - \sigma_{svf}(z))Q_{sw,dir}^0 \bar{a} \quad (1)$$

with  $Q_{sw}^0$  being the incoming shortwave radiation at the upper boundary of the model in its direct ( $Q_{sw,dir}$ ) and diffuse ( $Q_{sw,diff}$ ) components. The term  $\sigma_{svf}$  is the local sky view factor, a measure of the amount of sky seen from the centre of a grid cell; it ranges from 0 (no sky visible) to 1 (completely free sky). The coefficients  $\sigma_{sw,dir}$  and  $\sigma_{sw,diff}$  describe the influence of vegetation on direct and diffuse shortwave radiation; such coefficients range from 0 for total absorption to 1 for undisturbed fluxes. The additional last term considers reflection of shortwave radiation from the environment, with  $\bar{a}$  denoting the average albedo of all walls within the model area.

The downward and upward longwave radiant fluxes at level  $z$  are defined as follow:

$$Q_{lw}^{\downarrow}(z) = \sigma_{lw}^{\downarrow}(z, z_p)Q_{lw}^{\downarrow,0} + (1 - \sigma_{lw}^{\downarrow}(0, z))\epsilon_f \sigma_B \bar{T}_{f+}^4 + (1 - \sigma_{svf}(z))\epsilon_w \sigma_B \bar{T}_w^4 \quad (2)$$

$$Q_{lw}^{\uparrow}(z) = \sigma_{lw}^{\uparrow}(0, z)\epsilon_s \sigma_B \bar{T}_{so}^4 + (1 - \sigma_{lw}^{\uparrow}(0, z))\epsilon_f \sigma_B \bar{T}_{f-}^4 \quad (3)$$

being  $Q_{lw}^{\downarrow,0}$  the incoming longwave radiation at the upper edge of the model,  $Q_{lw}^{\downarrow}(z)$  the downward and  $Q_{lw}^{\uparrow}(z)$  the upward longwave radiation fluxes at  $z$  height. The coefficients  $\sigma_{lw}^{\downarrow}$  and  $\sigma_{lw}^{\uparrow}$  describe the influence of vegetation on the downward and upward long wave radiation respectively. The terms  $\bar{T}_{f+}$  and  $\bar{T}_{f-}$  are the average foliage temperature of the overlying and underlying vegetation layer,  $\bar{T}_w$  is the average wall temperature of walls as 'seen' from the grid point and  $\bar{T}_{so}$  is the ground surface temperature. The terms  $\epsilon_f$ ,  $\epsilon_s$  and  $\epsilon_w$  denote the emissivity of the foliage, ground surface and walls, in order.  $\sigma_B$  is the Stephan-Boltzmann constant ( $5.67 \cdot 10^{-8} \text{ W} \cdot \text{m}^{-2} \cdot \text{K}^{-4}$ ).

In the longwave radiant balance, it is assumed that shielding vegetation layers will absorb part of the radiant flux and replaces it with their own longwave radiation, whereas the last term in Eq. (2) takes into account the influence of surrounding buildings by adding additional fluxes weighted by the sky-view-factor (Huttner, 2012).

Starting with ENVI-met 4.0, an improvement of the reflective shortwave calculation has been achieved through the addition of the Indexed View Sphere (IVS) model (Govehovitch et al., 2018). This model aims at better evaluating the reflected radiation received by building façades from their surrounding environment. In particular, each urban element is considered using its actual state (sun reflection, thermal radiation) instead of averaged fluxes. In light of this, the incoming shortwave radiation for a building is given by:

$$Q_{Bldg,sw,in}(x, y, z) = \sigma_{svf,Bldg,in}(x, y, z)Q_{Bldg,sw,refl}(x, y, z) \quad (4)$$

with  $Q_{sw,Bldg,in}$  representing the incoming shortwave radiation,  $\sigma_{svf,Bldg,in}$  is the Sky View Factor (SVF) and  $Q_{Bldg,sw,refl}$  is the shortwave radiation reflected by the close surrounding. On the other hand, the reflected radiation coming from a façade is evaluated as follows:

$$Q_{Bldg,sw,refl}(x, y, z) = \frac{1}{36} \sum_{az=0}^{35} \sum_{h=0}^8 \xi(h, az) Q_{sw,refl}^{out}(h, az) \quad (5)$$

$\xi(h, az)$  is the actual shielding,  $az$  is the azimuth and  $h$  is the height of the sun. The use of the IVS module can have a large impact on the simulation time: preliminary simulations indeed showed a doubling of the time needed for simulations for the case study area discussed in Section 4.

Finally, the introduction of the plant-as-object model allows considering plants as dynamic objects that react to outdoor weather conditions through detailed evapotranspiration processes using an adaptation of the well-known empirical Jacob's model. This, along with the use of full-forcing weather data boundaries, has been demonstrated to correctly simulate the transpiration rate of trees at least under clear and slightly cloudy sky conditions (Simon et al., 2018).

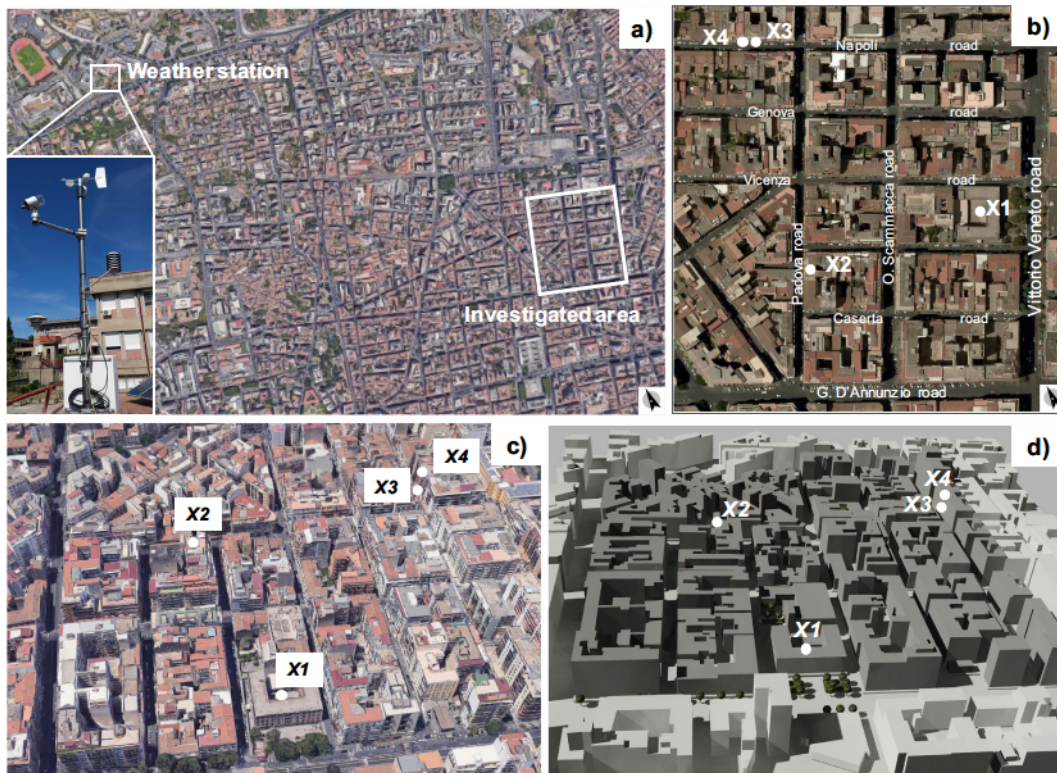


Fig. 5. Investigated area in downtown Catania: a) Digital 2D map including the study area and the suburban weather station location; b) 2D view; c) axonometric view; d) 3D model of the area.

### 3.5. Statistical analysis for model validation

Different statistical indices are used to quantify the discrepancies between the experimental and simulated data. Considering the measured ( $m$ ) and simulated ( $s$ ) variables for each time step  $i$  for a total of  $n$  data samples, the quantitative indicators adopted in this study are reported in Table 2.

The Mean Absolute Error (MAE) is the average of all absolute errors and expresses the difference between actual and predicted values. It represents the vertical or horizontal distance between each point and the equality line (Battista et al., 2016).

The Root Mean Square Error (RMSE) is instead the standard deviation of the residuals (i.e. the differences between observed and predicted values). Residuals are a measure of how far from the regression line data points are. It is worth to notice that few large errors can lead to a great RMSE value (Battista et al., 2016; Ramos Ruiz and Fernández Bandera, 2017).

The index of agreement ( $d$ ) describes the relative variability of predicted ( $s_i$ ) and observed ( $m_i$ ) values from an estimate of the true mean, that is the mean observed value ( $m$ ). It was developed by Willmott as a standardized measure of the degree of model prediction error and varies between zero and one. A value of one indicates a perfect match, while zero indicates no agreement at all (Willmott, 1982; Willmott et al., 2012).

The Pearson's coefficient ( $r$ ) measures the intensity of the correlation between two random variables or two quantitative statistical characters. It is the ratio between the covariance of the two variables and the product of their mean square deviations.

Finally, the coefficient of determination ( $R^2$ ) indicates how close simulated values are to the regression line of the measured values. The index is defined as the proportion of the variance in the dependent variable ( $s_i$ ) that is predictable from the independent variable ( $m_i$ ).  $R^2$  is limited to between 0 and 1, where the upper value means that the simulated values match the measured ones perfectly and the lower ones do not (Ramos Ruiz and Fernández Bandera, 2017).

## 4. Case study area

### 4.1. Morphological and typological characteristics

A neighborhood in the urban area of Catania is selected as a case study. Catania is a city located in southern Italy (Lat. 37.30 North, Long. 15.07 East), with a climate characterized by warm and humid summer and moderately cold and wet winter seasons (the reported Köppen-Geiger classification is Csa). The selected area is a district resulted from the expansion process that the city experienced in the 1960s. The altitude level of the investigated urban district is 100 m lower than the site where the reference weather station is located,



**Table 3**  
Morphological parameters of the investigated area.

District parameters	Symbol	Value	Unit
Plan area of the site	$A_{site}$	129,000	$m^2$
Building area	$A_{bldg}$	60,528	$m^2$
Building density (site coverage ratio)	$\rho_H$	47%	–
Vertical to horizontal built ratio (aspect ratio)	$VH_u$	1.36	–
Impervious surface fraction	$A_{imp}/A_{site}$	97%	–
Pervious surface fraction	$A_{per}/A_{site}$	3%	–
Vegetation surface	$A_{veg}/A_{site}$	1%	–
Weight average building height	$h_{wtd}$	16.10	m

**Table 4**  
Input parameters for the UWG model.

Parameters	Setting	Unit
Microclimate characteristics		
Urban Boundary Layer Height – Daytime	1000	m
Urban Boundary Layer Height – Night time	50	m
Inversion height	150	m
Rural Station Model (RSM) temperature reference height	10	m
Rural Station Model (RSM) wind reference height	10	m
Circulation coefficient	1.2	–
UCM – UBL exchange coefficient	1	–
Heat flux thresholds for daytime conditions	150	$W/m^2$
Heat flux thresholds for night-time conditions	50	$W/m^2$
Minimum wind velocity	0.3	m/s
Rural average obstacle height	0.1	m
Urban characteristics		
Average building height	16.1	m
Fraction of waste heat into canyon	0.7	–
Building density (site coverage ratio)	0.47	–
Vertical to horizontal ratio	1.36	–
Urban area characteristic length	250	m
Roof albedo	0.10	–
Pavement thickness	0.50	m
Sensible Anthropogenic Heat (peak)	30.0	$W/m^2$
Latent Anthropogenic Heat (peak)	3.0	$W/m^2$
Vegetation parameters		
Urban area vegetation coverage	0.001	–
Urban area tree coverage	0.009	–
Start month of vegetation participation	March	–
End month of vegetation participation	October	–
Vegetation albedo	0.25	–
Latent fraction of grass	0.6	–
Latent fraction of tree	0.7	–
Rural vegetation coverage	0.01	–

while the distance between them is of about 4 km. Fig. 5 reports the digital 2D map of the urban context of Catania, along with 2D and 3D aerial views and the geometrical 3D model used for simulation purposes. The points X1, X2, X3 and X4 represent the places where the microclimate portable station was placed during the ground survey. The investigated area has a high building density, with majority of mid-rise residential buildings, stand-alone retail and warehouses at the street level, and is characterized by remarkable repetitiveness and low quality of both the settlement patterns and the formal characteristics of the buildings. Consequently, buildings with scarce sunshine and ventilation conditions characterize the settlement. The area has a public space of poor quality and the vegetation areas are almost absent. The total land area of the investigated neighborhood is approximately 129,600  $m^2$ .

In total, 167 buildings are considered, out of which 165 are residential buildings, one is a primary school and the last one is a supermarket. Table 3 reports the district parameters of the urban area.

The pervious surface fraction is about 3% of the total area, while vegetation occupies about 1% of the total area and it is characterized by a few street trees and some trees and shrubs in the garden of a school. With reference to the district parameters (see Table 3), the selected area is classified as ‘Compact midrise’ according to classification of Local Climate Zone (LCZ) proposed by Oke and Stewart (Stewart and Oke, 2012).

#### 4.2. UWG data for the morphing procedure

The parameters used for modelling the selected area in UWG v.4.1 tool are categorized into three groups: microclimate

**Table 5**  
Settings of building parameters implemented in the UWG.

Building parameters	Residential	Primary school	Unit
Glazing ratio	0.48	0.35	–
Wall U-value	1.15	1.50	W/m <sup>2</sup> K
Roof U-value	1.00	1.10	W/m <sup>2</sup> K
Window U-value	4.0	4.5	W/m <sup>2</sup> K
Window SHGC	0.80	0.85	–
Infiltration rate	0.5	0.5	ACH
Lighting load density	8	15	W/m <sup>2</sup>
Equipment load density	12	10	W/m <sup>2</sup>
Occupancy density	25	8	m <sup>2</sup> /person
Indoor air temperature set point	26	26	°C
Chiller COP	2.5	2.5	–

characteristics, district parameters and vegetation variables. A summary of the key input parameters of the UWG model are reported in Table 4.

As for the choice of the various parameters, the Urban Boundary Layer (UBL) model is delimited at the top by a height that varies in relation to the horizontal scale of the urban morphology and to time. For a neighborhood of size ranging from  $100 \times 100 \text{ m}^2$  to  $1000 \times 1000 \text{ m}^2$ , the daytime boundary layer height can be assumed equal to 1000 m while for bigger sizes the height of UBL usually ranges from 1000 m to 2000 m (Bueno et al., 2013a; Barlow, 2014). On the other hand, during night time the UBL is usually much lower (Bueno et al., 2013a). In relation with the investigated urban scale, an UBL height of 1000 m for daytime and 50 m for nighttime has been set accordingly.

The Rural Station Model (RSM) is instead a rural canopy model that takes as input the hourly values of air temperature and wind speed measured at the rural site and then calculates the sensible heat fluxes to be provided to the Vertical Diffuse Model (VDM) and the Urban Boundary Layer (UBL) models (Bruse and Fleer, 1998). Under urban-breeze circulation, a circulation velocity coefficient equal to 1.2 was used to calculate the characteristic circulation velocity according to (Bueno et al., 2013a; Bueno et al., 2013b).

In terms of anthropogenic heat sources, average values range from 20 to 40 W/m<sup>2</sup> in summer and from 70 to 210 W/m<sup>2</sup> in winter according to the literature (Bueno et al., 2013b; Sailor, 2011). Taha gathered data from a number of early inventory-based approaches and found that the city-wide estimates of anthropogenic heat typically ranged from 15 to 150 W/m<sup>2</sup> (Taha, 1997). In relation with existing published data concerning buildings' energy consumption and population density of a compact mid-rise city, the peak values of 150 W/m<sup>2</sup> for daytime and 50 W/m<sup>2</sup> for nighttime are adopted. With a reference to a mid-dense city, a fraction of waste heat into canyon of 0.7 is selected.

Urban characteristic such as average building height, site coverage ratio, vertical to horizontal ratio, area vegetation and area tree coverage come from the Digital Surface Model (DSM) of Catania in GIS environment (*Laboratorio per la Pianificazione Territoriale Ambientale (LAPTA) of the Department Civil Engineering and Architecture of the University of Catania, 2021*).

Albedo and emissivity values were taken from various literature references (Santamouris et al., 2011; McIlvaine et al., 2000). In particular, the albedo values of the urban materials were chosen based on a comparison between the values measured in the visible range as described in Section 3.2 and the corresponding integral solar values reported in the literature for the same materials. This is because the albedo value required by the software to correctly model the radiant heat transfer from every surface is the integral solar value (i.e. in the range 250–2500 nm), while the instrument was able to report only the visible range (380–780 nm).

This procedure should ensure a better predictive power of the simulations as suggested by Maggioletto et al. (Maggioletto et al., 2014).

The key parameters of the building thermo-physical properties, energy loads and HVAC system, are all set as weighted averages based on corresponding area (or volume) according to average model (AM). Table 5 summarizes these building parameters.

The thermo-physical properties of building components (U-value, SHGC, infiltration rate and coefficient of performance COP) of the cooling systems come from existing studies on similar building typologies in this area (Evola et al., 2020). As for the density of internal loads (occupancy, lighting and equipment) and indoor air temperature set points, the values taken from national standards and technical recommendations are considered in relation to the specific use of the buildings.

#### 4.3. Simulation model in ENVI-met

In the input file editor of the ENVI-met graphical interface, an area of 129,600 m<sup>2</sup> is implemented as the simulation domain. Because ENVI-met has been found to not be grid independent even in the case of absence of buildings and other urban obstacles (Crank et al., 2018), two different mesh resolutions have been tested according to the computational capabilities of our PC (Intel i7-4790K; RAM 32 GB, Free disk space 550 GB): one with  $3.0 \times 3.0 \times 1.0 \text{ m}^3$  dimensions and another with  $4.0 \times 4.0 \times 1.0 \text{ m}^3$  dimensions. Given that air temperature results deviated, on average, less than 5% between the two mesh options, the coarser mesh of  $4.0 \times 4.0 \times 1.0 \text{ m}^3$  was finally retained. As a result, a total area of  $360 \times 360 \text{ m}^2$  in the horizontal extension and a vertical extension of 100 m are obtained. The grid has a fixed spacing in the x and y-axes while along the vertical z-axis a telescoping grid is adopted. The telescoping starts from the height of 38 m above ground, which corresponds to the highest building within the domain, in order to maintain a constant value of 1 m along z-axis in the core area. Above this height, a mesh size of 2 m along z-axis and a number of grid cells equal to 50 was set in order to have sufficient space between building top and model border (a telescoping factor of 20% was set here). In light of these

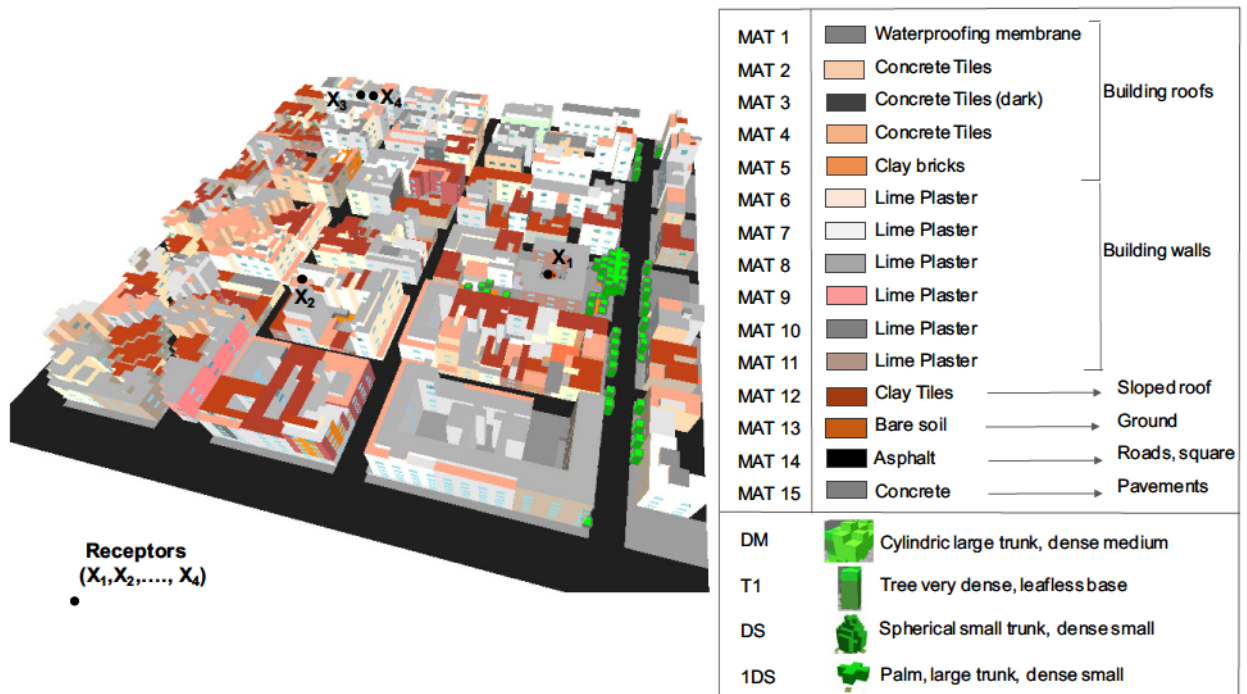


Fig. 6. ENVI-met simulation model: 3D view with location of the receptor points and list of building materials and trees implemented.

Table 6  
Optical and physical properties of outer surface materials.

MAT	Materials	Color	Surface	Albedo ( $\rho$ )	Emissivity ( $\epsilon$ )
1	Waterproofing	Dark grey	Flat roof	0.15	0.92
2	Concrete tiles	Beige	Flat roof	0.40	0.90
3	Concrete tiles	Dark	Flat roof	0.10	0.90
4	Concrete tiles	Clear beige	Flat roof	0.40	0.90
5	Clay bricks	Reddish	Flat roof	0.30	0.95
6	Lime plaster	Beige	Wall	0.50	0.93
7	Lime plaster	White	Wall	0.60	0.90
8	Lime plaster	Light grey	Wall	0.40	0.90
9	Lime plaster	Red	Wall	0.30	0.95
10	Lime mortar	Grey	Wall	0.30	0.93
11	Lime plaster	Brown	Wall	0.25	0.90
12	Clay tiles	Red	Sloped roof	0.30	0.95
13	Bare soil	Brown	Ground	0.20	0.98
14	Asphalt	Dark grey	Roads	0.10	0.90
15	Concrete	Grey	Pavements	0.30	0.90

settings, the mesh of  $4.0 \times 4.0 \times 2.0 \text{ m}^3$  and a grid of  $90 \times 90 \times 50$  cells were retained for simulations. Along the lateral domain borders, six cells for every dimension in space are set as nesting grids.

Fig. 6 displays the 3D Model of the investigated area in the current conditions.

In ENVI-met model, the time step dynamically adapts to the sun height. Three intervals are defined by 2 boundary values of the sun height, and are set by default to 10 s, 5 s and 2 s) respectively. In this work, a constant simulation time step of 2 s was used in order to avoid stability problems, while two cycles of simulations were carried out for the analyzed periods. A simulation time of 78 h was set for the period 7th–9th August 2019 and one of 75 h for the period 16th–18th September 2019, in order. Simulations started at 6.00 am of the previous day respect to the selected days so that materials can adequately heat up over the first day. Thus, the first cycle of simulation goes from 6.00 a.m. on 6th to 12.00 a.m. on 9th August while the second cycle from 6.00 a.m. on 15th to 9.00 a.m. on 18th September.

In the domain core, four receptors are selected for the analysis of the results named X1, X2, X3 and X4 respectively. The receptor (X1) is placed at the floor level of the internal courtyard of a primary school, while receptor X2 is placed on the flat roof of a building 15 m tall. The receptors X3 and X4 are located on the roof terrace of two different buildings of 18 m and 15 m height respectively. The position of the receptors in the model is chosen in the corresponding points where the actual measurements were carried out.

**Table 7**  
Plant physiological and physical parameters.

	Typology	Species	Height (m)	Number of trees	LAD (–)	Albedo $\rho$ (–)	Transmissivity $\tau$ (–)
DM	Cylindric, large trunk, dense medium	Deciduous	15.0	3	2	0.18	0.30
T1	Tree very dense, leafless base	Deciduous	10.0	21	2.18	0.20	0.30
SS	Spherical, small trunk, dense small	Deciduous	5.0	6	2	0.18	0.30
1DS	Palm, large trunk, dense small	Deciduous	5.0	2	2	0.18	0.30
GG	Base grass, averagely density	–	0.50	–	0.30	0.20	0.30
XX	Base grass, averagely density	–	0.30	–	0.30	0.20	0.30

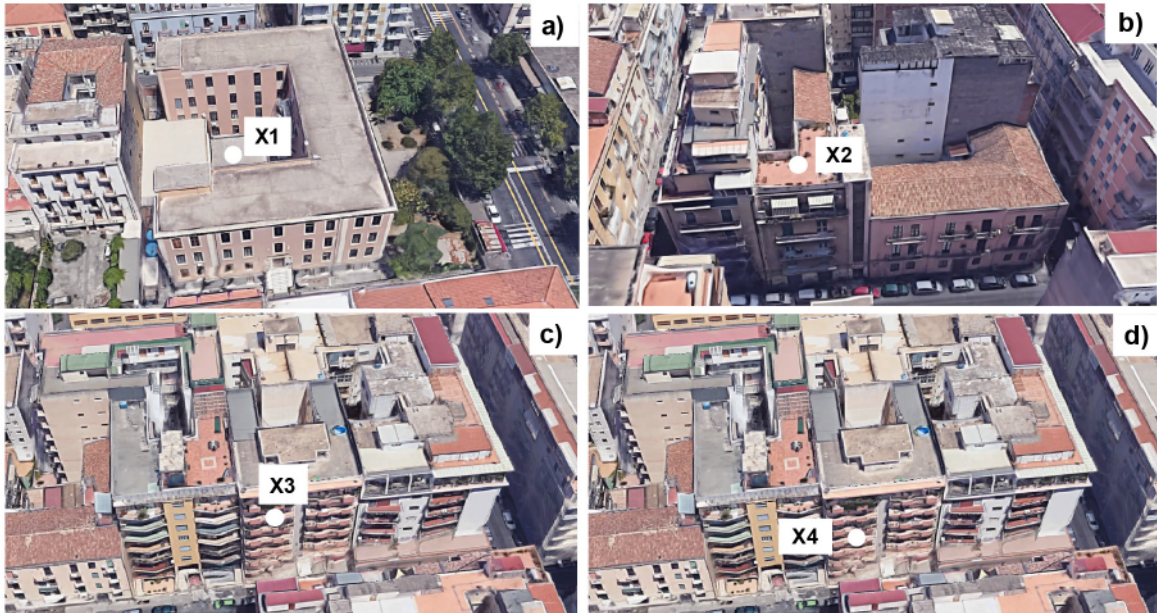


**Fig. 7.** 3D views of the locations where the portable microclimate station was placed: a) X1,  $h = 1.1$  m (7–8 August 2019); b) X2,  $h = 15$  m (8–9 August 2019); c) X3,  $h = 18$  m (16–17 September 2019); d) X4,  $h = 15$  m (17–18 September 2019).

The selected area is modelled with materials' thermal properties chosen according to the criteria discussed in section 4.2 in order to be consistent with the morphing procedure carried out with the UWG tool. Table 6 reports the values of the optical and physical properties thus chosen for the outer surfaces.

The existing trees are predominantly deciduous species but also some small, grass plants are present so that five plant types are implemented in the end: cylindrical large trunk dense medium, tree very dense leafless base, spherical small trunk dense small, palm large trunk dense small and grass averagely dense. The thermo-physical and optical properties of plants, coming from the database manager embedded within ENVI-met, are reported in Table 7. As regards soil conditions, the soil temperatures assigned to the superficial layers were deduced from thermal profile of the soil based on estimates for a typical Mediterranean climate (Busby et al., 2009). The soil temperature below 2 m depth was kept constant during the simulation, while relative humidity values were kept as default values because they are refined using the water content at field capacity value.

#### 4.4. On site weather measurements

The portable microclimate station Delta Ohm Type HD32.3 described in Section 3.1 is used to record the air temperature and relative humidity at the four receptor points (X1, X2, X3 and X4 in order) in the periods between 7th–9th August and 16th–18th September 2019.

Because balconies have been chosen as on site measurement locations for receptors X3 and X4 to analyze also the vertical gradient of temperature within the urban canopy layer, a particular attention is paid to avoid potential boundary effects along the vertical wall facades that could affect the quality of measurements. In this vein, based on the recommendations of Niachou (Niachou et al., 2008), the tripod was placed at a distance of 60 cm from the exterior building wall.

Fig. 7 shows the actual locations where the portable weather station was placed during the field measurement and surveys.

The portable station was placed at 1.1 m above the ground level in the middle of the backyard of a primary school (point X1) from 11.00 a.m. on 7th August to 12.00 a.m. on 8th August (Fig. 7a).

The mobile station was mounted on a tripod of 1.1 m height and placed in the middle of a flat roof of a building 15.0 m tall (point

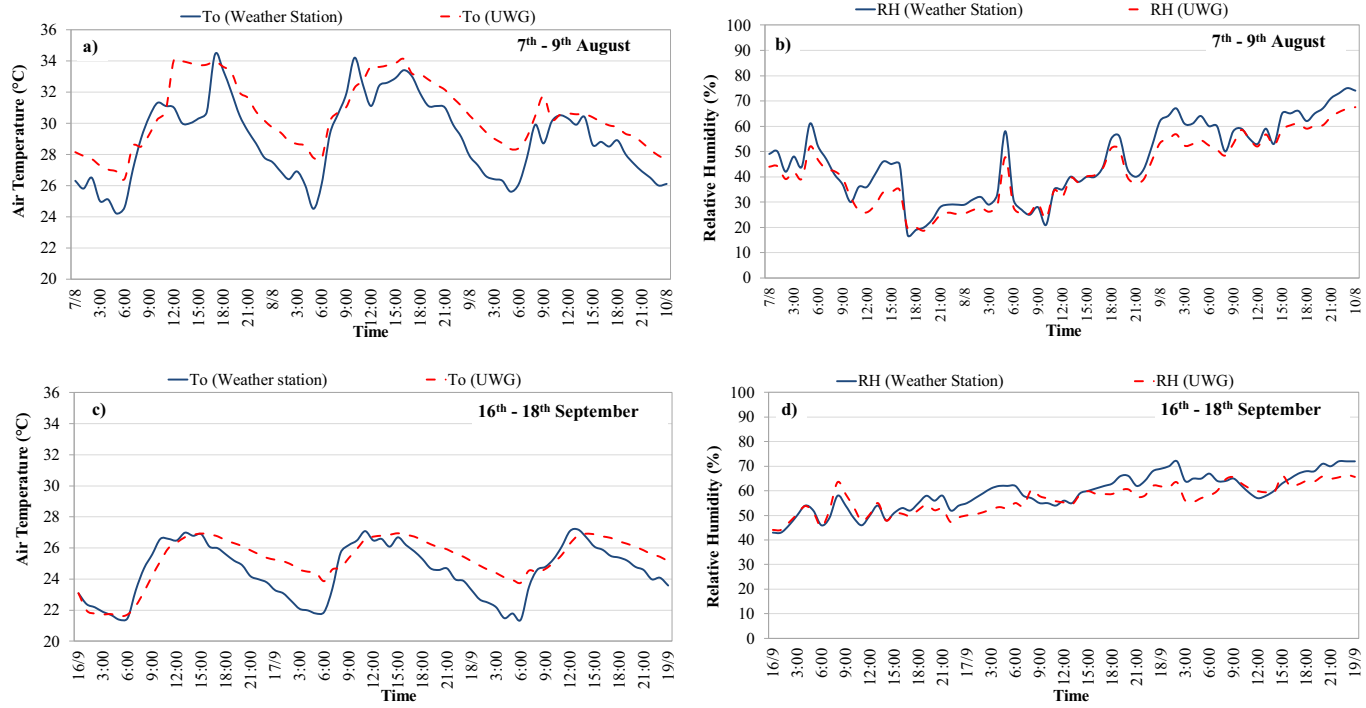


**Fig. 8.** Comparison between suburban weather station data and UWG data: a) Air Temperature during 7th–9th August; b) Relative Humidity during 7th–9th August; c) Air Temperature during 16th–18th September; d) Relative Humidity during 16th–18th September.

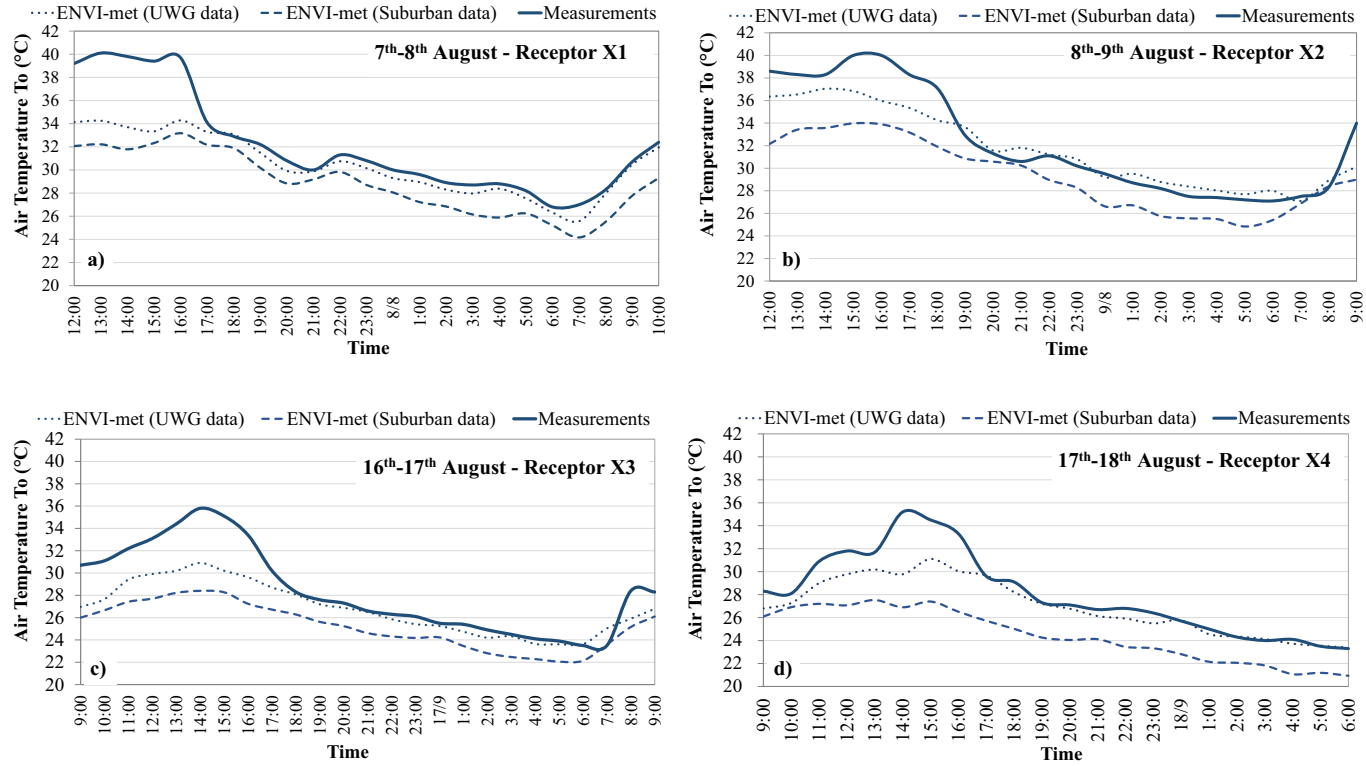


Fig. 9. Comparison between simulated and measured air temperature: a) receptor X1 (h = 1.20 m); b) receptor X2 (h = 15 m); c) receptor X3 (h = 18 m); d) receptor X4 (h = 15 m).

X2) from 12.00 a.m. on 8th August to 12.00 a.m. on 9th August. Afterwards, the same instrument was placed on a sixth floor balcony (point X3) and on a fifth floor balcony (point X4) of the same building (see Fig. 7c and d). The measurements were carried out on from 9.00 a.m. on the 16th to 9.00 a.m. on the 17th of September for receptor point X3 and from 9.00 a.m. on 17th to 9.00 a.m. on 18th September for receptor point X4. Despite receptors X3 and X4 have almost the same position, the location X4 is taken into account because on-site measurements carried out on X4 are referred to the next day. In fact, the validated numerical model in different periods can offer more accuracy in microclimate simulation results especially in the case when a CFD model is set with a low grid resolution.

## 5. Results and discussion

### 5.1. Urban microclimate morphing

Fig. 8 depicts the hourly profiles of air temperature and relative humidity calculated by UWG in comparison with those registered by the reference weather station.

It is worth noticing that the hourly values of outdoor air temperature calculated by the UWG tool are around 2–3 °C higher during the night and early morning (6 am) if compared with those recorded by the reference weather station during the period 7th–9th August (Fig. 8a). This result is in line with another study regarding the validation of the microclimate model of an urban canyon realized with UWG tool (Rotach, 2005).

An average increase of about 1–2 °C with respect to the air temperature registered by the stationary meteorological station can be observed starting from the early afternoon (Fig. 8a and c).

Consequently, a decrease in the relative humidity of about 10% in the urban area is achieved with respect to the rural area at night during the periods 7th–9th August and 16th–18th September (see Fig. 8b and d).

The increase of air temperature in the urban area is likely due to the different surface net-wave radiation budget between rural and urban environment and to the anthropogenic heat. In particular, during daytime urban surfaces and building materials absorb and store more solar radiation than vegetation or bare soil surfaces do. As a result, the outdoor surface temperature in the urban areas are higher than that of the surrounding rural areas (so-called Surface Urban Heat Island effect, SUHI (Roth, 2013)). During the evening and night time, the radiation budget is determined by the long wave radiation amongst surfaces and the sky, so the urban area releases – by means of infrared radiation and also convection with the air – a remarkable heat flux towards the surroundings.

In addition, a delay of the peak value of air temperature is estimated by the UWG. This depends on the admittance of the urban surfaces that transfer the heat towards the atmosphere more slowly with respect to plants, shrubs and bare soil surfaces.

### 5.2. Validation of ENVI-met modelling results with field measurements

#### 5.2.1. Air temperature

In order to perform the validation of the ENVI-met microclimate model, the profiles of air temperature, relative humidity and specific humidity from ENVI-met modelling for both scenario S\_1 (forcing with suburban weather data) and scenario S\_2 (forcing with UWG weather data) are compared against those of the measurement campaign.

Fig. 9 shows the comparison between the actual air temperature measurements at the various receptor locations and the corresponding simulated profiles. The comparison reveals an excellent agreement between measured data (solid blue lines) and simulated data from scenario S\_2 (point blue lines) throughout the days considered, while predictions based on scenario S\_1 (dashed blue lines) deviate the most from actual measurements during the hours of maximum solar irradiance (dotted blue line). In fact, for all receptors, the simulated profiles of air temperature are well below the actual measured profiles: the model shows a greater flattening in the simulated data curve if compared to the measured one. In particular, a difference in the air temperature of about 7.5 °C in the simulated data is found at around 14:00 on the 17th of September for receptor X1 and scenario S\_1. Very similar trends are instead reported from late afternoon until early morning for all the receptor positions, and this holds true also for results from scenario S\_2.

The discrepancies during daytime hours, which reach a maximum for scenario S\_2 of 5.5 °C for receptor X1, may be attributed to the simplifications of the Advanced Radiation Transfer Scheme (IVS method) implemented in ENVI-met. In fact, despite the radiation balance offered by the IVS method looks notably improved if compared to that implemented in previous versions of the software, inaccuracies in the calculation within urban canyons as reported in (Liu et al., 2020) may affect the calculation of urban air temperature during the hours of maximum insolation. It is then expected that if applying the approach proposed to either milder climates or considering winter conditions, the discrepancies between measurements and simulations would be lower because of the minor role played by solar radiation in determining the urban energy balance. In fact, lower sun angles would reduce the amount of solar radiation absorbed by building facades and roads within the urban canyons, and consequently the convective heat transfer from these surfaces to the air, thus affecting less air temperature predictions.

Indeed, a similar result has been reported in a recent study that investigated the ENVI-met model's accuracy of an urban canyon in London (UK). The model of an urban area with a similar size ( $300 \times 500 \text{ m}^2$ ), forced with the air temperature and relative humidity generated with the UWG and radiation fluxes calculated with the IVS model, showed an underestimation of the air temperature up to 3.0 °C during the hours of maximum solar radiation (Salvati and Kolokotroni, 2019).

#### 5.2.2. Relative and specific humidity

Fig. 10 reports the profiles of the simulated relative humidity against the values observed during the periods 8th–9th August and 16th–18th September. In this case, both scenarios S\_1 and S\_2 tend to slightly underestimate the relative humidity values of about 8% if

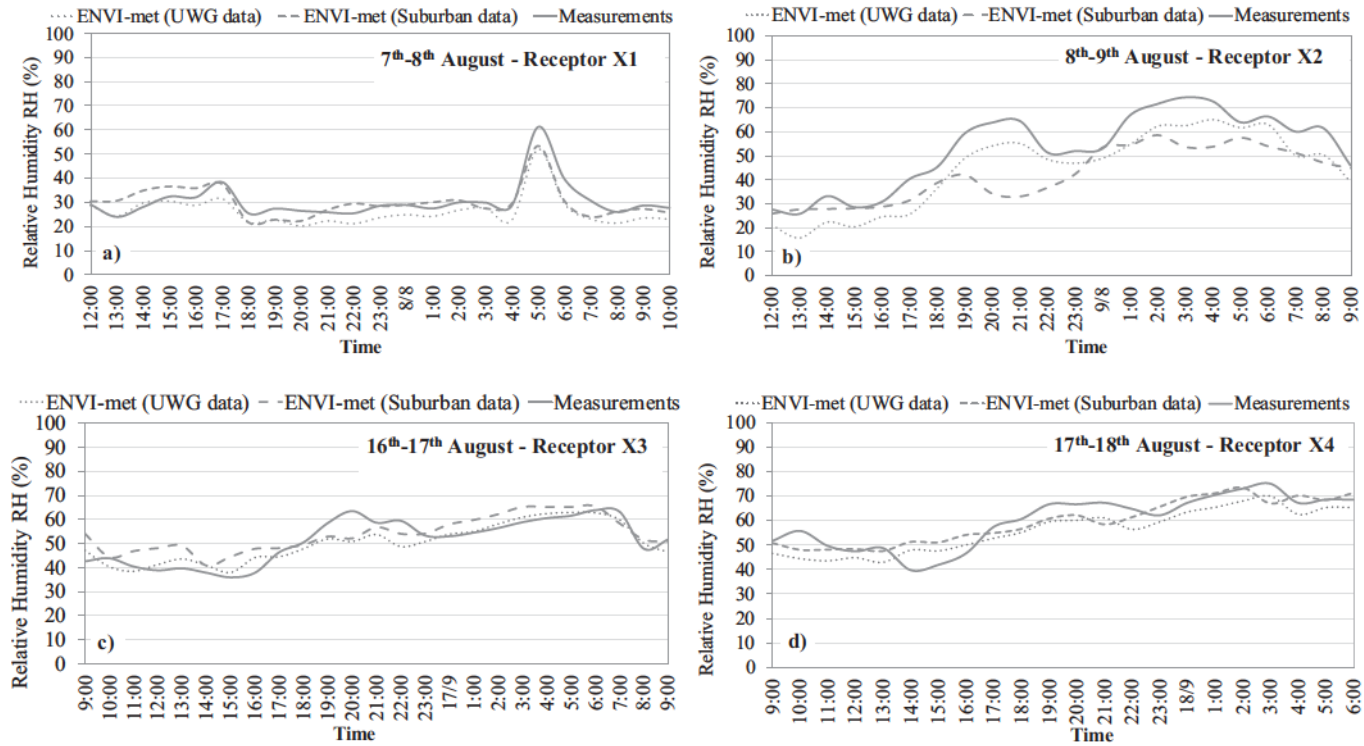


Fig. 10. Comparison between simulated and measured relative humidity: a) receptor X1 (h = 1.20 m); b) receptor X2 (h = 15 m); c) receptor X3 (h = 18 m); d) receptor X4 (h = 15 m).



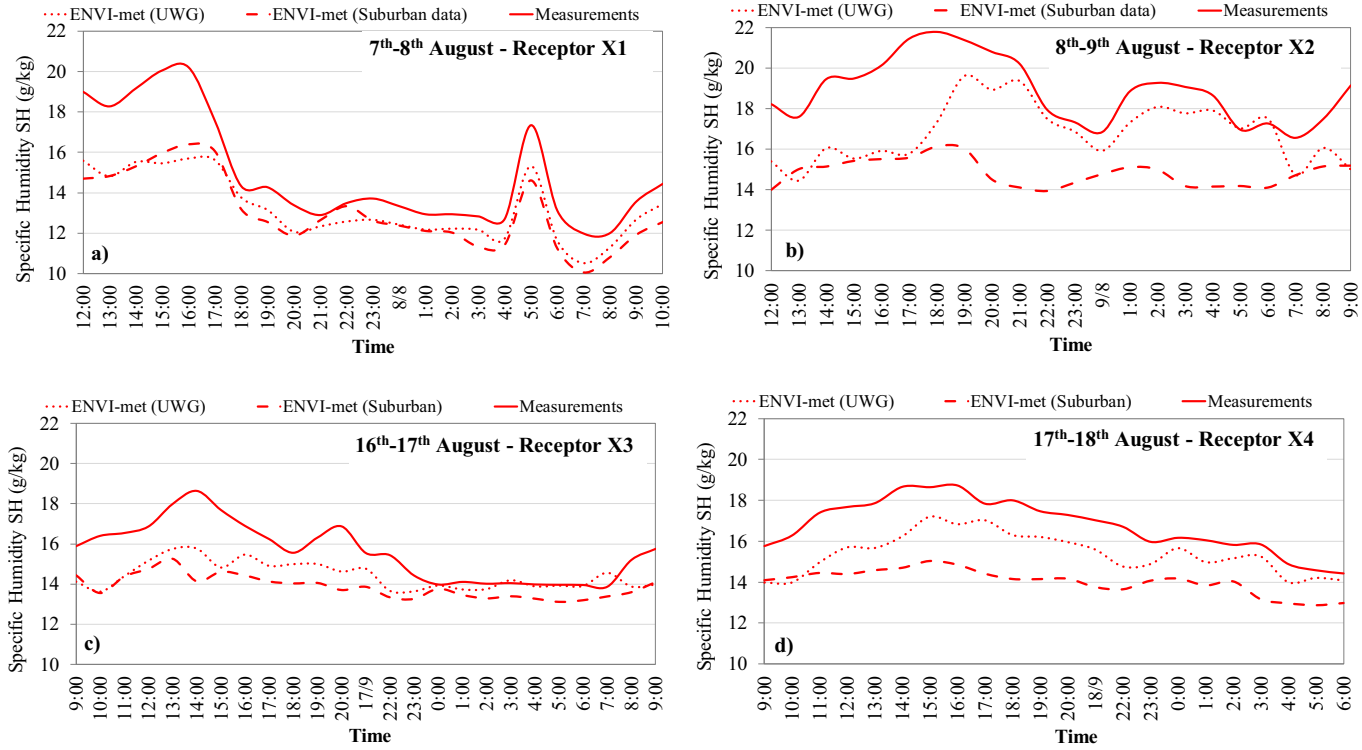


Fig. 11. Comparison between simulated and calculated specific humidity: a) receptor X1 (h = 1.20 m); b) receptor X2 (h = 15 m); c) receptor X3 (h = 18 m); d) receptor X4 (h = 15 m).

**Table 8**  
Validation indices of the ENVI-met model for both scenarios S\_1 and S\_2.

Variable	Statistical indices and units		Locations							
			X1 (h = 1.20 m)		X2 (h = 15.00 m)		X3 (h = 18.00 m)		X4 (h = 15.00 m)	
			7th – 8th August		8th - 9th August		16th - 17th September		17th - 18th September	
			S_1	S_2	S_1	S_2	S_1	S_2	S_1	S_2
T <sub>o</sub>	%error	–	10%	7%	9%	4%	11%	6%	12%	4%
	MAE	°C	3.26	1.70	3.02	1.39	3.16	1.52	3.63	1.17
	RMSE	°C	3.95	2.72	3.61	1.83	3.71	2.36	4.00	1.80
	d	–	0.73	0.85	0.81	0.94	0.71	0.86	0.70	0.90
	r	–	0.90	0.92	0.94	0.96	0.95	0.96	0.92	0.96
	R <sup>2</sup>	–	0.81	0.85	0.90	0.92	0.88	0.92	0.84	0.91
RH	%error	–	14%	12%	18%	17%	11%	7%	10%	9%
	MAE	%	4.70	3.28	10.83	8.18	5.14	3.65	6.10	5.42
	RMSE	%	4.20	5.23	13.86	8.79	6.22	4.79	6.45	5.78
	d	–	0.87	0.90	0.77	0.92	0.85	0.92	0.90	0.91
	r	–	0.83	0.93	0.83	0.97	0.80	0.87	0.86	0.91
	R <sup>2</sup>	–	0.69	0.87	0.67	0.94	0.64	0.77	0.74	0.83
SH	%error	–	12%	10%	21%	11%	11%	7%	16%	8%
	MAE	g/kg	1.90	1.60	4.06	2.11	1.75	1.25	2.74	1.37
	RMSE	g/kg	2.24	2.10	4.26	2.52	2.02	1.56	2.85	1.53
	d	–	0.78	0.79	0.38	0.52	0.56	0.62	0.47	0.70
	r	–	0.94	0.95	0.59	0.42	0.80	0.75	0.86	0.85
	R <sup>2</sup>	–	0.88	0.91	0.64	0.57	0.56	0.64	0.73	0.76

compared to the observed values for all the receptor points during daytime. Nevertheless, the comparative assessment reveals that the simulated profiles show high similarity with those actually measured. In fact, Fig. 10 shows that the hourly profiles of computed and measured values have the same trend for receptors X1, X2 and X4. As shown in Fig. 10b, the RH values observed from the site measurement campaign and the RH calculated by ENVI-met for receptor X2 are those that deviate the most in the case of scenario S\_1 (a difference of about 30% is recorded at 9 pm of the 8th of August). On the other hand, for the same receptor, the peak difference is lower than 10% for scenario S\_2.

In the case of receptors X3 and X4, the simulated and measured values tend to overlap (see Fig. 10c and d). It is worth highlighting that measured and predicted relative humidity values are almost the same during nighttime, in particular, from 12.00 am to 9.00 am of 17th of September right when the simulated and measured temperatures are coincident.

In order to evaluate the possible influence of air temperature on relative humidity predictions, the specific humidity SH (g/kg) has been calculated through psychrometric relations and air pressure values obtained from the local weather web service for the selected days. The results of this calculation, reported in Fig. 11, show that overall the measured trend (solid lines) is followed well by scenario S\_2 (forcing with UWG weather data, point lines), with a maximum deviation of 4 g/kg for receptors X1 and X2 during early afternoon. The upper receptors (X3 and X4, placed at 18 m and 15 m above the ground respectively) show instead a maximum deviation that is always below 2 g/kg.

On the other hand, such discrepancies are higher for scenario S\_1, i.e. when forcing ENVI-met with suburban weather data: in this case, SH can be under-estimated by about 6 g/kg at late evening (receptor X2).

### 5.3. Calculation of statistical indices for model validation

To evaluate numerically the deviation between the modelling outputs and the actual measured data, the statistical indices presented in Section 3.4 are calculated and reported in Table 8 for all the four receptors and the two simulation scenarios.

As it is possible to see, the best performances are reported for scenario S\_2 (i.e. when forcing the tool with UWG morphed weather data): in fact, in the case of air temperature, the maximum MAE is predicted for receptor X1 and amounts to 1.7 °C while for all other points it keeps below 1.5 °C. The good correlation with experimental measurements is rebated by the very high values of the correlation coefficient  $r$  and of the coefficient of determination  $R^2$  (both always higher than 0.81). These values are in line and even better than those reported in previous studies as summarized in Section 2.

When it comes to scenario S\_1, it is shown that the estimation of dry bulb air temperature ( $T_o$ ) is in a good approximation with the measured values for all receptors, whose values of Pearson correlation coefficient ( $r$ ) are higher than 0.90 and the values of the determination coefficient ( $R^2$ ) are always above 0.81. In particular, the best result is achieved for receptor X2, where MAE value is 3.02 °C and RMSE is 3.61 °C. In addition, the index of agreement ( $d$ ) approaches 0.81 and the Pearson's correlation coefficient ( $r$ ) achieves a value of 0.94. However, ENVI-met generally tends to underestimate air temperature during daytime, and this is especially true for receptors X1, X3 and X4 for which the value of the index of agreement keeps around 0.70.

As far as relative humidity is concerned, both scenarios predict rather similar results, especially for receptors X3 and X4 that are placed on two consecutive balconies at 18 m and 15 m respectively above the street level. The worst predictions are expected for receptor X2, with a MAE of around 10% and a coefficient of determination  $R^2$  of 0.67 for scenario S\_1 (the corresponding figures for scenario S\_2 are 8% and 0.94 respectively).

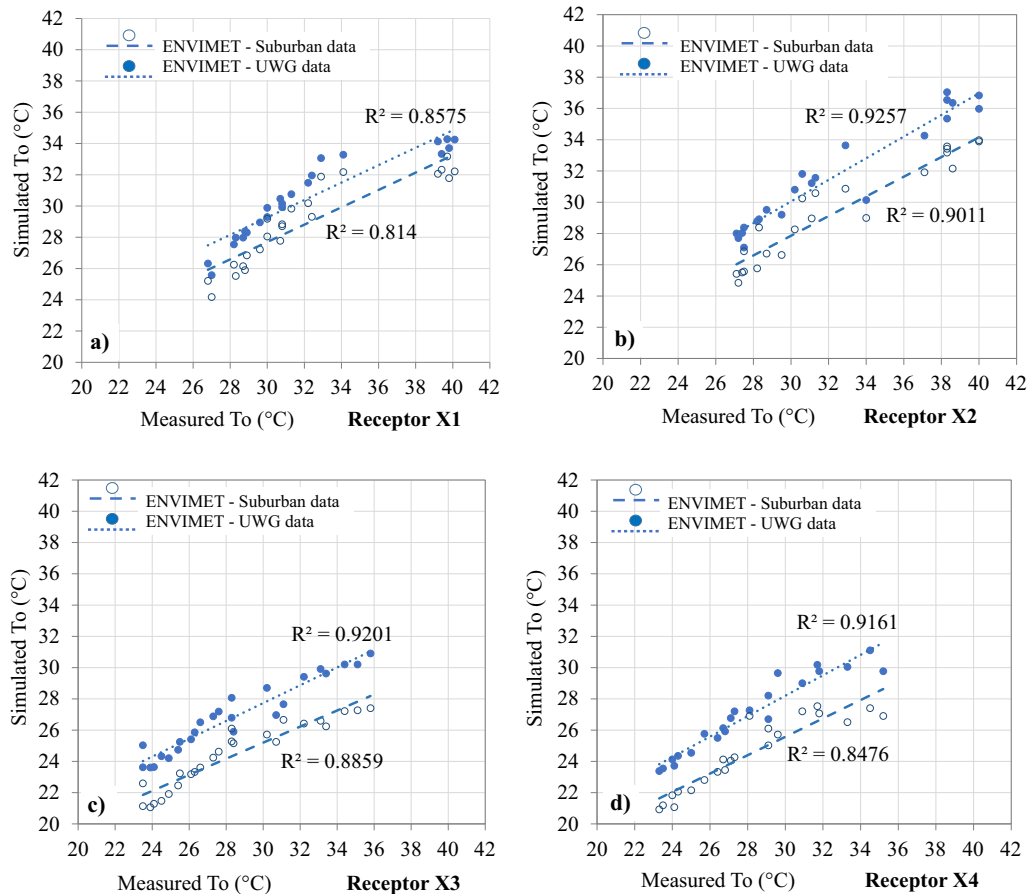


Fig. 11. Linear regression of air temperature (measured vs predicted): a) receptor X1; b) receptor X2; c) receptor X3; d) receptor X4.

Similar conclusions can be drawn also in terms of specific humidity, where once again the poorest prediction pertains to receptor X2 under both scenarios: a MAE of 4.06 g/kg and an index of agreement (d) of 0.38 are calculated for scenario S<sub>1</sub>, while in the case of scenario S<sub>2</sub> the corresponding figures are 2.11 g/kg and 0.52 respectively.

A graphical representation of the results obtained by both simulation scenarios is given also in Figs. 11–13, where regression lines are plotted for air temperature, relative humidity data and specific humidity along with the attained coefficient of determination  $R^2$ .

## 6. Conclusions

This paper explored a methodological approach to calibrate a CFD model realized with the ENVI-met software by forcing it with weather data morphed through the Urban Weather Generator (UWG) tool. Taking as demonstration case a densely built urban district in the city of Catania (Italy) for which urban stationary weather stations are not available, the UWG has been employed to generate neighborhood-specific hourly profiles of air temperature and relative humidity from data recorded at a suburban meteorological station to account for the UHI effect. This approach has been compared to results obtained running ENVI-met simulations forced with suburban weather data and validated against on-site measurements at different points in the study domain and for different days of the year.

Despite some simplifications embedded in the Town Energy Balance (TEB) scheme implemented by the UWG tool leading to the definition of an “average” urban canyon representative of the city district under study, results show a close match between locally measured and simulated data of air temperature, relative humidity and specific humidity.

In fact, the calculation of various statistical indices show how the maximum discrepancy in terms of air temperature pertains to a receptor placed in the middle of a courtyard at the street level (receptor X1, MAE = 1.70 °C, d = 0.85). On the other hand, the highest deviations from measured values of relative and specific humidity pertain to receptor X2, which is placed on a terrace at 15 m above the ground. For such a point, the MAE is of 8.18% and 2.11 g/kg for relative and specific humidity respectively, while the corresponding values of the index of agreement d are 0.92 and 0.52 in order.

The corresponding figures for the simulations run forcing ENVI-met with suburban weather data are consistently worse for all receptor points. As examples, the MAE for air temperature at receptor X1 is of 3.26 °C and the index of agreement d is equal to 0.73,

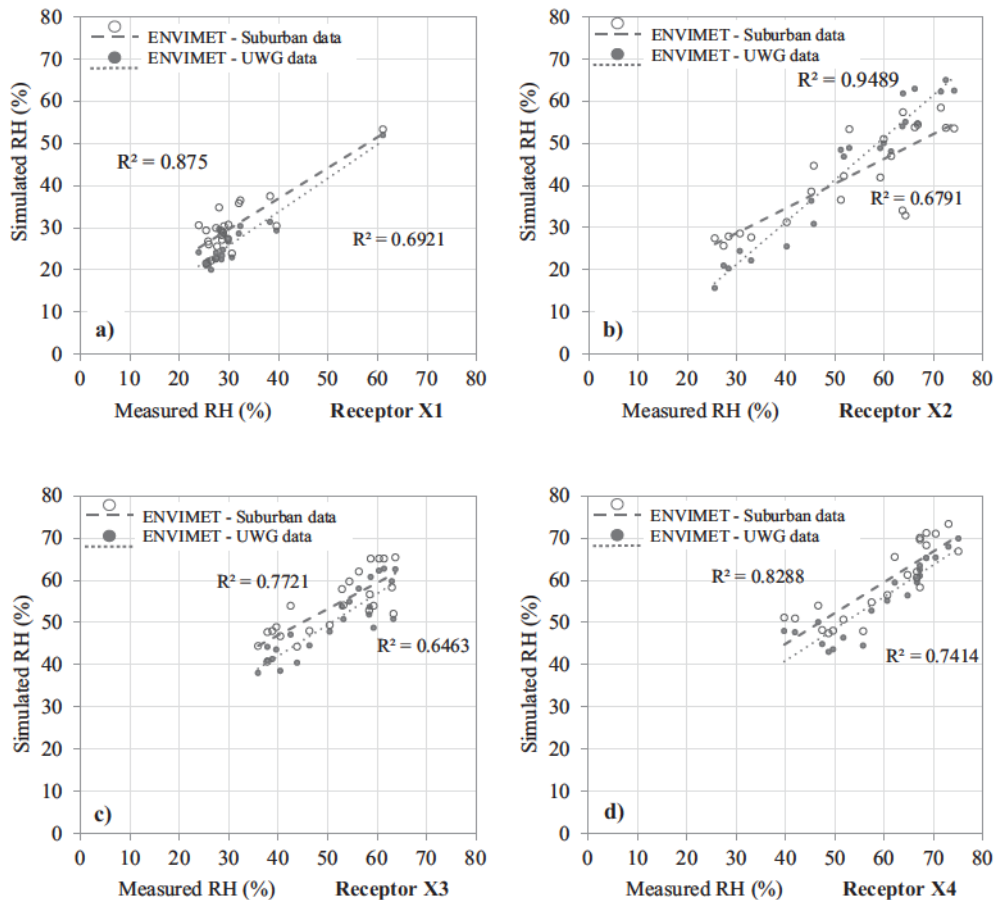


Fig. 12. Linear regression of relative humidity (measured vs predicted): a) receptor X1; b) receptor X2; c) receptor X3; d) receptor X4.

while the corresponding figures in terms of relative humidity for receptor X2 are 10.83% and 0.77.

Based on the statistical analysis and on the detailed investigation of the hourly profiles of weather variables, the proposed approach for calibrating and validating urban ENVI-met models can be considered reliable enough for micro-climate simulation purposes. However, some discrepancies are recorded during the hours of maximum insolation in summer (up to 5.5 °C) for receptors placed in semi-open spaces. These deviations are likely due to inaccuracies of the Advanced Radiation Transfer Scheme (IVS method) implemented in ENVI-met for calculating the radiant energy balance, which in turn affects the convective heat exchanged with the air. Future investigations using the same approach described in this paper should thus analyze different climate conditions and urban layouts in order to gain a wider knowledge of the magnitude of the error.

### Authorship contributions

Please indicate the specific contributions made by each author (list the authors' initials followed by their surnames, e.g., Y.L. Cheung). The name of each author must appear at least once in each of the three categories below.

#### Category 1

Conception and design of study: V. Costanzo, M. Detommaso, F. Nocera; acquisition of data: V. Costanzo, M. Detommaso, F. Nocera; analysis and/or interpretation of data: V. Costanzo, M. Detommaso, F. Nocera;

#### Category 2

Drafting the manuscript: V. Costanzo, M. Detommaso, F. Nocera; revising the manuscript critically for important intellectual content V. Costanzo, M. Detommaso, F. Nocera.

#### Category 3

Approval of the version of the manuscript to be published (the names of all authors must be listed): V. Costanzo, M. Detommaso, F. Nocera.

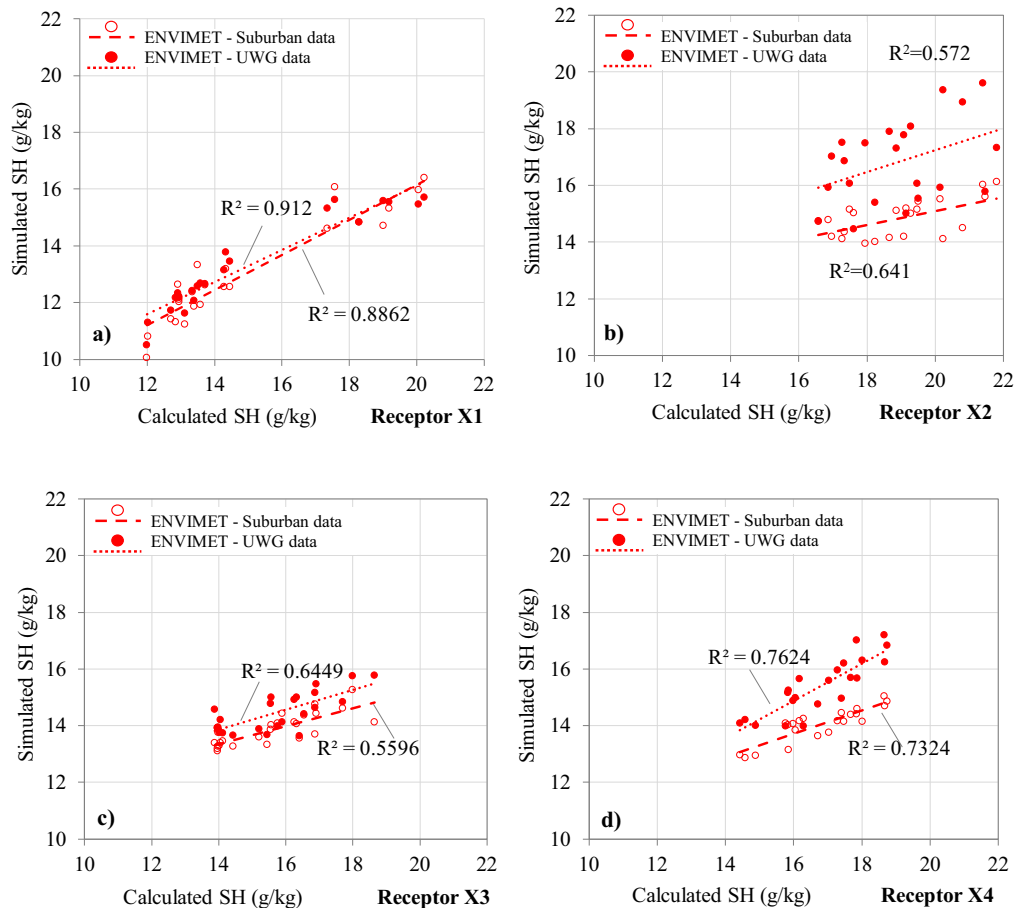


Fig. 13. Linear regression of specific humidity (calculated vs predicted): a) receptor X1; b) receptor X2; c) receptor X3; d) receptor X4.

### Declaration of Competing Interest

The authors declare that they have no known competing financial interests or personal relationships that could have appeared to influence the work reported in this paper.

### Acknowledgements

All persons who have made substantial contributions to the work reported in the manuscript (e.g., technical help, writing and editing assistance, general support), but who do not meet the criteria for authorship, are named in the Acknowledgements and have given us their written permission to be named. If we have not included an Acknowledgements, then that indicates that we have not received substantial contributions from non-authors.

### References

- Ali-Toudert, F., Mayer, H., 2006. Numerical study on the effects of aspect ratio and solar orientation on outdoor thermal comfort in hot and dry climate. *Build. Environ.* 41, 94–108. <https://doi.org/10.1016/j.buildenv.2005.01.013>.
- Andreou, E., 2013. Thermal comfort in outdoor spaces and urban canyon microclimate. *Renew. Energy* 55, 182–188. <https://doi.org/10.1016/j.renene.2012.12.040>.
- Bande, L., Afshari, A., Al Masri, D., Jha, M., Norford, L., Tsoupos, A., Marpu, P., Pasha, Y., Armstrong, P., 2019. Validation of UWG and ENVI-met models in an Abu Dhabi District, based on site measurements. *Sustainability* 11, 4378. <https://doi.org/10.3390/su11164378>.
- Barlow, F.J., 2014. Progress in observing and modelling the urban boundary layer. *Urban Clim.* 10, 216–240. <https://doi.org/10.1016/j.uclim.2014.03.011>.
- Battista, G., Camiolo, E., De Lieto Vollaro, R., 2016. Thermal impact of a redeveloped area on localized urban microclimate: a case study in Rome. *Energy Build.* 133, 446–454. <https://doi.org/10.1016/j.enbuild.2016.10.004>.
- Battista, G., De Lieto Vollaro, R., Zinzi, M., 2019. Assessment of urban overheating mitigation strategies in a square in Rome. Italy. *Solar Energy* 180, 608–621. <https://doi.org/10.1016/j.solener.2019.01.074>.
- Bruse, M., 1999. Die Auswirkungen kleinskaliger Umweltgestaltung auf das Mikroklima. Entwicklung des prognostischen numerischen Modells ENVI-met zur Simulation der Wind-, Temperatur- und Feuchteverteilung in städtischen Strukturen. Dissertation. Ruhr-Universität Bochum.
- Bruse, M., 2006. ENVI-met 3.0: Updated Model Overview. Available at: <http://www.envi-met.com> (last accessed on 15/06/2020).
- Bruse, M., 2018. ENVI-met Technical Model Webpage. <http://www.envi-met.info/doku.php?id=start> (last accessed on 15/06/2020).

- Bruse, M., Fleer, H., 1998. Simulating surface–plant–air interactions inside urban environments with a three dimensional numerical model. *Environ. Model. Softw.* 13, 373–384. [https://doi.org/10.1016/S1364-8152\(98\)00042-5](https://doi.org/10.1016/S1364-8152(98)00042-5).
- Bueno Unzeta, B., 2010. An Urban Weather Generator Coupling a Building Simulation Program with an Urban Canopy Model. *Industrial Engineer, University Malaga*, pp. 74–75.
- Bueno, B., Norford, L., Hidalgo, J., Pigeon, G., 2013a. The urban weather generator. *J. Build. Perform. Simul.* 6 (4), 269–281. <https://doi.org/10.1080/19401493.2012.718797>.
- Bueno, B., Norford, L., Masson, V., 2013b. Calculation of air temperatures above the urban canopy layer from measurements at a rural operational weather station. *J. Appl. Meteorol. Climatol.* 52, 472–483. <https://doi.org/10.1175/JAMC-D-12-083.1>.
- Bueno, B., Roth, M., Norford, L., Li, R., 2014. Computationally efficient prediction of canopy level urban air temperature at the neighborhood scale. *Urban Clim.* 9, 35–53. <https://doi.org/10.1016/j.uclim.2014.05.005>.
- Bueno, B., Nakano, A., Norford, L., 2015. Urban weather generator: a method to predict neighborhood-specific urban temperatures for use in building energy simulations. In: *Proceedings of 9<sup>th</sup> ICUC Conference, Toulouse*.
- Busby, J., Lewis, M., Reeves, H., Lawley, R., 2009. Initial geological considerations before installing ground source heat pump systems. *J. Eng. Geol. Hydrogeol.* 42, 295–306.
- Chatziniakolaou, E., Chalkias, C., Dimopoulou, E., 2018. Urban microclimate improvement using Envi-met climate model. In: *The International Archives of the Photogrammetry, Remote Sensing and Spatial Information Sciences, Vol. XLII-4*. <https://doi.org/10.5194/ISPRS-ARCHIVES-XLII-4-69-2018>. ISPRS TC IV Mid-term Symposium “3D Spatial Information Science – The Engine of Change”, 1–5 October 2018, Delft, The Netherlands.
- Chen, Y.C., Lin, T.P., Matzarakis, A., 2014. Comparison of mean radiant temperature from field experiment and modelling: a case study in Freiburg, Germany. *Theor. Appl. Climatol.* 118, 535–551. <https://doi.org/10.1007/s00704-013-1081-z>.
- Crank, P.J., Sailor, D.J., Ban-Weiss, G., Taleghani, M., 2018. Evaluating the ENVI-met microscale model for suitability in analysis of targeted urban heat mitigation strategies. *Urban Clim.* 26, 188–197. <https://doi.org/10.1016/j.uclim.2018.09.002>.
- Elnabawi, M.H., Hamza, N., Dudek, S., 2015. Numerical modelling evaluation for the microclimate of an outdoor urban form in Cairo, Egypt. *Hous. Build. Natl Res. Cent. HBRC J.* 11, 246–251. <https://doi.org/10.1016/j.hbrj.2014.03.004>.
- Emmanuel, R., Rosenlund, H., Johansson, E., 2007. Urban shading—a design option for the tropics? A study in Colombo, Sri Lanka. *Int. J. Climatol.* 27 (14), 1995–2004. <https://doi.org/10.1002/joc.1609>.
- ENVI-met V4.4, 2020. Urban Environment Through Holistic Microclimate Modelling. Available at: <https://www.envi-met.com/> (last accessed on 13/06/2020).
- Evola, G., Costanzo, V., Magri, C., Margani, G., Marletta, L., Naboni, E., 2020. A novel comprehensive workflow for modelling outdoor thermal comfort and energy demand in urban canyons: results and critical issues. *Energy Build.* 216, 109946. <https://doi.org/10.1016/j.enbuild.2020.109946> 0378-7788/.
- Fabbri, K., Costanzo, V., 2020. Drone-assisted infrared thermography for calibration of outdoor microclimate simulation models. *Sustain. Cities Soc.* 52, 101855. <https://doi.org/10.1016/j.scs.2019.101855>.
- Fabbri, K., Gaspari, J., Bartoletti, S., Antonini, E., 2020. Effect of façade reflectance on outdoor microclimate: an Italian case study. *Sustain. Cities Soc.* 54, 101984. <https://doi.org/10.1016/j.scs.2019.101984>.
- Forouzandeh, A., 2018. Numerical modeling validation for the microclimate thermal condition of semi-closed courtyard spaces between buildings. *Sustain. Cities Soc.* 36, 327–345. <https://doi.org/10.1016/j.scs.2017.07.025>.
- Gál, C.V., Kántor, N., 2020. Modeling mean radiant temperature in outdoor spaces, a comparative numerical simulation and validation study. *Urban Clim.* 32, 100571. <https://doi.org/10.1016/j.uclim.2019.100571>.
- Gaspari, J., Fabbri, K., Lucchi, M., 2018. The use of outdoor microclimate analysis to support decision making process: case study of Bufalini square in Cesena. *Sustain. Cities Soc.* 42, 206–215. <https://doi.org/10.1016/j.scs.2018.07.015>.
- Giridharan, X., Emmanuel, R., 2018. The impact of urban compactness, comfort strategies and energy consumption on tropical urban heat island intensity: a review. *Sustain. Cities Soc.* 40, 677–687. <https://doi.org/10.1016/j.scs.2018.01.024>.
- Goldber, V., Kurbjuhn, C., Bernhofer, C., 2013. How relevant is urban planning for the thermal comfort of pedestrians? Numerical case studies in two districts of the City of Dresden (Saxony/Germany). *Meteorol. Z.* 22 (6), 739–751. <https://doi.org/10.1127/0941-2948/2013/0463>.
- Govehovitch, B., Giroux-Julien, S., Peyrol, É., Ménezou, C., 2018. Building Integrated Photovoltaic (PV) systems: energy production modeling in urban environment. In: *EuroSun 2018 / ISES Conference Proceedings*. <https://doi.org/10.18086/eurosun2018.06.06>.
- Gusson, C.S., Duarte, D.H.S., 2016. Effects of built density and urban morphology on urban microclimate - calibration of the model ENVI-met V4 for the subtropical Sao Paulo, Brazil. *Procedia Eng.* 169, 2–10. <https://doi.org/10.1016/j.proeng.2016.10.001>.
- Hidalgo, J., Masson, V., Pigeon, G., 2008. Urban-breeze circulation during the CAPITOL experiment: numerical simulations. *Meteorol. Atmos. Phys.* 102 (3–4), 243. <https://doi.org/10.1007/s00703.008.0345.0>.
- Huttner, S., 2012. Further Development and Application of the 3D Microclimate Simulation ENVI-Met. *Johannes Gutenberg-Universität*.
- Huttner, S., Bruse, M., 2009. Numerical modelling of the urban climate – A preview on ENVI-met 4.0. In: *Proceedings of 7<sup>th</sup> ICUC Conference, Yokohama*.
- Ignatius, M., Wong, N.H., Jusuf, S.K., 2015. Urban microclimate analysis with consideration of local ambient temperature, external heat gain, urban ventilation, and outdoor thermal comfort in the tropics. *Sustain. Cities Soc.* 19, 121–135. <https://doi.org/10.1016/j.scs.2015.07.016>.
- ISO 7724-1, 1984. *Paints and varnishes — Colorimetry — Part 1: Principles*.
- ISO 7726, 1998. *Ergonomics of the Thermal Environment – Instruments for Measuring Physical Quantities. International Organization for Standardization, Geneva*.
- Koutra, S., Becue, V., Gallas, M.A., Ioakimidis, C.S., 2018. Towards the development of a net-zero energy district evaluation approach: a review of sustainable approaches and assessment tools. *Sustain. Cities Soc.* 39, 784–800. <https://doi.org/10.1016/j.scs.2018.03.011>.
- Laboratorio per la Pianificazione Territoriale e Ambientale (LAPTA) of the Department Civil Engineering and Architecture of the University of Catania. Web site: [www.lapta.dicar.unict.it](http://www.lapta.dicar.unict.it).
- Lee, S.H., Park, S.U., 2008. A vegetated urban canopy model for meteorological and environmental modelling. *Bound.-Layer Meteorol.* 126 (1), 73–102. <https://doi.org/10.1007/s10546.007.9221.6>.
- Li, X.X., Koh, T.Y., Entekhabi, D., Roth, M., Panda, J., Norford, L.K., 2013. A multi-resolution ensemble study of a tropical urban environment and its interactions with the background regional atmosphere. *J. Geophys. Res. Atmos.* 118 (17), 9804–9818. <https://doi.org/10.1002/jgrd.50795>.
- Li, J., Zheng, B., Shen, W., Xiang, Y., Chen, X., Qi, Z., 2019. Cooling and energy-saving performance of different GreenWall design: a simulation study of a block. *Energies* 12, 2912. <https://doi.org/10.3390/en12152912>.
- Liu, D., Hu, S., Liu, J., 2020. Contrasting the performance capabilities of urban radiation field between three microclimate simulation tools. *Build. Environ.* 175, 106789. <https://doi.org/10.1016/j.buildenv.2020.106789>.
- Ma, L., Jia, Z., Ma, J., Deng, S., Zhang, L., 2019. Microclimate simulation and model optimization of the effect of roadway green space on atmospheric particulate matter. *Environ. Pollut.* 246, 932–944. <https://doi.org/10.1016/j.envpol.2018.12>.
- Maggiotto, G., Buccolieri, R., Santo, M.A., Leo, L.S., Di Sabatino, S., 2014. Validation of temperature-perturbation and CFD-based modelling for the prediction of the thermal urban environment: the Lecce (IT) case study. *Environ. Model. Softw.* 60, 69–83. <https://doi.org/10.1016/j.envsoft.2014.06.001>.
- Makropoulou, M., 2017. Microclimate improvement of inner-city urban areas in a Mediterranean coastal city. *Sustainability* 9 (6), 882. <https://doi.org/10.3390/su9060882>.
- Maleki, A., Kiesel, K., Vuckovic, M., Mahdavi, A., 2014. Empirical and computational issues of microclimate simulation. In: *Linawati, M., Mahendra, S., Neuhold, E.J., Min Tjoa, A., You, I. (Eds.), Lecture Notes in Computer Science 8407, Information and Communication Technology*. Springer, pp. 78–85.
- Mao, J., 2018. *Automatic Calibration of an Urban Microclimate Model under Uncertainty*. MSc thesis. Massachusetts Institute of Technology.
- Masson, V., 2000. A physically-based scheme for the urban energy budget in atmospheric models. *Bound.-Layer Meteorol.* 94, 357–397. <https://doi.org/10.1023/A:1002463829265>.
- McIlvaine, J.E.R., Barkaszi, S.F., Beal, D.J., Anello, M.T., 2000. *Laboratory Testing of the Reflectance Properties of Roofing Materials* Florida Solar Energy Center (FSEC).

- MIT 2030 East Campus Urban Design Study. <http://web.mit.edu/mit2030/projects/eastcampusgateway/index.html>, 2014 (last accessed on 17/06/2020).
- Niachou, K., Livada, I., Santamouris, M., 2008. Experimental study of temperature and air flow distribution inside an urban street canyon during hot summer weather conditions—part I: air and surface temperatures. *Build. Environ.* 43 (8), 1383–1392. <https://doi.org/10.1016/j.buildenv.2007.01.039>.
- O'Malley, C., Piroozfar, P., Farr, E.R.P., Pomponi, F., 2015. Urban Heat Island (UHI) mitigating strategies: a case-based comparative analysis. *Sustain. Cities Soc.* 19, 222–235.
- Ramos Ruiz, G., Fernández Bandera, C., 2017. Validation of calibrated energy models: common errors. *Energies* 10, 1587. <https://doi.org/10.3390/en10101587>.
- Rotach, M.W., 2005. BUBBLE an urban boundary layer meteorology project. *Theor. Appl. Climatol.* 81, 231–261. <https://doi.org/10.1007/s00704-004-0117-9>.
- Roth, M., 2013. Urban heat islands. In: *Handbook of Environmental Fluid Dynamics*, vol. two. CRC Press, New York, US.
- Rui, L., Buccolieri, R., Gao, Z., Gatto, E., Ding, W., 2019. Study of the effect of green quantity and structure on thermal comfort and air quality in an urban-like residential district by ENVI-met modelling. *Build. Simul.* 12, 183–194. <https://doi.org/10.1007/s12273-018-0498-9>.
- Sailor, D.J., 2011. Review of methods for estimating anthropogenic heat and moisture emissions in the urban environment. *Int. J. Climatol.* 31, 189–199. <https://doi.org/10.1002/joc.2106>.
- Salata, F., Golasi, I., De Lieto Vollaro, R., De Lieto Vollaro, A., 2016. Urban microclimate and outdoor thermal comfort. A proper procedure to fit ENVI-met simulation outputs to experimental data. *Sustain. Cities Soc.* 26, 318–343. <https://doi.org/10.1016/j.scs.2016.07.005>.
- Salvati, A., Kolokotroni, M., 2019. Microclimate data for building energy modelling: study on ENVI-met forcing data. In: *Proceedings of 16<sup>th</sup> IBPSA, Rome*. <https://doi.org/10.26868/25222708.2019.210544>.
- Salvati, A., Coch, H., Cecere, C., 2016. Urban heat island prediction in the Mediterranean context: an evaluation of the urban weather generator model. *Archit. City Environ.* 11 (32), 135–156. <https://doi.org/10.1016/j.enbuild.2017.04.025>.
- Santamouris, M., Synnefa, A., Karlessi, T., 2011. Using advanced cool materials in the urban built environment to mitigate heat islands and improve thermal comfort conditions. *Sol. Energy* 85, 3085–3102. <https://doi.org/10.1016/j.solener.2010.12.023>.
- Simon, H., 2016. *Dissertation zur Erlangung des Grades. Modeling Urban Microclimate. Development, Implementation and Evaluation of New and Improved Calculation Methods for the Urban Microclimate Model ENVI-Met.* Johannes Gutenberg-Universität Mainz, Mainz.
- Simon, H., Lindén, J., Hoffmann, D., Braun, P., Bruse, M., Esper, J., 2018. Modeling transpiration and leaf temperature of urban trees – a case study evaluating the microclimate model ENVI-met against measurement data. *Landsc. Urban Plan.* 174, 33–40. <https://doi.org/10.1016/j.landurbplan.2018.03.003>.
- Sözen, I., Koçlar Oral, G., December 2018. Outdoor thermal comfort in urban canyon and courtyard in hot arid climate: a parametric study based on the vernacular settlement of Mardin. *Sustain. Cities Soc.* 1–15. <https://doi.org/10.1016/j.scs.2018.12.026>.
- Stewart, I.D., Oke, T.R., 2012. Local climate zones for urban temperature studies. *Am. Meteorol. Soc.* 1879–1900. <https://doi.org/10.1175/BAMS-D-11-00019.1>.
- Taha, H., 1997. Urban climates and heat islands: albedo, evapotranspiration, and anthropogenic heat. *Energy Build.* 25, 99–103. [https://doi.org/10.1016/S0378-7788\(96\)00999-1](https://doi.org/10.1016/S0378-7788(96)00999-1).
- Tsitoura, M., Michailidou, M., Tsoutsos, T., 2016. Achieving sustainability through the management of microclimate parameters in Mediterranean urban environments during summer. *Sustain. Cities Soc.* 26, 48–64. <https://doi.org/10.1016/j.scs.2016.05.006>.
- Tsoka, S., Tsikaloudaki, K., Theodosiou, T., 2017. Urban space's morphology and microclimatic analysis: a study for a typical urban district in the Mediterranean city of Thessaloniki, Greece. *Energy Build.* 156, 96–108. <https://doi.org/10.1016/j.enbuild.2017.09.066>.
- Vuckovic, M., Maleki, A., Kiesel, K., Mahdavi, A., 2015. Simulation-based assessment of uhi mitigation measures in central European cities. In: *Proceedings of 14<sup>th</sup> IBPSA, Hyderabad*.
- Willmott, C.J., 1982. Some comments on the evaluation of model performance. *Bull. Am. Meteorol. Soc.* 63, 1309–1313. [https://doi.org/10.1175/1520-0477\(1982\)063<1309:SCOTEO>2.0.CO;2](https://doi.org/10.1175/1520-0477(1982)063<1309:SCOTEO>2.0.CO;2).
- Willmott, C.J., Robeson, S.M., Matsuura, K., 2012. Short communication a refined index of model performance. *Int. J. Climatol.* 32, 2088–2094. <https://doi.org/10.1002/joc.2419>.
- Zhang, L., Zhan, Q., Lan, Y., 2018. Effects of the tree distribution and species on outdoor environment conditions in a hot summer and cold winter zone: a case study in Wuhan residential quarters. *Build. Environ.* 130, 27–39. <https://doi.org/10.1016/j.buildenv.2017.12.014>.

#### **4.6.2 Extract of the article “A risk index for assessing heat stress mitigation strategies. An application in the Mediterranean context”**

In this section, an extract of the article “A risk index for assessing heat stress mitigation strategies. An application in the Mediterranean context”, currently under review, is attached to the present thesis. This has been done in order to show the potential effectiveness of heat stress mitigation strategies on outdoor thermal comfort in a compact and high density built-up area using an urban Microscale approach.

The study area, named “Area 1” was described in the paper “Application of weather data morphing for calibration of urban ENVI-met microclimate models. Results and critical issues”.

##### **1. Proposed design scenario: morphological features and Microscale modelling**

In order to enhance the outdoor environmental microclimate conditions of the neighborhood above described, a design scenario was proposed which was based on minimal interventions in the existing urban settlement.

Such interventions are addressed to increase the liveability of public spaces with design strategies that do not imply radical transformation of the urban areas.

For this purpose, a Design Scenario aimed at increasing the existing Green Cover Ratio was fine-tuned respecting the limitations on greenery in urban areas such as the limited size due to the narrow footpaths.

In accordance with the proposed design configurations for the streets with width of 7-10 m and 10-15 m, public spaces were reorganized based on the principles of woonerf as described in sections 3.7.1 and 3.7.2.

In the first configuration (street with a width in the range 7-10 m), a row of car parking was eliminated in order to integrate a green space along the sidewalk. A row of deciduous trees (see Table 3.2) was inserted with distance of 3.0 m from each other.

In the second configuration (street sections with width 10-15 m), the row of car parking was replaced with a green space on both sides along the road. Therefore, two rows of trees were planned.

The introduction of trees led to an increase for greenery of 3.39%, and a reduction of about 80% of the parking places - those being maintained exclusively for residents.

The typology of trees adopted in the study area was selected on the basis of SVF values of the streets and other urban spaces respectively.

Figure 1a shows the 2D map of spatial distribution of Sky View Factor (SVF) of the investigated area at current state (CS). Along the streets, SVF values are predominantly between 0.20 and 0.40 (see



Figure 1a). For these areas, trees with average and/or short total height but high trunk and sparse crown were adopted because they are recommended according to the findings from previous studies. For the areas characterized by SVF values included in the range (0.40-0.60), dense foliage trees, with high total height and wide crown but short trunk were adopted.

Therefore, *Platanus Hispanica* were selected for areas where SVF is between 0.20 and 0.4 while *Platanus Acerifolia* was adopted for its wide crown in areas where SVF is between 0.40 and 0.60. Table 1.1 reports the thermo-physical and optical properties of selected trees according to the morphological configurations of the investigated area.

Table 1.1 Physical configurations, thermo-physical and optical properties of selected trees.

SVF	Name	Species	Trunk Height	Total Height	Crown	Albedo $\rho$ (-)
			$h_T$ (m)	TH (m)	Diameter D (m)	
< 0.45	<i>Platanus Hispanica</i> (PH)	Deciduous	4	9	5	0.15
0.40-0.60	<i>Platanus Acerifolia</i> (PA)	Deciduous	2	10	6	0.15

Based on the calibrated and validated model, comprehensively described in the paper “Application of weather data morphing for calibration of urban ENVI-met microclimate models. Results and critical issues”, the tree types reported in Table I were modelled in the 2D calculation grid.

Figure 1b shows the 2D map of the ENVI-met domain where the selected trees were implemented.

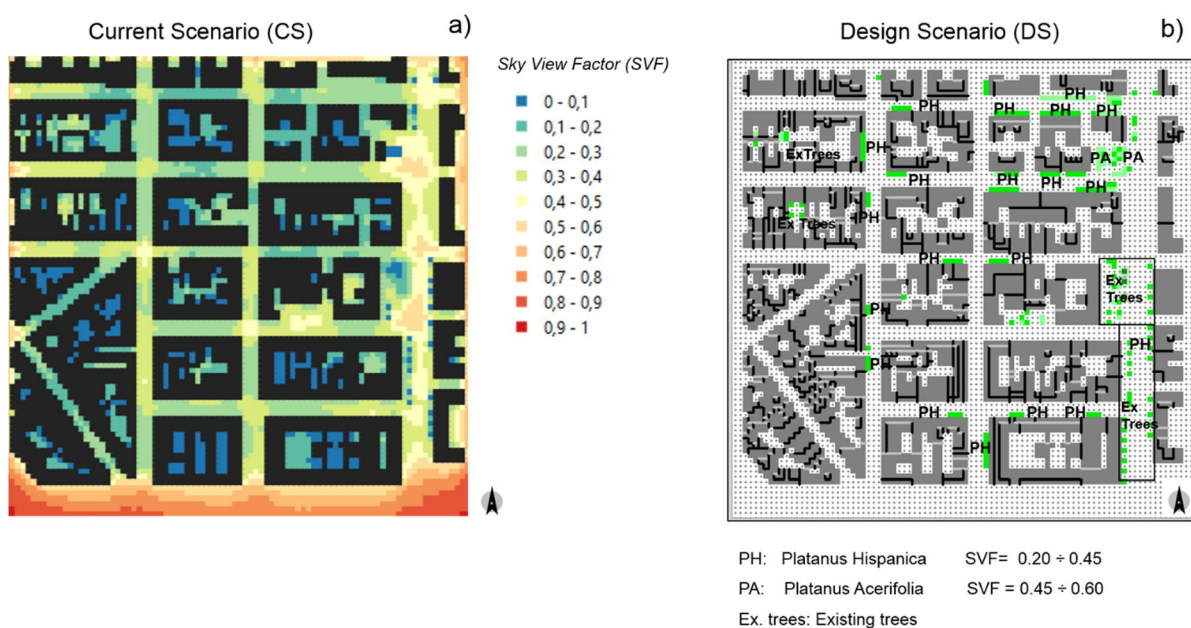


Figure 1. a) 2D map of the Sky View Factor at Current Scenario (CS); 2D calculation grid of the ENVI-met domain and location of tree types added in Design Scenario (DS).

Figure 1b depicts the placement of the trees “Platanus Hispanica and Platanus Acerifolia” in the space model of the investigated domain under Design Scenario (DS). “PH” and “PA” represent the models of Platanus Hispanica, and Platanus Acerifolia while “Ex trees” depicts the existing trees at current state.

The tree-planting selection strategies and Green Cover Ratio (GCR) adopted in the Design scenario are summarized in Table 1.2.

Table 1.2. The tree-planting selection strategies and Green Cover Ratio adopted in Design Scenario (DS).

Scenario	Urban greenery strategies	Green Cover Ratio (GCR)
Current (CS)	Existing trees distribution	1.04%
Design (DS)	Medium foliage trees along all the streets ( $0.20 < SVF < 0.40$ ) and dense foliage trees in open areas ( $0.40 < SVF < 0.60$ )	3.39%

The proposed scenario, tested in the study area, is applicable to a larger set of similar Mediterranean cities, with similar features. Forestation interventions can be implemented by applying actions which include public intervention, compensation, incentive-based strategies and tax exemptions.

## 2. Analysis of results

### 2.2. Spatial-temporal variations of mean radiant temperature on a hot day

Based on CFD simulation of the calibrated and validated ENVI-met model of the neighborhood as described in the article above reported, the spatial variations of  $T_{mrt}$  in the hottest hour on a warm day were investigated in order to assess the potential effectiveness in heat stress mitigation due to the integration of the vegetation.

With this aim, 2D spatial distribution of  $T_{mrt}$  at pedestrian height in Current and Design scenarios respectively was analyzed. The temporal variation of  $T_{mrt}$  was also analyzed in specific points located in areas where the planting of trees was planned according to Design Scenario (DS).

Figure 2.1 depicts the 2D map of the investigated ENVI-met domain in the Current Scenario (CS) (a) and Design Scenario (DS) (b). Figures c and d, instead show the spatial variations of  $T_{mrt}$  in the Current Scenario (CS) and Design Scenario (DS), while the (e) panel reports the reductions achieved by Design Scenario respectively at 1.50 m height above the ground level on a clear and hot summer day (7<sup>th</sup> August) at 12.00.

Panel (e) shows the reductions in  $T_{mrt}$  between Current and Design Scenarios notated as  $\Delta T_{mrt} = T_{mrt}(CS) - T_{mrt}(DS)$  for each pixel of the 2D digital map (CS-DS).

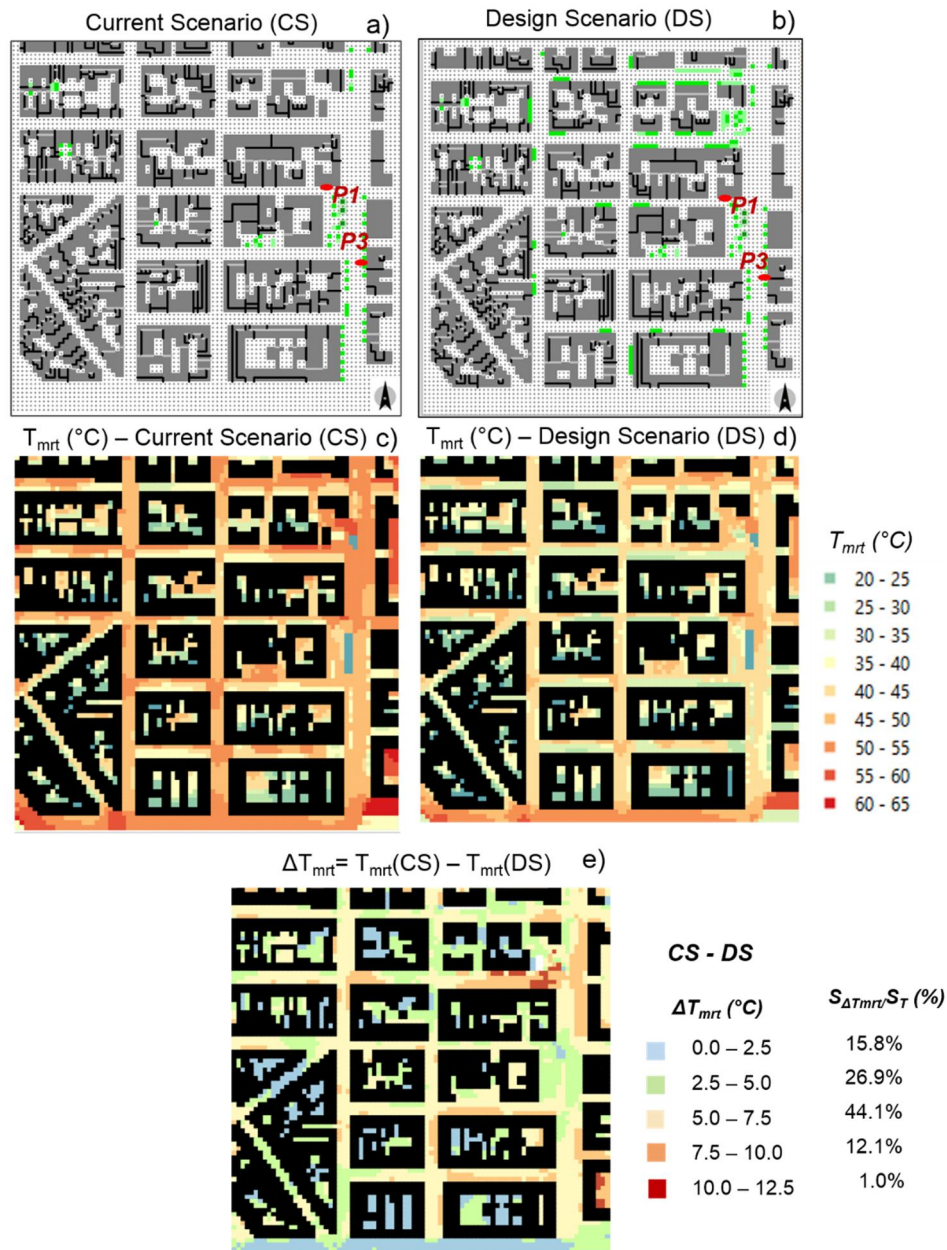


Figure 2.1. ENVI-met domain (a-b),  $T_{mrt}$  distribution in Current scenario (CS) (c) and in Design Scenario (DS) (d) and its reduction in Design Scenario(DS) (e) at  $z=1.50$  m at 12.00 on 7<sup>th</sup> August.

As shown in Figure 2.1a, Current Scenario (CS) has high values of  $T_{mrt}$  near the south-facing walls in the East-West roads and in the wide North-South road where the Sky View Factor values are higher than 0.40. In the sunlit locations of these roads,  $T_{mrt}$  values were predominantly between 55°C and 60°C and in some areas  $T_{mrt}$  exceeded 60°C. This is the result of intense shortwave and long wave radiation both from the ground and the walls.

Meanwhile the lowest values of  $T_{mrt}$  were found at the north side of the shaded East-West streets and in narrow streets in the densely built up areas in the centre of the investigated area. In particular, the narrow streets, where SVF values lie between 0.20 and 0.40,  $T_{mrt}$  values in the range of 35.0 °C to

45.0°C were found. It is worth highlighting that the crossroads have  $T_{mrt}$  values typically higher than those predicted in the streets due to the higher amount of direct and reflected shortwave radiation, as well as of the re-emitted long wave radiation from the neighbouring surfaces exposed to the sun.

In narrow built structures and internal courtyards,  $T_{mrt}$  values below 30.0°C were attained due to the mutual shading of the buildings.  $T_{mrt}$  values between 20 and 25°C were achieved below the trees.

When analysing the Design Scenario (DS) results, remarkable reductions in  $T_{mrt}$  were found both in areas where the trees were added and in areas far away from the trees (Figure 2.1d). As a result, a decrease in  $T_{mrt}$  values was achieved in all the 2D spatial domain of the investigated area. Although the  $T_{mrt}$  reductions are different, the whole study area is affected by the effects of vegetation integrated in the existing urban spaces.

Figure 2.1e shows a decrease in  $T_{mrt}$  values between 7.5 °C and 10.0 °C where the presence of the forestation interventions is dense. The area characterized by a similar decrease in  $T_{mrt}$  values represents about 12.1% of the investigated area.

In particular, it is worth noting that a decrease in  $T_{mrt}$  between 5.0 °C and 7.5 °C is quite widespread in the investigated domain, and accounts for about 44.1% of the study area.

The vegetation also influences the areas far from the forestation interventions because of reduced reflections and re-emissions from built up surfaces: such areas are indeed characterized by a decrease of  $T_{mrt}$  up to 5.0 °C and represent more than 40% of the investigated area. Since the mean radiant temperatures are meaningfully decreased, the ground level trees can be deemed a very effective measure to mitigate heat stress in urban spaces.

In order to investigate the temporal variation of  $T_{mrt}$  during the warmest hours of a hot sunny summer day, an hourly profile of  $T_{mrt}$  at Current Scenario (CS) was plotted against that of the Design Scenario (DS) in two specific points (P1 and P3) from 12.00 on 7<sup>th</sup> August to 12.00 on 9<sup>th</sup> August (Figure 2.2). Figure 2.2 depicts the hourly profile of  $T_{mrt}$  in Current and Design scenarios in locations P1 and P2 from 12.00 on 7<sup>th</sup> August to 12.00 on 9<sup>th</sup> August. In points P1 and P3, both located in sunlit areas at current state, the hourly trend of the mean radiant temperature ranges from a minimum value of 15°C to a maximum of 60°C. In P3,  $T_{mrt}$  value exceeded 60°C at 12.00 on 8<sup>th</sup> August as shown in Figure 2.2b. After forestation interventions, Point P1 is near the trees whereas P3 is under the trees planted along the roads.

Figure 2.2 shows that the Design Scenario (DS) allows reduction of the  $T_{mrt}$  values during the entire daytime thanks to the presence of the trees. During the warmest hours of daytime, a decrease of  $T_{mrt}$  up to 10°C was achieved in point P1 and a reduction of  $T_{mrt}$  up to about 20°C was attained in point P3.

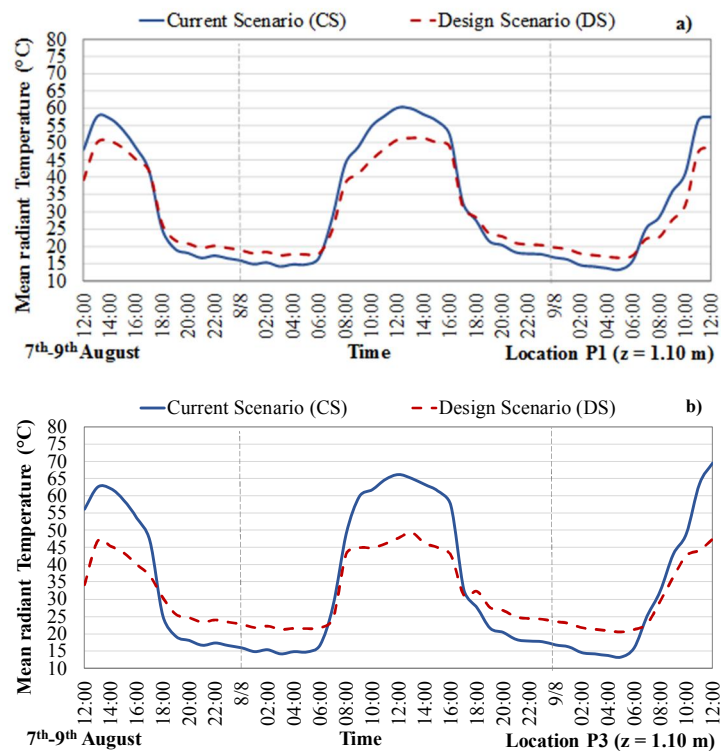


Figure 2.2. Hourly profile of mean radiant temperature at Current Scenario (CS) and at Design Scenario (DS) from 12.00 on 7<sup>th</sup> August to 12.00 on 9<sup>th</sup> August. a) Point P1; b) Point P3.

Since the point P3 is covered by a tree, the decrease achieved is substantially due to the shading effect by the crown. On the contrary, the point P1 is not below the tree and, thus, the reduction of 10°C can mainly be attributed to the evapotranspiration effects of the tree foliage. Nevertheless, it is worth highlighting that an increase in  $T_{mrt}$  was achieved at night time. This effect can be attributed to the reduction of Sky view factor due to the presence of a large crown that reduces the escape of heat through the long wave radiation towards the sky. As a result, the heat is trapped in the urban canopy layer contributing to increase the air temperature at night time. This phenomenon is more intense in the presence of trees with large crowns and high dense foliage. Although high trees with wide crowns significantly reduce the peak value of mean radiant temperature during the hottest hours, an increase in the air temperature can be achieved at night. In light of this, the forestation intervention should be based on a milder approach that takes into account the morphological properties of the investigated urban area.

Overall, a design scenario based on planting trees according to a mild approach allows the achievement of meaningful results in terms of mean radiant temperature reductions. This is confirmed by the outcomes of mean radiant temperature attained in areas far away from the points where the forestation interventions were planned. It is also worth highlighting that areas not shaded by the trees are characterized by meaningful reduction in mean radiant temperature.

Article

# Sustainable Urban Greening and Cooling Strategies for Thermal Comfort at Pedestrian Level

Maurizio Detommaso <sup>1</sup>, Antonio Gagliano <sup>2</sup>, Luigi Marletta <sup>2</sup> and Francesco Nocera <sup>1,\*</sup>

<sup>1</sup> Department of Civil Engineering and Architecture, University of Catania, 95125 Catania, Italy; maurizio.detommaso@phd.unict.it

<sup>2</sup> Department of Electric, Electronics and Computer Engineering, University of Catania, 95125 Catania, Italy; gagliano@dieei.unict.it (A.G.); luigi.marletta@unict.it (L.M.)

\* Correspondence: francesco.nocera@unict.it; Tel.: +39-095-738-2366

**Abstract:** The increase of the urban warming phenomenon all over the world is gaining increasing attention from scientists as well as planners and policymakers due to its adverse effects on energy consumption, health, wellbeing, and air pollution. The protection of urban areas from the outdoor warming phenomenon is one of the challenges that policy and governments have to tackle as soon as possible and in the best possible way. Among the urban heat island mitigation techniques, cool materials and urban greening are identified as the most effective solutions in reducing the urban warming phenomenon. The effects produced by the adoption of cool materials and urban forestation on the urban microclimate were investigated through a computational fluid-dynamic (CFD) model. The CFD model was calibrated and validated thanks to experimental surveys within the Catania University campus area. The urban microclimate thermal comfort analysis and assessment were carried out with the Klima–Michel Model (KMM) and Munich Energy Balance Model for Individuals (MEMI). In particular, three scenarios were performed: cool, low, and high levels of urban greening. The cool scenario, although it produces air temperature at around 1.00 °C, determines the worst condition of outdoor thermal comfort, especially at the pedestrian level. On the contrary, a high level of urban greening, obtained by the extensive green roofs together with an urban forestation, guarantees the wellbeing of pedestrians, showing more convenient values of PMV and PET.

**Keywords:** outdoor microclimate; pedestrian thermal comfort; heat thermal stress; urban greening; cool materials

**Citation:** Detommaso, M.; Gagliano, A.; Marletta, L.; Nocera, F. Sustainable Urban Greening and Cooling Strategies for Thermal Comfort at Pedestrian Level. *Sustainability* **2021**, *13*, 3138. <https://doi.org/10.3390/su13063138>

Academic Editor: Steve Kardinal Jusuf

Received: 18 February 2021

Accepted: 10 March 2021

Published: 12 March 2021

**Publisher's Note:** MDPI stays neutral with regard to jurisdictional claims in published maps and institutional affiliations.



**Copyright:** © 2021 by the authors. Licensee MDPI, Basel, Switzerland. This article is an open access article distributed under the terms and conditions of the Creative Commons Attribution (CC BY) license (<http://creativecommons.org/licenses/by/4.0/>).

## 1. Introduction

The increase of urban population all over the world is leading to environmental, energy, and health implications of urban warming [1]. A recent study has shown that heatwaves, which are estimated to become more frequent and last longer in a hot climate, interact with urban warming to produce rather high heat stress for urban residents [2].

Furthermore, the features of the urbanized environments exacerbate the effects of global climate change [3]. Urban areas tend to have air temperatures higher than the rural surroundings as a result of gradual ground changes that include replacing the vegetation with buildings and roads [4].

The increase in temperatures in urban spaces is known as urban heat island (UHI) [5]. This phenomenon is due to several factors such as the specific composition of urban areas in terms of people and activities, morphology of neighborhoods, geometries, urban canyons [6], as well as surfaces with low albedo [7]. On a clear summer afternoon, the air temperature in a typical city could come up 2.5 °C higher than in the surrounding rural areas [8]. These factors affect the urban climate, energy uses, and livability of cities [9]. Urban areas are often characterized by higher vehicular traffic and less vegetation than their surrounding environment [10].

The radiative properties of the surface used in outdoor spaces have a key role, as they influence the air temperature of the lowest layers of the urban canopy layer [11]. Road pavements, claddings of facades, and roofs of the buildings are fundamental in the energy balance of the urban areas. The materials absorb solar radiation and store and release it by means of infrared radiation and convection heat transfer to their surrounding area during the evening and night-time [12]. Urban surfaces are characterized by values of solar absorption higher than rural surfaces [13]. Thereby, they have a superficial temperature lower than that of the building surfaces. Building materials emit an amount of energy higher than rural surfaces, and it leads to persistent warming in urban areas [14].

Increased urban temperatures produce the rising of the energy demand for building cooling, which in turn increases the greenhouse gas emissions and the outdoor thermal discomfort [15,16].

For evaluating outdoor thermal comfort in the urban contexts, several models are available in the scientific literature. Fanger's indexes based on a steady-state energy balance model are implemented in many international standards [17,18]. Currently, the original equation of Fanger indexes is modified by Jendritzky and Nubler, 1981 [19,20], to evaluate the thermal comfort in external environments. They have produced the Klima-Michel Model (KMM) by adding the complex radiation balance in the outdoor environment and considering basic thermoregulatory processes through the human body, such as the constriction or dilation of peripheral blood vessels and the rate of physiological sweat [21].

The "Munich Energy-Balance Model for Individuals" (MEMI) [22,23] is the basis for the calculation of another index, called Physiological Equivalent Temperature (PET), which collected all the meteo-climatic factors in a single temperature index, namely the equivalent temperature. In KMM and MEMI models, the thermoregulatory processes are evaluated considering the human activity and climatic conditions.

Nowadays, mitigation strategies such as cool and green surfaces can enhance the outdoor thermal comfort in the urban areas, since both strategies reduce the sensible heat reaching the building surfaces, but the processes for reducing UHI are different [24]. Cool materials increase the reflectiveness of incoming solar radiation in urban areas reducing the net radiation [25]. Green surfaces increase the latent heat flux through the evapotranspiration process, while, thanks to the shading effect, reducing the incoming net radiation [26]. Cool materials applied on road pavements, with reflectivity 0.60, prove to be able to reduce the surface temperature by 5–6 °C compared to the conventional asphalt road [11]. In the Greek city of Florina, the application of cool pavements and cool roofs led to a reduction in the maximum air temperature by 1.39 °C and a decrease in soil temperature by 3.52 °C [27]. In Acharnes (Greece), reflective materials on the roofs allowed a reduction in surface temperature on the roofs between 1.51 °C to 10 °C and a decrease of 17% in energy consumptions [28]. The analysis of several mitigation strategies such as green roofs, green park, cool roofs, and cool pavements in an old densely populated neighborhood of Avola (Italy) highlighted that cool pavements reduce the environmental air temperature by over 2.0 °C [29]. Nevertheless, cool pavements can induce thermal discomfort to pedestrians and residents because of the high reflected solar radiation [30].

The adoption of vegetation in urban areas produces significant benefits by lowering air temperature and reducing air conditioning in the building [26,31]. It was found that medium trees and shrubs can cool down cities by from about 0.3 °C to 1.0 °C [4]. The results of CFD simulations on the effectiveness of several different mitigation strategies on the microclimate in Vienna showed that, at the pedestrian level, the planting trees allow achieving a decrease in air temperature of about 0.7 °C. A slight cooling in the air temperature, about 0.3 °C, was found when applying green roofs on all buildings of the investigated area. Moreover, the combined adoption of trees and green roofs can lead to a lower air temperature by around 1.0 °C [32].

However, few studies analyze critically the mitigation strategies that involve cool materials and urban forestation from the point of view of thermal comfort at pedestrian

level. The purpose of this paper is to provide a comprehensive assessment of the effectiveness of three different scenarios based on the adoption of cool materials and low and high levels of urban greening.

These analyses have been developed through computational thermo-fluid-dynamic (CFD) simulations, calibrated with experimental measurements within the investigated area. Different parameters such as air temperature, wind speed, relative humidity, mean radiant temperature, predicted mean vote, and physiological equivalent temperature indexes were calculated and analyzed for each scenario. Finally, a comparative analysis was carried out to highlight the weaknesses and strengths of the different strategies.

The paper is organized as follows:

- Section 2 describes the methodological approach, the tools and software used for CFD simulations, and analytic models for calculating comfort indicators. The equipment used for a ground survey is described too;
- Section 3 provides detailed descriptions of the case study;
- Section 4 discusses the methods used for calibrating and validating the model through statistical analysis approach;
- Section 5 provides the results of computational simulations (CFD) for Cool and Green scenarios;
- Section 6 reports scenarios' results and some critical issues through comparative analysis.

## 2. Materials and Methods

### 2.1. CFD Simulations

Computational fluid-dynamic simulations have been carried out through the ENVI-met software [33], which is a three dimensional numerical prognostic calculation code based on a holistic model. This tool is able to recreate the microclimate and thermo-physical behavior of the urban microscale. Three-dimensional modeling of the urban area is based on the discretization of simulation domain in finite volumes. Thereby, the model is composed of many three-dimensional cells with a typical horizontal resolution from 0.5 to 10 m.

The software implements theoretical physical models of nonlinear equations, including three main prognostic variables, that allow the analysis of the interactions between environment and atmosphere on a local basis [34,35]. The main variables are average air flow, temperature and humidity, and turbulence. The analytic model is based on Navier–Stokes equations for wind flow, atmospheric flow turbulence equations, energy and momentum equation, and boundary condition parameters [34]. ENVI-met software implements the energy and mass balance equations related to:

- Shortwave and longwave radiation fluxes attributable to shading, reflection, and re-radiation from building systems and the vegetation;
- Transpiration, evaporation, and sensible and latent heat flux from the vegetation, including full simulation of all plant physical parameters [36];
- Water and heat transfer inside the soil system.

The calculation procedure implies the following steps:

- Geometry modeling of simulation domain;
- Generation of the mesh of the calculation grid;
- Implementation of buildings, obstacles geometry, trees, shrubs, and plants;
- Definition of the boundary conditions and entering climate data;
- Definition of the radiative and thermo-physical properties of buildings and urban materials;
- Calculation of the field of temperature, humidity, wind speed, and comfort indicators;



- Extraction of the simulation outcomes in 2D and 3D maps and in specific points at different height.

The results of the simulations are collected in several outputs folders that can be extracted as plots or text files.

In this study, outdoor air temperature ( $T_o$ ), wind speed ( $w$ ), relative humidity (RH), soil temperature ( $T_{soil}$ ), and mean radiant temperature (MRT) were considered useful parameters for comparing different scenarios. The evaluation of outdoor thermal comfort at pedestrian level, 1.00 m above ground level, in the different scenarios is carried out using the Klima–Michel Model (KMM) for calculating PMV index and Munich Energy-Balance Model for Individuals (MEMI) based on the Physiological Equivalent Temperature (PET).

## 2.2. Comfort Indexes

### 2.2.1. PMV

Predicted mean vote (PMV) is a well-known index defined by ISO 7730 [17]. It was initially intended for indoor use. In 1990, Jendritzky [20] introduced the Klima–Michel model (KMM) in the PMV in order to take into account the outdoor conditions. It is an adaptation of the Fanger model [17], with a short wave radiation model, for the calculation of the mean radiant temperature. This model assumes a typical activity and clothing of a man, 35 years old, 1.75 m tall, 75 kg weight, walking at 4 km/h (2.3 met).

Therefore, the values of the adapted PMV index [19,20] for the outdoor environment can overcome the international standard graduation used for indoor spaces. Indeed, while the PMV scale is defined between  $-3$  (very cold) and  $+3$  (very hot), where 0 is the thermal neutral (comfort) condition, the PMV for outdoor environment, may reach values above  $+4$  or below  $-4$  [37].

### 2.2.2. PET

The “MEMI” model is used for calculating the physiological equivalent temperature (PET). It is based on the energy balance of the human body (Equation (1)) and some parameters of the Gagge two-node model [38]. The most important advantage of the model is the possibility of calculating the physiological sweat rate, as a function of the average skin temperature ( $T_{sk}$ ) and the core temperature ( $T_{cr}$ ). The evaluation of both the heat flowing from the parts of the body surface covered by clothes or not is also allowed.

According to the Gagge model, the human body is divided into the outer region “skin” and internal body “core”. Therefore, the equation of the thermal balance between the human body and the outdoor environment is given by:

$$M + W + R + C + E_d + E_{re} + E_{sw} = S = S_{cr} + S_{sk} \quad (1)$$

where  $S$ —the heat stored through body heating or cooling;  $S_{cr}$ —the heat stored in the core;  $S_{sk}$ —the heat stored in the skin;  $M$ —metabolic rate;  $W$ —Physical work output;  $R$ —Net radiative heat flux;  $C$ —convective heat flux;  $E$ —Latent heat flux exchanged through evaporation of moisture diffused through the skin ( $E_d$ ), respiratory ( $E_{re}$ ), and evaporation sweat ( $E_{sw}$ ).

The terms reported in Equation (1) are in ( $W/m^2$ ) and depend on the meteorological parameters [38], heat resistance of clothing, and human activity.

In particular,  $E_{sw}$  depends on sweat frequency that is a function of the core temperature ( $T_{cr}$ ), outdoor environmental conditions, and human activity. As the mean clothing temperature, mean skin temperature and sweat rate depend also on the climatic conditions; a substantial difference emerges with respect to Fanger’s theory.

The equation is solved under typical indoor settings (mean radiant temperature equal to air temperature  $MRT = T_a$ , water vapor pressure ( $pa$ ) of 12 hPa, approximately equivalent to a relative humidity of 50% at  $T_a = 20$  °C, and wind speed ( $w$ ) of 0.1 m/s. In these conditions, the air temperature obtained solving the system is the PET.

PET is defined as the air temperature at which, in a typical indoor setting, the heat balance of the human body (work metabolism 80 W of light activity, added to basic metabolism; heat resistance of clothing 0.9 clo) is maintained with core and skin temperatures equal to those under the actual environmental conditions. The relationship between PMV and PET is shown in Figure 1.

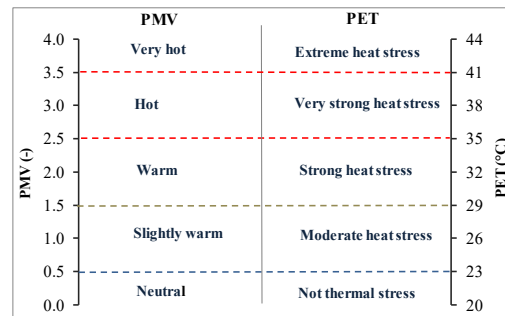


**Figure 1.** The relationship values for PMV and PET model according to [39].

### 2.3. Field Survey

The weather data implemented in ENVI-met are as follows: dry bulb temperature, relative humidity, global, direct and diffuse solar radiation, wind speed, and direction taken from a permanent weather station. The uncertainty, measurements range, and characteristics of the sensors are reported below:

- Air temperature and relative humidity sensors: (uncertainty: 0.10 °C and 0.1%; measurements range: −50–100 °C and 0–100%);
- Radiometer: (spectral response: 300–3000 nm; operative temperature −40 °C/+80 °C; uncertainty: ±4 W/m<sup>2</sup>);
- Anemometer: (measurement range: 0 ÷ 50 m/s; threshold: 0.36 m/s; uncertainty 1%; below 3 m/s and 1.5% above 3 m/s; resolution: 0.06 m/s).

For the validation of the CFD simulations, the measurements were carried out with a portable microclimate station Heat Shield Master ELR615M by LSI Lastem. Figure 2 shows all the components and sensors, such as a globe-thermometer, a thermo-hygrometric probe, and a rotor anemometer. Table 1 reports the technical characteristics of each probe.

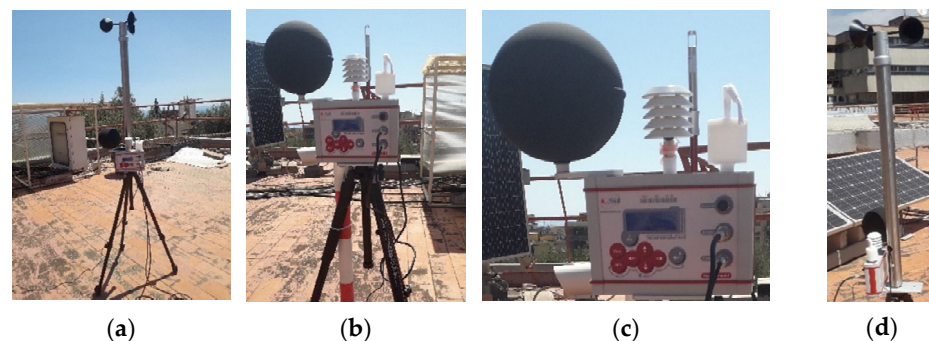


**Figure 2.** Microclimate portable station: (a) LSI Lastem BVA304 Tripod/Mast Assembly 1.2 m; (b) Heat Shield Master ELR615M; (c) Globe thermometer ELR615M probe: Pt100; Thermo-Hygrometric sensors; (d) Rotor Anemometer DNA 202.

**Table 1.** Technical features of probe.

Climatic Variables	Type of Probes	Accuracy	Range
Air temperature	Thermometer	$\pm 0.3$ °C, (@10, 40 °C)	$-20$ °C ÷ $60$ °C
	Silicon band gap	$\pm 0.8$ °C (@60 °C)	
Relative Humidity	Hygrometric Sensors	1.8% (10 ÷ 90%)	0 ÷ 100%
Wind speed	DNA205 Rotor Anemometer	2.5%	0 ÷ 0.75 m/s
Globe temperature	ELR615M globe thermometer	$\pm 0.3$ °C (@25 °C)	$-20$ ÷ $125$ °C
	probe ( $\varnothing = 150$ mm), Sensor type: 1/3 DIN-A Pt100		

The values of air temperature ( $T_a$ ), globe temperature ( $T_g$ ), wind speed ( $w$ ), and relative humidity ( $RH$ ) were recorded every minute. The instruments were tested and calibrated before the field survey, while the measurement process complied with the Standard ISO 7726 [40].

#### 2.4. Statistical Analysis

Table 2 reports the statistical indexes for quantifying the discrepancies between the observed ( $m_i$ ) and simulated ( $s_i$ ) data.

**Table 2.** Statistical indices used for validation.

Index	Name	Formula	U.M.
MAE	Mean absolute error	$MAE = \frac{\sum_{i=1}^n  m_i - s_i }{n}$	data-dependent
RMSE	Root mean square error	$RMSE = \sqrt{\frac{\sum_{i=1}^n (m_i - s_i)^2}{n}}$	data-dependent
r	Pearson correlation coefficient	$r = \frac{\sum_{i=1}^n (m_i - \bar{m})(s_i - \bar{s})}{\sqrt{\sum_{i=1}^n (m_i - \bar{m})^2} \cdot \sqrt{\sum_{i=1}^n (s_i - \bar{s})^2}}$	-
R <sup>2</sup>	Coefficient of determination	$R^2 = 1 - \frac{\sum_{i=1}^n (m_i - s_i)^2}{\sum_{i=1}^n (m_i - \bar{m})^2}$	-

The mean absolute error (MAE) is the average of all absolute errors and expresses the difference between actual and predicted values. It represents the vertical or horizontal distance between each point and the equality line [41].

The root mean square error (RMSE) is instead the standard deviation of the residuals (i.e., the differences between observed and predicted values). Residuals are a measure of how far from the regression line data points are. It is worth noticing that few large errors can lead to a great RMSE value [42–44].

The Pearson coefficient ( $r$ ) is given by the ratio between the covariance of the two variables and the product of their mean square deviations. It measures the intensity of the correlation between two random variables or two quantitative statistical characters.

The coefficient of determination ( $R^2$ ) is defined as the proportion of the variance in the dependent variable ( $s_i$ ) that is predictable from the independent variable ( $m_i$ ). It indicates how simulated values are close to the regression line of the measured values. The index  $R^2$  ranges between 0 and 1; the upper value means that the simulated values match the measured ones perfectly [45].

### 3. The Case Study

The investigated area is a part of the University Campus of the metropolitan city of Catania along the Mediterranean coast in Southern Italy (latitude 37°30' North and longitude 15°04' East). This area was selected for its peculiar urban texture, high population density, as well as urban density.

According to the international Köppen–Geiger climate classification, Catania is characterized by warm and humid summer and moderately cool, wet winter. In the summer, the average outdoor temperature ranges from 23 °C to 35 °C, with peaks of 39 °C when hot winds blow from North Africa. Figure 3 shows the investigated area.

The area has a surface of around 33,600 m<sup>2</sup> and includes five buildings 5.00 to 15.00 m high that host classrooms and Department offices. The squared buildings have huge sizes (35 × 35 m<sup>2</sup>), as shown in Figure 3b. Figure 4 shows the different typology of the land surface of the investigated area at current state.

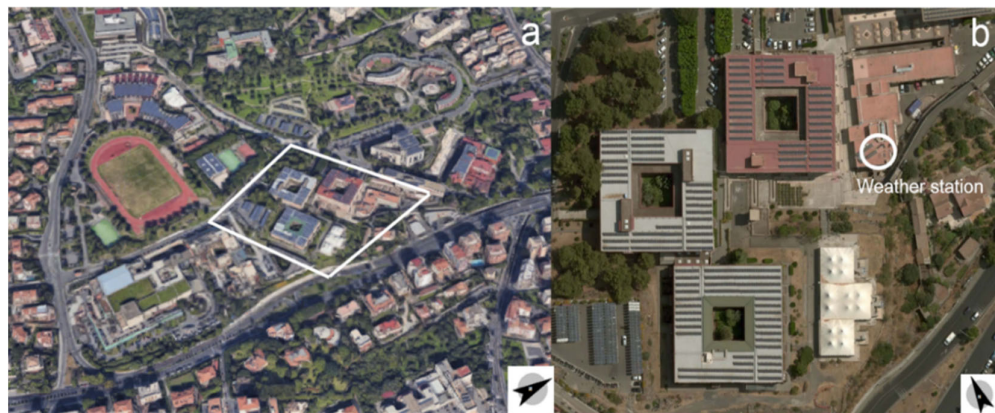


**Figure 3.** University Campus in the neighborhood of S. Sofia: (a) 3D views; (b) 2D view.

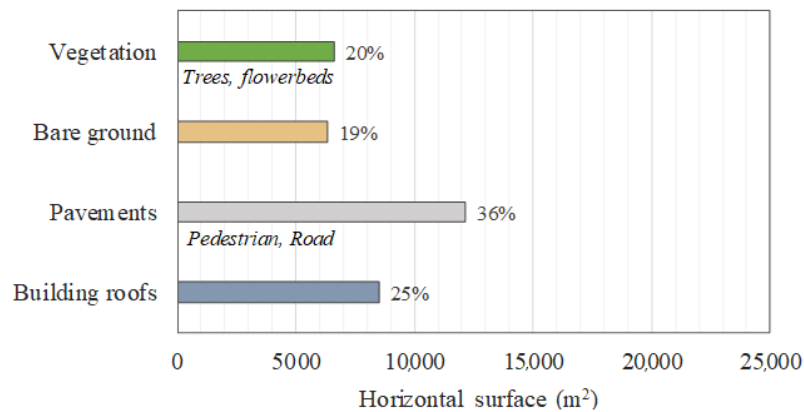


**Figure 4.** Land use and surface cover (%).

Currently, about 8496 m<sup>2</sup> are the building roofs and about 12,160 m<sup>2</sup> is a paved area (pavements, roads), while the presence of vegetation is estimated at around 6610 m<sup>2</sup> of the total investigated area.

The measurements were taken with a LSI-Lastem weather station (equipped with the air temperature sensor, black globe thermometric sensor, thermo-hygrometric sensor, and anemometer) located on the roof of the building of the Electric, Electronics, and Computer Engineering Department.

### 3.1. Baseline Scenario

#### 3.1.1. Model Simulation

The simulation model presents a domain with a number of grids equal to  $50 \times 42 \times 30$  featured by a mesh of  $4.0 \times 4.0 \times 1.0$  m. The total domain dimension is  $200.0 \times 168.0 \times 100.0$  m. The height along the z-axis of the domain is constant until 15.0 m, which represents the size of the tallest building; after that, it increases with a telescopic factor rate of 10%. Along all borders of the domain, six cells of nesting grids are set. The time step of the simulation was constant and equal to two seconds to avoid numerical instability and convergence issues.

Figure 5 displays the 3D Model of the investigated area in the baseline scenario where green color represents the vegetated area (trees or shrubs), black color represents the paved area (road, parking, square), dark gray represents photovoltaic panels, light gray represents pedestrians' roads, and light brown represents the unpaved area (ground, soil).



**Figure 5.** Baseline scenario (BS): 3D view of the model.

In the domain, three receptors, namely P1, P2, and P3, have been selected for the purpose of validating the CFD model (see Figure 6).

In the same way, two receptors (S1 and S2) have been selected to investigate locally the variation of microclimate and thermal comfort under the three proposed different scenarios (see Figure 5).

Two sequences of simulations were carried out: from 6.00 a.m. on July 28 to 6.00 a.m. on July 31 and from 6.00 a.m. on August 22 to 6.00 a.m. on August 25. The simulations started at sunrise when the energy balance is almost equal to zero.

Finally, the parameters for calculating PMV and PET were set up as follows: age of users, 24 years old, medium height of 1.70 m, average weight of 70 kg, metabolic rate equal to 1.50 Met, and clothing thermal insulation (clo) equal to 0.50.

#### 3.1.2. Materials and Thermo-Physical Properties

Materials and thermo-physical properties have been modeled according to international literature sources [12]. The outer surfaces of buildings, roads, pedestrian pavements, and other outdoor spaces are made up of “standard” materials that absorb remarkable solar radiation during daytime contributing to the release of high heat flux.

Globally, eight different kinds of urban surfaces have been identified and defined. Aiming to simplify the model, for each of them, a single value of albedo and emittance based on the material predominance was assigned.

Table 3 reports the values of albedo and solar emittance adopted for the model.

**Table 3.** Thermal and optical properties of existing material.

Urban Components	Albedo ( $\rho$ )	Solar Emittance ( $\epsilon$ )
Roads, parking, square (asphalt)	0.20	0.85
Pedestrian roads	0.30	0.85
Ground, soil	0.20	0.95
Concrete building roofs	0.30	0.90
Clay brick building roofs	0.30	0.90
Building walls	0.20	0.90
Photovoltaic panels	0.625	0.90
Shelter parking	0.20	0.90

It is worth highlighting that PV systems are installed on many roofs. Consequently, they have been modeled too. Indeed, they have been considered as conventional roofs with a reduction in reflectivity of around 0.625. The latter was calculated considering the conversion rate of the solar radiation into electricity (15%), the PV panel reflection (10%), and the portion of absorbed energy that comes back to the external environment by convection and radiation from the upper and lower surface of the PV modules (12.5%).

The vegetation occupies about 20% of the total land area in the model. Indeed, most trees and shrubs are placed to the north-west of the selected area, whereas the extensive vegetation and bare ground are facing south-east. The trees are predominantly conifers, but some deciduous plants are present, while flowerbeds are occupied by some small grass and evergreen plants. The plants identified on the area and simulated are conic: small trunk, sparse, medium 15 m (conifer); tree: 10.0 m height, dense foliage, leafless (conifer); and Populus Alba: 7.0 m height (deciduous) and base grass, average density, 0.50 m tall. All the plants are characterized by the albedo estimated in the range 0.25–0.40.

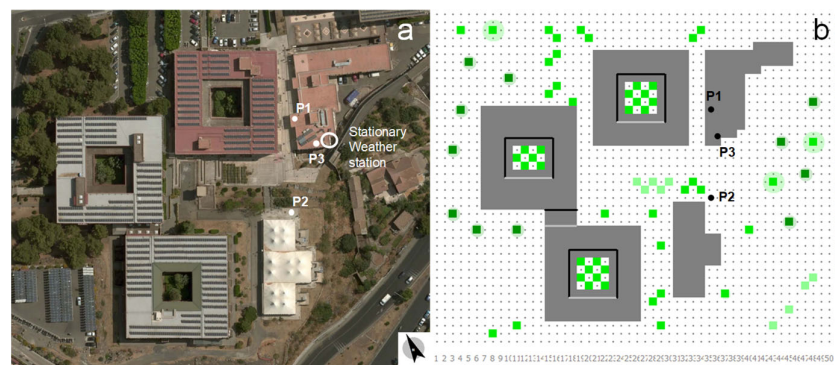
Thermo-physical and optical properties of plants as well as the leaf area density (LAD) are reported in Table 4.

**Table 4.** Thermo-physical and optical properties of plants included in the model.

Type	Species	Height (m)	LAD (-)	$\rho$ (-)	$\epsilon$ (-)
Conic, small trunk, dense	conifer	15.0	2.3	0.12	0.10
Tree dense foliage leafless	conifer	10.0	2.5	0.25	0.12
Populus alba	deciduous	7.0	2.0	0.40	0.20
Base grass, average density	-	0.30	0.30	0.25	0.15

### 3.2. On Site Weather Measurements

Figure 6 shows the actual locations where the portable weather stations have been placed during the field measurement and surveys. Table 5 reports the locations and time periods of the survey.

**Figure 6.** Position of the receptors P1, P2, and P3: (a) real geometry; (b) ENVI-met model.

**Table 5.** Locations and investigated periods selected for measurements survey.

No	Locations	Time Periods	Locations	Height a.g.l. (m)
1	P1	10.00 a.m. on July 29–6.00 p.m. on July 30	Roof Terrace of building. n. 13	5.4
2	P2	10.00 a.m.–6.00 pm. on July 30	Pavements	7.0
3	P3	12.00 a.m. on August 22–12.00 a.m. on August 24	Roof Terrace of building. n. 13	5.4

The portable station was settled at 1.2 m on the roof of the building n. 13 (P1 point) from 10.00 a.m. on July 29 to 6.00 p.m. on July 30 and in P3 point in close proximity to the stationary weather station from 12.00 a.m. on August 22 to 12.00 p.m. on August 24 (Figure 6a). The mobile station was installed on a tripod of 1.2 m height and placed close to the building n. 15 (P2 point) from 10.00 a.m. on July 30 to 6.00 p.m. on July 30.

#### 4. Calibration and Validation

The simulation model was calibrated using hourly data of weather station reported in Figure 7.

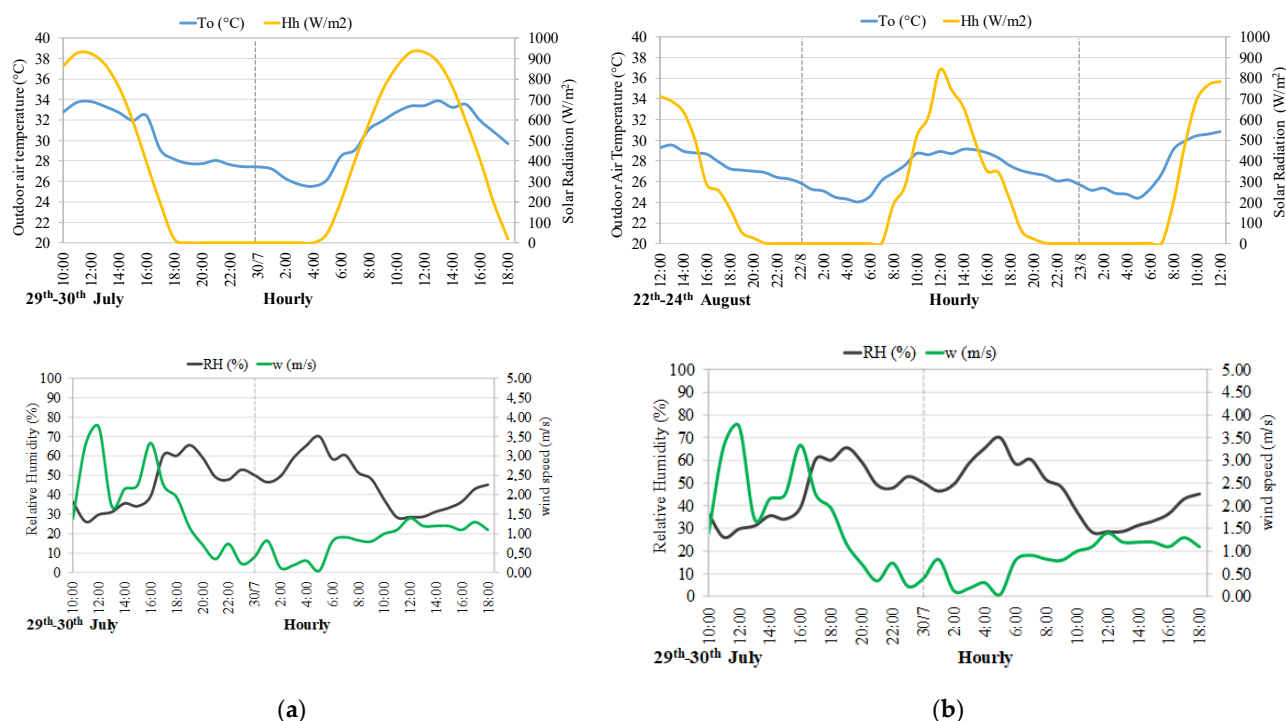


**Figure 7.** Hourly values of outdoor air temperature ( $T_o$ ), horizontal solar radiation ( $H_h$ ), relative humidity (RH), wind speed ( $w$ ): (a) July 29–30; (b) August 22–24.

The reliability of the ENVI-met model was evaluated against the statistical indicators introduced in Section 2.4 using the data recorded by the portable weather station in P1, P2, and P3. Table 6 reports the calculated statistical indicators.

The analysis of MAE and RMSE values for the air temperature and relative humidity reveal a not perfect correlation at the points P1 and P2, while at P3 the discrepancies are quite low. For the air temperatures, MAE at P3 is less of 1.0 °C, while anywhere else it exceeds 1.0 °C, and it is even above 2.0 °C at P2.

**Table 6.** Validation indices of the ENVI-met model.

Variables	Statistical Indices	Unit	Locations		
			P1 (h = 5.41 m) 29th–30th July	P2 (h = 1.20 m) 30th July	P3 (h = 1.20 m) 22th–24th August
$T_o$	MAE	°C	1.33	2.41	0.82
	RMSE	°C	1.60	2.50	0.69
	r	-	0.96	0.95	0.98
	R <sup>2</sup>	-	0.93	0.91	0.94
RH	MAE	%	4.76	4.95	3.04
	RMSE	%	5.49	6.02	2.15
	r	-	0.94	0.77	0.97
	R <sup>2</sup>	-	0.88	0.60	0.95

Nevertheless, a good correlation with experimental measurements is confirmed in terms of air temperature by the high values of the correlation coefficient “r” and of the determination coefficient R<sup>2</sup>, which are always higher than 0.90. Although the statistical indicators do not achieve optimal values, the profiles of air temperature and relative humidity are very close and similar in all points.

Indeed, as an example, the comparison between the measured and simulated values at P1, displayed in Figure 8a,b, highlight a good correlation for air temperature ( $T_o$ ) and relative humidity (RH).

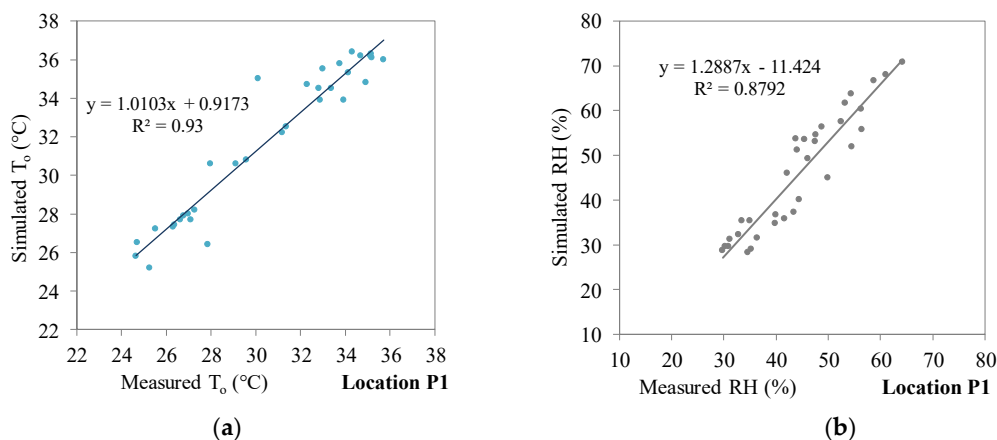


**Figure 8.** Correlation between measured and simulated data at P1 point: (a) air temperature ( $T_o$ ); (b) relative humidity (RH), on and July 29 and 30.

Nevertheless, during the night, the temperatures simulated are around 1.0 °C lower compared with the measured ones. This could be due to an overestimation of the low long-wave radiation exchange with the sky because of low sky temperatures or high values of emittance of the outer layer of the building’s surface. Despite this, the model does not seem to be affected by the fraction of anthropogenic heat that actually contributes to climate microscale.

During the hours of maximum solar radiation, the profile of simulated air temperature is lower than about 1.0–2.0 °C with respect to that measured trend. A similar result was also found in other studies [45]. For example, Mohamed et al. [46] have evaluated the microclimate of an urban area located within the Islamic Quarter of Cairo (Egypt). They have compared ENVI-met and measured data, discovering a difference in peak value of the temperature of 2.0 °C between 11.00 a.m. and 3.00 p.m. on a summer day.

Gusson and Duarte performed on-site microclimate measurements for the calibration of ENVI-met models of two densely populated districts in São Paulo in Brasil (Brasilândia and Bela Vista). A grid with a mesh of 3 × 3 × 3 m<sup>3</sup> was adopted for modeling both districts



in ENVI-met. Despite good correlation coefficients, they found out a difference in peak value of temperatures of 3.2 °C between simulated and recorded data at around 12 p.m. [47].

## 5. Proposed Scenarios

Three scenarios were proposed and evaluated to enhance outdoor environmental microclimate conditions:

- Cool scenario (Cs), in which a reflective paint is applied on the pedestrian pavements, roads, and building roofs;
- Green Roof scenario (GRs), in which extensive green roofs are installed with an increase of surface cover at around 25%;
- Green Saturation scenario (GSs), in which any available area is covered with vegetation and green roofs. In this way, the green surface cover increases by around 44%.

More in detail, the Cool scenario (Cs) consists in the replacement of conventional materials with cool paints for pedestrian roads, pavements roads, and the application of cool paint on the roofs of all buildings. The cool materials are supposed to have high albedo and high emissivity to reflect the solar radiation. Commercial products were adopted: their thermal and optical features are reported in Table 7 [48].

**Table 7.** Surface cover (%) treated with cool materials.

Urban Components	Surface (m <sup>2</sup> )	Surfaces Ratio (%)	Albedo (ρ)	Emissance (ε)
Cool pavements	12,160	36%	0.80	0.90
Cool roofs	8500	25%	0.80	0.90
Total	20,650	61%	-	-

The total surface treated with cool materials is 20,650 m<sup>2</sup>, which represents 61% of the investigated area. The Green Roof scenario (GRs) is based on the installation of 8500 m<sup>2</sup> extensive green roofs on the top of all buildings. The features of the substrate and vegetation layer of the green roof are reported in Tables 8 and 9, respectively.

**Table 8.** Features of the substrate layer.

Height	H	0.15	m
Thermal conductivity	λ	1.00	W·m <sup>-1</sup> ·K <sup>-1</sup>
Absorptance	α	0.60	-
Albedo	ρ	0.30	-
Emissance	ε	0.90	-
Moisture content	Θ <sub>sat</sub>	0.50	m <sup>-3</sup> ·m <sup>-3</sup>

**Table 9.** Features of the vegetation layer.

Height	H	0.30	m
Leaf Area Index	LAI	1.50	m <sup>2</sup> ·m <sup>-2</sup>
Absorptance	α	0.60	-
Albedo	ρ	0.25	-
Emissance	ε	0.95	-
Transmissivity	τ	0.15	-

Data available in the scientific literature [49] were considered for the thermo-physical properties of substrate and vegetation layers. The Green Saturation scenario (GSs), in addition to the green roofs, considers the planting of new trees, such as *Populus alba* and pine, with an average height of 10 m, and new grass until it reaches the saturation of bare soil. Pines and *Populus alba* have been adopted, because they are endemic species and have physical characteristics that are suitable for urban greening. The surface of vegetation is 14,800 m<sup>2</sup> in the green saturation scenario.

## 6. Results and Discussion

### 6.1. Microclimate and Thermal Comfort Daily Variation

This section reports the results of thermal comfort simulation for the Baseline, Cool, and Green scenarios. An accurate analysis has highlighted that Green Roofs (GRs) do not affect the microclimate at pedestrian level. For this reason, Figure 9a–d reports only the profile of air temperature, mean radiant temperature, predicted mean vote and physiological Equivalent Temperature for the Baseline (Bs), Cool (Cs), and Green Saturation (GSs) scenarios at the S1 and S2 receptors.

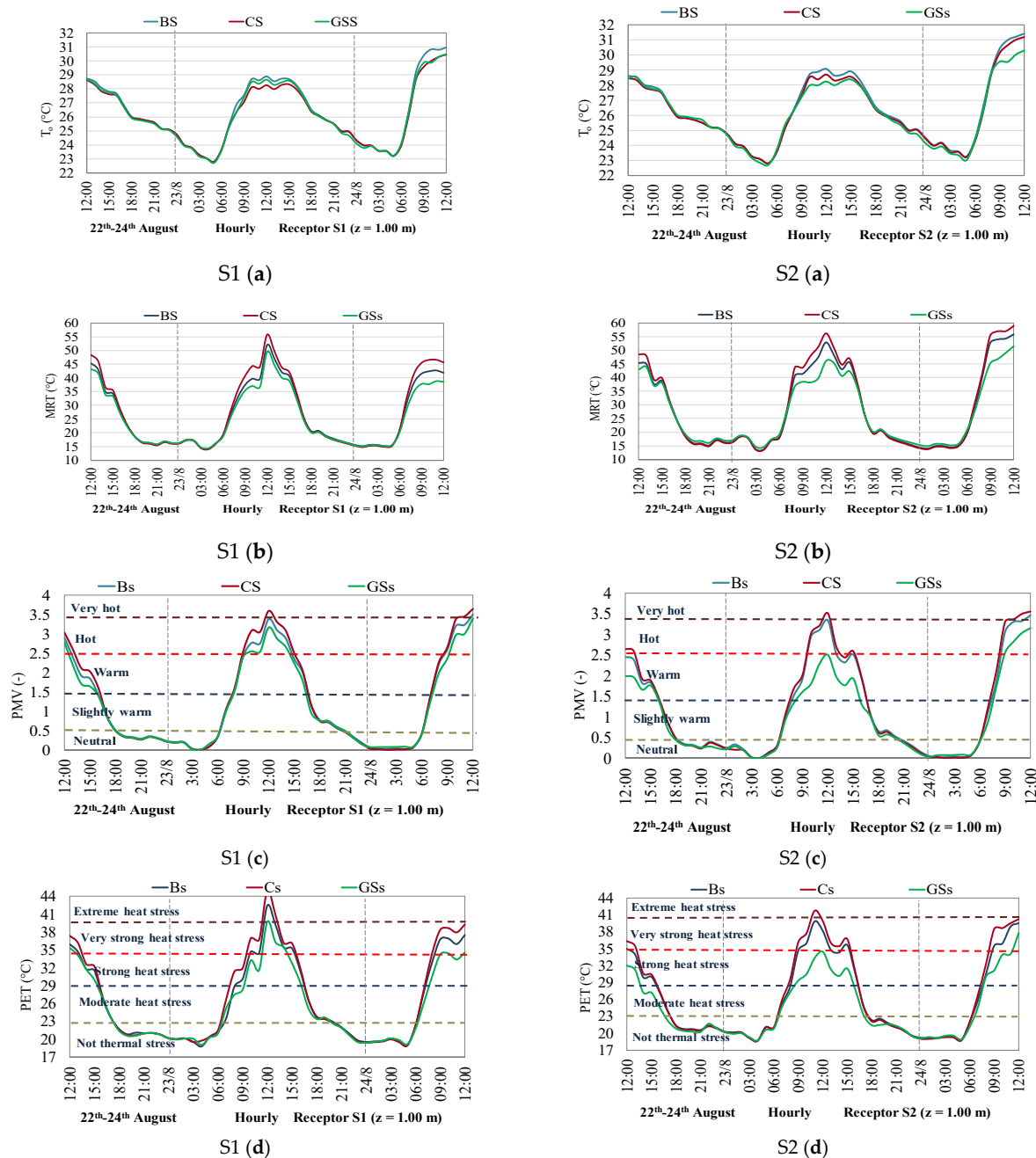


**Figure 9.** Outdoor temperature ( $T_o$ ) (a) and mean radiant temperature (MRT) (b) for the Baseline (Bs), Cool (Cs), and Green Saturation scenarios, Table 1 and S2.PMV (c) and PET (d) for the Baseline (Bs), Cool (Cs), and Green Saturation (GSs) scenarios at the receptor S1 and S2.

Under the Baseline scenario (Bs), the air temperature ranges from 22.8 °C to 31.0 °C for both S1 and S2 receptors. At noon, the Cool scenario (Cs), compared to the baseline scenario (Bs), gives place to a decrease of the air temperature by 0.5 °C at the S2 receptor and by 0.8 °C at the S1 receptor.

The Green Saturation scenario (GSs) shows the best performance at the receptors S2, which is close to green spaces, with a reduction in the air temperature of about 0.8 °C. Nevertheless, a decrease in the air temperature is also achieved at the receptor S1, which is quite far from green areas.

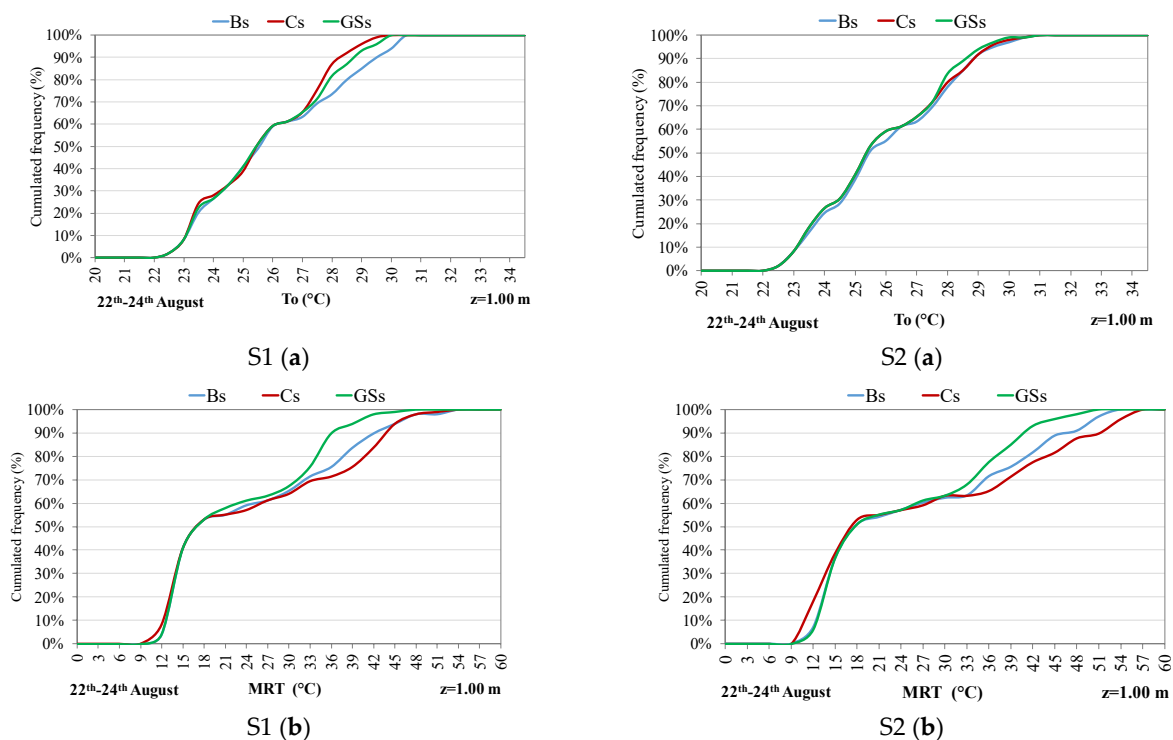
It is to outline that during the daytime the Cool scenario (Cs) shows values of MRT higher than in the green saturation (GSs) and baseline (Bs) scenarios; this happens for the zone closest to the building facades due to highest albedo of these surfaces. An increase of 4.0 °C is observed at S2 receptor and of 3.4 °C at S1 receptor.

As to the PMV, a value of 2.5 is exceeded for all scenarios for both receptors from 8:00 a.m. to 4.00 p.m. The only exception is observed at the receptor S2 for the Green Saturation scenario (GSs). A similar result is observed for the PET index, which is higher than 35.0 °C, “very strong heat stress”, excepting at the receptor S2 for the Green Saturation scenario (GSs).

However, during the hour of maximum solar radiation, the highest values of PMV and PET, according to the value of MRT, have been observed for the Cool scenario. It has to be highlighted that the trend of all investigated parameters show a rapid drop of the curve at around 2.00 p.m. on August 23 due to a decrease of direct solar radiation caused by clouds. In any case, the best results are achieved by the GSs, for which the PET ranges from 19.9 °C to 36.4 °C.

The cumulative frequency distribution was also calculated for the following parameters:  $T_o$ , MRT, PMV, and PET during the selected period from 12.00 p.m. on August 22 to 12.00 p.m. on August 24.

Actually, Figure 10a–d reports only the cumulative frequency distribution of air temperature and mean radiant temperature of the Baseline (Bs), Cool (Cs), and Green Saturation (GSs) scenarios in the S1 and S2 receptors.



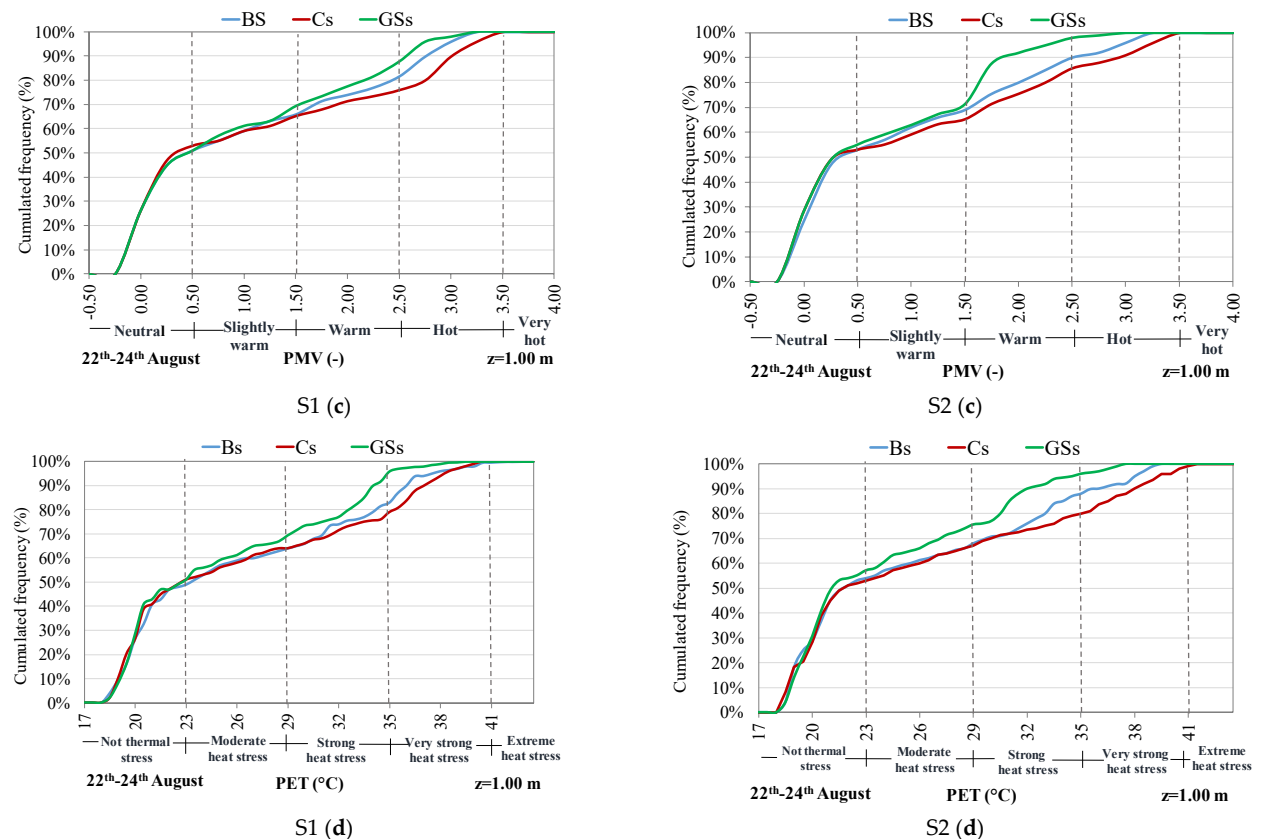


**Figure 10.** Cumulative frequency distribution of outdoor temperature ( $T_o$ ) (a) and mean radiant temperature (MRT) (b) for the Baseline (Bs), Cool (Cs), and Green Saturation (GSs) scenarios in the receptors S1 and S2. Cumulative frequency distribution of predicted mean vote (PMV) (c) and physiological equivalent temperature (d) for Table 1 and S2.

It can be seen that in the Cool scenario (Cs), the air temperature  $T_o$  exceeds  $28\text{ }^{\circ}\text{C}$  for 10% of the time. The situation is thus better than in the Baseline scenario (Bs), where  $T_o$  exceeds  $28\text{ }^{\circ}\text{C}$  for about 30% of the time. That may be explained on the basis of the previous remarks.

From Figure 10b, it is evident that the three scenarios are better differentiated in terms of MRT, especially for MRT higher than  $33\text{ }^{\circ}\text{C}$ . As to the parameters more strictly related to thermal comfort (PMV and PET), it can be seen from Figure 10c that all investigated scenarios reach the “Warm” level. Actually, the “warm level” is exceeded 25% of time in the (Cs) and 20% in the (Bs). The GSs exceeds for 10% of time the “Warm” category in the receptor S1. The effect of the Green Saturation scenario (GSs) is remarkable in receptor S2.

It worth highlighting that, as far as the PMV is concerned, the worst results were obtained in the (Cs), while the best performance was achieved by the GSs. This trend is even more evident in the cumulative frequency distribution of PET.

## 6.2. Spatial Analysis

### 6.2.1. Air Temperature, Wind Speed, and Relative Humidity

Figure 11 collects a horizontal view (x-y) of air temperature, wind speed, and relative humidity for the three scenarios at 1.00 m height above the ground level at 12:00 am on August 23.

In this section, the scenarios are analyzed according to a spatial point of view, considering the following parameters: air temperature ( $T_a$ ), wind speed ( $w$ ), and relative humidity (RH). In the Baseline scenario (Bs), the air temperature of 30.0 °C is reached in most of the areas analyzed.

The highest values of air temperature occur on waterproof surfaces, such as pedestrian pavement and roads, while the minimum value of temperature, of about 28.4 °C, occurs on unpaved surfaces. Under the Cool scenario (Cs), temperatures lower than 29.0 °C have been found in all the investigated areas.

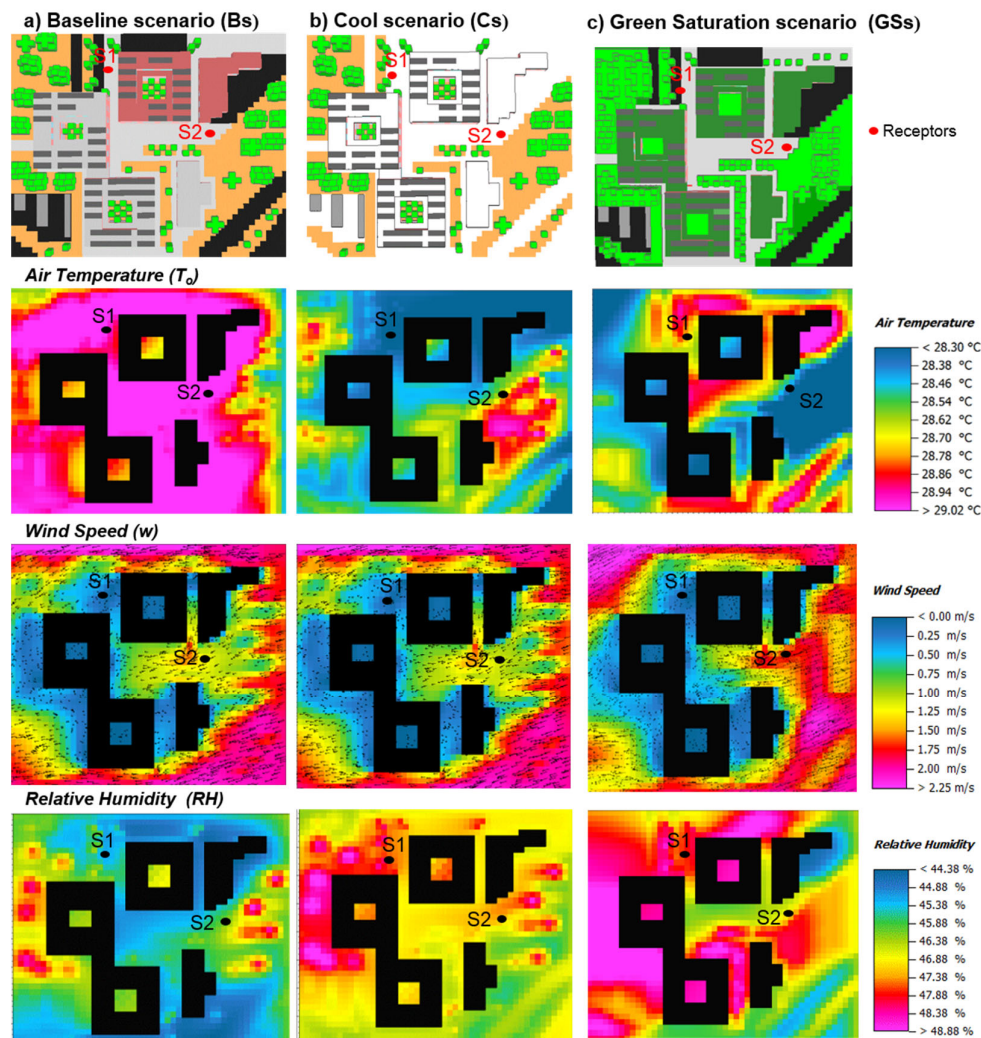


**Figure 11.** Air temperature, wind speed, and relative humidity on horizontal plan (x-y) at  $z = 1.00$  m and at 12.00 a.m. on August 23 for the Baseline (Bs), Cool (Cs), and Green Saturation (GSs) scenarios.

Above soil surfaces, the temperatures range between 28.5 to 28.8 °C and over the roads and pedestrian pavements, the temperature is about 28.2 °C. Globally, cool pavements and roofs allow to reduce the peaks of about 1.0 °C.

For the Green Saturation scenario (GSs), the maximum external air temperature is 29.2 °C, whereas the minimum is 28.0 °C. Consequently, this latest scenario is the most effective, especially regarding the magnitude of minimum values of air temperature.

However, it is worth noticing that the cooling effect of vegetation is not limited to spaces where the plants were added, but their effects are spread to all the surrounding areas.

As regards the field of wind, it is possible to observe that the wind comes from the east, and its speed ranges from 0 to 2.25 m/s. As predicted, the highest wind speed is observed in open areas, whereas areas of stagnation appear behind the buildings or in the narrow spaces between the buildings. Moreover, in areas where vegetation is most present, substantial disturbances of wind speed occur as a consequence of the highest roughness of the soil surface.

The maps of relative humidity, for the three scenarios, indicate that the areas where vegetation is present are characterized by the highest relative humidity (up to 49%). In the Green Saturation scenario (GSs), the highest values of relative humidity were found. A maximum value of 51.6% was recorded in areas where the vegetation is very dense.

### 6.2.2. Soil Temperature, Mean Radiant Temperature, and Thermal Comfort Indexes

In this section, the scenarios are analyzed by a spatial point of view considering the following parameters: soil temperature ( $T_{\text{soil}}$ ), mean radiant temperature (MRT), predicted mean vote (PMV), and physiological equivalent temperature (PET) (Figure 12).

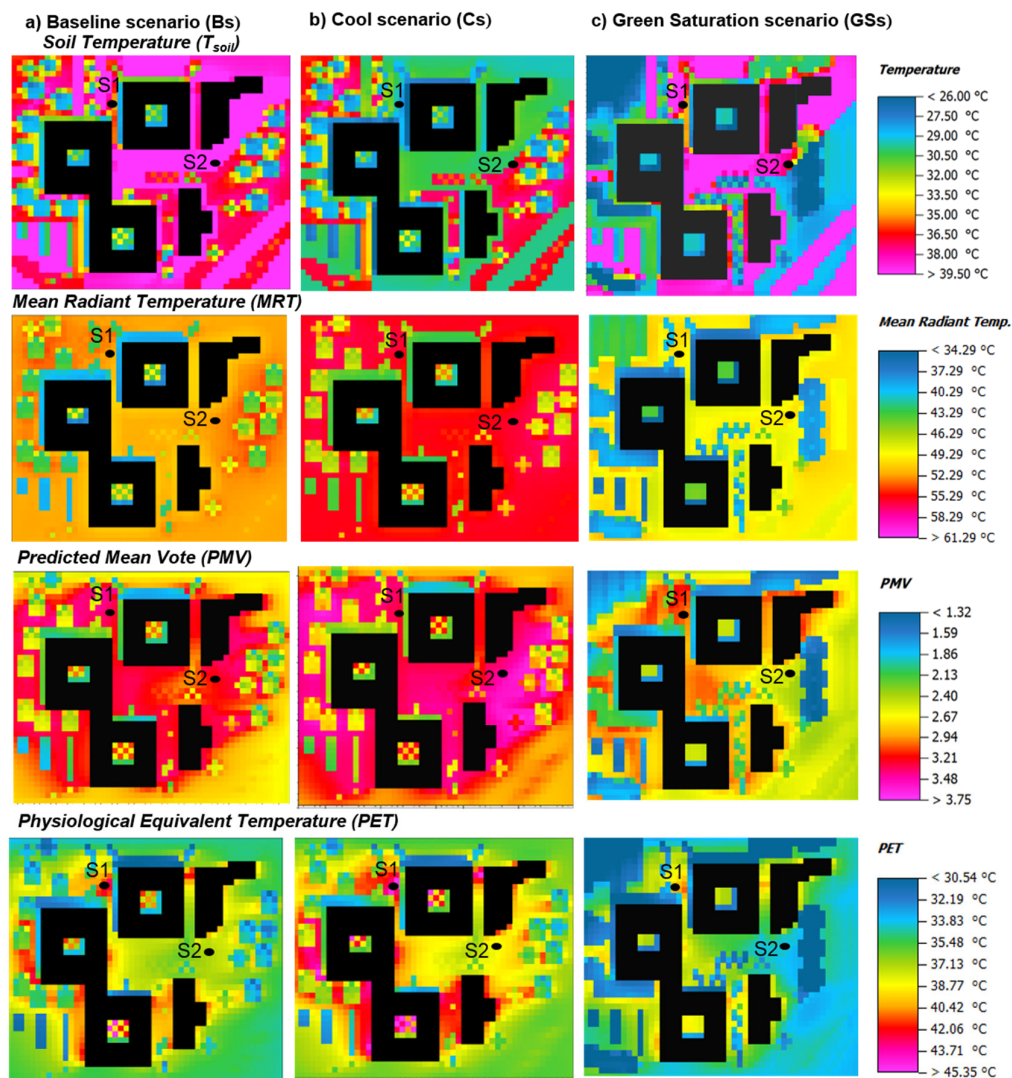


**Figure 12.** Soil temperature, mean radiant temperature, predicted mean vote, and physiological equivalent temperature for Baseline (Bs), Cool (Cs), and Green Saturation (GSs) scenarios on a horizontal plan (x-y) at  $z = 1.00$  m, at 12.00 a.m., on August 23.

For the Baseline scenario (Bs), the soil temperature reaches the maximum values of 44.2 °C in paved areas, while just 27.0 °C is observed in the vegetated or shaded areas. The MRT has an average value of 52.0 °C in the whole area, which drops to 43.0 °C in shaded areas. The PMV index has a maximum value of 3.03 and a minimum value of 1.99.

The areas occupied by pedestrian pavements and roads have PMV values of about 3.00 and can be classified as hot areas, whereas the green areas with PMV values of 2.00 can be classified as warm areas. The PET index has a maximum value of 47.0 °C in paved areas and a minimum of 30.5 °C in the vegetation areas. Therefore, the Baseline scenario can be classified as hot and characterized by rather strong heat stress. Thus, for most of the investigated areas, the environment is very far from comfortable conditions, and high degrees of discomfort are perceived by the people.

The Cool scenario (Cs) shows values of soil temperature between 25.1 °C and 38.8 °C. On the surface of cool pavements, one can observe a reduction at around 5.0 °C compared to the maximum value of the Baseline scenario (Bs) and a reduction by 2.0 °C in the minimum value. It has to be highlighted that the mean radiant temperature reaches values of 55.0 °C almost in the whole area with an increment of about 3.0 °C compared to the Baseline scenario. This quite unexpected outcome depends on the remarkable amount of solar radiation reflected from the cool pavements and able to cause an increase in the temperature of the surrounding surfaces. The PMV ranges from a minimum value of 2.08 to a maximum of 3.50. In the Cool scenario, both the minimum and maximum values of PMV are higher than in the Baseline case. The PET index has a maximum value of 47.6 °C and a minimum value of 31.4 °C, with an increment of about 1.6 °C and 1.0 °C with respect to the Baseline scenario. It is worth to be highlighted that in the areas between neighboring buildings and in the spaces between the cool pavements and buildings is apparently a strong increase of PET. These areas suffer because of high reflected radiation and relative humidity.

Although the surface temperature of the pavements is reduced, the multiple heat reflections lead to an increase of the human thermal stress, as deductible by observing the magnitude of the maximum and minimum values of PMV and PET, compared to the baseline scenario.

Looking at the map of the reflected radiation, it is worth underlining that the cool pavements reflect in the average 200 W/m<sup>2</sup> against 170 and 130 W/m<sup>2</sup> of the Baseline (Bs) and Green Saturation (GSs) scenarios, respectively. The previous outcome confirms that the application of cool paint over a paved area contributes to the deterioration of the outdoor thermal comfort due to the increase of the reflected solar irradiance.

Figure 13 reports the 2D maps of reflected solar radiation (Gr) for all investigated scenarios on a horizontal plane at pedestrian level, at 12.00 a.m., on August 23.

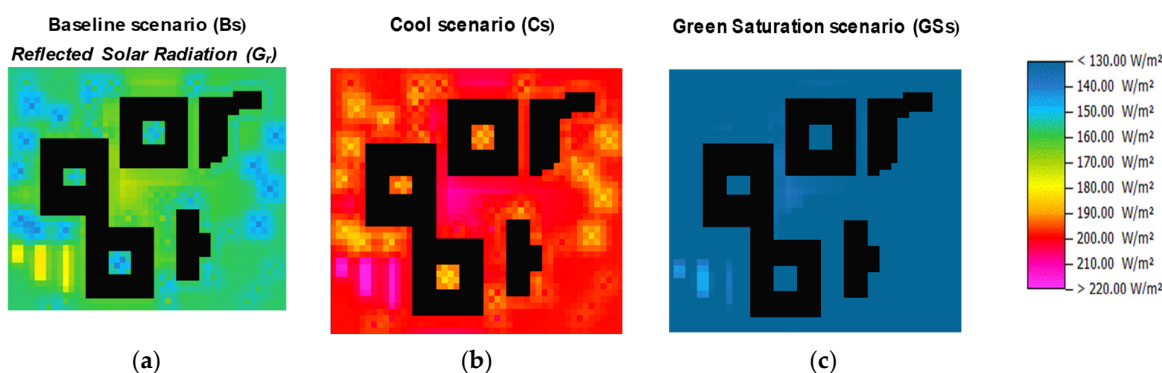


**Figure 13.** Reflected solar radiation (Gr) on a horizontal plan (x-y) at  $z = 1.00$  m, at 12.00 a.m., on August 23: (a) Baseline scenario (Bs); (b) Cool scenario (Cs); (c) Green Saturation scenario (GSs).

The Green Saturation scenario (GSs) offers the best behavior in terms of MRT, PMV, and PET. As a matter of fact, MRT ranges between 34.4 °C and 52.3 °C. In addition, PMV has a minimum value of 1.4 and a maximum value of 3.0. Finally, PET assumes values between 28.0 °C and 41.1 °C.

To further characterize the various scenarios, it is useful to introduce the indicator  $I_{PET}$  defined by the variation of PET between the Baseline (Bs) and the proposed scenarios ( $P_{s,i}$ ), as follows:

$$I_{PET,i} (\%) = \frac{PET_{P_{s,i}} - PET_{Bs}}{PET_{Bs}} \quad (2)$$

The  $i$  index is referred to the different proposed scenarios, i.e.,  $P_s = C_s$ ,  $P_s = GS_s$ .

Figure 14 depicts the  $I_{PET}$  for the Cool and Green Saturation scenarios at  $z = 1.00$  m at noon on August 23. The positive sign means an increase of PET, while the negative sign indicated a reduction.

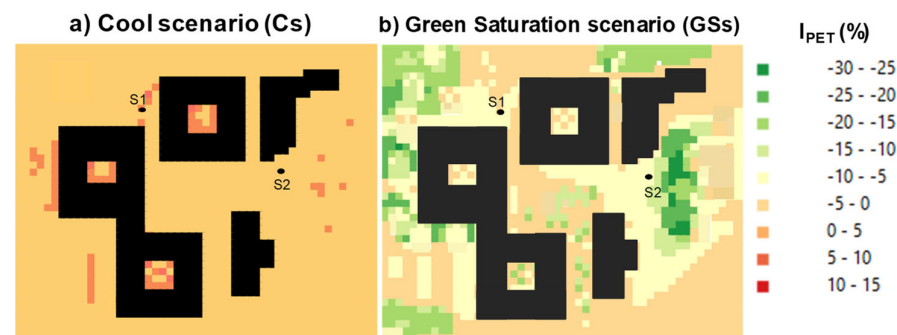


**Figure 14.** Normalized percentage variation of PET ( $I_{PET}$ ) (a) Cool scenario (Cs); (b) Green Saturation scenario (GSs) on a horizontal plan (x-y) at  $z = 1.00$  m, at 12.00 a.m., on August 23.

As it is possible to see, the Cool scenario shows an increase in the PET in all points of the investigated area. Figure 14 shows that the highest increase of the PET (10–15%) occurs in the internal courtyards of the buildings, mostly due to the multiple reflections. On the contrary, the Green Saturation scenario shows a reduction in the PET values in all investigated areas.

The highest reduction (−30% to −20%) is reached in the areas with trees and shrubs. It is worth pointing out that a decrease in PET of about 5% is achieved even in areas not provided with vegetation.

Of course, the beneficial effect of the Green scenario has to be attributed to the evapotranspiration of plants, which leads to a cooling effect in the surroundings. Moreover, the shading effect of trees and shrubs allows the creation of small areas where the warming sensation is attenuated.

Generally, under the Green Saturation scenario, it is possible to achieve acceptable outdoor thermal comfort with the exception of very limited areas represented by the surfaces between neighboring buildings and spaces around the buildings.

### 6.2.3. Spatial Cumulative Frequency Distribution

Figure 15 shows the cumulative frequency distribution of  $T_o$ , MRT, PMV, and PET for Baseline (Bs), Cool (Cs), and Green Saturation (GSs) scenarios with reference to the whole investigated area at height of 1.0 m above the ground level at 12.00 p.m. on August 23.

Overall, the graphs show that in spite of the fact that the Cool scenario (Cs) exhibits the best performance in terms of  $T_o$ , it proves to be the worst case in terms of MRT, because of the high reflectivity assumed by the surfaces treated with cooling paints.



The consequences can be seen in the PMV and PET, considering that both PMV and PET are more sensitive to MRT than to  $T_o$ .

This is a clear hint about the adverse effect that reflective paints may cause on the thermal sensation in the outdoor environment. In conclusion, compared to the baseline scenario, the best performance thus pertains to the GSs.

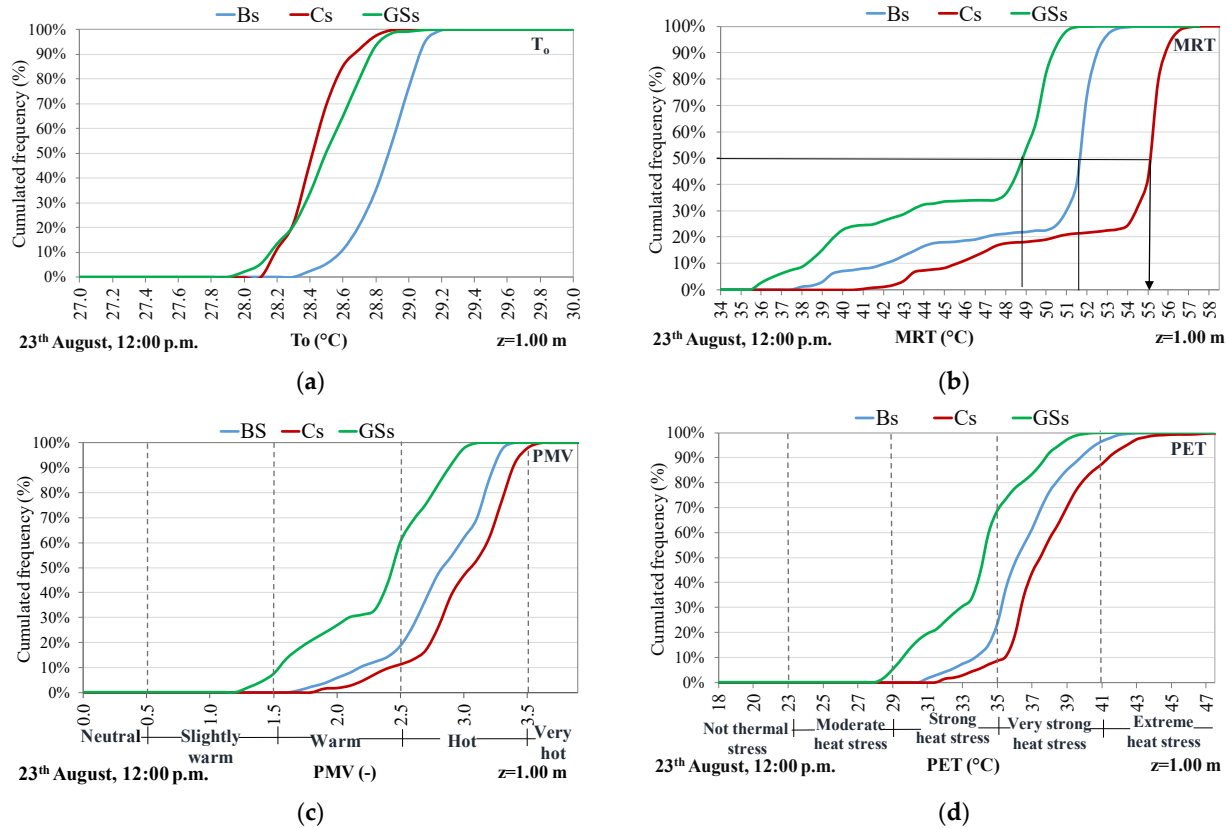


**Figure 15.** Cumulative frequency distribution referred to the whole surface of investigated area at 12.00 p.m. on August 23 at height of 1.0 m above the ground level for the Baseline (Bs), Cool (Cs), and Green Saturation (GSs) scenarios: (a) outdoor temperature ( $T_o$ ); (b) mean radiant temperature (MRT); (c) PMV; (d) PET.

### 6.3. Spatial Averages

In order to provide a synthetic comparison of the three proposed scenarios, the average values of the thermal parameters and the comfort indicators were calculated. The spatial average values on the whole area relating to air temperature, mean radiant temperature, relative humidity, predicted mean vote, and physiological equivalent temperature is as follows:

$$\bar{L} = \frac{\sum_{i=1}^n L_n}{n} \quad (3)$$

Here,  $\bar{L}$  is the average spatial value of any previously mentioned (L) parameter extended to all cells (n) of the domain.

The average values of the investigated parameters for each scenario are compared and reported in Figure 16. In particular, Figure 16a displays a comparison in terms of outdoor air temperature, mean radiant temperature, and relative humidity. Figure 16b reports the comparison in terms of the mean values of PMV and PET according to the thermal sensation scale and heat stress categories. All the microclimate parameters and thermal comfort indicators refer to 1.00 m above the ground level and at 12.00 a.m. on

August 23. Finally, PMV and PET normalized to their maximum values for the three analyzed scenarios are reported in Figure 16c.

Again, overall, Figure 16 shows that the best results are achieved by the Green Saturation scenario (GSs), which has the lowest of value  $T_o$ , MRT, PMV, and PET. These results are attributable to the synergic effect of shading and evapotranspiration processes. On the other hand, the Cool scenario (Cs) has the worst performance even with respect to the Baseline scenario (Bs), for all the mentioned parameters, with the exception of  $T_o$ .

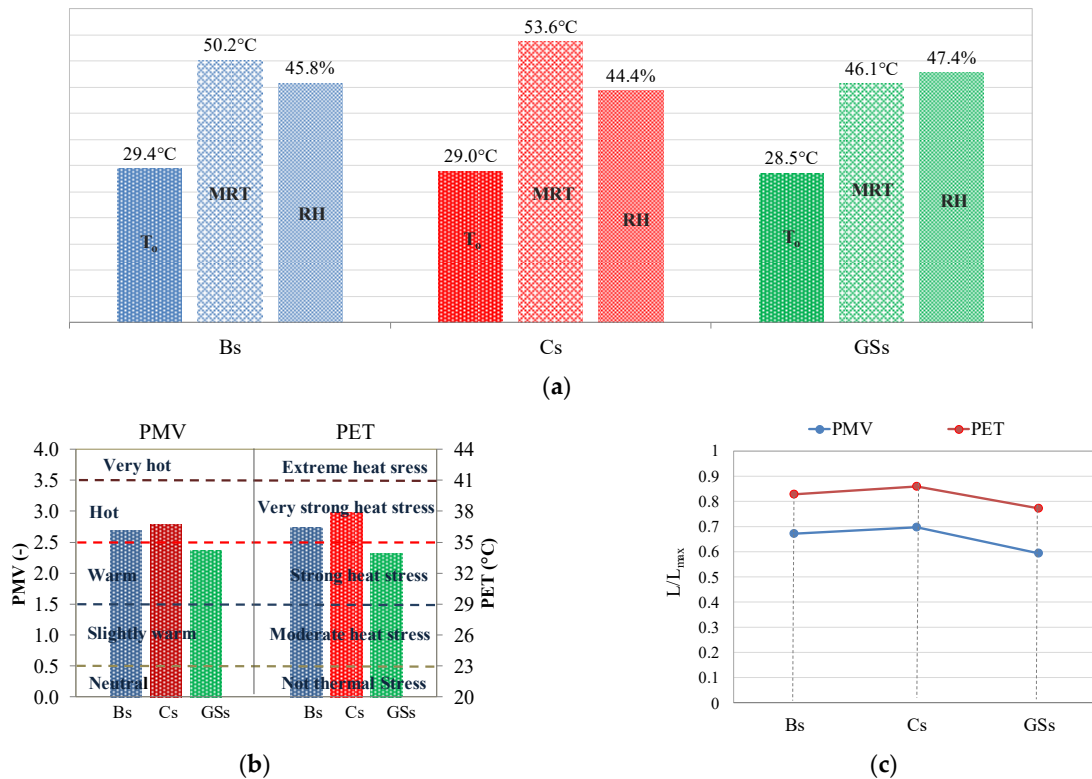


**Figure 16.** The average values of the investigated parameters for the Baseline (Bs), Cool (Cs) and Green Saturation (GSs) Scheme 1.00 m, at 12.00 a.m., on August 23. (a)  $T_o$ , MRT, and RH; (b) PMV and PET with threshold values of thermal sensation and stress category; (c) PMV and PET normalized to their maximum values.

It is to outline, that although the surfaces treated with green materials are less by 17% than those treated with cool materials, they allow achieving the greatest benefits for the urban microclimate and thermal comfort at the pedestrian level.

## 7. Conclusions

This paper aims to identify the effectiveness of urban greening and cool materials as strategies for the enhancement of urban micro-climate and well-being conditions of pedestrians. To this purpose, a micro-scale analysis, based on a numerical model and experimental field measurements, was carried out in the University Campus of the metropolitan city of Catania. The influence of materials and vegetation was analyzed to assess pedestrian comfort in different scenarios. The outcomes of the simulations reveal that the green roof does not affect the microclimate at the pedestrian level, while the application of cool materials can reduce the air temperature by almost 1.0 °C in the peak value compared to the other scenarios, while it is the Green Saturation scenario that ensured the best performance in terms of MRT, PMV, and PET.

Other meaningful results were also provided by the cumulative frequency curves. They allowed the estimation of how long a given condition of  $T_o$ , MRT, PMV, or PET is holding, and showed that the three scenarios are more sensitive to MRT than to  $T_o$ . Finally,

the evaluation of PET and PMV provided comparable results. All the gathered information made it easy to assess the effectiveness of the various mitigation measures.

In conclusion, the methodology used here may be useful to urban planners and policymakers searching for the optimal urban greening and cooling strategies in the urban environment.

**Author Contributions:** conceptualization: A.G. and F.N.; methodology: F.N., M.D., A.G., and L.M.; software: M.D. and F.N.; validation: M.D., A.G., and F.N.; formal analysis: L.M. and F.N.; investigation: M.D., A.G., and F.N.; resources: A.G., L.M., and F.N.; data curation: M.D., A.G., and F.N.; writing—original draft preparation: M.D., F.N., L.M., and A.G.; writing—review and editing: L.M., F.N., M.D., and A.G.; visualization: L.M. and A.G.; supervision: L.M., F.N., and A.G.; project administration: M.D., A.G., and F.N.; funding acquisition: A.G. and F.N. All authors have read and agreed to the published version of the manuscript.

**Funding:** This research received no external funding.

**Institutional Review Board Statement:** Not applicable.

**Informed Consent Statement:** Not applicable.

**Data Availability Statement:** Not applicable.

**Conflicts of Interest:** The authors declare no conflict of interest.

## References

- Heatwave Plan for England—Making the Case: The Impact of Heat on Health—Now and in the Future. Department of Health, 1–21, 2015. Available online: <https://www.england.nhs.uk/2015/06/2015-heatwave-plan> (accessed on 11 March 2021).
- Li, D.; Boud-Zeid, E. Synergistic interactions between urban heat islands and heat waves: The impact in cities is larger than the sum of its parts. *J. Appl. Meteorol. Climatol.* **2013**, *52*, 2051–2064, doi:10.1175/JAMC-D-13-02.1.
- Climate Change Impacts and Vulnerability European. An Indicator Based Report. European Environment Agency (EEA), Copenhagen, 2012. Available online: <https://energee-watch.eu/wp-content/uploads/2014/05/Climate-change-impacts-and-vulnerability-in-Europe-2012.pdf> (accessed on 11 March 2021).
- Akbari, H.; Levinson, R.; Miller, W.; Berdahl, W.P. Energy Saving Potentials and Air Quality Benefits of Urban Heat Island Mitigation, Lawrence Berkeley National Laboratory, 2005. Available online: <http://escholarship.org/u-c/item/20j676c9> (accessed on 11 March 2021).
- Akbari, H.; Cartalis, C.; Kolokotsa, D.; Muscio, A.; Pisello, A.L.; Rossi, F.; Santamouris, M.; Synnefa, A.; Wong, N.; Zinzi, M. Local climate change and urban heat island mitigation techniques—the state of the art. *J. Civ. Eng. Manag.* **2016**, *22*, 1–16, doi:10.3846/13923730.2015.1111934.
- Alexandri, E.; Jones, O. Temperature decreases in an urban canyon due to green walls and green roofs in diverse climates. *Build. Environ.* **2008**, *43*, 480–493, doi:10.1016/j.buildenv.2006.10.055.
- Akbari, H.; Konopacki, S. Calculating energy-saving potentials of heat-island reduction strategies. *Energy Policy* **2005**, *33*, 721–756, doi:10.1016/j.enpol.2003.10.001.
- Tzavali, A.; Paravantis, J.P.; Mihalakakou, G.; Fotiadi, A.; Stigka, E. Urban heat island intensity: A literature review. *Fresenius Environ. Bull.* **2015**, *24*, 4537–4554.
- Santamouris, M.; Synnefa, A.; Karlessi, T. Using advanced cool materials in the urban built environment to mitigate heat islands and improve thermal comfort conditions. *Sol. Energy* **2011**, *85*, 3085–3102, doi:10.1016/j.solener.2010.12.023.
- Takebayashi, H.; Moriyama, M. Surface heat budget on green roof and high reflection roof for mitigation of urban heat island. *Build. Environ.* **2007**, *42*, 2971–2979, doi:10.1016/j.buildenv.2006.06.017.
- Dimoudi, A.; Zoras, S.; Kantzioura, A.; Stogiannou, X.; Kosmopoulos, P.; Pallas, C. Use of cool materials and other bioclimatic interventions in outdoor places in order to mitigate the urban heat island in a medium size city in Greece. *Sustain. Cities Soc.* **2014**, *13*, 89–96, doi:10.1016/j.scs.2014.04.003.
- Akbari, H.; Matthews, H.D. Global cooling updates: Reflective roofs and pavements. *Energy Build.* **2012**, *55*, 2–6, doi:10.1016/j.enbuild.2012.02.055.
- Dandou, A.; Santamouris, M.; Synnefa, A.; Soulakellis, N.; Tombrou, M. On the Use of Cool Materials as a Heat Island Mitigation Strategy. *J. Appl. Meteorol. Climatol.* **2008**, *47*, 2846–2856.
- Oke, T.R. The energetic basis of the Urban Heat Island. *Q. J. R. Meteorol. Soc.* **1982**, *108*, 1–24, doi:10.1002/qj.49710845502.
- Salvati, A.; Roura, H.C.; Cecere, C. Assessing the urban heat island and its energy impact on residential buildings in Mediterranean climate: Barcelona case study. *Energy Build.* **2017**, *146*, 38–54, doi:10.1016/j.enbuild.2017.04.025.
- Mihalakakou, G.; Santamouris, M.; Papanikolaou, N.; Cartalis, C.; Tsangrassoulis, A. Simulation of the Urban Heat Island Phenomenon in Mediterranean Climates. *Pure Appl. Geophys.* **2004**, *161*, 429–451, doi:10.1007/s00024-003-2447-4.
- Fanger, P.O. *Thermal Comfort. Analysis and Applications in Environmental Engineering*; McGrawHill: New York, NY, USA, 1970.

18. ISO 7730. *Ergonomics of the Thermal Environment—Analytical Determination and Interpretation of Thermal Comfort Using Calculation of the PMV and PPD Indices and Local Thermal Comfort Criteria*; International Standards Organization: Geneva, Switzerland, 2005.
19. Honyo, T. Thermal Comfort in Outdoor Environment. *Glob. Environ. Res.* **2009**, *13*, 43–47.
20. Jendritzky, G.; Nübler, W. A model analysing the urban thermal environment in physiologically significant terms. *Meteorol. Atmos. Phys.* **1981**, *29*, 313–326, doi:10.1007/BF02263308.
21. Höppe, P. Heat balance modelling. *Experientia* **1993**, *49*, 741–746, doi:10.1007/BF01923542.
22. Höppe, P. Die Energiebilanz des Menschen. *Wiss. Mitt. Meteor. Inst. Univ. München* **1984**, *49*, 1–12.
23. Höppe, P. The physiological equivalent temperature—a universal index for the biometeorological assessment of the thermal environment. *Int. J. Biometeorol.* **1999**, *43*, 71–75, doi:10.1007/s004840050118.
24. Li, D.; Boud-Zeid, E.; Oppenheimer, M. The effectiveness of cool and green roof as urban heat mitigation strategies. *Environ. Res. Lett.* **2014**, *9*, 055002, doi:10.1088/1748-9326/9/5/055002.
25. Santamouris, M. Cooling the cities—A review of reflective and green roof mitigation technologies to fight heat island and improve comfort in urban environments. *Sol. Energy* **2014**, *103*, 682–703, doi:10.1016/j.solener.2012.07.003.
26. Taha, H.; Akbari, H.; Rosenfeld, A. Heat island and oasis effects of vegetative canopies: Micro-meteorological field-measurements. *Theor. Appl. Climatol.* **1991**, *44*, 123–138, doi:10.1007/BF00867999.
27. Zoras, S.; Tsermentselis, A.; Kosmopoulos, P.; Dimoudi, A. Evaluation of the application of cool materials in urban spaces: A case study in the center of Florina. *Sustain. Cities Soc.* **2014**, *13*, 223–229, doi:10.1016/j.scs.2014.01.007.
28. Kolokotsa, D.D.; Giannariakis, G.; Gobakis, K.; Giannarakis, G.; Synnefa, A.; Santamouris, M. Cool roofs and cool pavements application in Acharnes, Greece. *Sustain. Cities Soc.* **2018**, *37*, 466–474, doi:10.1016/j.scs.2017.11.035.
29. Gagliano, A.; Nocera, F.; Detommaso, M.; Evola, G. Thermal behavior of an extensive green roof: Numerical simulations and experimental investigations. *Int. J. Heat Technol.* **2006**, *34*, S226–S234, doi:10.18280/ijht.34S206.
30. Santamouris, M. Urban warming and mitigation: Actual status, impacts and challenges. In *Urban Climate Mitigation Techniques*, 1st ed.; Santamouris, M., Kolokotsa, D.D., Eds.; Taylor & Francis Group: London, UK, 2016; pp. 1–26, doi:10.4324/9781315765839.
31. Susca, T.; Gaffin, S.R.; Dell’osso G.R. Positive effects of vegetation: Urban heat island and green roofs. *Environ. Pollut.* **2011**, *159*, 2119–2226, doi:10.1016/j.envpol.2011.03.007.
32. Maleki, A.; Mahdavi, A. Evaluation of urban heat islands mitigation strategies using Three dimensional urban micro-climate model ENVI-met. *Asian J. Civ. Eng.* **2016**, *17*, 357–371.
33. ENVI-met V4.5. Urban Environment through Holistic Microclimate Modelling. Available online: <https://www.envi-met.com/last> (accessed on 13 February 2020).
34. Bruse, M.; Fleer, H. Simulating surface–plant–air interactions inside urban environments with a three dimensional numerical model. *Environ. Model. Softw.* **1998**, *13*, 373–384, doi:10.1016/S1364-8152(98)00042-5.
35. Bruse, M. ENVI-met 3.0: Updated Model Overview. 2004. Available online: <http://www.envi-met.net/documents/papers/overview30.pdf> (accessed on 11 March 2021).
36. Jacobs, C.M.J.; Van den Hurk, B.J.J.M.; de Bruin, H.A.R. Stomata behaviour and photosynthetic rate of unstressed grapevines in semi-arid conditions. *Agric. For. Meteorol.* **1996**, *80*, 111–134, doi:10.1016/0168-1923(95)02295-3.
37. Fang, Z.; Feng, X.; Lin, Z. Investigation of PMV Model for Evaluation of the Outdoor Thermal Comfort. *Procedia Eng.* **2017**, *205*, 2457–2462, doi:10.1016/j.buildenv.2017.11.028.
38. Gagge, A.P.; Stolwijk, A.J.A.; Nishi, Y. An effective temperature scale based on a simple model of human physiological regulatory response. *ASHRAE Trans.* **1971**, *77*, 247–257.
39. Giuffrida, S.; Gagliano, F.; Nocera, F.; Trovato, M.R. Landscape assessment and economic accounting in wind farm programming: Two cases in sicily. *Land* **2018**, *7*, 120.
40. ISO 7726. *Ergonomics of the Thermal Environment—Instruments for Measuring Physical Quantities*; International Organization for Standardization: Geneva, Switzerland, 1998.
41. Despotovic, M.; Nedic, V.; Despotovic, D.; Cvetanovic, S. Review and statistical analysis of different global solar radiation sunshine models. *Renew. Sustain. Energy Rev.* **2015**, *52*, 1869–1880, doi:10.1016/j.rser.2015.08.035.
42. Ramos Ruiz, G.; Fernández Bandera, C. Validation of calibrated energy models: Common errors. *Energies* **2017**, *10*, 1587, doi:10.3390/en10101587.
43. Trovato, M.R.; Nocera, F.; Giuffrida, S. Life-cycle assessment and monetary measurements for the carbon footprint reduction of public buildings. *Sustainability* **2020**, *12*, 3460.
44. Gagliano, A.; Patania, F.; Capizzi, A.; Nocera, F.; Galesi, A. A proposed methodology for estimating the performance of small wind turbines in urban areas. In *Sustainability in Energy and Buildings, Smart Innovation, Systems and Technologies*; M’Sirdi, N., Namaane, A., Howlett, R.J., Jain, L.C., Eds.; Springer: Berlin/Heidelberg, Germany, 2012, doi:10.1007/978-3-642-27509-8\_45.
45. Salvati, A.; Kolokotroni, M. Microclimate Data for Building Energy Modelling: Study on ENVI-Met Forcing Data. In Proceedings of the 16th International Building Performance Simulation Association IBPSA Conference, Rome, Italy, 2–4 September 2019.
46. Mohamed Elnabawi, H.; Hamza, N.; Dudek, S. Numerical modelling evaluation for the microclimate of an outdoor urban form in Cairo, Egypt. *Hous. Build. Natl. Res. Center J.* **2015**, *11*, 246–251, doi:10.1016/j.hbrj.2014.03.004.
47. Gusson, C.S.; Duarte, D.H.S. Effects of built density and urban morphology on urban microclimate-calibration of the model ENVI-met V4 for the subtropical Sao Paulo, Brazil. *Procedia Eng.* **2016**, *169*, 2–10, doi:10.1016/j.proeng.2016.10.001.

48. CRRC Rated Products Directory. Available online: [Coolroofs.org/products/search.php](https://coolroofs.org/products/search.php) (accessed on 12 June 2020).
49. Sailor, D.J. A green roof model for building energy simulation programs. *Energy Build.* **2008**, *40*, 1466–1478, doi:10.1016/j.enbuild.2008.02.001.

#### 4.7 Macroscale modelling vs Microscale modelling: a comparison in terms of $T_{mrt}$

The outcomes relating to the selected risk areas (area 1 and area 2) derived by numerical modelling at large scale were compared with those of the same areas modelled at urban Microscale level.

The comparison was carried out in terms of mean radiant temperature. The hourly profiles of mean radiant temperature predicted by models at urban Macroscale level (SOLWEIG) (dashed blue line) and at Microscale level (ENVI-met) (dotted brown line) respectively were compared to that measured (solid blue line) at specific points (receptors R1 and R2) located in the investigated areas 1 and 2.

Figure 4.52a show the hourly profiles of  $T_{mrt}$  calculated in the receptor R1 located in the area 1 modelled at urban large scale and Microscale respectively and plotted against the  $T_{mrt}$  measured profile from 12.00 on 7<sup>th</sup> August to 10.00 on 8<sup>th</sup> August at the same point.

Figure 4.52b depicts the hourly profiles of  $T_{mrt}$  calculated in the receptor R2 located in the area 2 modelled at urban large scale and Microscale respectively and plotted against the  $T_{mrt}$  measured from 8.00 on 30<sup>th</sup> July to 9.00 on 31<sup>st</sup> July at the same point.

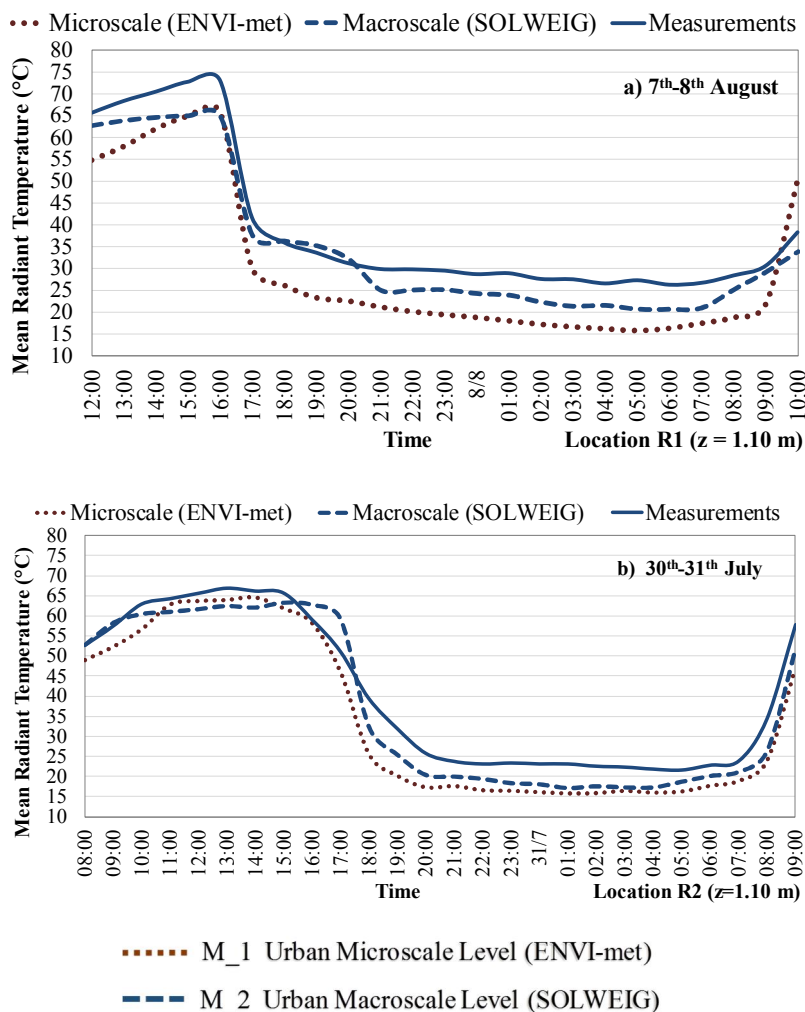


Figure 4.52. Hourly profiles of  $T_{mrt}$  predicted by urban Macroscale and Microscale models in receptors R1 (a) and R2 (b) against  $T_{mrt}$  measured profile.

The comparison revealed some discrepancies between measured data (solid brown lines) and simulated scenarios M\_1 (Urban Microscale model) and M\_2 (Urban Macroscale model) throughout the days considered. Although the discrepancies are less evident in SOLWEIG (M\_2 Urban Macroscale level), they are significant during night hours. Indeed, simulated profiles by means of ENVI-met (M\_1 Urban Microscale level) and SOLWEIG (M\_2 Urban Macroscale level) are below the actual measured profile at nighttime in both receptors R1 and R2. A difference in the mean radiant temperature of around 8 – 10°C between simulations and measurements was found during the period (from 18.00 to 8.00). This gap could be due to the overestimation of  $T_{mrt}$  measurements at nighttime because of the shelter device of the thermo-hygrometric sensor. The device has shielded the thermo-hygrometric probe under direct solar radiation but has reduced the heat transfer from device surface towards the surrounding air during the night hours. As a result, the cooling of the sensor was reduced and the mean radiant temperature measured at night was always above 23°C.

Nevertheless, both Macroscale and Microscale models have well approximated the  $T_{mrt}$  observed values during the hours of maximum solar radiation.

Table 4.11 reports the statistical indices between the predicted and measured data of mean radiant temperature in the receptors R1 and R2.

*Table 4.11. Validation indices of the Macroscale and Microscale models in the receptors R1 and R2.*

Variable	Indices	Unit	R1 (7 <sup>th</sup> – 8 <sup>th</sup> August)		R2 (30 <sup>th</sup> – 31 <sup>st</sup> July)	
			Microscale (ENVI-met)	Macroscale (SOLWEIG)	Microscale (ENVI-met)	Macroscale (SOLWEIG)
			M_1	M_2	M_1	M_2
$T_{mrt}$	%error	-	29%	10%	15%	14%
	MAE	°C	9.88	3.37	6.22	5.19
	RMSE	°C	9.92	3.77	7.50	6.44
	d	-	0.92	0.98	0.96	0.98
	r	-	0.96	0.99	0.96	0.98
	R <sup>2</sup>	-	0.93	0.97	0.94	0.96

When it comes to Macroscale (M\_2) and Microscale (M\_1) scenarios, it is shown that the estimation of mean radiant temperature ( $T_{mrt}$ ) is in a good approximation with the measured values for both of the two receptors, whose values of Pearson correlation coefficient (r) are higher than 0.96 and the values of the determination coefficient (R<sup>2</sup>) are always above 0.93.

$T_{mrt}$  predicted using the Microscale approach (M\_1) has shown a higher gap between simulations and measurements than that attained at Macroscale level at nighttime. This can be inferred from the MAE and RMSE values attained when a Microscale approach is adopted (Scenario M\_1) in all investigated receptors. As an example MAE = 9.88°C and RMSE = 9.92°C in receptor R1 under Scenario M\_1 were achieved. This deviation was probably due to some approximations used in the radiation

calculation in the ENVI-met model. Since the calculation of long wave radiation intensity emitted by building surfaces is based on mean temperature and not on the temperature of a single surface, a relatively large error can be determined when the long wave radiation intensity on different surfaces in an urban region is calculated (Huttner, 2012).

A graphical representation of the results obtained by simulation scenarios (M\_1 and M\_2) is also given in Figure 4.53, where a regression line is plotted for  $T_{mrt}$  data along with the attained coefficient of determination  $R^2$ .

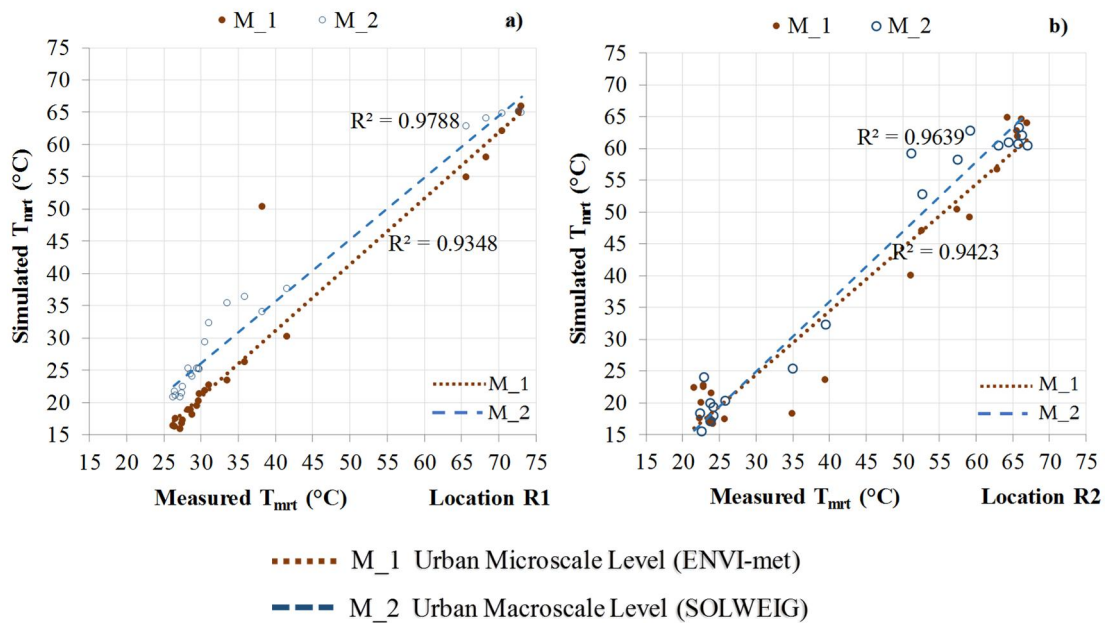


Figure 4.53. Linear regression of Mean Radiant Temperature predicted by Microscale and Macroscale models against the Mean Radiant Temperature observed: a) receptor R1, b) receptor R2.

As shown in Figures 4.53a and 4.53b, the mean radiant temperature profiles derived from the simulation of Macroscale model (M\_2) have a good correlation with the observed data ( $R^2 = 0.96$  and  $R^2=0.97$ ) in the receptors R1 and R2. The comparison between the outcomes achieved by the simulations of urban large-scale model and those attained by Microscale model was extended to the entire domain of the investigated areas (Area 1 and Area 2).

Figures 4.54a and 4.54b show the spatial cumulative frequency of  $T_{mrt}$  with reference to the investigated domain at 1.10 m above the ground level of Area 1 (at 12.00 on 7<sup>th</sup> August (a)) and Area 2 (at 12.00 on 30<sup>th</sup> July(b)) modelled at Macroscale and Microscale respectively.



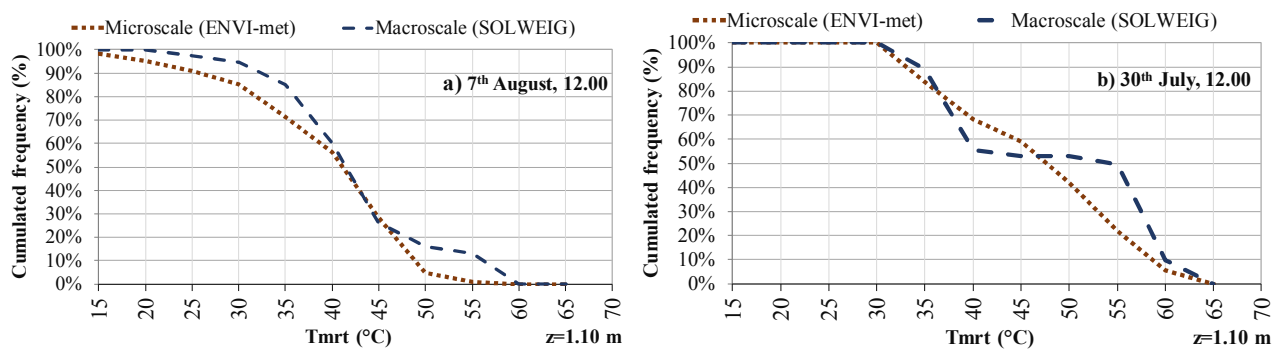


Figure 4.54. Spatial cumulative frequency distribution of  $T_{mrt}$  at 1.10 m a.g.l. in Macroscale and Microscale models: a) Area 1 (12.00 on 7<sup>th</sup> August), b) Area 2 (12.00 on 30<sup>th</sup> July).

Overall, although the graphs show that Macroscale and Microscale models exhibit trends rather similar to spatial cumulative frequency of  $T_{mrt}$  in both investigated areas, a discrepancy between Macroscale and Microscale models predominantly in the range of  $T_{mrt}$  between 50°C and 60°C was found in both areas 1 and 2.

This discrepancy is relevant in Area 2, characterized by open and sunlit areas where a deviation of 25% around 55°C was achieved (Figure 4.54 b). This means that Area 1 modeled at Macroscale level has a surface about 25% more than the Microscale model of the same area where the  $T_{mrt}$  value is higher than 55°C. In Area 1, a deviation of 10% for the same range of  $T_{mrt}$  was achieved.

In Area 1, a deviation within 10% between Microscale and Macroscale modelling for  $T_{mrt}$  values below 40°C was also found.

Overall, the areas modelled at large-scale by means of SOLWEIG are more sensitive with respect to the radiation field as the areas modelled at Macroscale have a percentage of surface higher than that of the Microscale model where the  $T_{mrt}$  values between 50°C and 60°C are exceeded. This result may be due to a different calculation method of the outgoing shortwave and long wave radiation adopted in SOLWEIG and ENVI-met software respectively. In particular, this outcome may be attributed to the method used to calculate the shortwave reflected radiation by buildings, ground and other surfaces in ENVI-met. In ENVI-met, the adoption of a domain-wide mean surface albedo can underestimate the magnitude of the reflected radiation.

In addition, the discrepancy between Macroscale and Microscale models may depend on the difference in vegetation models between the two software and approximation regarding the radiative properties of vegetation and wall surfaces of the SOLWEIG model. Since a single value of albedo and emissivity can be attributed to walls surface and ground of a wide-domain in SOLWEIG, an overestimation of a mean radiant temperature may be generated.

**CHAPTER FIVE:  
CONCLUSION AND PERSPECTIVES**

## Conclusions

“Heat waves” phenomena will be more frequent and last longer in warm and temperate climates typical of the Mediterranean context. The interactions between this phenomenon and urban heat island can produce rather high heat stress for urban residents. The implications of Urban Heat Island, which is caused by the combined effects of urbanization through poor design planning and decreased green areas, can lead to uncomfortably raised urban temperatures.

This prompted the carrying out of extensive research on the effects and consequences of urban heat stress and human health of urban residents. Most studies present in literature dealt with the assessment of the effects of UHI mitigation strategies through an approach based on Microscale analysis. In addition, these studies predominantly analysed the outdoor microclimate by means of parameters such as the air temperature. However, this parameter is not sufficient to investigate the outdoor thermal comfort and the correlation between outdoor comfort and heat stress pathologies. In literature, very few studies dealt with the assessment of the heat-related mortality risk based on urban climate analysis at large-scale.

In the light of this, the present thesis deals with the analysis of the urban microclimate and identification of the potential heat stress mitigation strategies in the most risk areas by means of top-down approach (from the Macroscale down to the Microscale).

The top-down approach adopted in this research is outlined based on three main steps:

- Identification of the most sensitive heat stress risk areas based on Macroscale analysis; to this aim, a new Local Climate Zones (LCZs) classification by means of the UMEP (Urban Multi-scale Environmental Predictor) tool was carried out.
- Urban Microscale analysis of two risk areas by means of accurate CFD models developed in ENVI-met. Based on Microscale modelling heat stress mitigation strategies were proposed.
- Climate simulations of almost the entire urban area were carried out by means of a Macroscale approach based on the SOLWEIG module in UMEP. Subsequently, urban Macroscale and Microscale simulations were compared in order to assess the reliability of the numerical modelling at large-scale to design suitable mitigation strategies.

The analysis was conducted using the mean radiant temperature as the main parameter owing to its capability for investigating human thermal comfort and heat stress in outdoor environments.

Moreover, high mean radiant temperature values are assumed as the hazard factor to identify outdoor climate conditions that can cause increased heat-related mortality risk for vulnerable urban residents. ENVI-met and UMEP models were calibrated and validated through different measurement campaigns conducted at four selected locations points in different summer periods as presented in the

article “Application of weather data morphing for calibration of urban ENVI-met microclimate models. Results and critical issues” reported in section 4.4. Air temperature, relative humidity, wind speed and mean radiant temperature were measured.

What has been found is that mean radiant temperature simulated by ENVI-met can be deemed well correlated and accurately predicted. Overall, a reasonable agreement between field measurement and ENVI-met simulations was achieved.

As reported in the published articles, the integration of urban heat mitigation strategies in the urban Microscale models has shown appreciable results in term of reductions of the main microclimate parameters.

Although ENVI-met is a reliable tool in the estimation of the effectiveness of mitigation heat stress strategies by virtue of high accuracy level of the modelling, the models are very complex. The modelling of urban areas with size of 500 m x 500 m and very high resolution of the calculation grid requires very long simulation time. Thus, climate analysis of areas larger than 500 m x 500 m cannot be dealt with using the Microscale approach.

In order to assess the reliability of SOLWEIG in the simulation of an urban large-scale area and overcome the spatial and temporal limitations of Microscale models, the urban Macroscale and Microscale simulations were compared with on-site measurements.

The SOLWEIG model, calibrated by means of urban climate morphing via SUEWS plugin has proved to accurately estimate the mean radiant temperature. Based on the comparison between predicted and measured mean radiant temperature, the values of statistical indices (MAE, d, r,  $R^2$ ) have shown a good correlation between simulated and measured data in the investigated receptors. In particular, the best result was achieved for receptor R1 under Macroscale modelling (M\_2), where MAE value is 3.07 °C and RMSE is 3.77 °C. In addition, the index of agreement (d) approaches 0.98 and the Pearson’s correlation coefficient (r) achieves a value of 0.98. In light of this, it was observed that the predicted data by SOLWEIG can be considered reliable.

According to Local Climate Zones (LCZs) classification, impervious and no shading areas were identified as the more critical areas during the warmest hours in clear sky and on a sunny day.

SOLWEIG simulations have confirmed this evidence. In open areas, mean radiant temperature values predominantly between 60°C and 65°C were found. Mean radiant temperature values even higher than 60°C were attained. Since the mean radiant temperatures of 55.5°C and 59.4°C represent the threshold values over which the heat-related mortality risk increase of 5% and 10% for age bands 80+, open areas can involve critical consequences for human health and “Very Strong Heat Stress” conditions for urban residents.

In compact dense built-up areas, mean radiant temperatures are predominantly between 50°C and 60°C. Mean radiant temperature values between 40°C and 50°C were achieved in shaded areas by virtue of the effect of the mutual shadings of buildings. According to UTCI values, “Strong Heat stress” conditions were predicted during the warmest sunny days.

The present study has also estimated also the potential effectiveness of heat stress mitigation strategies through SOLWEIG and ENVI-met models respectively. To this aim, a design scenario was proposed according to the morphological features of the investigated areas as described in section 3.7.

In compact and high built-up density area, a scenario based on the integration of greenery along existing street spaces rearranged according to the principles of traffic calming was proposed. It includes a reduction of the wide of streets and the planting of trees along the roads according to a mild approach as described in section 3.7.2. The tree type was selected according to morphological and geometrical features of the local urban area. Trees with sparse foliage and high trunk are implemented in dense built up areas.

In open and low-rise built areas, an intensive greening of existing urban spaces by means of the planting of high trees with large crown was proposed as in section 3.7.3.

In Design Scenario, an increase in the Green Cover Ratio of +6.34% was planned with respect to the Current Scenario.

In areas close to the street trees, mean radiant temperature reductions of up to 5°C were achieved during sunny hours. In these locations, a decrease in peak values of UTCI allowed the maintaining of the thermal sensation below the threshold of “Very Strong Heat Stress” at pedestrian levels.

Under canopy trees with wide crowns, mean radiant temperatures reductions up to 20°C were attained. In these points, UTCI values were predominantly within the “Moderate Heat Stress” class. Despite relevant results being attained at specific points nearby the trees, the entire investigated urban area is slightly affected by the presence of vegetation. This revealed that the increase of Green Cover Ratio of +6.34% is very low in comparison with the investigated area size. Areas far away from trees have shown small or negligible reductions in mean radiant temperature.

On the contrary, ENVI-met simulations have shown that the vegetation also influences the areas far away from the forestation interventions. Indeed, such areas are characterized by a decrease in mean radiant temperature of up to 5.0 °C as discussed in the section related to the interventions at the urban Microscale level. This could be attributed to the difference between analytical models adopted by both the two software. ENVI-met is based on the Computation Fluid-dynamic model and is accurate in the estimation of the interactions between plant surfaces and atmosphere as asserted in numerous

studies. In addition, this result could be due to the assumptions made with respect to the vegetation in SOLWEIG.

No relevant difference was found between the Macroscale and Microscale approaches in term of results. Macroscale modelling is recommended for analysis at large-scale both spatial and temporal because numerical simulations can be extended to an entire year.

In addition, as the Macroscale model is integrated in Qgis Environment the climate data and microclimate predictions are georeferenced.

By means of Qgis Environment the Macroscale model can be linked to a prediction system that allows the population to be notified on the most heat-wave risk days or hours.

Macroscale analysis is suggested to carry out studies aimed to alert the population on the risk heat wave.

Despite the intrinsic spatial and temporal limitations, ENVI-met remains the more accurate software that allows the detailed modelling of buildings, trees, and plants. Since the cool materials, green roofs, green façades and specific trees can be modelled into the spatial domain, ENVI-met software is recommended when a detailed analysis of the potential effects of the advanced mitigation strategies have to be carried out.

Based on the research findings and conclusions, the potential guidelines for providing mitigation strategies are as follows:

1. Forestation interventions have a relevant influence in urban environment. Therefore, it is suggested that planting tree species in appropriate quantities should be considered as additional guidelines in mitigation strategies, in the design of urban regeneration plans of existing scenarios. In the case of built-up urban areas, the replacement or adding of extra trees, with the right physical criteria is recommended to result in the desired cooling effect.
2. Choice of the right trees should be based on the morphological features of the trees such as trunk height, height and crown diameter, type of tree species, size of leaves and branching arrangement. These morphological features should be selected taking into account the sky view factor of the points of the investigated areas where the forestation interventions are planned. Medium foliage trees, with average and/or short total height but high trunk are recommended in high densely built-up areas with Sky view factor values predominantly between 0.20 and 0.45. In the light of this, deciduous trees such as *Platanus Hispanica* should be planted along the roads and in urban spaces where SVF is between 0.30 and 0.50. On the contrary, trees with high leaf density and a large crown are recommended in open areas with Sky view factor values between 0.50 and 0.90. Tree species such as *Platanus Acerifolia*

should be planted along large roads with width of around 20 m while *Platanus occidentalis* should be inserted in open areas such as bare soil, paved areas, parks and green areas.

The species selection also needs to take into consideration availability of native plants that are appropriate for the geographic and climate context. Making the right choice of the plants would result in a more effective and better radiation interception and also lowered urban temperatures. In addition, in order to provide optimum effect, trees with cluster planting design are recommended to offer a better quality of shade and cooling to influence the human energy budget and improve outdoor thermal comfort.

The outcomes of this study offer a solution to evaluate the influence of heat waves in the urban environment and identify the critical areas in term of pedestrian thermal comfort by means of city-based climate analysis.

The study has proposed a renovation scenario for the mitigation of urban heat in warm and temperate climates by assessing the potential cooling effect of trees. The proposed guidelines can be useful to city officials, architects, landscape architects, urban planners and environmentalists in order to develop mitigation urban heat stress scenarios.

Nevertheless, some issues and detailed findings need further investigations, in order to refine the simulation models, improve physical properties modelling and evaluation of outdoor climate.

Some suggestions for future research are recommended to refine the detailed procedures carried out for this study:

1. One of the critical issues of the present study regards the instruments used in measuring globe temperature during the experimental measuring campaign. Although the predicted data by simulation models have a good index of agreement and are well correlated with observed data, the mean radiant temperature could be slightly overestimated. This suggests that further research needs to consider grey globe thermometer and pyrgeometer with six flux directions that are able to evaluate globe temperature more accurately.
2. Despite a good correlation between predicted and observed data being achieved, there are some shortcomings which should be addressed. They concern the number of points selected for the on-site microclimate measurements and the length of period of experimental measurements campaigns. Two receptors and a measurement period of one day represent a limitation. Therefore, a number of higher points and a longer period of experimental measurements should be considered, compared to that selected.
3. Risk areas mapping of the entire investigated city.

4. Development of a predictive algorithm that allows the population to be notified in advance (48-72 h) the probability of a heat wave. In this way, it is also possible to plan temporary interventions.
5. Future investigations should be carried out considering a more advanced urban regeneration scenario that involves strong transformation of urban tissue, i.e. scenario with higher Green Cover Ratio values in respect of that adopted in this study. A renovation scenario based on reduction of unused building stock should be considered in order to increase the Green Cover Ratio. The free areas achieved by the demolition of buildings can be covered by vegetation.



## **Acknowledgments**

*First and foremost, I would like to express my gratitude and appreciation to my advisors Professors Francesco Nocera, Francesco Martinico and PhD Vincenzo Costanzo for the continuous support of my research, for guidance and advice over the past three years.*

*In particular, I would like to thank Professor Francesco Nocera for his motivation, great enthusiasm, remarkable knowledge, Kindness and patience. His guidance helped me during the whole period of the research and the writing of this thesis.*

*Besides my advisors, I would like to thank professor Antonio Gagliano for providing me the measurement devices necessary to carry out the experimental measurements campaign.*

*I would also like to thank the Laboratory “Osservatorio delle patologie edilizie”(OPE) – University of Catania, and in particular Engineer Alessandro Lo Faro, as technical manager, for helping me to carry out on site spectral reflectance measurements of urban and building materials.*

*My sincere thanks are also due to the administration of the “Mario Rapisardi” school, Engineer Luca Barbarossa, professor Giovanna Laudani and Mrs. Michela Messina for allowing me access to their own spaces in order to carry out the outdoor experimental measurements.*

*I am immensely grateful to my family members for their continued support and encouragement throughout my life.*

## Reference

- Aboelata, A., Sodoudi, S. (2020). Evaluating the effect of trees on UHI mitigation and reduction of energy usage in different built up areas in Cairo. *Building and Environment*, 168, 106490.
- Acero, J.A., Arrizabalaga, J. (2018). Evaluating the performance of ENVI-met model in diurnal cycles for different meteorological conditions. *Theor. Appl. Climatol.* 131 (1–2), 455–469.
- Acero, J.A., Herranz-Pascual, K., (2015). A comparison of thermal comfort conditions in four urban spaces by means of measurements and modelling techniques. *Building and Environment* 93, 245–257.
- Akbari, H., Pomerantz, M., and Taha, H. (2001). Cool surface and shade trees to energy use and improve air quality in urban areas. *Solar Energy*, 70(3). 295-310.
- Akbari H, Levinson R, Miller W, Berdahl P. (2005). Energy saving potentials and air quality benefits of urban heat island mitigation. Lawrence Berkeley National Laboratory.
- Akbari, H., Berdhal, P., Levinson, R., Wiel, S., Miller, B., and Desjarlais (2006). *Cool colour roofing material*. Lawrence Berkeley National Laboratory Report, Berkley and Oak Ridge, USA.
- Akbari, H., Cartalis, C., Kolokotsa, D., Muscio A., Pisello, A.L., Rossi, F., Santamouris, M., Synnefa A., Wong, N., Zinzi, M. (2016). Local climate change and urban heat island mitigation techniques – the state of the art. *Journal of Civil Engineering and Management*, 22(1), 1-16.
- Ali-Toudert, F., Mayer, H. (2006). Numerical study on the effects of aspect ratio and solar orientation on outdoor thermal comfort in hot and dry climate. *Building and Environment* 41, 94–108.
- Andreou, E. (2013). Thermal comfort in outdoor spaces and urban canyon microclimate. *Renewable Energy* 55, 182–188.
- Anderson, J. R., Hardy, E.E., Roach, J.T., Witmer and R.E. (1976). A land use and land cover classification system for use with remote sensor data. Geological Survey Professional Paper 964, 28.
- Armson, D., Stringer, P., Ennos, A. R. (2012). The effect of tree shade and grass surface on surface temperatures in an urban area. *Urban Forestry & Urban Greening*, 11, 245-255.
- Arnfield, A.J. (2003). Two decades of urban climate research: A review of turbulence, exchanges of energy and water, and the urban heat island. *International Journal of Climatology*, 23, 1–26.
- Åström, D.O., Forsberg, B., Rocklöv, J. (2011). Heat wave impact on morbidity and mortality in the elderly population: a review of recent studies. *Maturitas*, 69, 99–105.
- Auer, A. H. (1978). Correlation of land use and cover with meteorological anomalies. *Journal Applied Meteorology*, 17, 636–643.

- Azam, M.H. Morille, B., Bernard J., Musy, M., Rodriguez, F. (2018). A new urban soil model for SOLENE-microclimat: Review, sensitivity analysis and validation on a car park. *Urban Climate*, 24, 728-746.
- Bartesaghi, K., Osmond, P., Peters, A. (2017). Towards a comprehensive green infrastructure typology: a systematic review of approaches, methods and typologies, *Urban Ecosystems* 20(1): 15–35.
- Barlow, F.J. (2014). Progress in observing and modelling the urban boundary layer. *Urban Climate* 10, 216–240.
- Battista, G., Carnielo, E., Vollaro, RDL. (2016). Thermal impact of a redeveloped area on localized urban microclimate: A case study in Rome. *Energy and Buildings*, 133, 446-454.
- Battista, G., De Lieto Vollaro, R., Zinzi, M. (2019). Assessment of urban overheating mitigation strategies in a square in Rome, Italy, *Solar Energy*, 180, 608–621.
- Bechtel, B., Alexander, P.J., Böhner, J., Ching, J., Conrad, O., Feddema, J., Mills, G., See, L., Stewart, I. (2015). Mapping Local Climate Zones for a Worldwide Database of the Form and Function of Cities. *Int. J. Geo-Inf.* 4, 199-219.
- Berardi, U. (2016). The outdoor microclimate benefits and energy saving resulting from green roofs retrofits, *Energy and Buildings* 121, 217–229.
- Blazejczyk, K. (1994). New climatological-and-physiological model of the human heat balance outdoor (MENEX) and its applications in bioclimatological studies indifferent scales. *Zesz. IgiPZ PAN* 28, 27–58.
- Blazejczyk, K., Holmer, I., Nilsson, H. (1998). Absorption of solar radiation by an ellipsoid sensor simulated the human body. *Applied Human Science*, 17(6), 267-273.
- Blazejczyk, K., Epstein, Y., Jendritzky, G., Staiger, H., Tinz, B. (2012). Comparison of UTCI to selected thermal indices. *International Journal of Biometeorology*, 56, 515-535.
- Bowler, D. E., Buyung-Ali, L.; Knight, T. M.; Pullin, A. S. (2010). Urban greening to cool towns and cities: A systematic review of the empirical evidence, *Landscape and Urban Planning* 97(3), 147–155.
- Bozonnet, E., Doya, M., Allard, F. (2011). Cool roofs impact on building thermal response: A French case study. *Energy and Buildings*, 43, 3006–3012.
- Breil, M., Downing, C., Kazmierczak, A., Mäkinen, K., Romanovska, L. (2018). Social vulnerability to climate change in European cities – state of play in policy and practice. *Eur. Top Cent Clim. Chang. Impacts* 1–86 Vulnerability Adapt. (Fondazione CMCC).

- Brousse, O., Martilli, A., Foley, M., Mills, G., Bechtel, B. (2016). WUDAPT, an efficient land use producing data tool for mesoscale models? Integration of urban LCZ in WRF over Madrid. *Urban Climate*, 17, 116–134.
- Bruse, M. (1999) Die Auswirkungen kleinskaliger Umweltgestaltung auf das Mikroklima. Entwicklung des prognostischen numerischen Modells ENVI-met zur Simulation der Wind-, Temperatur- und Feuchteverteilung in städtischen Strukturen. Dissertation, Ruhr-Universität Bochum
- Bruse, M. "ENVI-met 3.0: Updated Model Overview", 2006. Available at: <http://www.envi-met.com>. (last accessed on 15/06/2020).
- Bruse, M., Fleer, H. (1998). Simulating surface–plant–air interactions inside urban environments with a three dimensional numerical model. *Environmental Modelling & Software* 13, 373–384.
- Bruse, M. ENVI-met Technical model webpage, 2018. <http://www.envi-met.info/doku.php?id=start> (last accessed on 15/06/2020).
- Cantón, M.A., Cortegoso, J.L., Derosa, C. (1994) Solar permeability of urban trees in cities of western Argentina. *Energy and Buildings*, 20(3), 219–230.
- Capozzoli, A., Gorrino, A., Corrado, V. Thermal characterization of green roofs through dynamic simulation. In: Proceedings of 13<sup>th</sup> conference of international building performance simulation association, Chambéry, France, 2013. 26-8. August.
- Carnielo, E., Zinzi, M. (2013). Optical and thermal characterization of cool asphalts to mitigate urban temperatures and building cooling demand. *Building and Environment* 60, 56-65.
- Cartalis, C., Synodinou, A., Proedrou, M., Tsangrasoulis, A., Santamouris, M. (2001). Modifications in energy demand in urban areas as a result of climate changes: An assessment for the Southeast Mediterranean region. *Energy Conversion and Management*, 42(14), 1647–1656.
- Carter, J.G. (2011). Climate change adaptation in European cities. *Curr. Opin. Environ. Sustain.* 3 (3), 193–198.
- Carter, J.G., Cavan, G., Connelly, A., Guy, S., Handley, J., Kazmierczak, A. (2015). Climate change and the city: building capacity for urban adaptation. *Prog. Plann.* 95, 1–66.
- Castleton, H.F., Stovin, V., Beck, S.B.M., Davison, J.B. (2010). Green roofs; building energy savings and the potential for retrofit. *Energy and Buildings*, 42, 1582–1591.
- Chandler, T. J. (1965). *The Climate of London*. Hutchinson, 292.
- Chapman, S., Watson, J.E.M., Salazar, A., Thatcher, M., Mc Alpine, C.A. (2017). The impact of urbanization and climate change on urban temperatures: a systematic review. *Landsc. Ecol.* 32 (10), 1921–1935.

- Chatzinikolaou, E., Chalkias, C., Dimopoulou, E. Urban microclimate improvement using Envi-met climate model. *The International Archives of the Photogrammetry, Remote Sensing and Spatial Information Sciences*, Volume XLII-4, 2018, ISPRS TC IV Mid-term Symposium “3D Spatial Information Science – The Engine of Change”, 1–5 October 2018, Delft, The Netherlands.
- Chen, Y.C., Lin, T.P., Matzarakis, A. (2014). Comparison of mean radiant temperature from field experiment and modelling: a case study in Freiburg, Germany. *Theoretical Applied Climatology*, 118 (3), 535–551.
- Chen, L., Yu, B., Yang, F., Mayer, H. (2016). Intra-urban differences of mean radiant temperature in different urban settings in Shanghai and implications for heat stress under heat waves: a GIS-based approach. *Energy and Building*, 130, 829–842.
- Chen, Y.H., Wu, J.T., Yu, K. (2020). Evaluating the impact of the building density and height on the block surface temperature, *Building and Environment*, 168 (1), 106493.
- Cheng, C.Y., Cheung, K. K. S., Chu, L. M. (2010). Thermal performance of a vegetated cladding system on facade walls, *Building and Environment*, 45(8), 1779–1787.
- Cheng, C.Y., Niu, J., Gao, N. (2012). Thermal comfort models: a review and numerical investigation, *Building and Environment*, 47, 13-22.
- Ching, J., See, L., Ren, C., Masson, V., Hidalgo, J., Wang, X., Feddema, J. (2017). The WUDAPT framework for generating urban morphology, material composition and activity data for modelling. Paper presented at the 97<sup>th</sup> 13 American Meteorological Society, Seattle.
- Chow, W.T.L., Pope R.L., Martin, C.A., Brazel A.J. (2011). Observing and modeling the nocturnal park cool island of an arid city: Horizontal and vertical impacts. *Theoretical Applied Climatology*, 103(1-2), 197–211.
- Chrysoulakis, N., Grimmond, C.S.B. (2016). Understanding and reducing the anthropogenic heat emission. *Urban Climate Mitigation Techniques*, 40, 27–40.
- Coccolo, S., Kämpf, J., Scartezzini, J.L., Pearlmutter, D. (2016). Outdoor human comfort and thermal stress: A comprehensive review on models and standards. *Urban Climate*, 18, 33–57.
- Cohen, P., Potchter, O., Matzarakis, A. (2012). Daily and seasonal climatic conditions of green urban open spaces in the Mediterranean climate and their impact on human comfort. *Building and Environment* 51, 285–295.
- Coseo P., Larsen L. (2014) How Factors of Land Use /Land Cover, Building Configuration, and Adjacent Heat Sources and Sinks Explain Urban Heat Islands in Chicago, *Landscape and Urban Planning*, 125, 117-129.

- Crank, P. J., Sailor, D.J., George Ban-Weiss, Taleghani, M. (2018). Evaluating the ENVI-met microscale model for suitability in analysis of targeted urban heat mitigation strategies. *Urban Climate* 26, 188-197
- Dahanayake, K.C., Chow, C. L., Long Hou, G. (2017). Selection of suitable plant species for energy efficient Vertical Greenery Systems (VGS), *Energy Procedia* 142, 2473–2478.
- Davenport, A.G., Grimmond, C.S.B., Oke, T.R, Wieringa, J. (2000). Estimating the roughness of cities and sheltered country. Proc 12<sup>th</sup> Conf Appl Climatol, Asheville, NC, p 96–99
- de' Donato, F., Leone, M., Scortichini, M. (2015). Changes in the effect of heat on mortality in the last 20 years in Nine European Cities. results from the PHASE project. *International Journal Environment Research Public Health* 12 (12), 15567–15583.
- De Jesus, M.P., Lourenço, J.M., Arce, R.M., Macias, M. (2017). Green façades and in situ measurements of outdoor building thermal behaviour, *Building and Environment* 119, 11–19.
- Deak Sjöman, J. (2016). The hidden landscape: On fine-scale green structure and its role in regulating ecosystem services in the urban environment. *Acta Universitatis Agriculturae Sueciae* 3.
- Department of Health. (2015). Heatwave Plan for England– Making the Case: the impact of heat on health – now and in the future. 2015 Edition: 1-21. Available: <https://www.england.nhs.uk/2015/06/2015-heatwave-plan/>
- Di Napoli, C., Barnard, C., Prudhomme, C., Cloke, H.L., Pappenberger, F. (2020). ERA5-HEAT: A global gridded historical dataset of human thermal comfort indices from climate reanalysis, *Geoscience Data Journal* 00, 1-9.
- Dimitrieva, T.B., Kirenskaya, A.V., Novototsky-Vlasov, V.Y. (2008). EEG concomitants of the emotional experience. *Int. J. Psychophysiol.* 69 (3), 200.
- Doick, K.; Hutchings, T. (2013). *Air temperature regulation by urban trees and green infrastructure*. Forestry Commission, UK.
- Economou, D., Petrakos, G., Psycharis, Y. (2007). Urban policy in Greece, In *National Policy Responses to Urban Challenges in Europe*, L Van den Berg, E Braun and J Van der Meer (eds.), pp. 193–216. Ashgate, Aldershot.
- Ekaterini, E., Dimitris. A. (1998). The contribution of a planted roof to the thermal protection of buildings in Greece. *Energy and Buildings*, 27, 29-36.
- Ellefsen, R., (1990/91) Mapping and measuring buildings in the urban canopy boundary layer in ten US cities. *Energy and Buildings*, 15–16, 1025–1049.
- Ellis, K. N., Hathaway, L., Mason, R., Howe, D. A., Epps, T. H., Brown, V. M. (2017). Summer temperature variability across four urban neighborhoods in Knoxville, Tennessee, USA, *Theoretical and Applied Climatology* 127(3–4), 701–710.

- Elnabawi, M.H., Hamza, N., Dudek, S. (2015). Numerical modelling evaluation for the microclimate of an outdoor urban form in Cairo, Egypt, Housing and Building National Research Center HBRC Journal 11, 246–251.
- Emmanuel, R. (2005). Thermal Comfort implications of urbanization in a warm-humid city: the Colombo Metropolitan Region (CMR), Sri Lanka. *Building and Environment*, 40, 1591-1601.
- Emmanuel, R., Fernando, H.J.S. (2007). Urban Heat Islands in humid and arid climates: role of urban form and thermal properties in Colombo, Sri Lanka and Phoenix, USA. *Climate Research* 34(3), 241-251.
- Emmanuel, R., Rosenlund, H., Johansson, E. (2007) Urban shading—a design option for the tropics? A study in Colombo, Sri Lanka. *International Journal of Climatology*, 27(14), 1995-2004.
- Environment Protection Agency United States (2010). Heat Island Impact, Available on line: <http://www.epa.gov/heatisland/impacts/insex.htm>.
- Erell, E., Pearlmutter, D., Williamson, T. (2011). Urban Microclimate Designing the Spaces between Buildings, New York.
- EU report, Cities of tomorrow: Challenges, visions, ways forward, (2011). European Commission—Directorate General for Regional Policy, Luxembourg: Publications Office of the European Union, 2011 — 112 pp. ISBN: 978-92-79-21307-6.
- Eurostat, Population Structure Indicators, 2020.  
[http://appsso.eurostat.ec.europa.eu/nui/show.do?dataset=demo\\_pjanind](http://appsso.eurostat.ec.europa.eu/nui/show.do?dataset=demo_pjanind). Data extracted on 02/11/2020.
- Fang, Z., Feng, X., Lin, Z. (2017). Investigation of PMV Model for Evaluation of the Outdoor Thermal Comfort. *Procedia Engineering*, 205, 2457–2462.
- Fang, Z., Feng, X., Liu, J., Lin, Z., Mak, C.M., Niu, J., Tse, K.T., Xu, X. (2019). Investigation into the differences among several outdoor thermal comfort indices against field survey in subtropics. *Sustainable Cities and Society* 44, 676–90.
- Fanger, P.O. (1972). *Thermal Comfort, Analysis and Application in Environmental Engineering*. McGraw-Hill, New York.
- Farajzadeh, H., Saligheh, M., Alijani, B. (2016). Application of universal thermal climate index in Iran from tourism perspective. *Nat. Environ. Chang* 5, 117–138.
- Feng, C., Meng, Q., Zhang, Y. (2010). Theoretical and experimental analysis of the energy balance of the green roof. *Energy Buildings*, 42(6), 959-966.

- Fiala, D., Lomas, K.J., Stohrer, M. (2001). Computer prediction of human thermoregulatory and temperature responses to a wide range of environmental conditions. *International Journal of Biometeorology*, 45 (3), 143–159.
- Fiala, D., Havenith, G., Peter, B., Bernhard, K., & Gerd, J. (2011). UTCI-Fiala multi-node model of human heat transfer and temperature regulation. *International Journal of Biometeorology* Special Issue, 1–13.
- Fiala, D., Havenith, G., Broode, P., Kampmann, B., Jendritzky, G. (2012). UTCI-Fiala multimode model of human heat transfer and temperature regulation. *International Journal of Biometeorology*, 56, 429–441.
- Forouzandeh, A. (2018). Numerical modeling validation for the microclimate thermal condition of semi-closed courtyard spaces between buildings. *Sustainable Cities and Society*, 36, 327–345.
- Gál, T., Bechtel, B., Unger, J. (2015). Comparison of two different Local Climate Zone mapping methods. Paper presented at the the 9<sup>th</sup> International Conference on Urban Climate, Toulouse, France.
- Gál, C.V., Kántor, N. (2020). Modeling mean radiant temperature in outdoor spaces, A comparative numerical simulation and validation study. *Urban Climate*, 32, 100571.
- Gabriel, K.M.A., Endlicher, W.R. (2011). Urban and rural mortality rates during heat waves in Berlin and Brandenburg, Germany. *Environmental Pollution* 159 (8–9), 2044–2050.
- Eckstein, D., Künzler, V., Schäfer, L., Winges, M. (2019). Global Climate Risk Index 2020.
- Gagge, A.P., Fobelets, A., Berglund, L.G. (1986). A standard predictive index of human response to the thermal environment. *ASHRAE Transactions* 92, 709–731.
- Gill, S. E., Handley, J. F., Ennos, A. R., Pauleit, S. (2007). Adapting cities for climate change: The role of the green infrastructure. *Built Environment* 33(1), 115–133.
- Ghobadi, A., Khosravi, M., Tavousi, T. (2018). Surveying of heat waves impact on the urban heat islands: Case study, the Karaj City in Iran, *Urban Climate* 24, 600–615.
- Goldberg, V., Kurbjuhn, C., Bernhofer, C. (2013). How relevant is urban planning for the thermal comfort of pedestrians? Numerical case studies in two districts of the city of Dresden (Saxony/Germany). *Meteorologische Zeitschrift* 22, 739–751.
- Gong, F.Y., Zeng, Z.C., Ng, E. (2019). Spatiotemporal patterns of street-level solar radiation estimated using Google Street View in a high-density urban environment, *Building and Environment*, 148 (1), 547–566.
- Govehovitch, B., Giroux-Julien, S., Peyrol, E., Ménézo, C. (2018). Building Integrated Photovoltaic (PV) Systems: Energy Production Modeling in Urban Environment, in: EuroSun 2018 / ISES Conference Proceedings, 2018.



- Grimmond, C.S.B., Oke, T.R. (1986). Urban water balance 2: results from a suburb of Vancouver, British Columbia. *Water Resour. Res.* 22, 1404–1412.
- Grimmond, C.S.B., Oke, T.R., (1991). An evaporation-interception model for urban areas. *Water Resour. Res.* 27, 1739-1755.
- Grimmond, C. S. B., Oke, T.R. (1999). Aerodynamic properties of urban areas derived from analysis of surface form. *Journal Applied Meteorology*, 38, 1262–1292.
- Grimmond, C.S.B., Best, M., Barlow, J., Arnfield, A.J., Baik, J.-J., Belcher, S., Bruse, M., Calmet, I., Chen, F., Clark, P., Dandou, A., Erell, E., Fortuniak, K., Hamdi, R., Kanda, M., Kawai, T., Kondo, H., Krayenhoff, S., Lee, S.H., Limor, S.-B., Martilli, A., Masson, V., Miao, S., Mills, G., Moriwaki, R., Oleson, K., Porson, A., Sievers, U., Tombrou, M., Voogt, J., Williamson, T. (2009). Urban surface energy balance models: model characteristics & methodology for a comparison study. In: Baklanov, A., Grimmond, C.S.B., Mahura, A. (Eds.), *Urbanization of Meteorological & Air Quality Models*. Springer-Verlag, Athanassiadou, 97– 123.
- Grimmond, C.S.B. (2011). Initial results from Phase 2 of the international urban energy balance model comparison. *International. Journal of Climatology*. 31, 244–272.
- Grimmond, C.S.B., Oke, T.R. (2002). Turbulent Heat Fluxes in Urban Areas: Observations and a Local-Scale Urban Meteorological Parameterization Scheme (LUMPS). *Journal Applied Meteorology*. 41, 792–810.
- Grigg, D. (1965). The logic of regional systems. *Ann. Assoc. Amer. Geogr.*, 55, 465–491.
- Gugler, J., Ed. (1996). *The Urban Transformation of the Developing World*. Oxford University Press, 327.
- Hajat, S., Vardoulakis, S., Heaviside, C., Eggen, B. (2014). Climate change effects on human health: projections of temperature-related mortality for the UK during the 2020s, 2050s and 2080s. *Journal of epidemiology and community health*, 1-8, ISSN 0143-005X.
- Hamada, S, Ohta, T. (2010). Seasonal variations in the cooling effect of urban green areas on surrounding urban areas. *Urban For Urban Green*, 9, 15–24.
- Hanna, S.R., Britter, R.E. (2002). Wind flow and vapor cloud dispersion at industrial and urban sites. American Institute of Chemical Engineers.
- Hansen, J.E. (2017). Scientific reticence and sea level rise. *Environmental Research Letters*, 2, 024002.
- Hassid, S., Santamouris, M., Papanikolaou, M., Linardi, A., Klitsikas, N., Georgakis, C. (2000). The effect of the Athens heat island on air conditioning load. *Energy and Buildings*, 32, 131–141.
- Hathway, E. A., Sharples, S. (2012). The Interaction of Rivers and Urban form in Mitigation the Urban Heat Island Effect: A UK Case Study, *Building Environment* 58, 14-22.

- Heaviside, C., Cai, X. M., Vardoulakis, S. (2015). The effects of horizontal advection on the urban heat island in Birmingham and the West Midlands, United Kingdom during a heatwave. *Q. J. R. Meteorol. Soc.* 141, 1429–1441.
- Herath, H.M.P.I.K., Halwatura, R.U., Jayasinghe, G.Y. (2018). Modeling a Tropical Urban Context with Green Walls and Green Roofs as an Urban Heat Island Adaptation Strategy. *Procedia Engineering* 212, 691–698.
- Herbert, J.M., Johnson, G.T., Arnfield, A.J. (2008) Modelling the thermal climate in city canyons. *Environment Modelling Software*, 13 (3), 267-277.
- Hintz, M.J., Luederitz, C., Lang, D.J., von Wehrden, H. (2018). Facing the heat: a systematic literature review exploring the transferability of solutions to cope with urban heat waves. *Urban Climate* 24, 714–727.
- Hoelscher, M., Nehls, T., Jänicke, B., Wessolek, G. (2016). Quantifying cooling effects of facade greening: Shading, transpiration and insulation. *Energy and Buildings* 114, 283–290.
- Holst, J., Mayer, H. (2011). Impacts of street design parameters on human-biometeorological variables. *Meteorol. Z.* 20 (5), 541–552.
- Höppe, P. (1992). Ein neues Verfahren zur Bestimmung der mittleren Strahlungstemperatur im Freien [a new method to determine the mean radiation temperature outdoors]. *Wetter und Leben* 44 (1–3), 147–151.
- Höppe, P.R. (1999). The physiological equivalent temperature – a universal index for the biometeorological assessment of the thermal environment. *International Journal of Biometeorology*, 43, 71–75.
- Hu, L., Wilhelmi, O.V., Uejio, C. (2019). Assessment of heat exposure in cities: combining the dynamics of temperature and population. *Science of Total Environment* 655, 1–12.
- Huang, J., Cedeno-Laurent, J.G., Spengler, J.D., (2014). CityComfort+: A simulation-based method for predicting mean radiant temperature in dense urban areas. *Building and Environment* 80, 84–95.
- Huttner, S. (2012). Further Development And Application of the 3D Microclimate Simulation ENVI-met (Doctoral dissertation). Johannes Gutenberg-Universität, Mainz, Germany.
- Irmak, M.A., Yilmaz, S., Mutlu, E., Yilmaz, A. (2018). Assessment of the effects of different tree species on urban microclimate. *Environ. Sci. Pollut. Res.*, 25, 15802-15822.
- Jaffal, I., Ouldboukhitine, S.E., Belarbi, R. (2012). A comprehensive study of the impact of green roofs on building energy performance. *Renewable Energy*, 43, 157-164.

- Jamei, E., Rajagopalan, P., Seyedmahmoudian, M., Jamei, Y. (2016). Review on the impact of urban geometry and pedestrian level greening on outdoor thermal comfort. *Renewable and Sustainable Energy Reviews*, 54, 1002–1017.
- Jamei, E., Seyedmahmoudian, M., Horan, B. (2019). Verification of a bioclimatic modeling system in a growing suburb in Melbourne. *Science of Total Environment*, 689 (11), 883–898.
- Jänicke, B., Meier, F., Hoelscher, M.T., Scherer, D., (2015). Evaluating the effects of façade greening on human bioclimate in a complex urban environment. *Advanced Meteorology*. 747259.
- Järvi, L., Grimmond C.S.B., Christen, A. (2011). The Surface Urban Energy and Water Balance Scheme (SUEWS): Evaluation in Los Angeles and Vancouver. *Journal of Hydrology* 411, 219–237.
- Jendritzky, G., Nübler, W. (1981). A model analysing the urban thermal environment in physiologically significant terms. *Arch. Meteorol. Geophys. Bioclimatol. SeriesB*, 29 (4), 313–326.
- Jendritzky, G., Staiger, H., Bucher, K., Graetz, A., Laschewski, G. The perceived temperature—the method of the Deutscher Wetterdienst for the assessment of cold stress and heat load for the human body, Internet Workshop on Windchill, 3–7 April 2000.
- Jendritzky, G., Havenith, G., Weihs, P., Batchvarova E. Towards a Universal Thermal Climate Index UTCI for assessing the thermal environment of the human being, Final Report, COST Action Brussels, Available at [http://w3.cost.eu/fileadmin/domain\\_files/ESSEM/Action\\_730/final\\_report/final\\_report-730.pdf](http://w3.cost.eu/fileadmin/domain_files/ESSEM/Action_730/final_report/final_report-730.pdf) Accessed 20 May 2014.
- Jiang, L., O’Neill, B.C. (2017). Global urbanization projections for the shared socioeconomic pathways. *Global Environment Change*, 42, 193–199.
- Jonsson, P., Eliasson, I., Holmer, B., Grimmond, C.S.B. (2006). Long wave incoming radiation in the Tropics: results from field work in three African cities. *Theoretical Applied Climatology*, 85,185–201
- Kaloustian, N., Bechtel, B. (2016). Local Climatic Zoning and Urban Heat Island in Beirut. *Proc. Eng.* 169, 216-223.
- Kántor, N., Unger, J. (2011). The most problematic variable in the course of human-biometeorological comfort assessment—the mean radiant temperature. *Open. Geosci.* 3 (1), 90–100.
- Kántor, N., Gál, C.V., Gulyás, Á., Unger, J. (2018). The impact of façade orientation and woody vegetation on summertime heat stress patterns in a central European square: comparison of radiation measurements and simulations. *Advanced Meteorology*, Article ID 2650642

- Kamal-Chaoui, L. (2008). Competitive cities and climate change: an introductory paper. *Competitive Cities Climate Change*, 29–47.
- Kleerekoper, L., Taleghani, M., van den Dobbelsteen, A. (2017). Urban measures for hot weather conditions in a temperate climate condition: a review study, *Renewable Sustainable Energy Reviews*. 75, 515–533.
- Koerniawan, M.D. The Simulation Study of Thermal Comfort in Urban Open Spaces of Commercial Area Using EnviMet Software, the Architectural Institute of Japan, Tokyo, 2015.
- Kouis, P., Kakkoura, M., Ziogas, K., Paschalidou, A.K.S., Papatheodorou, I.S. (2019). The effect of ambient air temperature on cardiovascular and respiratory mortality in Thessaloniki, Greece. *Science of The Total Environment*, 647, 2019, 1351-1358.
- Konarska, J., Lindberg, F., Larsson, A., Thorsson, S., Holmer, B. (2014). Transmissivity of solar radiation through crowns of single urban trees—application for outdoor thermal comfort modelling. *Theoretical Applied Climatology*, 117 (3–4), 363–376.
- Kong, L., Lau, K. K.-L., Yuan, C., Chen, Y., Xu, Y., Ren, C., Ng, E. (2017). Regulation of outdoor thermal comfort by trees in Hong Kong. *Sustainable Cities and Society*, 31, 12–25.
- Kontoleon, K.J., Eumorfopoulou, E.A. (2010). The effect of the orientation and proportion of a plant-covered wall layer on the thermal performance of a building zone. *Building and Environment* 45, 1287–1303.
- Kovats, R.S., Hajat, S. (2008). Heat Stress and Public Health: A Critical Review. *Public Health*, 29, 41–55.
- Kuttler, W. (2008). The urban climate: basic and applied aspects. *Urban ecology*, 233-248.
- Laboratorio per la Pianificazione Territoriale e Ambientale (LAPTA) of the Department Civil Engineering and Architecture of the University of Catania (2021).
- Lazzarin, R.M., Castellotti, F., Busato, F. (2005). Experimental measurements and numerical modeling of a green roof. *Energy and Buildings*, 37(12), 1260-1267.
- Lau, K.K.L., Ren, C., Ho, J., Ng, E. (2016). Numerical modelling of mean radiant temperature in high-density sub-tropical urban environment. *Energy and Building* 114, 80–86.
- Lee, H., Mayer, H. (2016). Validation of the mean radiant temperature simulated by the RayMan software in urban environments. *International Journal of Biometeorology*, 60 (11), 1775–1785.
- Lelovics, E., Unger, J., Gál, T. (2014). Design of an urban monitoring network based on Local Climate Zone mapping and temperature patternmodelling. *Clim. Res.*, 60, 51–62.

- Leontidou L., Afouxenidis A., Kourliouros E., Marmaras E. (2007), Infrastructure Related urban sprawl: mega-events and hybrid peri-urban landscapes in Southern Europe, In *Urban Sprawl in Europe: Landscapes, Land-use Change and Policy*, C Couch, L Leontidou and G Petschel-Held (eds.), pp. 71–101. Blackwell, Oxford
- Li, D., Boud-Zeid, E. (2013). Synergistic interactions between urban heat islands and heat waves: the impact in cities is larger than the sum of its parts. *Journal of applied Meteorology and Climatology* 52: 2051-2064. <https://doi.org/10.1175/JAMC-D-13-02.1>
- Li, D., Boud-Zeid, E., Oppenheimer, M. (2014). The effectiveness of cool and green roof as urban heat mitigation strategies. *IOP Publishing, Environmental Research Letters* 9: 055002.
- Li, J., Zheng, B., Shen, W., Xiang, Y., Chen, X., Qi, Z. (2019). Cooling and Energy-Saving Performance of Different Green Wall Design: A Simulation Study of a Block. *Energies* 12, 2912.
- Lindberg, F., Holmer, B., Thorsson, S. (2008). SOLWEIG 1.0 e modelling spatial variations of 3D radiant fluxes and mean radiant temperature in complex urban settings. *International Journal Biometeorology*, 52, 697-713.
- Lindberg, F., Grimmond, C.S.B. (2011). The influence of vegetation and building morphology on shadow patterns and mean radiant temperatures in urban areas: model development and evaluation. *Theoretical Applied Climatology*, 105 (3-4), 311–323.
- Lindberg, F., Grimmond, C.S.B., Martilli, A. (2015a). Sunlit fractions on urban facets - impact of spatial resolution and approach. *Urban Clim.* 12, 65-84.
- Lindberg, F., Onomura, S., Grimmond, C.S.B., (2016). Influence of ground surface characteristics on the mean radiant temperature in urban areas. *International Journal of Biometeorology*, 60(9), 1439–1452.
- Lindberg, F., Grimmond, C.S.B. (2018). Urban Multi-scale Environmental Predictor (UMEP): An integrated tool for city-based climate services. *Environmental Modelling & Software*, 99, 70-87.
- Lindberg, F. Grimmond, C.S.B., Gabey, A., Huang, B., Kent, C.W., Sun, T., Theeuwes, N., Järvi, L., Ward, H., Capel-Timms, I., Chang, Y.Y., Jonsson, P., Krave, N., Liu, D., Meyer, D., Olofson, F., Tan, J.G., Wästberg, D., Xue, L., Zhang, Z. (2017). Urban Multi-scale Environmental Predictor (UMEP) - An integrated tool for city-based climate services, *Environmental Modelling and Software* 99, 70-87.
- Lindberg, F., Grimmond, C.S.B., Gabey, A., Jarvi, L., Kent, C.W., Krave, N., Sun, T., Wallenberg, N., Ward, H.C. (2019). *Urban Multiscale Environmental Predictor University of Reading UK, University of Gothenburg Sweden, SIMS China*  
<https://umep-docs.readthedocs.io/>

- Liu, Z., Zheng, S., Zhao, L. (2018). Evaluation of the ENVI-met vegetation model of four common tree species in a subtropical hot-humid area. *Atmosphere*, 9 (5), 198.
- Liu, D., Hu, S., Liu J. (2020). Contrasting the performance capabilities of urban radiation field between three microclimate simulation tools. *Building and Environment*, 175, 106789.
- Loridan, T., Grimmond, C.S.B., Offerle, B.D., Young, D.T., Smith, T., Järvi, L., Lindberg, F. (2011). Local-scale urban meteorological parameterization scheme (LUMPS): longwave radiation parameterization and seasonality-related developments. *J. Appl. Meteor. Climatol.* 50, 185–202
- Lowry, W. P. (1977) Empirical estimation of the urban effects on climate: A problem analysis. *Journal Applied Meteorology*, 16, 129–135.
- Maloney, S.K., Forbes, C.F. (2011). What effect will a few degrees of climate change have on human heat balance? Implications for human activity. *International Journal of Biometeorology*, 55, 147–160.
- Maronga, B., Gryscha, M., Heinze, R., Hoffman, F., Kanani-Sühring, F., Keck, M., Ketelsen, K., Letzel, M.O., Sühring, M., Raasch, S. (2015). The Parallelized Large-Eddy Simulation Model (PALM) version 4.0 for atmospheric and oceanic flows: model formulation, recent developments, and future perspectives. *Geoscientific Model Development* 8, 1539-1637.
- Martinez, G.S., Diaz, J., Hooyberghs, H. (2018). Heat and health in Antwerp under climate change: projected impacts and implications for prevention. *Environ. Int.* 111, 135–143.
- Matzarakis, A., Rutz, F., Mayer, H., Modelling the thermal bioclimate in urban areas with the RayMan Model, Proceedings from the 23<sup>rd</sup> Conference on Passive and Low Energy Architecture (PLEA), Geneva, 6-8 September 2006.
- Matzarakis, A., Rutz, F., Mayer, H. (2007). Modelling radiation fluxes in simple and complex environments—application of the RayMan model. *International Journal of Biometeorology*, 51, 323-334.
- Matzarakis, A., Amelung, B. (2008). Physiological Equivalent Temperature as Indicator for Impacts of Climate Change on Thermal Comfort of Humans Seasonal Forecasts, Climatic Change and Human Health, Springer, 161-172
- Matzarakis, A., Rutz, F., Mayer, H., (2010). Modelling radiation fluxes in simple and complex environments: basics of the RayMan model. *International Journal and Biometeorology*, 54 (2), 131–139.
- Mayer, H., Höpfe, P. (1987) Thermal comfort of man in different urban environments. *Theoretical and Applied Climatology*, 38, 43–49.

- Mayer, H., Holst, J., Dostal, P., Imbery, F., Schindler, D. (2008). Human thermal comfort in summer within an urban street canyon in Central Europe. *Meteorol. Z.* 17 (3), 241–250.
- McIlvaine, J.E.R. Barkaszi, D.J. Beal, M.T. Anello, S.F. (2000). Laboratory Testing of the Reflectance Properties of Roofing Materials Florida Solar Energy Center (FSEC).
- McMichael, A.J., Wilkinson, P., Kovats, R.S. (2008). International study of temperature, heat and urban mortality: the ‘ISOTHURM’ project. *International Journal Epidemiology*, 37 (5), 1121–1131.
- Michelozzi, F., De’ Donato, L., Bisanti, A., Russo, E., Cadum, M., De Maria, M., D’Ovidio, G., Costa, A., Perucci C.A. (2005). The impact of the summer 2003 heat waves on mortality in four Italian cities, *Euro Surveill*, 10(7), 161-165.
- Michelozzi, P., Accetta, G., De Sario, M. (2008). High temperature and hospitalizations for cardiovascular and respiratory causes in 12 European cities. *Am. J. Respir. Crit. Care Med.*, 179 (5), 383–389.
- Monteith, J.L. (1965). Evaporation and environment. *Symp. Soc. Exp. Biol.* 19, 205–224.
- Morabito, M., Crisci, A., Gioli, B., Gualtieri, G., Toscano, P., Di Stefano, V., Orlandini, S., Gensini, G.F. (2015). Urban-hazard risk analysis: Mapping of heat-related risks in the elderly in major Italian cities. *PLoS One*, 10.
- Morakinyo, T.E., Dahanayake, K.W.D.K.C., Ng, E. (2017). Temperature and cooling demand reduction by green-roof types in different climates and urban densities: A co-simulation parametric study, *Energy and Buildings*, 145, 226–237.
- Morakinyo, T.E., Lau, K.K.L., Ren, C., Ng, E. (2018). Performance of Hong Kong’s common trees species for outdoor temperature regulation, thermal comfort and energy saving, *Building and Environment*, 137, 157–170.
- Morakinyo T. E., Laib A., Ka-Lun Laua K., Ng, E. (2019). Thermal benefits of vertical greening in a high-density city: Case study of Hong Kong. *Urban Forestry & Urban Greening*, 37, 42-55.
- Morakinyo, T. E., Ouyang, W., Ng, C.E. (2020). Right tree, right place (urban canyon): Tree species selection approach for optimum urban heat mitigation - development and evaluation. *Science of Total Environment*, 719, 137461.
- Morille, B., Lauzet, N., Musy, M. (2015). SOLENE-microclimate: A tool to evaluate envelopes efficiency on energy consumption at district scale. *Energy Procedia*, 78, 1165–1170.
- Morini, E., Touchaei, A.G., Castellani, B., Rossi, F., Cotana, F. (2016). The impact of albedo increase to mitigate the urban heat island in Terni (Italy) using the WRF model. *Sustainability*, 8, 999.

- Morris, C., Simmonds, I. (2000). Associations Between Varying Magnitudes of the Urban Heat Island and the Synoptic Climatology in Melbourne, Australia. *International Journal of Climatology*, 20, 1931- 1957.
- Muscio, A., Libbra, A., Siligardi, C., Tartarini, P. (2011). Sviluppo di materiali ad elevata riflessione solare per l'ottimizzazione delle prestazioni energetiche degli edifici durante la stagione estiva, Modena.
- Muscio, A. (2018). The solar reflectance index as tool to forecast the heat released to the urban environment: potentiality and assessment issues. *Climate*, 6(12): 1–21.
- Musy, M., Malys, L., Morille, B., Inard, C. (2015). The use of SOLENE-microclimat model to assess adaptation strategies at the district scale. *Urban Climate* 14, 213–223.
- Nestoras A., Montazeri H., Neophytou, M. (2019). CFD simulation of urban microclimate: validation using high-resolution field measurements. *Science of Total Environment*, 695 (12), 133743.
- Niachou, K., Papakonstantinou, K., Santamouris, A., Tsagroussoulis, A., Mihalakakou, G. (2001). Analysis of the green roof thermal properties and investigations of its energy performance. *Energy and Buildings*, 33, 719-729.
- Nice, K.A., Coutts, A.M., Tapper, N.J. (2018). Development of the VTUF-3D v1. 0 urban microclimate model to support assessment of urban vegetation influences on human thermal comfort. *Urban Climate*, 24: 1052–1076.
- Ng, E., Chen, L., Wang, Y., Yuan, C. (2012). A study on the cooling effects of greening in a high-density city: An experience from Hong Kong, *Building and Environment*, 47, 256–271.
- Offerle, B., Grimmond, C.S.B., Fortuniak, K. (2005). Heat storage and anthropogenic heat flux in relation to the energy balance of a central European city centre. *International Journal of Climatology*. 25, 1405–1419.
- Oke, T.R. (1973). City size and urban heat island. *Atmospheric Environment*, 7, 769-779.
- Oke, T. (1976). The Distinction Between Canopy and Boundary-Layer Urban Heat Islands, *Atmosphere*, 14, 277- 268.
- Oke, T.R. (1977). Urban Climates and Global Environmental Change, in: Russell, T., Perry, A. *Applied climatology. Principles and practice*.
- Oke, T.R. (1978). *Boundary Layer Climates*. Methuen & Co Ltd., London.
- Oke, T.R. (1982). The energetic basis of the urban heat island. *Q. J. R. Meteorological Society*, 1982; 108 (455), 1–24.
- Oke, T.R. (1987). *Boundary layer climates*, Second edition, Inc. NY, USA, 1987; 452.
- Oke, T.R. (1988). Street design and urban canopy layer climate. *Energy and Buildings*, 7, 769-779.



- Oke, T.R., Johnson, G.T., Steyn, D.G., Watson, I.D. (1991). Simulation of surface urban heat islands under «ideal» conditions at night part 2: Diagnosis of causation. *Boundary-Layer Meteorology* 56, 339–358.
- Oke, T.R. (2002). *Boundary layer climates*. Routledge.
- Oke, T.R. (2004). Initial guidance to obtain representative meteorological observations at urban sites. IOM Rep.81, WMO/TD-No. 1250, 47 pp. [Available online at [www.wmo.int/pages/prog/www/IMOP/publications/IOM-81/IOM-81-UrbanMetObs.pdf](http://www.wmo.int/pages/prog/www/IMOP/publications/IOM-81/IOM-81-UrbanMetObs.pdf).]
- Oke, T.R. (2008). Urban observations. Guide to meteorological instruments and methods of observation, Part II of Observing Systems, 7<sup>th</sup> ed., WMO-No. 8, II-11-1–II-11-25.
- Oke, T., Mills, G., Christen, A., Voogt, J.A. (2017). *Urban Climates*. Cambridge, University press.
- Paravantis, J., Santamouris, M., Cartalis, C., Efthymiou, C., Kontoulis, N. (2017). Mortality Associated with High Ambient Temperatures, Heatwaves, and the Urban Heat Island in Athens, Greece. *Sustainability*, 9, 606.
- Parizzotto, S., Lamberts, R. (2011). Investigation of green roof thermal performance in temperate climate: a case study of an experimental building in Florianopolis city, Southern Brazil. *Energy and Buildings*, 43, 1712-1722.
- Perera, N. G. R., Emmanuel, M. P. R., & Mahanama, P. K. S. (2012). Mapping “Local Climate Zones” and relative Warming Effects in Colombo, Sri Lanka. Paper Presented at ICUC8–8th International Conference on Urban Climates. Dublin, Ireland.
- Pérez, L., Cañero, R.F., Salas, A.F., Egea, G. (2015). Vertical Greening Systems and Sustainable Cities. *Journal of Urban Technology*, 22 (4), 65-85.
- Perez, R., Stewart, R., Arbogast, C., Seals, R., Scott, J. (1986). An anisotropic hourly diffuse radiation model for sloping surfaces: Description, performance validation, site dependency evaluation. *Solar Energy*, 36 (6), 481-497.
- Petkova, E.P., Gasparrini, A., Kinney, P.L. (2014). Heat and mortality in New York city since the beginning of the 20<sup>th</sup> century. *Epidemiology*, 25 (4), 554–560.
- Pickup, J., de Dear, R. An Outdoor Thermal Comfort Index (OUT\_SET\*)—Part I—The model and its assumptions, in: R. de Dear, J. Kalma, Oke, T., Auliciems, A.(Eds.), *Biometeorology and urban climatology at the turn of the millennium*, World Meteorological Organization, Geneva, Switzerland, 2000.
- Piselli, C., Castaldo, V.L., Pigliautile, I., Pisello, A.L., Cotana, F. (2018). Outdoor comfort conditions in urban areas: on citizens' perspective about microclimate mitigation of urban transit areas. *Sustainable Cities and Society*, 39, 16–36.

- Prado, A., Tedeu, R., Ferreira, L. (2005). Measurement of albedo and analysis of its influence the surface temperature of building materials. *Energy and Buildings*, 37, 295-300.
- Privitera R., Palermo, V., Martinico, F., Fichera, A., La Rosa D. (2018), Towards lower carbon cities: urban morphology contribution in climate change adaptation strategies, *European Planning Studies*, 26 (4), 812-837.
- Raasch, S., Schröter, M. (2021). PALM - a large-eddy simulation model performing on massively parallel computers. *Meteorologische Zeitschrift* 10, 363–372.
- Reindl, D.T., Beckman, W.A., Duffie, J.A. (1990). Diffuse fraction correlation. *Solar Energy*, 45, 1–7.
- Robitu, M., Musy, M., Inard, C., Groleau, D. (2006). Modeling the influence of vegetation and water pond on urban microclimate. *Sol Energy* 80, 435–447.
- Romeo, C., Zinzi, M. (2013). Impact of a cool roof application on the energy and comfort performance in an existing non-residential building. A Sicilian case study. *Energy and Buildings*, 67, 647–657.
- Rosenzweig, C., Solecki, W.D., Hammer, S.A., Mehrotra, S. (2011). *Climate Change and Cities: 2 First Assessment Report of the Urban Climate Change Research Network*. Cambridge University Press.
- Roth, M. (2002). Effects of cities on local climates. Paper presented at the Workshop of IGES/APN Mega-City Project, 23-25 January 2002, Kitakyushu, Japan.
- Roth, M. (2013). Urban Heat Islands, in: *Handbook of environmental fluid dynamics, volume two*, US: New York. CRC Press.
- Rui, L., Buccolieri, R., Gao, Z., Gatto, E., Ding, W. (2019). Study of the effect of green quantity and structure on thermal comfort and air quality in an urban-like residential district by ENVI-met modelling. *Building Simulation*, 12, 183–194.
- Sailor, D.J., Vasireddy, C. (2006). Correcting aggregate energy consumption data account for variability in local weather. *Environ. Modelling Software*. 21, 733–738.
- Sailor, D.J. (2011). Review of methods for estimating anthropogenic heat and moisture emissions in the urban environment. *International Journal Climatology*, 31, 189–199.
- Sakakibara, Y., Matsui, E. (2005). Relation between heat island intensity and city size indices/urban canopy characteristics in settlements of Nagano basin, Japan. *Geogr. Rev. Japan*, 78, 812–824.
- Sakka, A., Santamouris, M., Livada, I., Nicol, F., Wilson, M. (2012). On the thermal performance of low income housing during heat waves. *Energy and Buildings*, 49, 69–77.

- Salata, F., Golasi, I., De Lieto Vollaro, R., De Lieto Vollaro, A. (2016). Urban microclimate and outdoor thermal comfort. A proper procedure to fit ENVI-met simulation outputs to experimental data. *Sustainable Cities and Society*, 26, 318–343.
- Salvati, A., Roura, H.C., Cecere, C. (2017). Assessing the urban heat island and its energy impact on residential buildings in Mediterranean climate: Barcelona case study. *Energy and Buildings*, 146: 38-54.
- Salvati, A., Kolokotroni, M. Microclimate data for building energy modelling: study on ENVI-met forcing data, in: Proceedings of 16<sup>th</sup> IBPSA, Rome, 2019.
- Salvati, A., Kolokotroni, M. Impact of urban albedo on microclimate and thermal comfort over a heat wave event in London, Proceedings from the 11th Windsor Conference on Thermal Comfort, Windsor, 16-19 April 2020.
- Sam, C., Hui, M. (2009). Study of thermal and Energy Performance of Green Roof System, Final Report, The University of Hong Kong, Pokfulam Road, Hong Kong.
- Santamouris, M., Papanikolaou, N., Livada, I., Koronakis, I., Georgakis, C., Argiriou, A. (2001). On the impact of urban climate to the energy consumption of buildings. *Solar Energy*, 70(3), 201–216.
- Santamouris, M. (ed.) (2001). *Energy and Climate in the Urban Built Environment*. James & James (Science Publishers) Ltd., United Kingdom.
- Santamouris, M. (2006). Special Issue of the Solar Energy Program devoted to Natural Ventilation in Urban Areas, *Editorial in Solar Energy*, 80, 369–370.
- Santamouris, M. (2007). Heat island research in Europe: The state of the art. *Advanced Building Energy Resource*, 1, 123–150.
- Santamouris, M., Synnefa, A., Karlessi, T. (2011). Using advanced cool materials in the urban built environment to mitigate heat islands and improve thermal comfort conditions. *Solar Energy*, 85: 3085–3102.
- Santamouris, M., Xirafi, F., Gaitani, N., Spanou, A., Saliari, M., Vassilakopoulou, K. (2012). Improving the microclimate in a dense urban area using experimental and theoretical techniques: the case of Marousi, Athens. *International Journal of Ventilation*, 11(1), 1-16.
- Santamouris M. (2013). Using cool pavements as a mitigation strategy to fight urban heat island - A review of the actual developments. *Renewable Sustainable Energy Rev.* 26, 224–240.
- Santamouris, M., (2014a). On the energy impact of urban heat island and global warming on buildings. *Energy and Buildings*, 82, 100–113.

- Santamouris, M. (2014b). Cooling the cities – A review of reflective and green roof mitigation technologies to fight heat island and improve comfort in urban environments. *Solar Energy*, 103: 682–703.
- Santamouris, M., Kolokotsa, D. (2015a). On the impact of urban overheating and extreme climatic conditions on housing, energy, comfort and environmental quality of vulnerable population in Europe. *Energy and Buildings*. 98, 125–133.
- Santamouris, M., Cartalis, C., Synnefa, A., Kolokotsa, D. (2015b). On the impact of urban heat island and global warming on the power demand and electricity consumption of buildings—A review. *Energy and Buildings*, 98, 119–124.
- Santamouris, M. (2016). Urban warming and mitigation: Actual status, impacts and challenges. *Urban Climate Mitigation Techniques*, 1-26.
- Santamouris, M., Ding, L., Fiorito, F., Oldfield, P., Osmond, P., Paolini, R., Prasad, D., Synnefa, A. (2017). Passive and active cooling for the outdoor built environment – Analysis and assessment of the cooling potential of mitigation technologies using performance data from 220 large scale projects, *Solar Energy* 154, 14–33.
- Santamouris, M., Ban-Weiss, G., Osmond, P., Paolini, P., Synnefa A., Cartalis, C., Muscio, A., Zinzi, M., Morakinyo, T.E., Ng, E., Tan, Z., Takebayashi, H., Sailor, D., Crank, P., Taha, H., Pisello, A.L., Rossi, F., Zhang, J., Kolokotsa, D. (2018). Progress in urban greenery mitigation science – assessment methodologies advanced technologies and impact on cities. *Journal of Civil Engineering and Management*, 24 (8), 638–671.
- Simon, H. (2016). *Modeling urban microclimate: Development, Implementation And Evaluation Of New And Improved Calculation Methods For The Urban Microclimate Model ENVI-met (Doctoral dissertation)*. Johannes Gutenberg-Universität, Mainz, Germany.
- Simon, H., Lindén, J., Hoffmann, D., Braun, P., Bruse, M., Esper, J. (2018). Modeling transpiration and leaf temperature of urban trees – A case study evaluating the microclimate model ENVI-met against measurement data. *Landscape and Urban Planning*, 174, 33–40.
- Shashua-Bar, L., Hoffman, M. (2000). Vegetation as a climatic component in the design of an urban street: An empirical model for predicting the cooling effect of urban green areas with trees. *Energy and Buildings* 31(3), 221–235.
- Shuttleworth, W.J., (1978). A simplified one-dimensional theoretical description of the vegetation-atmosphere interaction. *Boundary-Layer Meteorol.* 14, 3–27.
- Skoulika, F., Santamouris, M., Kolokotsa, D., Boemia, N. (2013). On the thermal characteristics and the mitigation potential of a medium size urban park in Athens, Greece. *Landscape and Urban Planning* 123, 73–86.

- Song, B.G., Park, K.H., Jung, S.G. (2014). Validation of ENVI-met model with in situ measurements considering spatial characteristics of land use types, *J. Kor. Assoc. Geogr. Inf. Stud.* 17 (2), 156–172.
- Sözen, I., Koçlar Oral, G. (2018). Outdoor thermal comfort in urban canyon and courtyard in hot arid climate: A parametric study based on the vernacular settlement of Madrid, *Sustainable Cities and Society*, 1–15.
- Staiger, H., Laschewski, G., Grätz, A. (2012). The perceived temperature—a versatile index for the assessment of the human thermal environment, Part A: scientific basics. *International Journal of Biometeorology*, 56, 165-176
- Stathopoulou, E., Mihalakakou, G., Santamouris, M., Bagiorgas, H.S. (2008). On the impact of temperature on tropospheric Ozone concentration levels in urban environments, in: *Journal of Earth System Science*, 227–236.
- Stewart, I.D., Oke, T.R. (2010). Thermal differentiation of local climate zones using temperature observations from urban and rural field sites. *Extended Abstracts, Ninth Symp. on Urban Environment*, Keystone, CO, Amer. Meteor. Soc., 1.1. [Available online at <http://ams.confex.com/ams/19Ag19BLT9Urban/webprogram/Paper173127.html>.]
- Stewart, I.D., Oke, T.R. (2012). Local climate zones for urban temperature studies, *American meteorological society*, 1879-1900.
- Suehercke, H., Peterson, E.L., Selby, N. (2008). Effect of solar reflectance on the building heat gain in a hot climate. *Energy and Buildings*. 40, 2224-2235.
- Synnefa, A., Santamouris, M., Apostolakis, K. (2007). On the development, optical properties and thermal performance of cool colored coatings for the urban environment. *Solar Energy*, 81(4):488e97.
- Synnefa, A., Saliari, M., Santamouris, M. (2012). Experimental and numerical assessment of the impact of increased roof reflectance on a school building in Athens. *Energy and Buildings*, 55, 7–15.
- Synnefa, A., Santamouris, M. (2012). Advances of technical, policy and market aspects of cool roof technology in Europe: the cool roof project. *Energy Buildings*, 45, 35-41.
- Szücs, Á., Gál, T., Andrade, H. (2014). Comparison of measured and simulated mean radiant temperature. Case study in Lisbon (Portugal). *Finisterra-Revista Portuguesa de Geografia* 98, 95–111.
- Taha, H., Akbari, H., Rosenfeld, A., Huang, J. (1988). Residential cooling loads and the urban heat island-the effects of albedo. *Building and Environment* 23, 271–283.

- Taha, H. (1997). Urban climates and heat islands: albedo, evapotranspiration, and anthropogenic heat. *Energy and Buildings* 25, 99–103.
- Taha, H. (2007). Urban surface modification as a potential ozone air-quality improvement strategy in California – Phase 2: Fine-resolution meteorological and photochemical modeling of urban heat islands. Final report prepared by Altostratus Inc. for the California Energy Commission, Sacramento, California, PIER Environmental Research.
- Taha, H. (2015a). Cool cities: counteracting potential climate change and its health impacts. *Current Climate Change Reports* 1(3), 163–175.
- Taleb, D., Abu- Hijleh, B. (2013). Urban Heat Island: Potential Effect of Organic and Structured Urban Configurations on Temperature Variations in Dubai, *Renewable Energy*, 50, 747-762.
- Taesler, R. (1980). Studies of the development and thermal structure of the urban boundary layer in Uppsala. Uppsala University Meteorological Institute Rep. 61, 221.
- Tan, Z., Lau, K. K. L., Ng, E. (2017). Planning strategies for roadside tree planting and outdoor comfort enhancement in subtropical high-density urban areas. *Building and Environment*, 120, 93–109.
- Theodosiou, T.G. (2003). Summer period analysis of the performance of planted roof as a passive cooling technique. *Energy and Buildings*, 35, 909-917
- Thorsson, S., Lindberg, F., Eliasson, I., Holmer, B. (2007). Different methods for estimating the mean radiant temperature in an outdoor urban setting. *International Journal of Climatology*, 27 (14), 1983–1993.
- Thorsson, S., Lindberg, F., Björklund, J., Holmer, B. (2011). Rayner, Potential changes in outdoor thermal comfort conditions in Gothenburg, Sweden due to climate change: the influence of urban geometry. *International Journal of Climatology*, 31, 324–335.
- Thorsson S, Rocklöv J., Konarska J., Lindberg F., Holmer B, Dousset B, Rayner D. (2014). Mean radiant temperature – A predictor of heat related mortality. *Urban Climate*, 10, 332-345.
- Tsoka, S., Tsikaloudaki, K., Theodosiou, T. (2017). Urban space’s morphology and microclimatic analysis: A study for a typical urban district in the Mediterranean city of Thessaloniki, Greece, *Energy and Buildings*, 156, 96-108.
- Tsoka, S., Tsikaloudaki, A., Theodosiou, T. (2018). Analyzing the ENVI-met microclimate model's performance and assessing cool materials and urban vegetation applications—a review. *Sustainable Cities and Society*, 43, 55–76.
- Tsitoura, M., Michailidou, M., Tsoutsos, T. (2016). Achieving sustainability through the management of microclimate parameters in Mediterranean urban environments during summer. *Sustainable Cities and Society* 26, 48–64.

- Tzavali, A., Paravantis, J.P., Mihalakakou, G., Fotiadi, A., Stigka, E. (2015). Urban heat island intensity: A literature review. *Fresenius Environmental Bulletin*, 24(12): 4537-4554.
- UN, 2014. World urbanization prospects. <https://doi.org/10.18356/527e5125-en>
- Underwood, C.R., Ward, E.J. (1966). The solar radiation area of man. *Ergonomics* 9 (2), 155–168.
- United Nations D of E and SA. (2014). Revision of the world urbanization prospects. World Urban Prospect, 1–26.
- Vallati, A., Mauri, L., Colucci, C. (2018). Impact of shortwave multiple reflections in an urban street canyon on building thermal energy demands. *Energy & Buildings*, 174, 77–84
- van Vuuren, D.P., Edmonds, J., Kainuma, M. (2011). The representative concentration pathways: an overview. *Climate Change*, 109 (1), 5–31.
- Vanos, J. K., Warland, J. S., Gillespie, T. J., and Kenny N.A. (2010). Review of the physiology of human thermal comfort while exercising in urban landscapes and implications for bioclimatic design. *International Journal of Biometeorology*, 54, 319–334.
- Verein Deutscher Ingenieure, 2001. Umweltmeteorologie: Wechselwirkungen zwischen Atmosphäre und Oberflächen, Berechnung der spektralen Bestrahlungsstärken im solaren Wellenlängenbereich [Environmental Meteorology: Interactions between atmosphere and surfaces, calculation of spectral irradiances in the solar wavelength range] (VDI 3789, Part 3). Beuth, Berlin.
- Voogt, J., Oke, T. (2003). Thermal remote sensing of urban climates. *Remote Sensing Environment*, 86, 370–384.
- Vuckovic, M., Maleki, A., Kiesel, K., Mahdavi, A. Simulation-based assessment of uhi mitigation measures in central European cities, in: Proceedings of 14<sup>th</sup> IBPSA, Hyderabad, 2015.
- Wang, Y., Berardi, U., Akbari, H. (2016). Comparing the effects of urban heat island mitigation strategies for Toronto, Canada, *Energy and buildings*, 114, 2-19.
- Wang, R., Ren, C., Xu, Y., Lau, K.K.L., Shi, Y. (2018). Mapping the Local Climate Zones of Urban Areas by GIS-based and WUDAPT Methods: A Case Study of Hong Kong, *Urban Climate*, 24, 567-576.
- Ward, K.; Lauf, S.; Kleinschmit, B.; Endlicher, W. (2016). Heat waves and urban heat islands in Europe: A review of relevant drivers, *Science of the Total Environment*, 527–539.
- Ward, H.C., Kotthaus, S., Järvi, L., Grimmond, C.S.B. (2016). Surface urban energy and water balance scheme (SUEWS): development and evaluation at two UK sites. *Urban Climate* 18, 1-32.

- Watkins, R., Palmer, J., Kolokotroni, M. (2007). Increased temperature and intensification of the urban heat island – implications for human comfort and urban design. *Built Environment*, 33(1), 85-96.
- Weih, P., Staiger, H., Tinz, B., Batchvarova, E., Rieder, H., Vuilleumier, L. (2012) The uncertainty of UTCI due to uncertainties in the determination of radiation fluxes derived from measured and observed meteorological data. *International Journal of Biometeorology*, 6, 537-355.
- WHO, 2018. Health and sustainable development. Climate risk [WWW Document]. URL <http://www.who.int/sustainable-development/cities/health-risks/climate-risks/en/>
- WHO, 2019. Health Impact Assessment (HIA). <https://www.who.int/hia/evidence/doh/en/>.
- Willmott, C.J. (1982). Some comments on the evaluation of model performance, *Bulletin of the American Meteorological Society* 63, 1309–1313.
- Willmott, C.J., Robeson, S.M., Matsuura, K. (2012). Short Communication A refined index of model performance. *International Journal of Climatology* 32, 2088–2094.
- Wilmers, F. (1991). Effects of vegetation on urban climate and buildings. *Energy and Buildings*, 15–16, 507–514.
- Wong, N.H., Kardinal Yusuf, S., Aung La Win, A., Kyaw Thu, H., Syatia Negara, T., and Xuchao, W. (2007). Environmental study of the impact of greenery in an institutional campus in the tropics. *Building and Environment*, 42(8), 2949-2970.
- Wong, N.H., Yu, C. (2009). *Tropical urban heat islands: Climate, buildings and greenery*. Taylor and Francis, New York, USA.
- World Development Indicators, 2020. <https://databank.worldbank.org/source/world-development-indicators>. Data extracted on 02/11/2020
- Yang, X., Zhao, L., Bruse, M., Meng, Q. (2013). Evaluation of a microclimate model for predicting the thermal behavior of different ground surfaces. *Building and Environment* 60, 93–104.
- Yanwen Duan, (2017). Research on Evaluation of Urban Microclimate Simulation Tools Based on Green Plants, Nanjing University.
- Yin, S., Lang, W., Xiao, Y. (2019). Correlative impact of shading strategies and configurations design on pedestrian-level thermal comfort in traditional shophouse neighbourhoods, southern China. *Sustainability*, 11 (5), 1355.
- Young, A. (2017). Universal Thermal Climate Index. [http://www.utci.org/utci\\_doku.php](http://www.utci.org/utci_doku.php).
- Yow, D. M. (2007). Urban heat islands: observations, impacts, and adaptation. *Geography Compass*, 1(6), 1227-1251.
- Yu, C.; Wing H.N. (2006). Thermal benefits of city parks, *Energy and Buildings* 38, 105–120.



- Yuan, J., Emura, K., Farnham, C. (2016). Potential for Application of Retroreflective Materials instead of Highly Reflective Materials for Urban Heat Island Mitigation. *Urban Studies Research*, 16, 1-10.
- Zare, S., Hasheminejad, N., Shirvan, H.E., Hemmatjo, R., Sarebanzadeh, K., Ahmadi, S. (2018). Comparing Universal Thermal Climate Index (UTCI) with selected thermal indices/environmental parameters during 12 months of the year. *Weather and Climate Extremes*, 19, 49-57.
- Zauli Sajani, S., Tibaldi, S., Scotto, F., Lauriola, P. (2008). Bioclimatic characterization of an urban area: A case study in Bologna (Italy). *International Journal of Biometeorology*, 52, 779–785.
- Zhang, L., Zhan, Q., Lan, Y., (2018). Effects of the tree distribution and species on outdoor environment conditions in a hot summer and cold winter zone: a case study in Wuhan residential quarters. *Building and Environment* 130, 27–39.
- Zhang, W., Mak, C.M., Ai, Z.T., Siu, W.M. (2012). A Study of the Ventilation and Thermal Comfort of the Environment Surrounding a New University Building under Construction. *Indoor and Built Environment*, 21, 568-582.
- Zhao, T.F., Fong, K.F. (2017). Characterization of different heat mitigation strategies in landscape to fight against heat island and improve thermal comfort in hot–humid climate (part I): measurement and modelling. *Sustainable Cities and Society* 32, 523–531.
- Zinzi, M. (2015). Cool materials, in: *Energy Performance of Buildings: Energy Efficiency and Built Environment in Temperate Climates*. 415–436.
- Zoras, S., Tsermentselis, A., Kosmopoulos, P., Dimoudi, A. (2014). Evaluation of the application of cool materials in urban spaces: A case study in the center of Florina. *Sustainable Cities and Society*, 13, 223–229.